

**RENAN FRANCISCO SOARES**

**DRAG OF ROAD CARS: COST-EFFECTIVE CFD  
SETUP, PROPOSAL OF AN AERODYNAMIC  
CONCEPT AND CASE STUDIES**



UNIVERSIDADE FEDERAL DE UBERLÂNDIA  
FACULDADE DE ENGENHARIA MECÂNICA

**2015**



**RENAN FRANCISCO SOARES**

**DRAG OF ROAD CARS: COST-EFFECTIVE CFD SETUP, PROPOSAL  
OF AN AERODYNAMIC CONCEPT AND CASE STUDIES**

**Dissertação** apresentada ao Programa de Pós-graduação em Engenharia Mecânica da Universidade Federal de Uberlândia, como parte dos requisitos para a obtenção do título de **MESTRE EM ENGENHARIA MECÂNICA**.

Área de Concentração: Transferência de calor e Mecânica dos fluidos

Orientador: Prof. Dr. Francisco José de Souza.

**UBERLÂNDIA - MG**

**2015**

Dados Internacionais de Catalogação na Publicação (CIP)  
Sistema de Bibliotecas da UFU, MG, Brasil.

---

S676d      Soares, Renan Francisco, 1990-  
2015      Drag of road cars: cost-effective CFD setup, proposal of an  
aerodynamic concept and case studies / Renan Francisco Soares. - 2015.  
163 p. : il.

Orientador: Francisco José de Souza.  
Dissertação (mestrado) - Universidade Federal de Uberlândia,  
Programa de Pós-Graduação em Engenharia Mecânica.  
Inclui bibliografia.

1. Engenharia mecânica - Teses. 2. Arrasto (Aerodinâmica) - Teses.  
3. Indústria automobilística - Brasil - Teses. 4. Fluidodinâmica  
computacional - Teses. I. Souza, Francisco José de, 1973-.  
II. Universidade Federal de Uberlândia, Programa de Pós-Graduação em  
Engenharia Mecânica. III. Título.

CDU: 621

---



## **FOLHA DE APROVAÇÃO**

*Essa página que deverá vir assinada pela Banca Examinadora será fornecida pela Secretaria de Pós-graduação após a defesa. Entretanto o aluno deverá solicitá-la somente depois de realizadas todas as correções sugeridas pela Banca e confirmadas pelo orientador.*



## **DEDICATION**

*À minha família;*

*Aos amigos e a todos que fizeram parte dos dois anos do curso de pós-graduação,  
desde minha chegada à universidade até a defesa deste trabalho.*



## ACKNOWLEDGEMENTS

*Aos meus pais, Osvaldo e Rosinha, e à minha irmã, Renata, pelo amor e apoio de todo o sempre.*

*À minha namorada, Mariana, por todo o amor, carinho, paciência e compreensão quanto às longas rotinas de trabalho noturno e em finais de semana.*

*Ao Prof. Dr. Francisco José de Souza, pela disposição de aceitar e orientar este trabalho; além da gentileza de compartilhar seus conhecimentos e amizade.*

*À Universidade Federal de Uberlândia e ao Laboratório de Mecânica dos Fluidos, por oferecer sua infraestrutura.*

*Ao Conselho Nacional de Desenvolvimento Científico e Tecnológico (CNPq), pelo suporte financeiro durante a pesquisa por meio de bolsa.*

*À CD-Adapco, por disponibilizar o uso do software Star-CCM+.*

*A todos os professores da rede pública brasileira de ensino, desde o nível fundamental ao de pós-graduação, que inspiraram e contribuíram para minha educação ao longo de 18 anos contados até a realização deste trabalho.*



“Our doubts are traitors  
And make us lose the  
good we oft might win  
by fearing to attempt.”  
(William Shakespeare)

*“No que diz respeito ao empenho, ao compromisso,  
ao esforço, à dedicação, não existe meio termo.  
Ou você faz uma coisa bem feita ou não faz.”*  
(Ayrton Senna)





SOARES, R. F. **Drag of Road Cars: Cost-effective CFD setup, Proposal of an aerodynamic concept and Case studies.** 2015. 163 p. MSc Thesis, Universidade Federal de Uberlândia, Uberlândia.

## ABSTRACT

This research investigates the drag in automotive aerodynamics. The main aim is to maximize the fuel efficiency of road cars, mainly those produced in Brazil. This is believed to be possible by means of aerodynamic development in drag reduction. In order to achieve this aim, this research investigates starting from the computational solution of vehicle aerodynamics, an aerodynamic concept is proposed and some cases are investigated.

Regarding the computational solution, this research outlines a best practice for the best cost-efficiency of computational resources, from the point of drag prediction over realistic car geometries. It may lead to improve the current aerodynamic development time in the automotive industry. As consequence, the increase in the amount of results would ground new concepts and shape optimization in a shorter time.

The proposal of an aerodynamic concept for fastback car models is aligned to the drag reduction, and subsequently the fuel efficiency aspect. Even though it is a concept, it has been based on a systematic CFD (Computational Fluid Dynamics) analysis of blowing and suction jet methods. In addition, it also would be feasible in the view of manufacturing process.

The third part of this work analyses the Brazilian Hatch 2015 cars and investigates the effect of exhaust gases on the drag coefficient of a realistic car model. The former compares the aerodynamic forces and geometry features of the best-selling Hatch 2015 car profiles, while the latter part deals with the quantitative effect of tailpipe position on the drag of a car model.

---

Keywords: Drag, Road car, Aerodynamics, CFD, Best practice, Brazilian automotive industry, Exhaust gas.



SOARES, R. F. **Arrasto Aerodinâmico de Automóveis: Melhores práticas de CFD para melhor custo-benefício, Proposta de conceito aerodinâmico e Estudos de caso.** 2015. 163 f. Dissertação de Mestrado, Universidade Federal de Uberlândia, Uberlândia

## RESUMO

O arrasto aerodinâmico de automóveis é o tema abordado neste trabalho. O objetivo principal é maximizar a eficiência energética de veículos, principalmente aqueles produzidos no Brasil. Tal objetivo pode ser alcançado através de tecnologia em aerodinâmica automotiva focada na redução de arrasto. Para isto, esta pesquisa trata desde a solução computacional de escoamentos ao redor da geometria de veículos, até a proposta de conceito aerodinâmico e estudo de casos.

No que se refere a solução computacional, este trabalho resulta uma metodologia de melhores práticas para uso da técnica CFD, em caráter de melhor custo-benefício dos recursos computacionais para predição de arrasto aerodinâmico. Isto pode levar a melhoramento do tempo de desenvolvimento em aerodinâmica pelas indústrias automobilística. Consequentemente, a possibilidade de mais resultados pode levar a novos conceitos e/ou otimização de geometria em período de tempo mais curto.

O conceito aerodinâmico proposto para carros tipo fastback destina-se a redução do arrasto e, consequentemente, atuar beneficemente na questão de eficiência energética. Apesar de ser uma proposta conceitual, este fundamenta-se em um estudo sistemático via CFD dos métodos de sucção e soprimento de jatos. Ainda, o conceito é aplicável do ponto de vista de projeto.

A terceira parte da pesquisa recai sobre a análise de veículos modelo Hatch 2015, e também sobre o efeito dos gases do escapamento no arrasto aerodinâmico. O primeiro tema compara forças aerodinâmicas e características da geometria através do perfil dos modelos Hatch 2015 brasileiros mais vendidos de dez marcas, enquanto o segundo tema aborda quantitativamente o efeito da posição da saída do escapamento no arrasto de uma geometria veicular.

---

Palavras chave: Arrasto aerodinâmico, Veículo, Aerodinâmica, CFD, Melhores práticas, Indústria automobilística brasileira, Gases de escape veicular.



## LIST OF FIGURES

Figure 1.1: Sample of drag coefficient over different geometries.....	2
Figure 1.2: Sample of design tools in automotive aerodynamics: DrivAer body in a wind tunnel (left), and the flow analysis of same car model via CFD technique (right). ....	3
Figure 2.1: Ahmed Body: geometry and drag coefficient. ....	10
Figure 2.2: Rover Model: geometry and drag coefficient for (a) stationary and (b) moving ground conditions. ....	10
Figure 2.3: Sketch of MIRA reference car. ....	11
Figure 2.4: DrivAer body: 1:2.5 scale dimension. ....	13
Figure 2.5: DrivAer vehicle category: (a) Fastback, (b) Notchback, and (c) Estateback.....	13
Figure 2.6: DrivAer underbody: (a) smooth underbody, and (b) detailed underbody.....	13
Figure 3.1: DrivAer body variations: (a) Fastback, (b) Notchback, and (c) Estateback. ....	26
Figure 3.2: DrivAer Fastback model: (a) woMwoW, (b) wMwoW, (c) woMwW, and (d) wMwW. ....	27
Figure 3.3: DrivAer Notchback model: (a) woMwW, and (b) wMwW.....	27
Figure 3.4: DrivAer Estateback model: (a) woMwW, and (b) wMwW.....	28
Figure 3.5: DrivAer Fastback profile for two-dimensional studies.....	28
Figure 3.6: Ten Brazilian Hatch 2015 car profiles. ....	29

Figure 3.7: Definition of the ground simulation approach ( <i>with GS &amp; W</i> ).	31
Figure 3.8: Boundaries of two-dimensional numerical domain.	32
Figure 3.9: Boundaries of three-dimensional numerical domain over a half-car model.	32
Figure 3.10: Boundaries of three-dimensional numerical domain over a full-car model.	33
Figure 3.11: Illustration of (a) regions of meshing control over the car and (b) impact of refinement on the ground surface.	35
Figure 3.12: Regions of meshing control: front and rear wheels refinement of 10 <i>mm</i> .	35
Figure 3.13: Regions of meshing control: vortex refinement of 20 <i>mm</i> .	36
Figure 3.14: Regions of meshing control: near wake refinement of 20 <i>mm</i> .	36
Figure 3.15: Regions of meshing control: larger wake refinement of 40 <i>mm</i> .	36
Figure 3.16: Regions of meshing control: diffuser edge refinement of 05 <i>mm</i> .	37
Figure 3.17: Regions of meshing control: spoiler edge refinement of 05 <i>mm</i> .	37
Figure 3.18: Regions of meshing control: lateral edge refinement of 05 <i>mm</i> .	37
Figure 3.19: Regions of meshing control: surrounding mirror refinement of 05 <i>mm</i> and mirror wake refinement of 10 <i>mm</i> .	38
Figure 3.20: Regions of meshing control: front bumper refinement of 05 <i>mm</i> .	38
Figure 3.21: Regions of meshing control: hood end refinement of 05 <i>mm</i> .	38
Figure 4.1: Comparison of pressure contours between the height of computational domain equal to 2.2 <i>Lref</i> (above) and 4.4 <i>Lref</i> (below).	42
Figure 4.2: Illustration of four level of mesh base size setting surrounding the vehicle profile: (a) 40 <i>mm</i> , (b) 20 <i>mm</i> , (c) 10 <i>mm</i> , and (d) 05 <i>mm</i> .	43
Figure 4.3: Realizable <i>k-ε</i> two-layer turbulence model: comparison of drag coefficient among all mesh base size and gradient schemes.	44

Figure 4.4: SST $k-\omega$ turbulence model: comparison of drag coefficient among all mesh base size and gradient schemes. ....	44
Figure 4.5: Drag coefficient prediction over different mesh base sizes and turbulence models, in 2 <sup>nd</sup> -order Green-Gauss gradient scheme.....	45
Figure 4.6: 2 <sup>nd</sup> -order Green-Gauss gradient scheme: comparison of drag coefficient prediction.....	46
Figure 4.7: 2 <sup>nd</sup> -order Hybrid Gauss-LSQ gradient scheme: comparison of drag coefficient prediction.....	46
Figure 4.8: Effects of Time regime on drag coefficient prediction.....	51
Figure 4.9: Effects of the mesh base size on drag coefficient prediction.....	52
Figure 4.10: Mesh base size over the car surface: (a) 20 mm, (b) 10 mm, and (c) 05 mm. ...	53
Figure 4.11: Effects of the gradient method on drag coefficient prediction.....	54
Figure 4.12: Effects of the total prism layer thickness on drag coefficient prediction.....	55
Figure 4.13: Sample of prism layers contouring the rear-end edge.....	56
Figure 4.14: Effects of the ground condition in different car assemblies on drag coefficient prediction.....	57
Figure 4.15: Effects of the ground condition at different flow regimes on the drag coefficient prediction.....	59
Figure 4.16: Vector velocity field on the ground and wheel surfaces: stationary ground & wheels (above), ground & wheels movement (centre), and front-right wheel in detail (below). ....	61
Figure 4.17: Comparison of Realizable $k-\epsilon$ two-layer and SST $k-\omega$ turbulence models.....	62
Figure 4.18: Effects of turbulence models on drag coefficient prediction at different freestreams. ....	63

Figure 4.19: Effects of car model type on drag coefficient prediction. ....	66
Figure 5.1: Turbulent kinetic energy magnitude over: (a) FSwMwW, with GS & W at 16 <i>m/s</i> and (b) FSwoMwW, with GS & W at 16 <i>m/s</i> ; and (c) FSwoMwW, with GS & W at 40 <i>m/s</i> . ....	70
Figure 5.2: Comparison of RANS steady-state simulations via iso-vorticity surface of 100 <i>rad/s</i> <sup>2</sup> over the three DrivAer variations. Each car type are presented in: wMwW, with GS & W (upper row); woMwW, with GS & W (middle row); and woMwW, wo/GS (lower row). ....	71
Figure 6.1: Exemplification of the three slot positions on the vehicle profile. ....	80
Figure 6.2: Jet speed at 10 <i>m/s</i> : Global (above) and corrected (below) drag coefficient. ....	83
Figure 6.3: Jet speed at 20 <i>m/s</i> : Global (above) and corrected (below) drag coefficient. ....	83
Figure 6.4: Streamlines over the DrivAer Fastback baseline profile at 40 <i>m/s</i> (above), and wake region behind its rear (below). ....	84
Figure 6.5: Velocity magnitude: blowing jet at 10 <i>m/s</i> . ....	85
Figure 6.6: Velocity magnitude: blowing jet at 20 <i>m/s</i> . ....	86
Figure 6.7: Velocity magnitude: suction jet at 10 <i>m/s</i> . ....	87
Figure 6.8: Velocity magnitude: suction jet at 20 <i>m/s</i> . ....	88
Figure 6.9: Representative sketch of the passive aerodynamic system concept over the DrivAer fastback model. ....	90
Figure 7.1: The best-seller 2015 model of each one of the ten best-seller manufactures. ....	95
Figure 7.2: Influence of roof end angle in the drag of a full-scale car production. ....	96
Figure 7.3: Comparison of rear-end spoilers among Chevrolet Onix (small, sharing the roof curve), Citroen C3 (small, with slight change of trailing angle) and Nissan March (extended roof spoiler with a protuberance). ....	97



Figure 7.4: Definition of the three slant angles proposed: $\alpha$ , $\beta$ , and $\gamma$ .	99
Figure 7.5: Flow direction: realistic 3D car body (above) and simplified 2D car profile (below).	101
Figure 7.6: Comparison Drag force and profile height over the ten Hatch car models.	102
Figure 7.7: Drag coefficient and drag coefficient ratio over the ten Hatch car models.	103
Figure 7.8: Lift force and profile height over Hatch car models.	104
Figure 7.9: Comparison of fuel consumption (ethanol and gasoline) in highway cycle and drag force among the car models, from the lowest to the highest energy consumption.	105
Figure 8.1: Sketch of tailpipe, in horizontal position in the Y-Z plane.	108
Figure 8.2: Definition of the tailpipe position on the rear car.	108
Figure 8.3: The ten positions of symmetric tailpipes on the rear car.	109
Figure 8.4: Illustrations of the optimum tailpipe position (position 5) on the DrivAer Fastback car model.	117
Figure 8.5: Plot of drag coefficient map via interpolation process.	118
Figure 8.6: Drag coefficient map from all ten tailpipe positions on the rear car.	118
Figure 8.7: Comparison of streamlines from the tailpipes in position 5 (above), position 7 (centre), and position 10 (below). The car surface display the pressure on the vehicle.	119
Figure 12.1: Iso-vorticity surface of 100 rad/s <sup>2</sup> : wMwW, with GS & W.	129
Figure 12.2: Iso-vorticity surface of 100 rad/s <sup>2</sup> : woMwW, with GS & W.	130
Figure 12.3: Iso-vorticity surface of 100 rad/s <sup>2</sup> : woMwW, wo/ GS.	131
Figure 12.4: TKE magnitude from 8 to 15 J/kg: wMwW, with GS & W.	132
Figure 12.5: TKE magnitude from 8 to 15 J/kg: woMwW, with GS & W.	133
Figure 12.6: TKE magnitude from 8 to 15 J/kg: woMwW, wo/ GS.	134

Figure 12.7: Q-criterion at 10 rad/s <sup>2</sup> : wMwW, with GS & W. ....	135
Figure 12.8: Q-criterion at 10 rad/s <sup>2</sup> : woMwW, with GS & W. ....	136
Figure 12.9: Q-criterion at 10 rad/s <sup>2</sup> : woMwW, wo/ GS. ....	137
Figure 12.10: Q-criterion at 200 rad/s <sup>2</sup> : wMwW, with GS & W. ....	138
Figure 12.11: Q-criterion at 200 rad/s <sup>2</sup> : woMwW, with GS & W. ....	139
Figure 12.12: Q-criterion at 200 rad/s <sup>2</sup> : woMwW, wo/ GS. ....	140
Figure 12.13: DES simulation: vorticity magnitude in xy planes (above) and zx planes (above). .....	141
Figure 12.14: DES simulation: Q- (above) and Lambda-2 criteria (below) at 1 <i>rad/s</i> <sup>2</sup> .....	142
Figure 12.15: DES simulation: Q- (above) and Lambda-2 criteria (below) at 10 <i>rad/s</i> <sup>2</sup> ....	143
Figure 12.16: DES simulation: Q- (above) and Lambda-2 criteria (below) at 100 <i>rad/s</i> <sup>2</sup> ..	144
Figure 12.17: DES simulation: Q- (above) and Lambda-2 criteria (below) at 1000 <i>rad/s</i> <sup>2</sup> ..	145
Figure 12.18: DES simulation: Q- (above) and Lambda-2 criteria (below) at 10000 <i>rad/s</i> <sup>2</sup> . .....	146
Figure 12.19: DES simulation: Q-criterion at 10000 <i>rad/s</i> <sup>2</sup> , highlighting the vortex structures into the wheelhouses. ....	147
Figure 12.20: Hatch 2015 car profiles: Fiat Palio, Volkswagen Gol, and Chevrolet Onix. ...	148
Figure 12.21: Hatch 2015 car profiles: Hyundai HB20, Ford New Fiesta, and Renault Sandero. .....	149
Figure 12.22: Hatch 2015 car profiles: Toyota Etios, Ford New Fiesta, and Renault Sandero. .....	150
Figure 12.23: Hatch 2015 car profiles: Peugeot 208. ....	151
Figure 12.24: Hatch 2015 car meshing: Fiat Palio, and Volkswagen Gol.....	152

Figure 12.25: Hatch 2015 car meshing: Chevrolet Onix, Hyundai HB20, and Ford New Fiesta. .....	153
Figure 12.26: Hatch 2015 car meshing: Renault Sandero, Toyota Etios, and Citroen C3.....	154
Figure 12.27: Hatch 2015 car meshing: Nissan March, and Peugeot 208.....	155
Figure 12.28: Rear car view: the ten positions of symmetric tailpipes tested. ....	156
Figure 12.29: Perspective view: the ten positions of symmetric tailpipes tested.....	157
Figure 12.30: Vector velocity field crossing the tailpipes in the zx plane (part A).....	158
Figure 12.31: Vector velocity field crossing the tailpipes in the zx plane (part B).....	159
Figure 12.32: Vector velocity field crossing the tailpipes in the zx plane (part C).....	160
Figure 12.33: Streamlines from exhaust system (part A).....	161
Figure 12.34: Streamlines from exhaust system (part B).....	162
Figure 12.35: Streamlines from exhaust system (part C).....	163



## LIST OF TABLES

Table 3.1: Frontal area of DrivAer model variations and assemblies. ....	26
Table 3.2: Comparative of mesh types. ....	34
Table 3.3: Meshing model. ....	34
Table 4.1: Numerical setup factors and levels. ....	40
Table 4.2: Physical setup. ....	40
Table 4.3: Boundary conditions. ....	40
Table 4.4: Proposal of best practice in CFD setup for two-dimensional automotive cases. ....	47
Table 4.5: Physical setup. ....	48
Table 4.6: Boundary conditions. ....	49
Table 4.7: Description of numerical factors and levels. ....	50
Table 4.8: Experimental drag coefficient of DrivAer model assemblies (Heft <i>et al.</i> 2012). ...	50
Table 4.9: Recommended CFD methodology: best cost-effective setup for drag prediction, biased towards the low computational cost. ....	67
Table 4.10: Alternative CFD methodology: best cost-effective setup for drag prediction, biased towards the numerical accuracy. ....	68
Table 5.1: Comparison of the external flow: wMwW DrivAer models, with GS & W. ....	71

Table 5.2: Comparison of the external flow: woMwW DrivAer models, with GS & W. ....	73
Table 5.3: Comparison of the external flow: woMwW DrivAer models, wo/ GS. ....	74
Table 5.4: Comparison of external flow phenomena over DrivAer Fastback model: Q-criterion versus Lambda 2 criterion at $104 \text{ rad/s}^2$ via DES unsteady-state simulation. ....	75
Table 6.1: Physical setup. ....	81
Table 6.2: Boundary conditions. ....	81
Table 7.1: Slant angles ( $\alpha$ , $\beta$ , and $\gamma$ ) of Brazilian Hatch 2015 models. ....	99
Table 7.2: Physical setup. ....	100
Table 7.3: Boundary conditions. ....	100
Table 8.1: Position and orientation of tailpipe on the rear car. ....	109
Table 8.2: Parameters for estimation of exhaust mass flow. ....	112
Table 8.3: Physical setup. ....	114
Table 8.4: Best practices for CFD setup: exhaust flow analysis. ....	114
Table 8.5: Boundary conditions. ....	115
Table 8.6: Comparison of drag coefficient from several tailpipe positions. ....	115

## LIST OF ACRONYMS

CFD	Computational Fluid Dynamics
INMETRO <sup>1</sup>	<i>Instituto Nacional de Metrologia, Qualidade e Tecnologia</i>
IPI <sup>2</sup>	<i>Imposto sobre Produtos Industrializados</i>
LSQ	Least squared
MGU-H	Motor Generator Unit - Heat
MGU-K	Motor Generator Unit - Kinetic
NACA	National Advisory Committee for Aeronautics
RANS	Reynolds-Averaged Navier-Stokes
RSM	Reynolds Stress Model
RNG	Renormalization Group (theory used with $k$ -epsilon turbulence models)
SA	Spalart-Allmaras
SST	Shear-Stress Transport
TKE	Turbulent Kinetic Energy
URANS	Unsteady Reynolds-Averaged Navier-Stokes

---

<sup>1</sup> National Institute of Metrology, Quality and Technology, in English. This institute was created to support the Brazilian enterprises, to increase their productivity and the quality of goods and services. Its major task is to improve the quality of life of the ordinary citizen as well as to seek the competitiveness of the economy through metrology and quality (INMETRO, 2015).

<sup>2</sup> Tax on Industrialized Products, in English. Indeed, it is a tax on industrialized products either manufactured or imported to Brazil. In the case of products manufactured in Brazil, taxes are imposed on the product sales price, while in the case of imported products, the tax base is the sales price plus import taxes and other required fees (ICCT, 2013)





## LIST OF SYMBOLS

$2D$	two-dimensional
$3D$	three-dimensional
$A_{ref}$	reference area
$C_D$	drag coefficient
$C_{D_{global}}$	global drag coefficient
$C_{D_{profile}}$	profile drag coefficient
$C_{D_{jet}}$	non-dimensional jet momentum correction for drag coefficient
$C_L$	lift coefficient
$C_p$	pressure coefficient
$ES$	estateback model with smooth underbody
$F_D$	drag force
$FS$	fastback model with smooth underbody
$H_{wt}$	section test height of wind tunnel
$H_{ref}$	reference height
$I$	turbulence intensity
$L_{ref}$	reference length
$l_t$	turbulence length scale
$\dot{m}_{air}$	mass rate of air
$\dot{m}_{exhaust}$	mass rate of an exhaust tailpipe
$\dot{m}_f$	mass rate of fuel
$\dot{m}_T$	mass rate of air and fuel combined in the exhaust system
$NS$	notchback model with smooth underbody
$r$	air mixture ratio of engine operation
$R$	wheel radius
$Re$	Reynolds number
$U_\infty$	relative air speed

$U_V$	vehicle speed
$U_w$	wind speed
$U_{GS}$	ground speed
$U_{jet}$	jet speed
$W_{wt}$	test section width of wind tunnel
$woM$	without mirrors
$wM$	with mirrors
$woW$	without wheels and wheelhouses
$wW$	with wheels and wheelhouses
$wo/ GS$	without ground movement
$with GS$	with ground movement
$with GS \& W$	with ground simulation & wheel surfaces under local rotation rate
$y^+$	non-dimensional distance from the wall
$\sim$	approximately
$\delta$	blockage ratio
$\Delta_f$	volumetric rate of fuel consumption
$\varepsilon$	turbulence dissipation rate
$k$	turbulent kinetic energy
$k-\varepsilon$	$k$ -epsilon turbulence model
$k-\omega$	$k$ -omega turbulence model
$\phi_{eq}$	theoretical fuel/air mass ratio
$\phi_r$	real fuel/air mass ratio
$\rho$	air density
$\rho_f$	fuel density
$\rho_{jet}$	jet fluid density
$\mu$	dynamic viscosity
$\mu_t$	turbulence viscosity
$\chi$	fuel consumption
$\omega$	turbulence dissipation specific rate
$\omega_w$	rotation rate of the wheels

## SUMMARY

Dedication .....	vii
Acknowledgements .....	ix
List of Figures.....	xvii
List of Tables.....	xxv
List of Acronyms.....	xxvii
List of Symbols.....	xxix
Summary .....	xxx
Chapter I - Introduction .....	1
1.1 Motivation .....	1
1.2 Research ObjeCtives.....	4
1.3 Relevance.....	5
1.4 Thesis Outline.....	6
Chapter II - Literature Review .....	9
2.1 Reference Car Geometry .....	9
2.1.1 DrivAer body .....	12
2.2 CFD Analysis of Vehicles .....	14
2.2.1 Geometry and Drag of High Performance Bicycle.....	14
2.2.2 Drag of Truck Shapes .....	15
2.2.3 Performance of Rally Car .....	17
2.2.4 Rear Spoiler of Road Car.....	18

2.3	Turbulence Models for Automotive Applications .....	19
2.4	Meshing Features .....	22
Chapter III - General Methodology .....		25
3.1	Geometry.....	25
3.1.1	Main Approach: three-dimensional geometries .....	25
3.1.2	Alternative Approach: two-dimensional profiles .....	28
3.2	Ground Treatment.....	30
3.2.1	Stationary Condition.....	30
3.2.2	Moving Condition .....	30
3.3	Numerical Domain.....	31
3.3.1	Two-Dimensional Cases.....	31
3.3.2	Three-Dimensional Cases.....	32
3.4	Meshing Process .....	33
3.4.1	Mesh Type.....	33
3.4.2	Meshing Model.....	34
3.4.3	Meshing Refinement .....	35
Chapter IV - Effects of CFD Setup for Automotive Applications.....		39
4.1	Two-Dimensional Qualitative Analysis.....	39
4.1.1	Effect of Blockage Ratio for Two-Dimensional Cases .....	41
4.1.2	Meshing Process.....	42
4.1.3	Analysis of Two-Dimensional CFD Setup.....	44
4.1.4	Summary of Two-Dimension Analysis.....	47
4.2	Three-Dimensional Quantitative Analysis.....	48
4.2.1	Analyses of Three-Dimensional CFD Setup .....	50
4.2.2	Summary of Three-Dimensional Analysis .....	67
Chapter V - Analysis of the flow over the DrivAer car Models .....		69
5.1	Analysis of the Flow via RANS Steady-State Simulations .....	69

5.1.1	Brief analysis of the flow via turbulent kinetic energy .....	69
5.1.2	Comparison of the external flow via iso-vorticity surface.....	71
5.2	Analysis of the Flow via DES Unsteady-State Simulation .....	75
5.3	Summary of Chapter V .....	77
Chapter VI - Proposal of an Aerodynamic Concept for Drag Reduction.....		79
6.1	Background.....	79
6.2	Methodology.....	80
6.3	Analysis of Results .....	81
6.4	Proposal of a Road Car Aerodynamic Concept.....	89
6.5	Summary of Chapter VI .....	91
Chapter VII - The Brazilian Automotive Scenario over the Hatch 2015 Car Models .....		93
7.1	Background.....	93
7.2	Hatch 2015 Car Models.....	95
7.3	Geometry Features.....	96
7.3.1	Roof End Angle .....	96
7.3.2	Rear-end Roof Spoiler .....	97
7.3.3	Rear Slant Angle.....	98
7.4	Analysis of Aerodynamic forces .....	100
7.4.1	Drag.....	102
7.4.2	Lift.....	103
7.4.3	Comparison of Drag and Fuel Consumption .....	105
7.5	Summary of Chapter VII .....	106
Chapter VIII - Effect of Tailpipe Position on the Drag Coefficient.....		107
8.1	Vehicle Geometry.....	107
8.2	Tailpipe Geometry.....	108
8.3	Exhaust Flow Modelling .....	110
8.3.1	Mass Rate of Fuel .....	110

8.3.2	Fuel/Air Mass Ratio .....	110
8.3.3	Exhaust Mass Flow .....	111
8.3.4	Estimation of a Realistic Exhaust Flow .....	112
8.4	Computational Approach .....	114
8.5	Results of Drag Coefficient.....	115
8.6	Analysis of Results.....	116
8.6.1	Qualitative Perspective.....	116
8.6.2	Quantitative Perspective.....	116
8.6.3	Drag Coefficient Map of Tailpipe Position.....	117
8.7	Summary of Chapter VIII .....	120
Chapter IX - Research Summary .....		121
Chapter X - Future Research recommendations .....		123
Bibliography.....		125
Appendix .....		128

# CHAPTER I

## INTRODUCTION

### 1.1 MOTIVATION

Aerodynamic drag has been the main focus of engineering interest in vehicle aerodynamics along the last decades. Both drag force and its non-dimensional number have practically become synonyms for automotive aerodynamics. In fact, important attributes of a vehicle such as performance, top speed, fuel consumption and emissions, are all influenced by drag (Hucho, 1998).

The aerodynamic force known as drag is defined as the component force against freestream direction on a body. In other words, a force that provides resistance to forwards motion of a vehicle. This aerodynamic force acts externally on the surface of a vehicle, and affects car performance in both speed and fuel economy, since engine power is required to overcome such opposing force. The non-dimensional form of drag is the drag coefficient ( $C_D$ ), which is defined as how aerodynamic a body shape is against to incoming airflow. This coefficient may be greater than 1, in case of the air is pushed outward in such way that the effective area of the air movement is greater than the real front area of body, *e. g.*, race cars, as seen in Figure 1.1.

As the body shapes are concerned, streamlined bodies are identified by attached flow trend. The influence of pressure on the drag force (component of aerodynamic force parallel to undisturbed flow) of these aerodynamic shapes is small. Drag is caused mostly by shear stresses on the body surface. Since shear forces are small, and pressure drag is minimal,

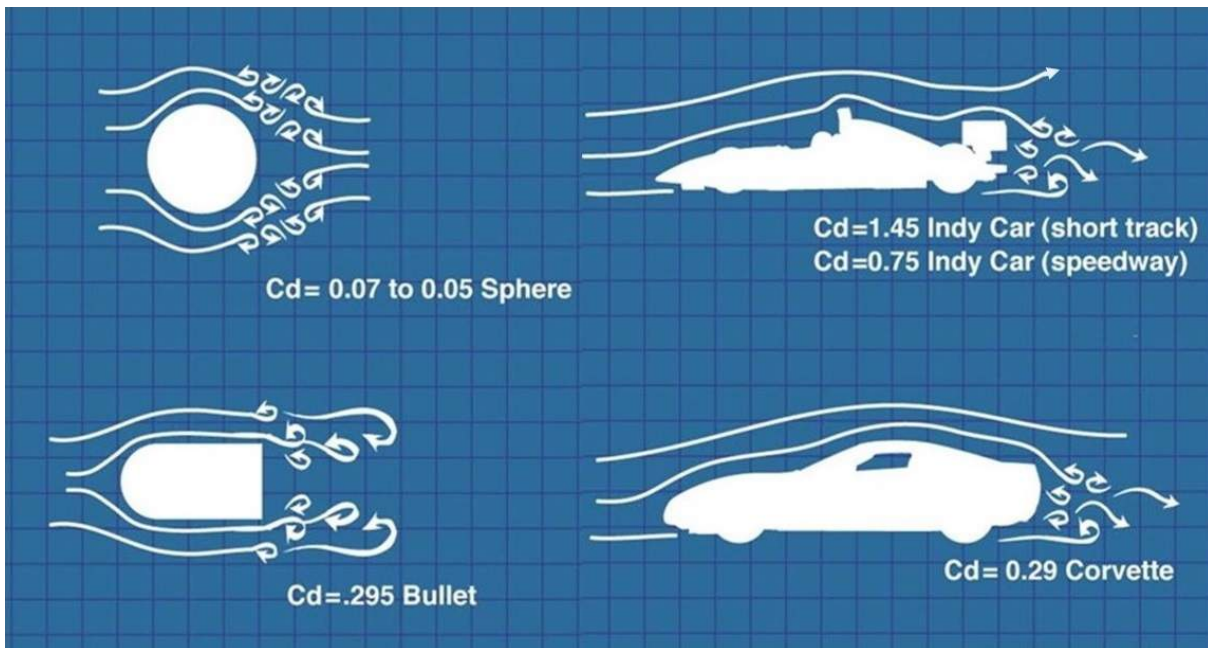


Figure 1.1: Sample of drag coefficient over different geometries.

drag coefficient is relatively small. On the other side, bluff bodies such as road cars usually have massive detachment backwards. As one of the most cited experiments in automotive aerodynamics, a generic car-type bluff body known as Ahmed body indicates that approximately 85% of the drag comes from the wake region (Ahmed, 1983).

Recently, environment pollution and economics issues have been some of the reason to several countries around the world encourage the automotive industry to achieve reduction of fuel consumption over the modern vehicles. As fuel consumption is directly related to drag force, it has been an area of development in vehicle aerodynamics.

Even the highest level of motorsport has been focusing in fuel efficiency. While it was completely correct to refer to “engines” of F1 cars few years ago, nowadays they are denoted as “power units”. Strictly speaking, the actual F1 power unit is composed by: an internal combustion engine, two turbochargers, a battery, an ERS (Energy Recovery System) control unit, a MGU-K (kinetic energy into electrical energy), and a MGU-H (heat energy into electrical energy). Since 2014, F1 engines were downsized from 2.4 to 1.6 litres, and each race car can use 100 *kg* of fuel only. Therefore, more than a mere change of nomenclature, it implies in a changing of thinking, where the development aiming at the maximum power of engines become the maximum energy-efficient of power units.

Engineering tools like wind tunnel test and computational fluid dynamics (CFD) have been employed as a solution tool for aerodynamic automotive development. However, a





Figure 1.2: Sample of design tools in automotive aerodynamics: DrivAer body in a wind tunnel (left), and the flow analysis of same car model via CFD technique (right).

wind tunnel is an expensive facility for the current economic situation. For instance, General Motors broke ground last year on a new \$30 million reduced-scale wind tunnel to expand its aerodynamic testing facility in USA, according to the GM media (2014). Since it is costly to build and maintain experimental tools for aerodynamics development, the industry is trying to reduce wind tunnel time by investing in CFD and advanced processing capability of the virtual development. Figure 1.2 illustrates the use of both design tool over a same car model.

To circumvent this, computational tools arise as best cost-effective solution. A main advantage of CFD techniques (Computational Fluid Dynamics) is test several changes in geometry without physical models, or even testing in other environment condition virtually.

This thesis is based in the use of CFD technique for automotive aerodynamics purpose. The main goal is to minimize the computational cost for drag prediction of road cars, in order to achieve a better cost-effective CFD methodology for automotive industrial applications.

## 1.2 RESEARCH OBJECTIVES

The purpose of this research is to build a complete background of drag analysis via CFD technique, from the detailed analysis of numerics for CFD methodology up to case studies. The main objectives of the research from a scientific perspective are:

- i. To develop a CFD methodology for drag prediction at lower computational cost.
- ii. To propose an aerodynamic concept for fastback vehicles for drag reduction.
- iii. To investigate the influence of exhaust gases of road cars on the drag coefficient.
- iv. To compare qualitatively the best-sellers Hatch 2015 car profiles manufactured in Brazil.

From the professional point of view, the researcher pursues the strengthening of knowledge in automotive aerodynamics. The goals in the professional perspective are:

- v. To increase the understanding of flow phenomena in automotive aerodynamics.
- vi. To strength the expertise of computational tools for solutions in aerodynamics.
- vii. To develop the capability to working with optimization of vehicle aerodynamics.

### 1.3 RELEVANCE

The aerodynamic development is one of the key factors for fuel efficiency, and the development of commercial vehicles should be embrace in more intensive manner, especially by the automotive manufactures in Brazil.

Since the Brazilian government established the Inovar-Auto programme in 2012, the automotive industry has pursued tax savings by signing up for the programme. This new plan (from 2013 to 2017) has three main objectives: fortification of the industry and domestic market; increase incentives for investment and innovation; and enhance energy efficiency of vehicles produced in Brazil. For instance, manufacturers can gain up to 2% extra in IPI tax credits (aside 30% from Inovar-Auto achievements) by producing even more fuel-efficient models.

From the view of manufactures, not all automakers are in path to reach program requirements. "Energy efficiency is the great nightmare of automotive industry during next 12 to 16 months along," says Valter Pieracciani (2015). He refers to the period that automakers have to implement adjustments before submitting results to the government, which must take place up to November 2016. An estimation made by Automotive Business shows that manufactures can spend around R\$ 8000 (roughly US\$ 2600, by present exchange rate) per car sold in taxes if requirements of fuel consumption and emissions are not achieved in 2017.

Briefly speaking, it means that a manufacturer might be obliged to add around R\$ 8000 in the car price only due to taxes. Consequently, this car will lose its competitiveness enormously, as well as market share and profitability.

In conclusion, the main contribution of this research is to provide the automotive industry with a best practice in CFD setup for drag prediction, under low computational cost. Such methodology may be used to improve the efficiency of aerodynamic development of road cars, enhancing the competitiveness of the automotive industry, fuel efficiency of vehicles and contributing to reduction of environmental impact.

## 1.4 THESIS OUTLINE

This master thesis is divided into three parts: (I) Background, (II) Conceptual Studies, and (III) Case Studies.

The first part deals with the Literature Review (Chapter II) and General Methodology (Chapter III), where the grounds of this research are described. The second part presents a detailed study of CFD setup (Chapter IV), analysis of the external flow phenomena of road cars (Chapter V), and also proposes an aerodynamic concept (Chapter VI), both in the view of road cars aerodynamics. The third part focuses in the applied automotive aerodynamics, where both the qualitative comparison of real car profiles (Chapter VII) and the quantitative optimization of realistic car model (Chapter VIII) are concerned.

The Chapter II describes the literature review of reference car models, CFD analyses of vehicles, turbulence models and meshing model in automotive aerodynamics.

The Chapter III presents the general methodology adopted throughout this research, where is provided the description of geometry, ground treatment, numerical domain, and meshing process.

The Chapter IV presents the analysis of CFD simulations for automotive aerodynamics in two- and three-dimensional cases, and establishes best practices in simulation of three-dimensional realistic car models at low computational cost.

Subsequently, the Chapter V discusses the flow phenomena by means of RANS simulations over the three car types: Fastback, Notchback, and Estateback. Additionally, a DES simulation provides a more detailed flow over the DrivAer Fastback car model, in which the flow visualization via the Q-criterion and the Lambda-2 criterion are compared.

A proposal of aerodynamic concept for automotive drag reduction is presented in Chapter VI. The objective is to identify the potential of blowing and suction methods of momentum over the wake region of the car model. The main contributions of this chapter are to highlight the optimum configuration found and to offer an aerodynamic concept to improve drag reduction of road cars to automotive engineering.

The Chapter VII deals with the profile comparison of ten Hatch 2015 cars models produced in Brazil, in regards to aerodynamic forces and geometry features: roof end angle, rear-end spoiler, and slant angle. The best-seller 2015 model of each one of the ten best-seller 2014 manufactures in Brazil are analysed. The main contribution of this study is a qualitative

comparison of the best-seller car profiles produced and commercialised in Brazil, in two-dimensional domain, in a view of aerodynamic drag and geometry features.

The Chapter VIII investigates the effect of exhaust tailpipe position on the drag coefficient over the 3D realistic car model, based on the best practices of CFD setup established in Chapter IV. The objective is to estimate the magnitude of drag variation and identify an optimum position on the rear of DrivAer Fastback car model, with the goal of drag reduction.

In the end, Chapter IX and Chapter X state the final comments of this master thesis and recommendations for future research, respectively.



## **CHAPTER II**

### **LITERATURE REVIEW**

This chapter describes the literature review about reference car models, CFD analysis of vehicles, turbulence models and meshing model in automotive aerodynamics. Reference vehicle models are related to the use of experimental database for numerical validation purpose, and even for comparison and/or calibration of wind tunnels. The second subtopic deals with CFD methodology in different areas on high performance aerodynamics, such as rally and passenger cars, trucks and even high performance road cycling. Afterwards, a brief description of turbulence models and meshing process are presented.

#### **2.1 REFERENCE CAR GEOMETRY**

In the early 1980s, the experimental research performed by Ahmed became a milestone in automotive aerodynamics. In 1981, Ahmed published the analysis of wake structure over typical automobile shapes. Later, Ahmed (1983) perform the experimental analysis of aerodynamics over a simplified model, which is well-known as Ahmed body. The Ahmed body represents a simplified, ground vehicle geometry with a bluff-body shape, as displayed in Figure 2.1. The author provided pressure and force distribution over the model. In addition, the turbulent wake is investigated as function of rear slant angle, which vaguely represents the rear window surface of a realistic vehicle model. Ahmed (1983) concluded that roughly 85% of the drag on a vehicle body would be consequence of the pressure drag only.

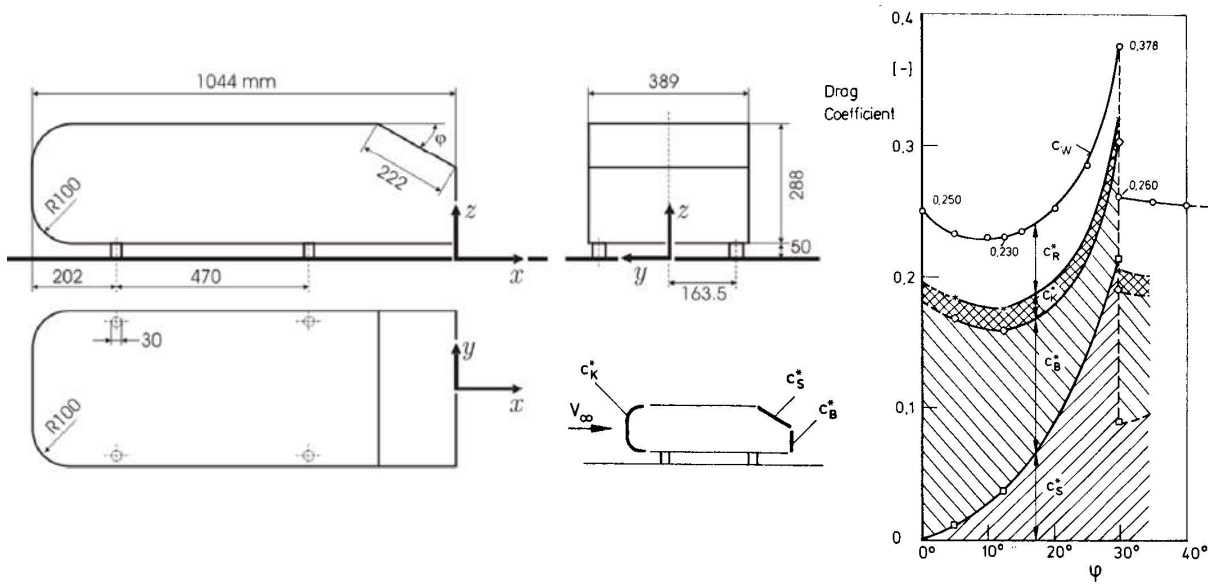


Figure 2.1: Ahmed Body: geometry and drag coefficient.

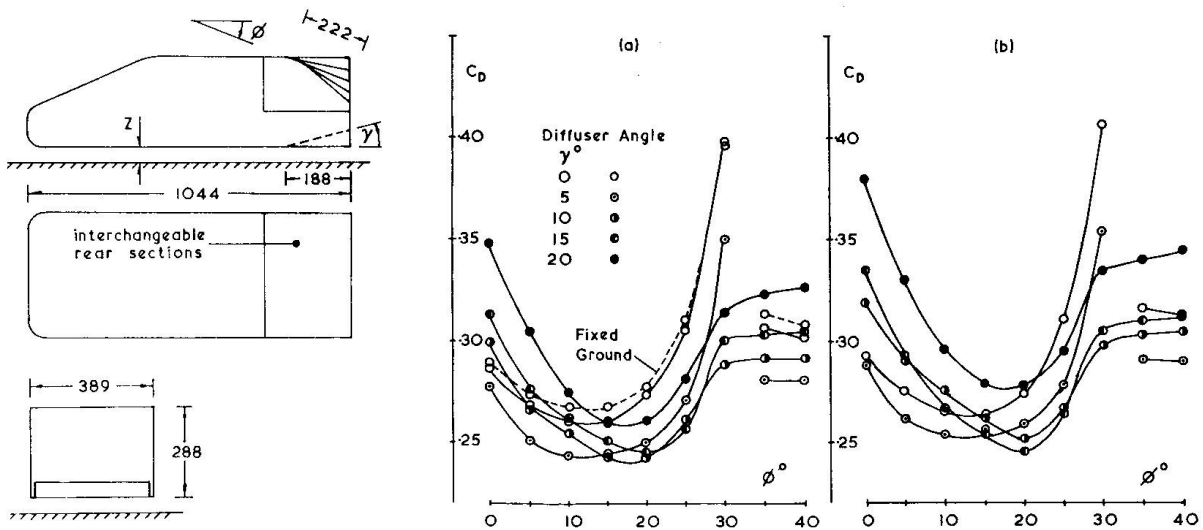


Figure 2.2: Rover Model: geometry and drag coefficient for (a) stationary and (b) moving ground conditions.

New automotive benchmark were created and studied, decreasing gradually the degree of simplification, *e. g.*, Rover Model (Figure 2.2) and MIRA reference car (Figure 2.3).

As evolution of reference car models are concerned, Le Good *et al.* (2004) summarized splendidly the use of reference models in automotive aerodynamics. The authors suggested classifying vehicles shapes into three classes: (i) Simple Bodies, (ii) Basic Car Shapes, and (iii) Production Cars. The authors highlighted three beneficial characteristics of such vehicle models. The first advantage is related to the simplicity of geometries, which enable



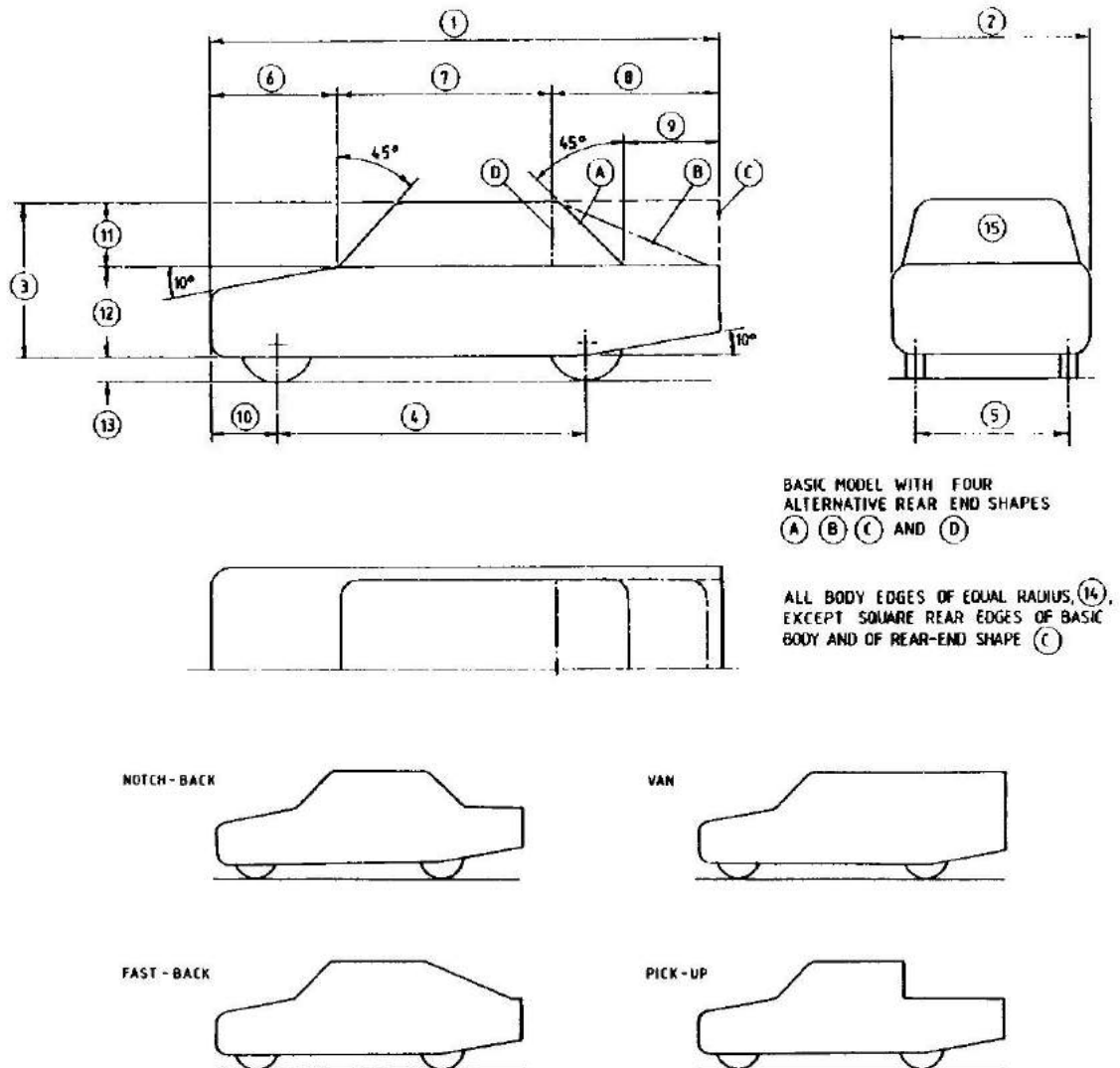


Figure 2.3: Sketch of MIRA reference car.

researchers to easily replicate models either physically or as electronic data such as CAD models for use in CFD analysis. The repeatability of simple models result in wind tunnels is pointed as the second benefit because it gives confidence to researchers and supports a good comparison of outcomes. The third advantage is applicability, where the trends in the effects on aerodynamic characteristics of systematic shape changes can be used directly in the development of production cars.

The conclusion of the authors is that the use of simple reference models has provided an extensive insight into the fundamental aerodynamic characteristics of automobiles. The same models have also been priceless in the development of experimental techniques, providing systematic database for the development of wind tunnel blockage correction theories,

as well as the calibration and correlation of wind tunnels. In recent times, the models have helped to provide further fundamental data in the field of unsteady effects and been used as test cases in the validation of CFD codes. In addition, the continued use of existing reference models in future investigations will help widen the data set which already exists and provide valuable comparative data. Therefore, it is recommended that new models only be designed where the proportions of modern vehicles are necessary in the research and, whenever possible, the new geometries should be based on existing geometries in the literature.

### **2.1.1 DrivAer body**

One of the most recent benchmark in automotive aerodynamics is the DrivAer body. In cooperation with two main vehicle manufacturing companies (Audi AG and BMW Group), Heft *et al.* (2012) proposed a new realistic generic car model for aerodynamic research, illustrated in Figure 2.4. The experiments were performed in the wind tunnel belonging to Institute of Aerodynamics and Fluid Mechanics, at the Technische Universität München. The geometry have been available on the website of the German institute.

The vehicle model is a blending on two typical medium-class vehicles (Audi A4 and BMW 3 series geometries) and includes three interchangeable tops and two different underbody geometries, in order to allow high universality. In other words, the DrivAer model components enables a researcher to reproduce three categories of vehicle design: (i) fastback, (ii) notchback, and (iii) estateback (Figure 2.5); while the vehicle underbody is available in two shapes: (i) smooth and (ii) detailed geometry (Figure 2.6). Moreover, the DrivAer assemblies make optional the analysis of vehicle with or without mirrors and/or wheels.

According to Heft *et al.* (2012), generic car models permit to associate the observed phenomena to specific areas, and consequently, help to understand basic flow structures, *e. g.*, Ahmed body. However, more complex flow phenomena cannot be reproduced around simple model due to the oversimplification of these geometries, *e. g.*, into the wheelhouses and at the underbody. By contrast, the investigation of flow phenomena on a particular production car is generally not feasible, as generally little validation data is available due to its short life span and restricted access to academia. Hence, the authors proposed the DrivAer body as the model that combines the strengths of both approaches.

The authors presented experimental results of force (drag coefficient) and pressure measurements, concerning all combinations of DrivAer assembly. Regarding flow

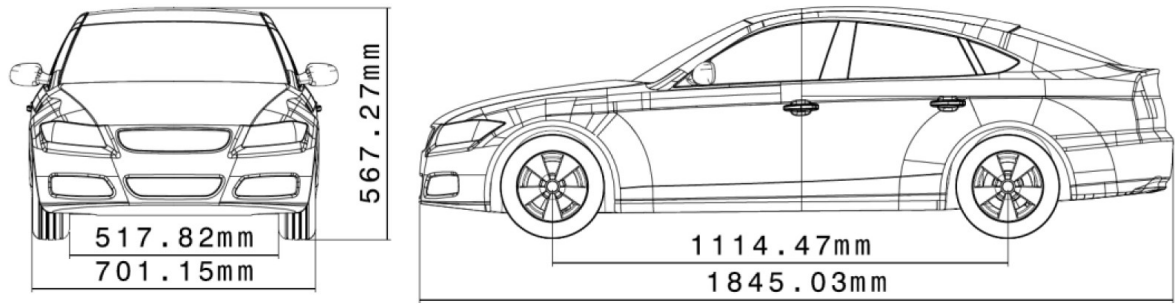


Figure 2.4: DrivAer body: 1:2.5 scale dimension.

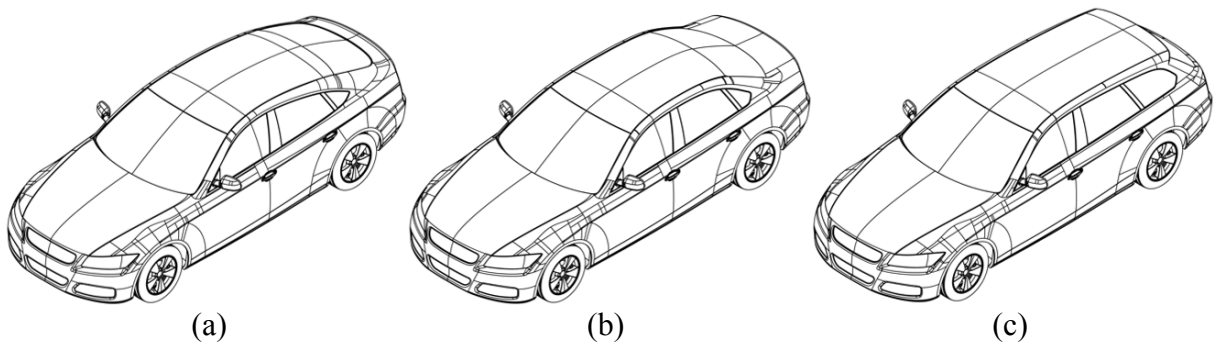


Figure 2.5: DrivAer vehicle category: (a) Fastback, (b) Notchback, and (c) Estateback.

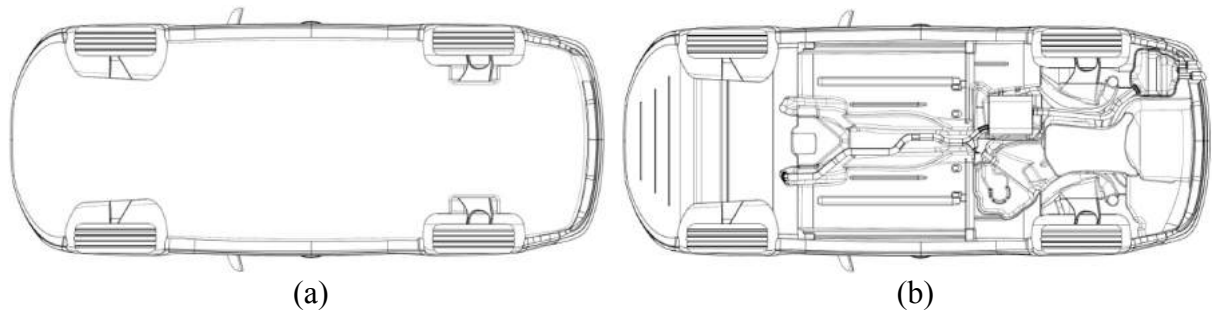


Figure 2.6: DrivAer underbody: (a) smooth underbody, and (b) detailed underbody.

condition, it was demonstrated that the influence of the Reynolds number on the drag coefficient minimises with increasing of Reynolds numbers. Thus, the investigation of the DrivAer body at the reduced Reynolds number of  $Re = 4.87 \times 10^6$  is therefore feasible to determine constant drag coefficients.

As the researchers studied the drag coefficients of the different configurations, two interesting observations were made: both the fastback and the notchback DrivAer model showed a substantial impact of the operating moving belt on the results for attached rotating wheels. Whenever the wheelhouses are closed, the difference do not occur. Consequently, it

was deduced that the vortices shedding from the rotating rear wheels interact with the C-pillar vortices at the backlight of the fastback and the notchback geometry. On the other side, the estate back configuration was not influenced significantly by ground simulation, neither for attached wheels nor for closed wheelhouses.

Moreover, the researchers evaluated the pressure distribution on different parts of the vehicle surface. The moving belt does not influence considerably the distribution of the pressure coefficient at the top of the vehicle. However, the mirrors have a substantial effect on the distribution on the windshield and the side window, since the flow accelerates over the A-pillar and the respective vortex intensifies robustly.

Therefore, such model is one of the most recent and realistic benchmark for automotive purpose, and the database and geometry available provide an excellent method to achieve validation of numerical simulations such as CFD method.

## 2.2 CFD ANALYSIS OF VEHICLES

### 2.2.1 Geometry and Drag of High Performance Bicycle

Doval (2012) developed a remarkable methodology for numerical simulation of aerodynamic cycling. The main goal of Doval's research is to investigate feasibility of using non-contact digitizers for developing finite element models of large objects. Subsequently, the CFD technique is employed for analysis of aerodynamics concerning time-trial bicycle rider efficiency.

The author highlighted that the prediction of drag coefficient often requires wind tunnel experiments and can be costly, or even impossible, for large objects or systems. The aerodynamic analysis via Computational Fluid Dynamics (CFD) offers an alternative approach and is an effective design tool in many industries. Thus, Doval (2012) investigated an alternative method to optimize the aerodynamic efficiency of the rider, since the rider contributes the majority of the drag force of the rider-bicycle system. The drag should be reduced significantly in case of small riding position adjustments are performed during a race. It is assumed that adjusting the time-trial handlebars on the bicycle could reduce the frontal area of the rider in the wind direction, and consequently, reducing the aerodynamic drag.

The first step of such research was generating of numerical bicycle models. The geometry of Trek TTX bicycles were obtained via the Konica Minolta Vivid 910 3D non-contact digitizer, which was used to scan two separate riders in several positions (yaw angles from  $-45^\circ$  to  $45^\circ$ ). The software Geomagic assembled the 3D images and STL files were generated. Afterwards, the three-dimensional geometries were imported into the Star-CCM+ CFD software package, and several simulations were run for each rider-bicycle geometry. A wind speed of  $10\text{ m/s}$  was used in the  $4 \times 4\text{ m}$  test section. No-slip condition was applied on all surfaces, including walls and floor of the test section to align with wind tunnel experimentation. The SST  $k-\omega$  turbulence model was adopted since it is the accepted model for low Reynolds number case. The meshing process was based on trimmer cells, where all test section boundaries had two prism layers, while four prism layers are set over the rider and bicycle boundary. The prism layers retained parallel orientation to the surface. Such feature increases the resolution of boundary layer effects for more accurate drag prediction.

The preliminary results supported the theory that asymmetrical riding position decreases drag at significant wind yaw angles, whereas the normal riding position does not. Controversy, the investigation of different riders and bicycles reached less conclusive results.

Finally, Doval (2012) stated recommendations for both areas of 3D scanning and CFD modelling. The 3D scanned model must be obtained in high quality, since scanners that produce significant noise and surface inaccuracies will cause problems during the meshing process. The focal range of the scanner must also capture images of a large portion of the object or system, which would improve the process of assembling and merging images. If a more efficient scanning process were available, many different models could be simulated without requiring significant time investment. Regarding CFD analysis, there are numerous parameters used for adjusting physics and mesh conditions that could provide a more stable solution. Hence, investigation on meshing generation is advised. Extremely refined meshes could be investigated to better understand the mechanics of the study, whereas additional computer resources are required.

### **2.2.2 Drag of Truck Shapes**

From the truck industry perspective, the reduction of fuel consumption is a key issue. Håkansson *et al.* (2010) investigated one of the most impacting area in fuel saving of

truck shapes: aerodynamic drag. The goal was investigation of the influence on the flow around the truck, simulating different aerodynamic trailer devices and shaped via CFD technique.

The researcher obtained the baseline geometry from Volvo, and used the ANSA software for geometry modifications. Such add-ons applied are: gap treatment (sealed gap, vortex stabilizer, gap fairing); base treatment (side plates, base plates, frame extension); undercarriage treatment (side skirts, sealed wheels, smooth underbody); and aerodynamic trailer designs (teardrop and basedrop).

The virtual tests were performed with Star-CCM+ software, where it was adopted the typical speed of 90 km/h, at yaw angles of 0° and 5°. Each simulation runs for 5000 iterations. The drag coefficient of both yaw angles were estimated via mean value of the last 500 iterations. Håkansson *et al.* (2010) adopted the RANS approach, with SST  $k-\omega$  turbulence model. In order to save meshing size, prism layer treatment (“All  $y^+$  Wall Treatment” approach) was employed to simulate the wall effects. The mesh size around the vehicle was set from 40 to 43 million cells.

According to Håkansson *et al.* (2010), the results showed that the largest effects of the trailer devices are reached at 5° yaw, mainly for the undercarriage treatment. Devices in the undercarriage and base region achieved the best results, *i. e.*, regions most vulnerable for drag improvements. Nevertheless, a balanced base wake was hardly achieved. Devices placed at the rear trailer enhanced the flow from the roof and the upper sides, whereas the air at ground level was very difficult to affect due to a disturbed undercarriage flow. The gap treatment improved the flow over the gap and along the trailer roof, even though a larger clearance might intensify the effect of such technique.

In conclusion, the authors stated that is better include add-on devices rather than change the geometry of the trailer, since the both methods may lead to equivalent results. Also, some vehicles (*e. g.* Volvo tractor) already have a relatively good aerodynamic shape and adjustments are limited. Therefore, these companies should consider the entire truck during the aerodynamic development, in order to achieve further saving in fuel and emissions. In other words, communication between tractor and trailer manufactures should be established more intensively. Form the CFD perspective, it is important to highlight one of the recommendations for future research: repeat the simulation with another turbulence model from the  $k-\epsilon$  family.

### 2.2.3 Performance of Rally Car

The stimulating research of Cañada (2011) investigated the aerodynamics of a World Rally Championship vehicle, especially on the rear wing.

At first, the geometry used in his project was based on a provided 3DS file containing the external body, doors, front bumper, trunk and rear wing of the 2008 Subaru Impreza WRC S14. This 3ds file was generated exporting it from the used CAD software with a low tessellation setting. However, according to Cañada (2102), the CFD code required the geometry in STL format, and the conversion to such format had failed. Then, the author decided to rebuild the entire geometry via CATIA V5 CAD software, achieving success in the geometry generation.

Subsequently, the author performed the CFD stage with the Star-CCM+ package. As the geometry was imported, the mesh generation could be done. Two different types of simulations were carried out: (i) symmetric case (only half-car is simulated using a symmetry plane), and (ii) non-symmetric case (full-car is simulated). All meshes were based on trimmer cells, with prism layer for wall treatment. The RANS approach was used with realizable  $k-\varepsilon$  two-layer as turbulence model, in steady-state and using segregated flow algorithm. The ground boundary adopted the same velocity as the freestream flow, at 40 m/s.

Cañada (2011) described that the first portion of his research demonstrated the benefits of using a complex geometry including different elements like a Gurney flap and a dam under the wing. The results also indicated the general trends and behaviour of a WRC car on straight line by means of downforce, drag and balance. The second analysis covers the results of simulations at different distances from the ground. The effects of vehicle stability during jumps confirmed the general behaviour already predicted on the published literature. The last analysis covers the high yaw situations and the effects of the part included on the wing design to improve the stability of the car on this situation. Surprisingly, the results suggested that the adopted solution decreases the performance of the car.

Finally, the author recommended as future work to simulate more detailed car models, which will lead to more accurate results on the underbody and surface details.

#### 2.2.4 Rear Spoiler of Road Car

An exciting research in automotive aerodynamics was performed by Cakir (2012). The author investigated numerically the aerodynamic lift, drag and flow characteristics of a high-speed generic sedan passenger vehicle with and without spoiler. In other words, it was a CFD-based research, concerning the lift and the drag prediction on the car model with different spoilers mounted at the rear edge of the vehicle.

The geometry vehicle was a three-dimensional notchback car designed via SolidWorks software, as well as the different spoilers, placed in different locations at the rear end of vehicle. The ANSYS software package was employed in the CFD study. All meshes were tetra-based with prism layer around the vehicle and the ground. However, the meshing resolution can be considered too coarse for automotive applications, while the domain has acceptable dimensions. The ANSYS Fluent was the solver used by Cakir (2012) during the simulation process. The preliminary results indicated that the  $k-\varepsilon$  turbulence model is the most appropriate for external flows around the car body. The study of another two cases showed that results can be imprecise if the meshing refinement is not set properly. Other two cases showed that higher meshing resolution leads to more accurate results.

The researcher achieved in the validation case a difference of 6% in comparison to experimental benchmark. The case of passenger car with first rear spoiler design showed that the drag coefficient was reduced in 17% (from 0.232 to 0.192). In the same case, the negative lift (downforce) increased as the lift coefficient was reduced by 7% (from -0.222 to -0.239). In addition, the recirculation zone above the rear window was almost eliminated by using wing style spoiler (first spoiler design). The air sloped gently above the rear window, thus no dust would be placed in the rear window. The second spoiler design was mounted on the rear-end of the car model without allowing any gap between spoiler and vehicle surfaces. Such position provided more downforce than the previous design, however, drag is slight reduced. Although the reduction of 6% was reach in the drag coefficient (from 0.232 to 0.217), the lift coefficient decreased by 17% (from -0.222 to -0.268).

Therefore, Cakir (2012) performed a significant example of optimization in automotive aerodynamics, from car geometry to the aerodynamic comparison via CFD. Nevertheless, the CFD validation with difference of 6% from experimental reference should be acceptable to evaluated trends only. The quantitative values of the research might be have inaccuracies, especially because the coarse tetra-based meshes.



## 2.3 TURBULENCE MODELS FOR AUTOMOTIVE APPLICATIONS

In recent research, Taştan (2011) compared the reliability and performance of turbulence models used in CFD software to determine the aerodynamic features over passenger cars. The geometry adopted in the simulations were based in a BMW 3-series passenger car, in 1/6 scale. The Rhinoceros and Catia CAD software were employed to generate the vehicle in IGES format. Afterwards, the geometry was imported into Gambit software and the surface meshing was created. The Tgrid software concluded the volume meshing process. The same geometry had been studied in wind tunnel by Aka (2003), and his results were the experimental reference for Taştan (2011).

The researcher ran the CFD simulations in the ANSYS Fluent software, where the reliability and performance of seven turbulence models were tested: (i) Spalart-Allmaras, (ii) standard  $k-\varepsilon$ , (iii) RNG  $k-\varepsilon$ , (iv) realizable  $k-\varepsilon$ , (v) standard  $k-\omega$ , (vi) SST  $k-\omega$ , and (vii) Reynolds Stress Model. The results were expressed by drag and pressure coefficients, streamlines, velocity and pressure distributions in different positions in the symmetry plane.

As the main contribution of Taştan (2011), the researcher established the following brief description of each turbulence model tested.

### 2.3.1.1 Standard $k-\varepsilon$ Model

Drag results are not acceptable. The  $C_D$  is overestimated for 5 m/s and 9 m/s about 35% and 10%, respectively, and it is underestimated for high velocities (21 m/s and 25 m/s) about 5% and 9% respectively. Pressure coefficient results are on the average of other models except for one tested point, where it presented the most inaccurate  $C_p$  result obtained among other models: difference of 66% from experimental reference. General flow pattern around the car is predicted unrealistically. In the wake region, any vortex is not fully sensed, as well as no separation and vortex formation are observed at the sides of the car. Time and memory usage of this model is good. In terms of computational cost, this model is very economical compared to other models.

#### 2.3.1.2 RNG $k$ - $\varepsilon$ Model

Drag results are on the average of other models. This model is the most accurate in terms of general trend of  $C_p$  variation. Pressure coefficients at challenging points are relatively accurate. The general flow pattern around the car is predicted realistically. Two counter rotating vortices are observed at the wake region, which are typical for fastback/notchback car models. Likewise, two local separation and reattachment zones are observed at the sides of the car. Furthermore, separated flow on the rear window is detected at lower velocities. This model is one of the most economical models in regards to computational cost.

#### 2.3.1.3 Realizable $k$ - $\varepsilon$ Model

The accuracy of drag prediction is under the average of the other models. Pressure coefficient results are on the average of other models. Like other models, pressure peak at a same point is not detected. The general flow pattern around the car is predicted realistically. Computational cost of this model is a bit high compared to other  $k$ - $\varepsilon$  models. Despite higher computational cost, this model does not excel RNG  $k$ - $\varepsilon$  model.

#### 2.3.1.4 Standard $k$ - $\omega$ Model

Regarding drag force, this model gives most accurate results. For velocities between 13 and 25  $m/s$ , the error in  $C_D$  is under 2%. Pressure distribution is relatively accurate. Whenever compared to the other models, this turbulence model predicts the most accurate pressure coefficient at rear-end edge. However, the wake vortex predicted is much stronger and recirculation region at the wake is larger. A tiny vortex formation is observed at the beginning of the windshield due to local separation bubble. Flow at the sides is predicted as similar to other models. Computational cost is higher than  $k$ - $\varepsilon$  models, but this model outshines  $k$ - $\varepsilon$  models according to overall results.

#### 2.3.1.5 SST $k$ - $\omega$ Model

Drag results are on the average of the other models, similarly to the pressure coefficient results. The prediction of general flow pattern around the car is realistic.

Contribution of side flow separation to recirculation region at the wake is predicted as much stronger compared to other models. In the view of computational effort, this model is the most expensive two-equation turbulence model. Nevertheless, the computational time is similar to the average value of other two-equation models.

#### 2.3.1.6 Reynolds Stress Model

The drag results are on the average of other models, as well as the pressure coefficient results are on the average of other models. General flow pattern around the car is predicted realistically. A little vortex formation inside separation bubble is observed at the beginning of the windshield. Also, separated flow on the rear window is observed at lower velocities. The separation at the rear side edge of the car is predicted early, in contrast to standard  $k-\omega$ , Spalart-Allmaras and  $k-\varepsilon$  models. The RSM turbulence model is the most time and memory consuming. However, it has no clear advantage over  $k-\omega$  models.

#### 2.3.1.7 Spalart-Allmaras Model

Most inaccurate drag results are obtained with this turbulence model. The general flow pattern around the car is predicted unrealistically. The prediction of wake region is very unrealistically, and it is not captured any vortex. In addition, it is not observed any separation bubble at the sides of the car. This is the most economical turbulence model tested in this study, and the computational time is much less than the average of the other models.

#### 2.3.1.8 Summary of Turbulence Models

In conclusion, Taştan (2011) indicated that RNG  $k-\varepsilon$  and standard  $k-\omega$  models stand one step ahead of the other turbulence models, where drag and pressure can be predicted with considerable accuracy. In addition, the same turbulence models provide realistic flow patterns around the vehicle. Their computational costs were average compared to other two-equation models. In the determination of drag coefficient, the standard  $k-\omega$  model achieves results that are more accurate, rather than Spalart-Allmaras and standard  $k-\varepsilon$ .

## 2.4 MESHING FEATURES

The meshing process has significant impact on the CFD simulation, especially in drag prediction. In the automotive perspective, Ahmad *et al.* (2010) performed an excellent investigation of mesh optimization, aiming at better accuracy in drag prediction of ground vehicle shapes. Adopting the MIRA Reference Car fast-back variant as reference model, the authors carried out the simulations with Star-CCM+ CFD package over the simplified car model at three different scales.

The first stage of the research investigated the mesh base size with and without volumetric control over the car model. The results indicated that the smallest mesh base size (50 mm) leads to better accuracy. However, the use or suppression of volumetric control over the model differs less than 1%, while 61% of time saving is possible without volumetric control. The second part compared simulations concerning full- and half-car geometry. The computation error in the drag coefficient between both models was less than 1%, whereas the half-car model saved around 50% in simulation time. In the third and most relevant stage, the authors performed the optimization of mesh parameters via statistical analysis. The research was based on Design of Experiment technique, where five mesh parameters in two level each were selected, *i. e.*, (i) car surface mesh size, (ii) surface growth rate, (iii) mesh type, (iv) number of prism layers, and (v) prism layer thickness.

Afterwards, the authors showed that the scaling of optimized mesh size with the length of car model was used to predict the drag of the other car sizes with reasonable accuracy. Prediction of the drag coefficient within 4% of the wind tunnel reference was possible.

According to the authors, the polyhedral mesh provides better resolution than trimmer mesh whenever the flow in the wake region is concerned. Although, the polyhedral type requires around twice the computational time and memory resources with the same number of cells, in comparison to trimmer type.

The ideal car surface mesh size indicated is 10% of mesh base size, with surface growth rate of 1.3. Both are considered the most important parameters. Reducing the car surface and surface growth rate parameters substantially affects the flow solution. In any case, the parameter  $y^+$  should be into the valid range, *i. e.*, the velocity profile into the inner region, also known as the log-law of the wall zone. The combination of two prism layers, with total thickness of 33.3% of mesh base size, provided the better results.

Regarding meshing regions, meshing with constant growth rate may require less memory and time than set regions of different mesh sizes (volumetric control) around the vehicle, as well as the half-car approach is a suitable choice.



## CHAPTER III

### GENERAL METHODOLOGY

This chapter presents the general methodology adopted throughout this research. The description of the geometry, ground treatment, numerical domain, and meshing process are provided.

#### 3.1 GEOMETRY

Whenever a comparison to experimental reference is required, the realistic DrivAer model has been adopted. The choice of such model is based on its high universality and realistic geometry, as previously discussed (2.1.1 DrivAer body). The geometry is available on the website cited by Heft *et al.* (2012). Both two- and three-dimensional approaches have been used in this research.

##### 3.1.1 Main Approach: three-dimensional geometries

The nomenclature assumed in this research follows the original work of Heft *et al.* (2012), where *wM* and *woM* indicate the model with or without mirrors. The terms *wW* and *woW* are related to the presence or suppression of wheels, respectively. All models used has smooth underground (*S*), and therefore the variation of DrivAer body model are indicated as *FS* (fastback), *NS* (notchback), and *ES* (estateback).

Figure 3.1 shows the three categories of vehicle design available with the DrivAer variations, while the Figure 3.2, Figure 3.3, and Figure 3.4 present the DrivAer assemblies employed (Fastback, Notchback and Estateback, respectively).

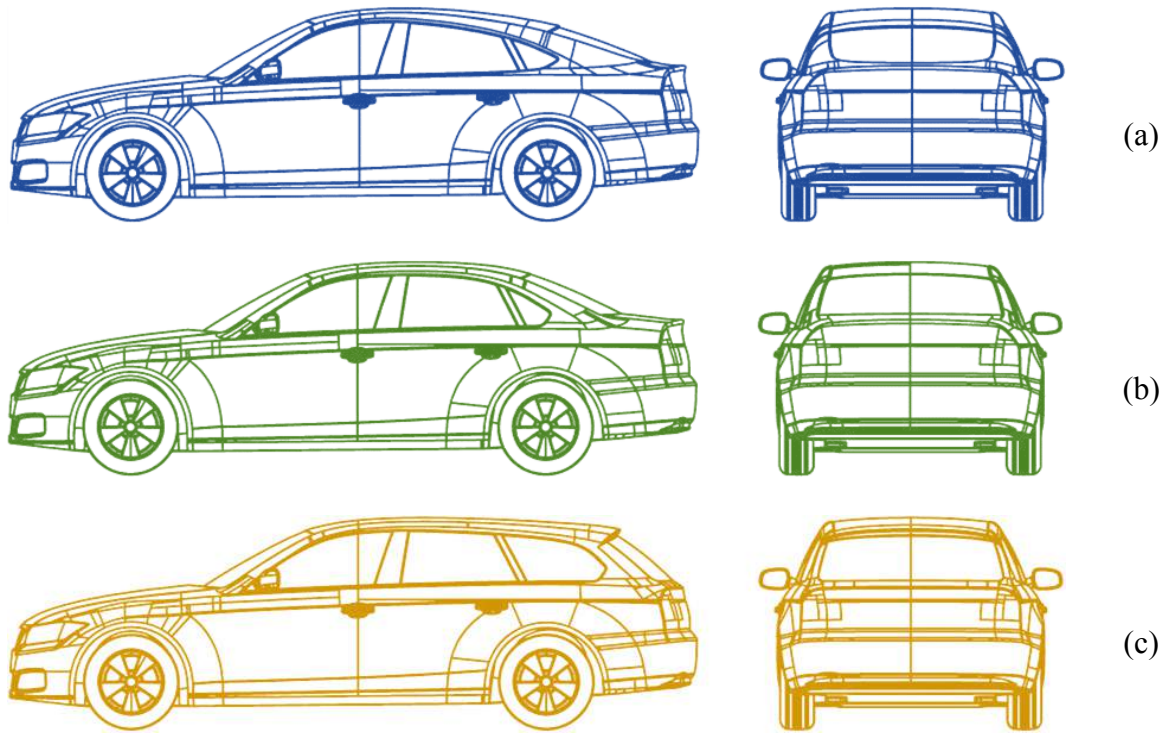


Figure 3.1: DrivAer body variations: (a) Fastback, (b) Notchback, and (c) Estateback.

The drag coefficient of each model is associated to the frontal area of a respective DrivAer model assembly, whose values were measured and expressed in Table 3.1.

Table 3.1: Frontal area of DrivAer model variations and assemblies.

DrivAer variation	woMwoW	wMwoW	woMwW	wMwW
Fastback	$1.016465 \text{ m}^2$	$1.043409 \text{ m}^2$	$1.050307 \text{ m}^2$	$1.050307 \text{ m}^2$
Notchback	---	---	$1.052000 \text{ m}^2$	$1.078937 \text{ m}^2$
Estateback	---	---	$1.052518 \text{ m}^2$	$1.079454 \text{ m}^2$



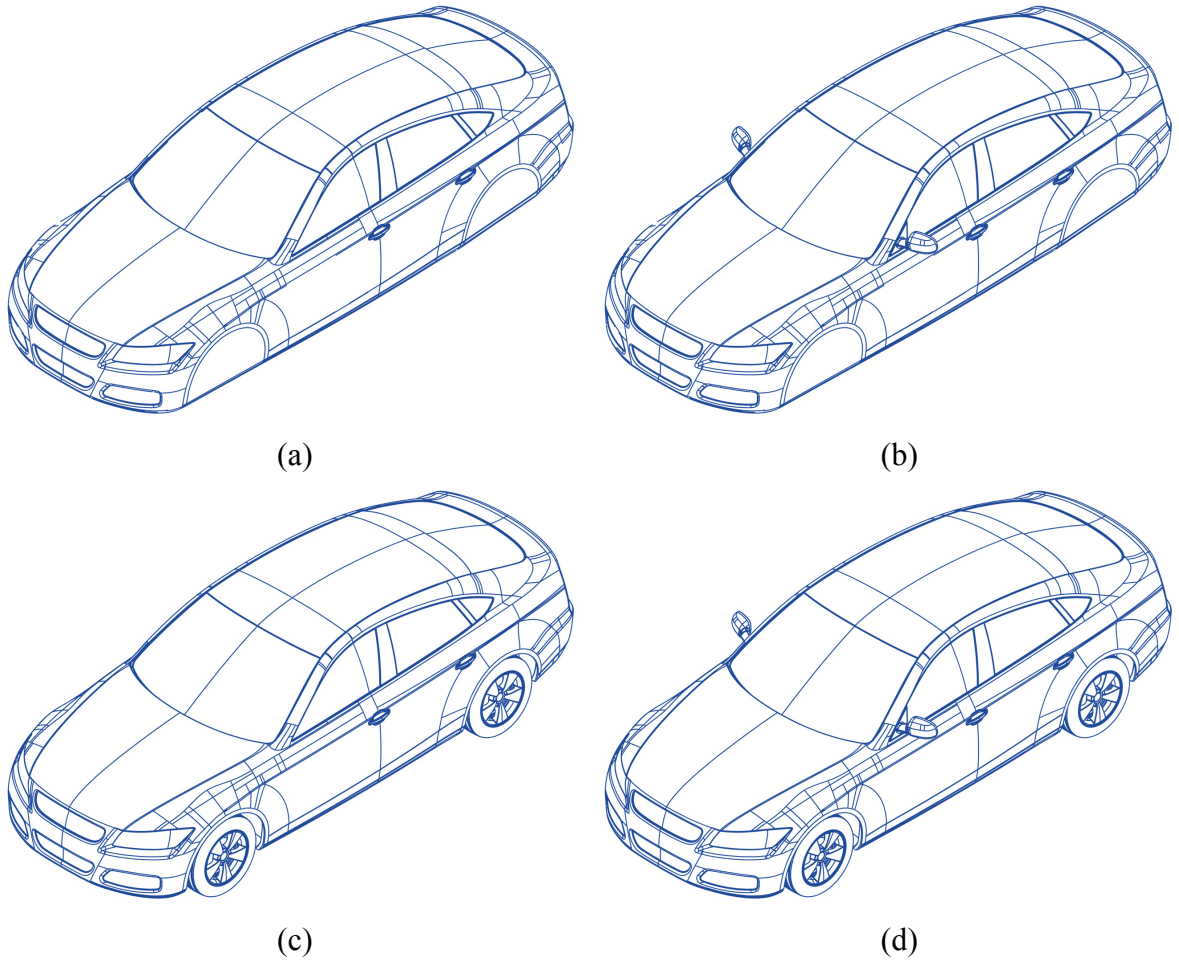


Figure 3.2: DrivAer Fastback model: (a) woMwoW, (b) wMwoW, (c) woMwW, and (d) wMwW.

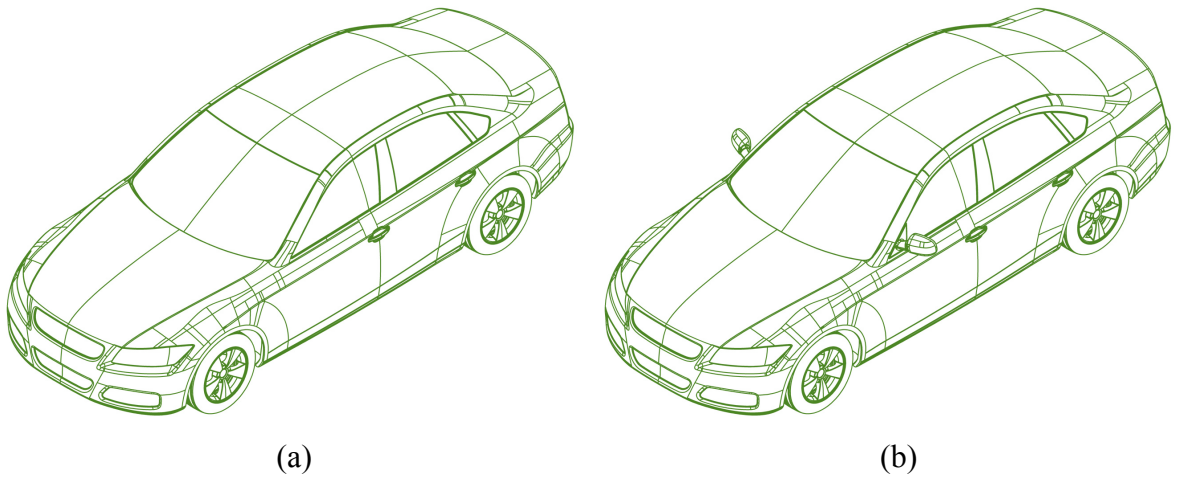


Figure 3.3: DrivAer Notchback model: (a) woMwW, and (b) wMwW.

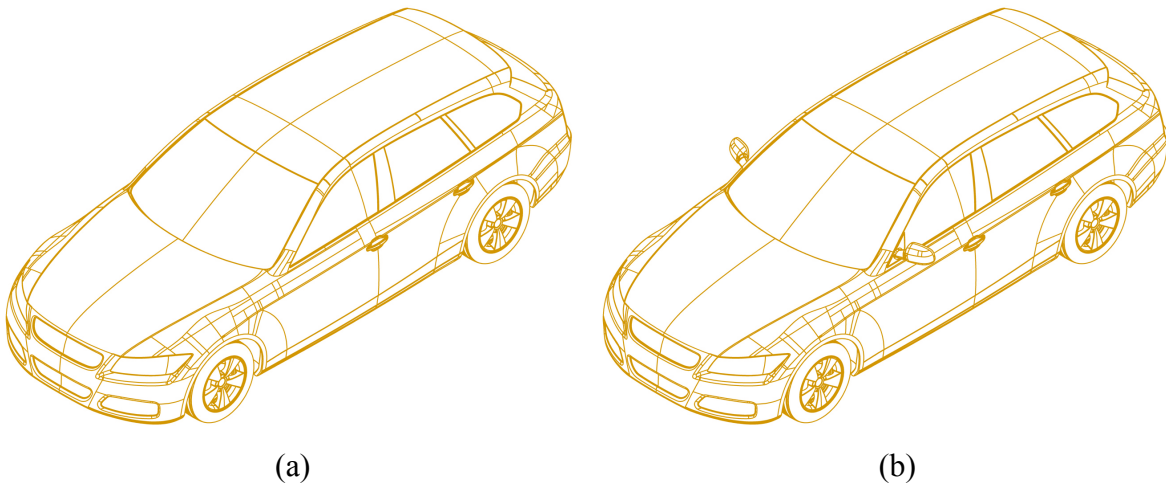


Figure 3.4: DrivAer Estateback model: (a) woMwW, and (b) wMwW.

### 3.1.2 Alternative Approach: two-dimensional profiles

#### 3.1.2.1 DrivAer car profile

This approach has been used for qualitative analysis only, since there is no experimental data for such cases. The geometry chosen in these simulations is the symmetry plane profile of the DrivAer Fastback model, as shown in Figure 3.5.

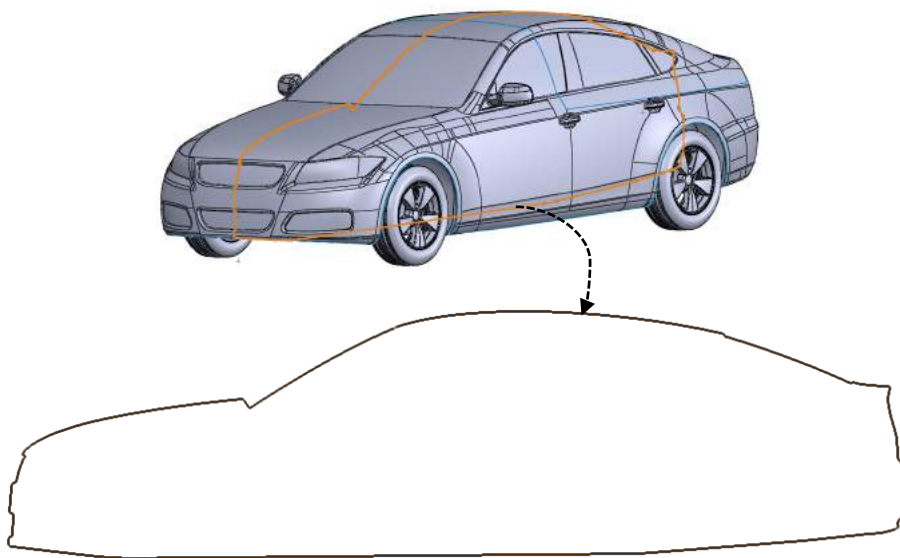


Figure 3.5: DrivAer Fastback profile for two-dimensional studies.

### 3.1.2.2 Hatch 2015 car profiles

Regarding the Chapter VI, two-dimensional investigation of ten Brazilian Hatch 2015 car profiles are performed. The symmetry plane profile of the hatch models are extracted via PlotDigitizer software, which allow extracting points from promoting figures of these vehicles. The car profiles are shown in Figure 3.6. All profiles are full-scale, sharing the respective front axle as coordinate origin of each plot, similarly to the DrivAer CAD geometry.

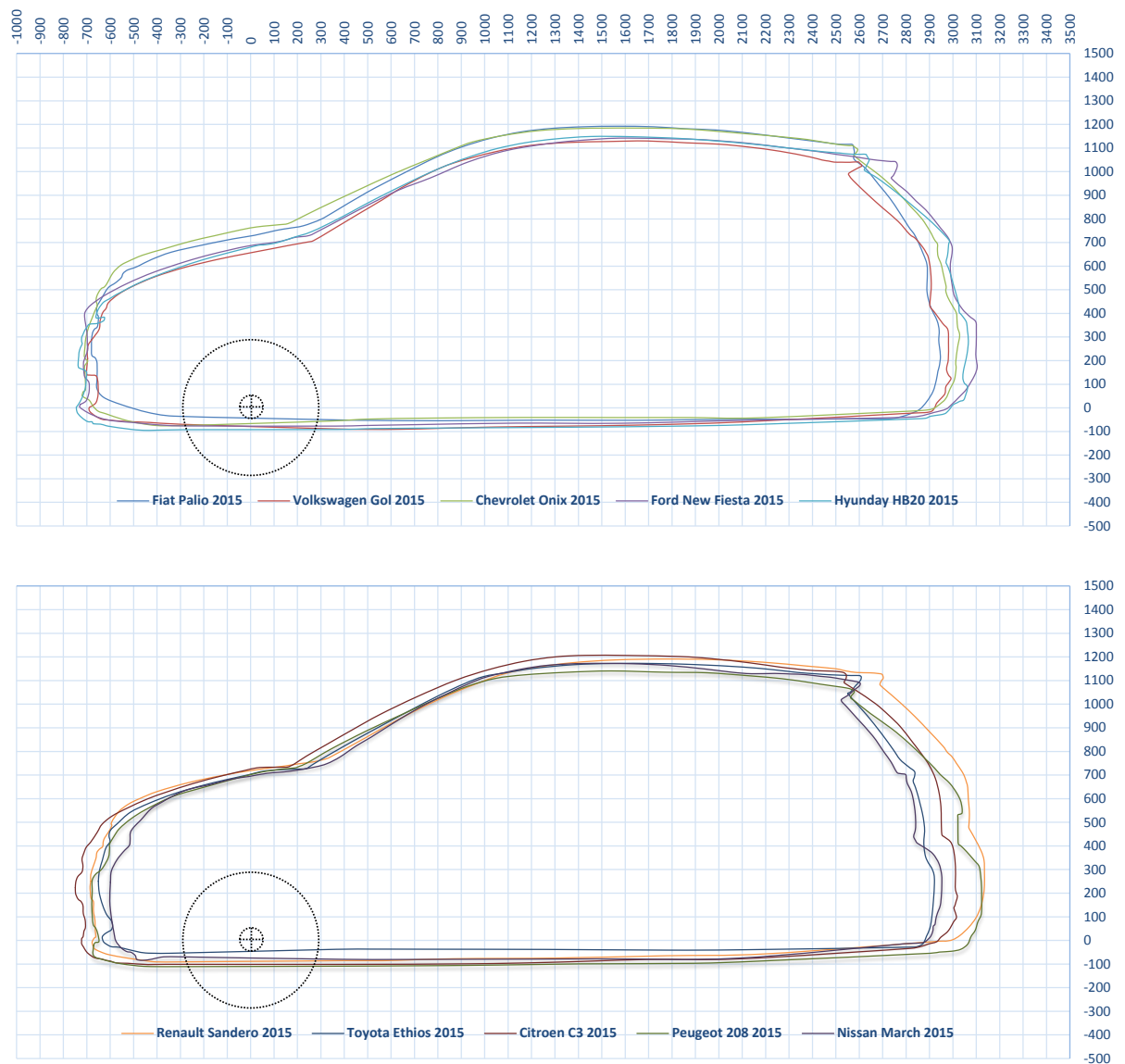


Figure 3.6: Ten Brazilian Hatch 2015 car profiles.

## 3.2 GROUND TREATMENT

The simulations employed two approaches for ground treatment: (i) stationary and (ii) moving condition.

### 3.2.1 Stationary Condition

The stationary approach does not provide realistic ground effects of real phenomena of vehicles. However, wind tunnel experiments often simulate such condition due to the lack of experimental devices, *e.g.*, a belt convey. Thus, the simulation under this condition establishes the ground boundary as a no-slip wall with no relative movement in comparison to the car model. In three-dimensional cases, whenever the wheels are included, the boundaries on the wheel surfaces are similar to the ground condition. This approach hereafter will be referred to as “without ground simulation” (*wo/ GS*).

### 3.2.2 Moving Condition

This ground simulation consisted in the approach of relative movement between the vehicle and the ground boundaries. In order to reach a realistic representation of vehicle motion, the ground boundary is set as a no-slip wall with velocity as the same of freestream. Such feature is referred to as “*with GS*” throughout this text. Likewise, only in three-dimensional cases, the boundaries on the wheel surfaces receive a special treatment, whenever they were included. Hence, the term “ground simulation” will refer to the moving ground approach with artificial wheels movement (*with GS & W*).

The wheel simulation approach is a function of rotation rate and position axle. The rotation rates of the front and rear wheels correspond to the front and rear axle, respectively. The coordinate of the front axle matches with the origin of the DrivAer CAD geometry, *i.e.*,  $(0\text{ m}, 0\text{ m}, 0\text{ m})$ , while the position of the rear axle is evaluated as  $(2.793\text{ m}, 0\text{ m}, 0\text{ m})$ . Based on the original CAD coordinates, the realistic rotation of each axle would be positive in the  $(0, -1, 0)$  direction.

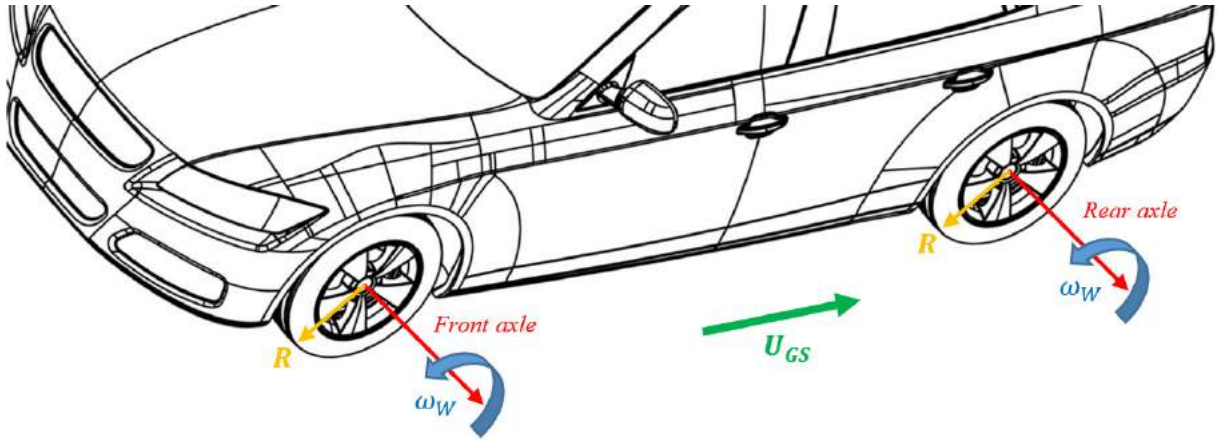


Figure 3.7: Definition of the ground simulation approach (*with GS & W*).

Afterwards, the rotational speed of the wheels boundaries are associated to the local rotation rate ( $\omega_W$ ). The rotation rate is calculated via Eq. (3.1), where it is function of the ground velocity ( $U_{GS}$ ) and the wheels radius ( $R$ , constant and equal to 315 mm).

$$\omega_W = \frac{U_{GS}}{R} \quad (3.1)$$

Figure 3.7 illustrates the definitions of the kinematic features presented in the ground simulation approach.

### 3.3 NUMERICAL DOMAIN

This research used CFD method to evaluate drag force in two- and three-dimensional cases, as described below.

#### 3.3.1 Two-Dimensional Cases

Generally, all boundaries of two-dimensional numerical domain are split into five boundaries: (i) INLET, (ii) OUTLET, (iii) GROUND, (iv) CAR profile, and (v) TOP; as displayed in Figure 3.8.

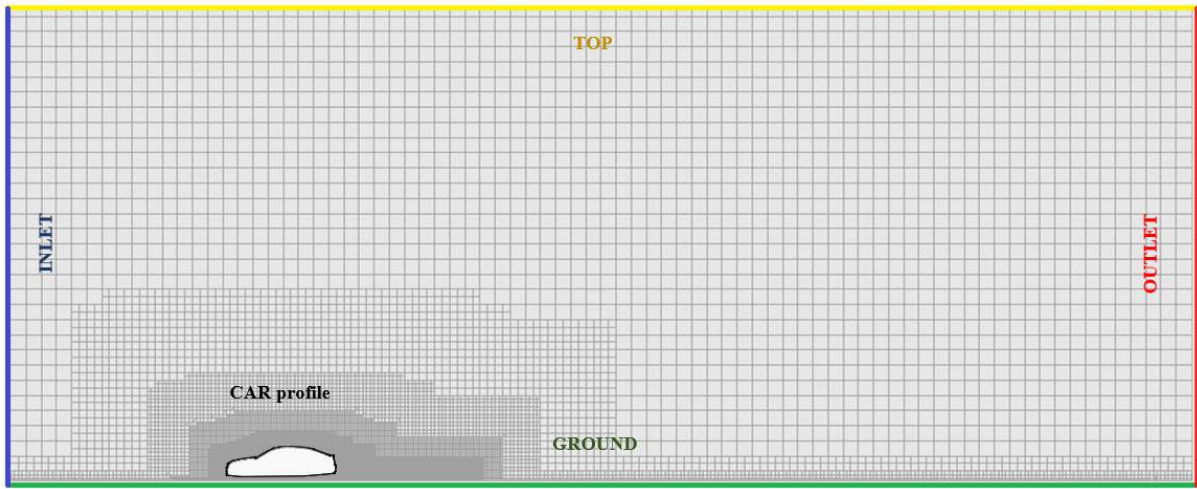


Figure 3.8: Boundaries of two-dimensional numerical domain.

### 3.3.2 Three-Dimensional Cases

The simulations are based in two kinds of three-dimensional numerical domain: half- and full-car model. The Figure 3.9 exemplifies the position of six boundaries for half-car simulation: (i) INLET, (ii) OUTLET, (iii) GROUND, (iv) SIDES, (v) Half-car geometry, and (vi) SYM. In full-car cases, the SYM plane is not presented, and the sides and the upper surfaces of numerical domain are merged into SIDES boundary, displayed in Figure 3.10.

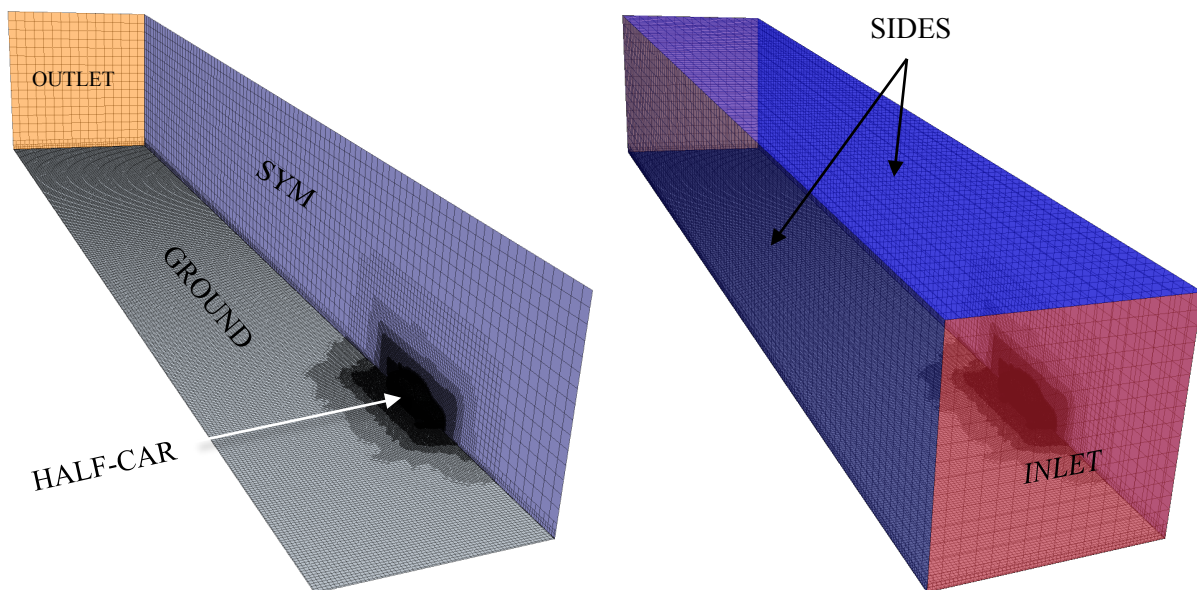


Figure 3.9: Boundaries of three-dimensional numerical domain over a half-car model.



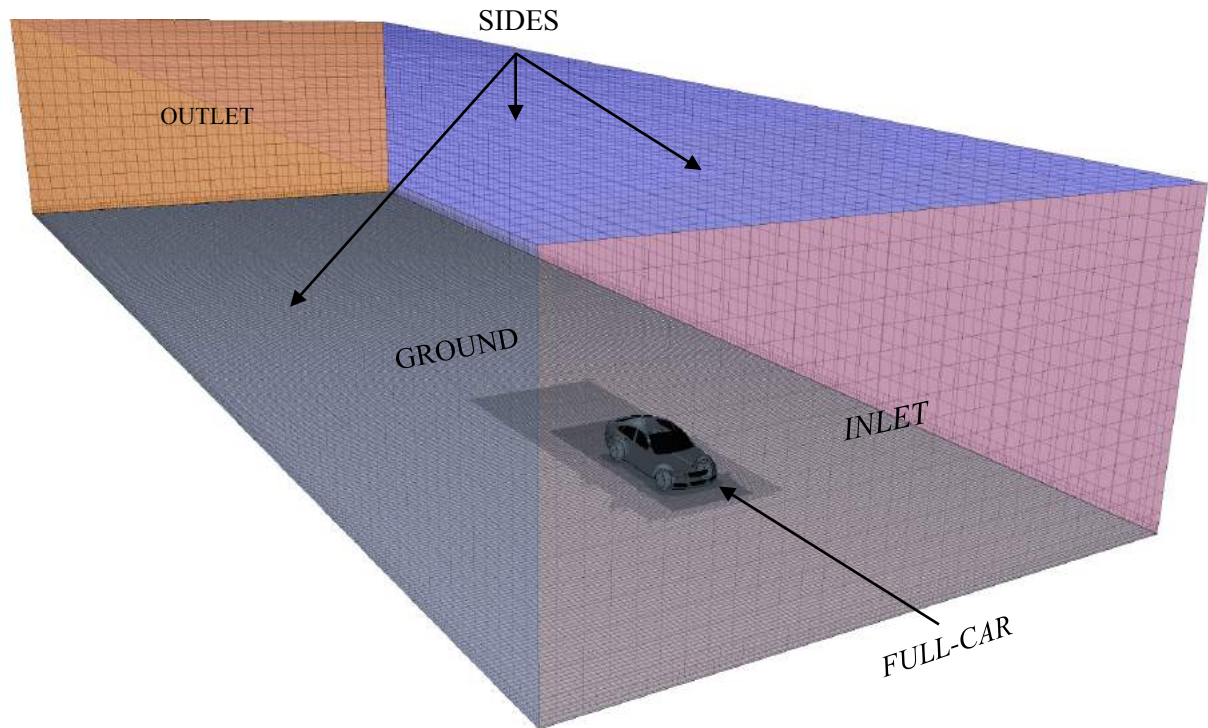


Figure 3.10: Boundaries of three-dimensional numerical domain over a full-car model.

### 3.4 MESHING PROCESS

#### 3.4.1 Mesh Type

Three mesh topologies have been evaluated: tetrahedral, polyhedral and trimmed cell meshes. A brief comparison is presented in Table 3.2.

Even though the option for polyhedral mesh would be the most adequate for accuracy of the turbulence phenomena, the requirement of computational resources is against the main goal of CFD methodology for lower computational cost. According to Cañada (2012), the volumetric trimmer meshing method is the most robust and efficient method of producing a high quality grid for the both simple and complex geometries, especially via Star-CCM+ CFD package. The Star-CCM+ manual user indicates that polyhedral meshing might achieve better results, whereas it requires twice as much of RAM memory as trimmer meshing.

Table 3.2: Comparative of mesh types.

Type	Advantage	Disadvantage
Tetrahedral	<ul style="list-style-type: none"> <li>• High geometry adaptation</li> </ul>	<ul style="list-style-type: none"> <li>• Very dissipative</li> <li>• Convergence can be slow</li> </ul>
Polyhedral	<ul style="list-style-type: none"> <li>• More accurate and faster than tetrahedral meshes</li> <li>• Conformal mesh at the interface between separate regions</li> </ul>	<ul style="list-style-type: none"> <li>• Requires roughly twice the computational cost as trimmer cells</li> </ul>
Trimmer	<ul style="list-style-type: none"> <li>• Require less memory to generate than polyhedral mesh.</li> </ul>	<ul style="list-style-type: none"> <li>• Do not allow conformal mesh at the interface between separate regions.</li> </ul>

Preliminary simulations indicate that polyhedral mesh requires around 4GB of RAM memory for each one million cells, while 2GB of RAM memory would be required for trimmer mesh in the same mesh size. In reason of this, the trimmer meshing has been chosen as the best cost-effective solution, which provides significant robustness under moderate computational cost.

### 3.4.2 Meshing Model

Briefly speaking, the meshing model employed in this research on the Star-CCM+ software is summarized in the Table 3.3.

Table 3.3: Meshing model.

Mesh type	Wall meshing	Geometry meshing
Trimmer cell Mesher	Prism Layer Mesher	Surface Remesher & Automatic Surface Repair

In all cases, the total of 3 prism layers has stretching rate equal to 1.2, just as the surface growth rate. The maximum cell size allowed is 1 *m*. The mesh base size has been defined as the cell size on the car surface. In Chapter IV, the optimum values of both mesh base size and prism layer thickness are investigated.



### 3.4.3 Meshing Refinement

In compliance with the goal of lower computational cost, the meshing refinement over the car model has been performed as optimized as possible. Such methodology offers a considerable saving in mesh size, allowing simulations with difference under 1% from the experimental reference with mesh size in the magnitude of 3 to 4 million cells. Figure 3.11 displayed all regions of meshing control over the car, and the resulting ground refinement under the car.

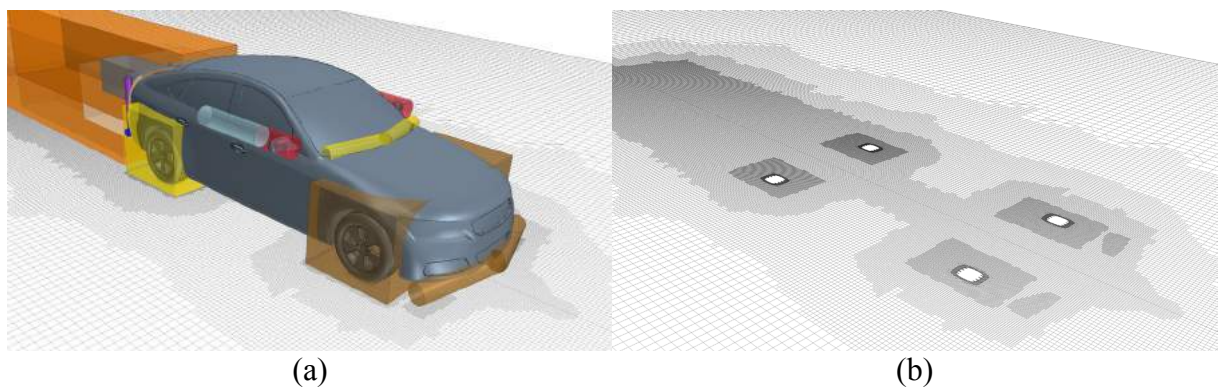


Figure 3.11: Illustration of (a) regions of meshing control over the car and (b) impact of refinement on the ground surface.

Each region of meshing control recommended is highlighted, with the corresponding meshing size, from Figure 3.12 to Figure 3.21.

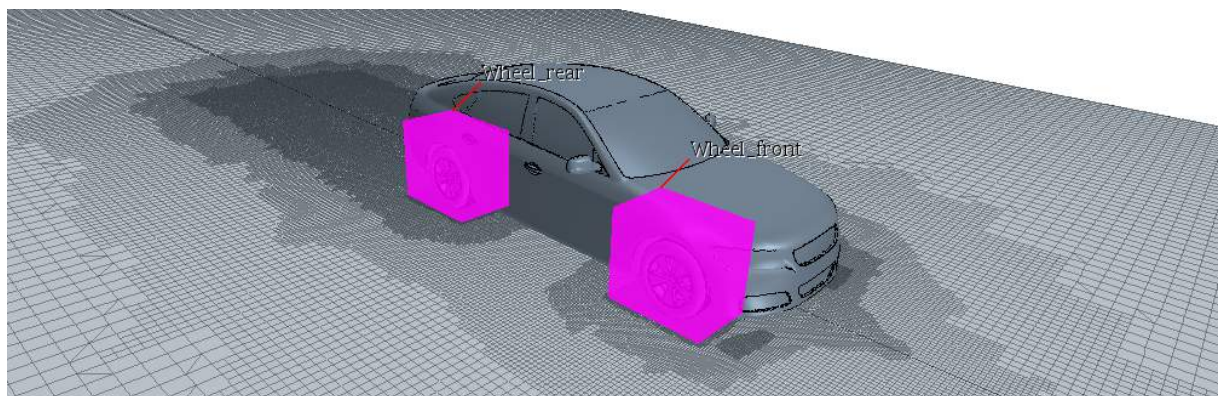


Figure 3.12: Regions of meshing control: front and rear wheels refinement of 10 *mm*.

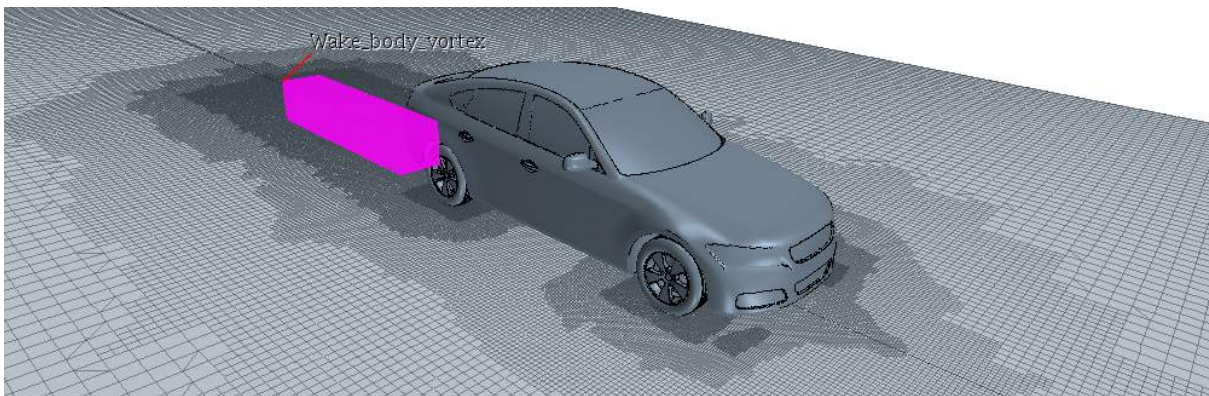


Figure 3.13: Regions of meshing control: vortex refinement of 20 *mm*.

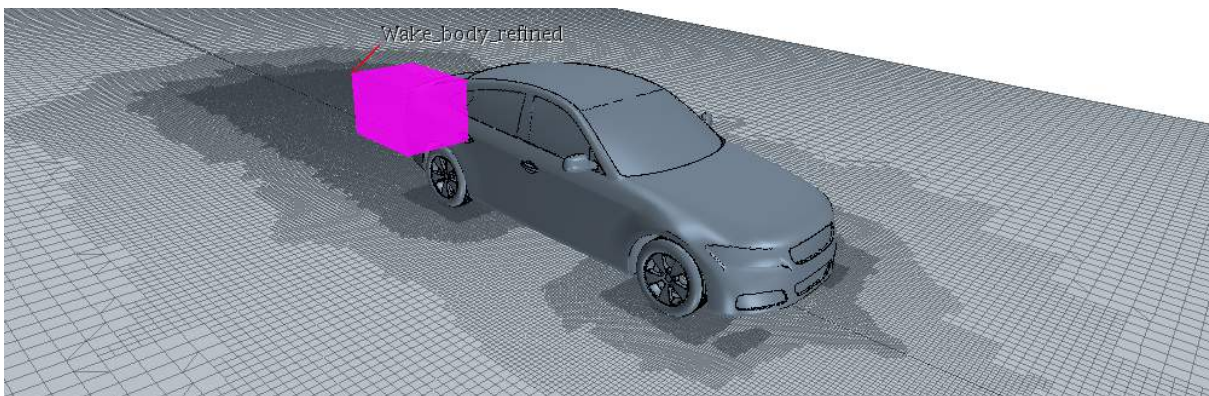


Figure 3.14: Regions of meshing control: near wake refinement of 20 *mm*.

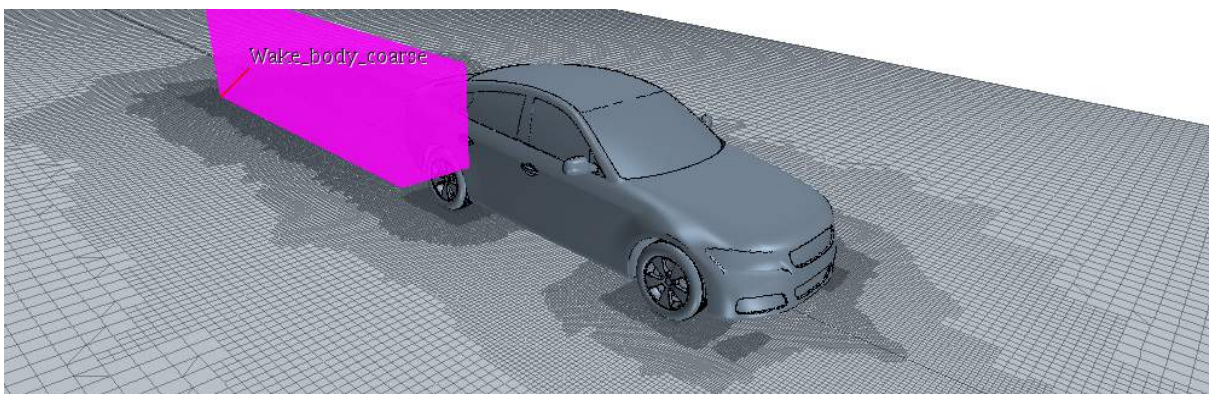


Figure 3.15: Regions of meshing control: larger wake refinement of 40 *mm*.



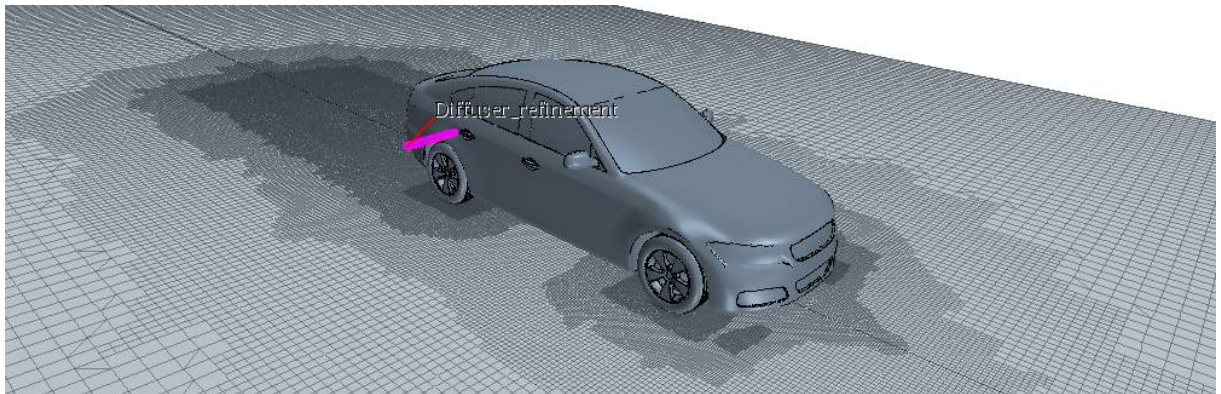


Figure 3.16: Regions of meshing control: diffuser edge refinement of 05 *mm*.

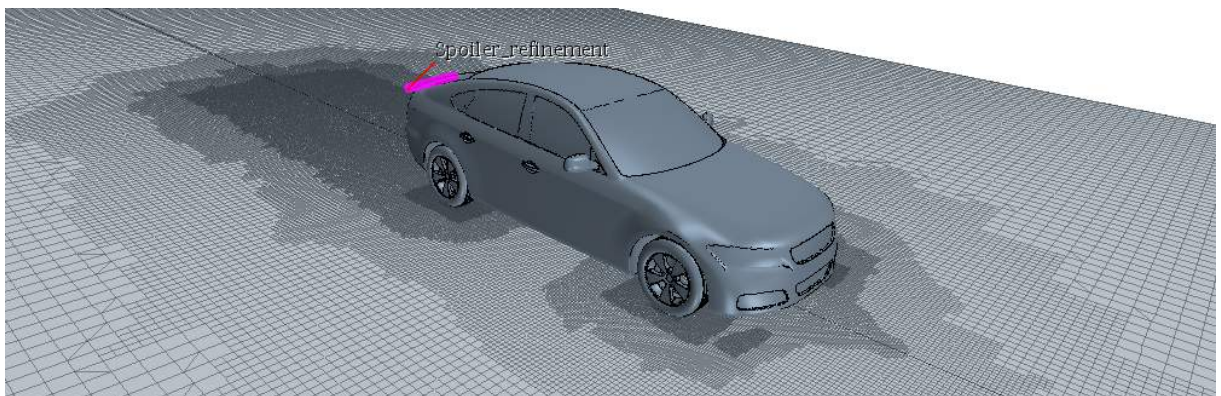


Figure 3.17: Regions of meshing control: spoiler edge refinement of 05 *mm*.

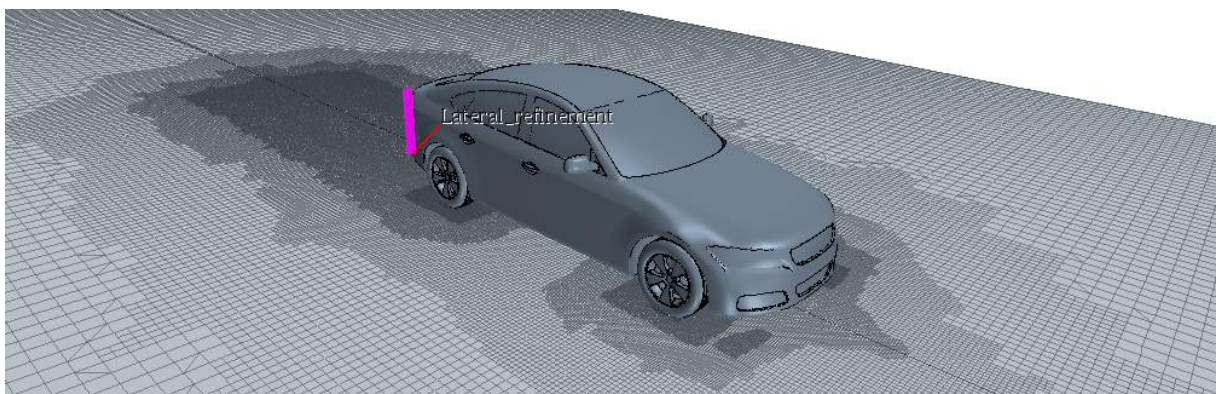


Figure 3.18: Regions of meshing control: lateral edge refinement of 05 *mm*.



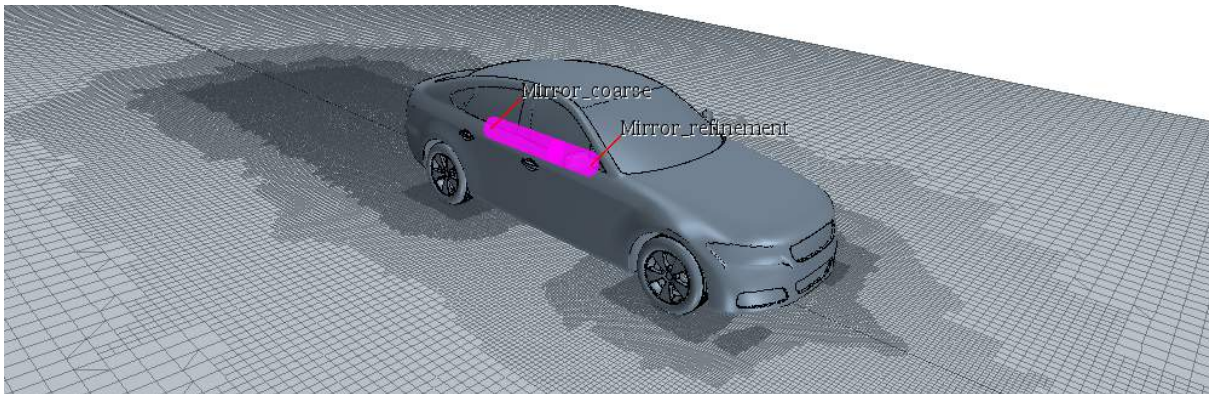


Figure 3.19: Regions of meshing control: surrounding mirror refinement of 05 *mm* and mirror wake refinement of 10 *mm*.

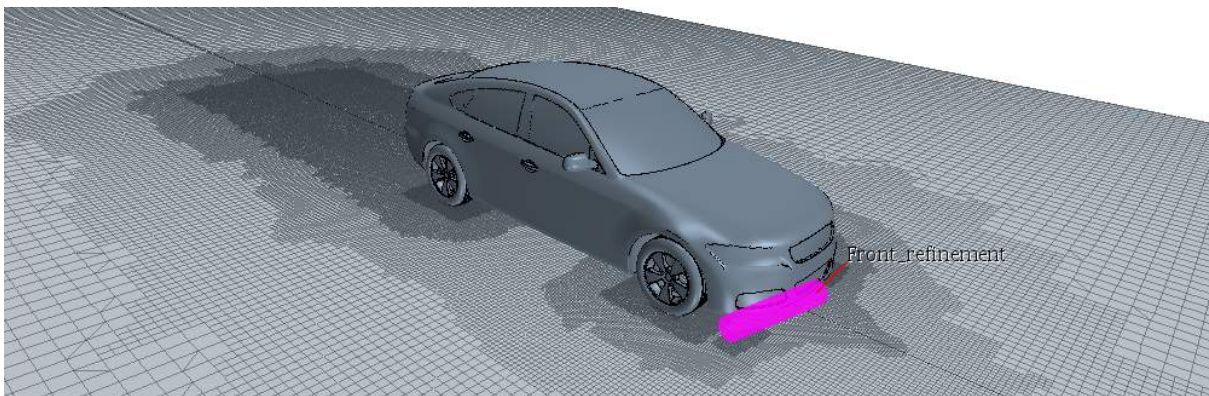


Figure 3.20: Regions of meshing control: front bumper refinement of 05 *mm*.

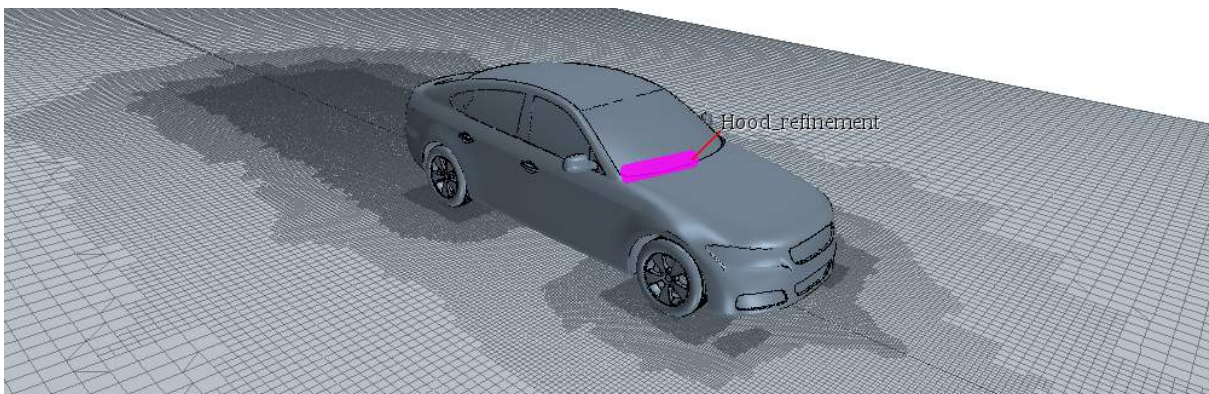


Figure 3.21: Regions of meshing control: hood end refinement of 05 *mm*.

## **CHAPTER IV**

### **EFFECTS OF CFD SETUP FOR AUTOMOTIVE APPLICATIONS**

This chapter presents the analysis of CFD simulations of automotive aerodynamics in two- and three-dimensional cases. The first subtopic investigates the qualitative influence of three factors on the drag coefficient prediction of a car profile, while the second subtopic indicates the quantitative effects of several CFD parameters on the drag.

The main goal is to understand the effect of numerical parameters on the drag prediction of road car profiles (2D) and bodies (3D). In other words, the contribution of this chapter is to outline the numerical influence of the CFD setup on drag prediction. Consequently, a best practice in simulation of three-dimensional realistic car models with lower computational cost is established.

#### **4.1 TWO-DIMENSIONAL QUALITATIVE ANALYSIS**

This section aims to identify the optimum combination of three numerical factors via qualitative analysis of drag prediction. Hence, the numerical parameters investigated are: (i) Turbulence model, (ii) Mesh base size, and (iii) Gradient method, as shown in Table 4.1. These parameters have significant influence on robustness and accuracy of numerical solution of drag coefficient over car-based geometries.

In order to achieve results of this preliminary study within a short period of time, computational domain of all simulations are two-dimensional.

Table 4.1: Numerical setup factors and levels.

Factor	Number of Levels	Description
Mesh base size	4	40 mm, 20 mm, 10 mm, 05 mm
Turbulence model	2	SST $k-\omega$ , Realizable $k-\varepsilon$ two-layer
Gradient method	3	Green-Gauss (1 <sup>st</sup> -, 2 <sup>nd</sup> -order); Hybrid Gauss-LSQ (2 <sup>nd</sup> -order)

The symmetry plane profile of DrivAer Fastback model in 1:1 scale has been adopted for studies as baseline in this investigation (Heft *et al.*, 2012), where the car length ( $L_{ref}$ ) is equal to 4.612 m. Since there is no experimental data available for this geometry in two-dimensional domain, the freestream of  $U_\infty = 40 \text{ m/s}$  is chosen to better fit a real car operation. Air density ( $\rho$ ) is assumed constant and set as  $1.18415 \text{ kg/m}^3$ , with dynamic viscosity ( $\mu$ ) of  $1.85508 \times 10^{-5} \text{ Ns/m}^2$  in all cases studies throughout this study.

Steady-state simulations are carried out using the STARCCM+ code, employing two RANS turbulence models: Realizable  $k-\varepsilon$  two-layer and SST  $k-\omega$ . Each turbulence model has been simulated with three different gradient methods mentioned in Table 4.1. In summary, the physical setup and the boundary conditions are presented in Table 4.2 and Table 4.3, respectively.

Table 4.2: Physical setup.

Feature	Properties
Domain	Two-dimensional
Time regime	Steady-state
Fluid properties	Air ( $\rho = 1.18415 \text{ kg/m}^3$ ; $\mu = 1.85508 \times 10^{-5} \text{ Ns/m}^2$ )
Flow Solver	Segregated
Equation of State	Constant density
Flow regime	Turbulent

Table 4.3: Boundary conditions.

Boundary	Condition
Car profile	wall: no slip
Inlet	velocity-inlet: $U_\infty = 40 \text{ m/s}$ ; $I = 0.1\%$ ; $\mu_t/\mu = 10$
Outlet	pressure-outlet

Boundary	Condition
Top	symmetry
Ground	wall: no-slip, ground movement of $U_{GS} = 40 \text{ m/s}$

Analogous to the computational domain illustrated in Figure 3.8, the inlet is positioned  $2L_{ref}$  upstream of the car profile, the ground is  $12L_{ref}$  long, and it has a gap of  $0.065L_{ref}$  ( $300 \text{ mm}$ ) from the front axle position. The appropriate height of this rectangular domain is estimated next.

Regarding the drag force, drag ( $F_D$ ) of a vehicle is proportional to its size (frontal area,  $A_{ref}$ ) and density of the ambient air ( $\rho_\infty$ ), and also it is squared to relative air speed in the direction of vehicle motion ( $U_\infty$ ). In other words, drag is proportionally squared to difference between wind ( $U_W$ ) and vehicle speeds ( $U_V$ ), in such direction of vehicle movement. Hence, a formal expression for drag and drag coefficients are given in Eqs. (4.2) and (4.3), respectively:

$$F_D = \frac{1}{2} \rho_\infty A_{ref\ car} U_\infty^2 \quad (4.2)$$

$$C_D|_{3D} = \frac{F_D|_{3D}}{\frac{1}{2} \rho_\infty A_{ref\ car} U_\infty^2} \therefore C_D|_{2D} = \frac{F_D|_{2D}}{\frac{1}{2} \rho_\infty h_{ref\ car} U_\infty^2} \quad (4.3)$$

#### 4.1.1 Effect of Blockage Ratio for Two-Dimensional Cases

As demonstrated in previous studies of Soares *et al.* (2013), the pressure contours show that the typical height of a three-dimensional domain might compromise the two-dimensional results, since the pressure might not be constant as freestream on the top boundary.

Generally, in a 3D domain, typical wind tunnel height of  $5 \text{ m}$  (with width at same size) over a frontal car model of  $1 \text{ m}^2$  would result in a blockage ratio of approximately 4%. If the same case have been simplified for 2D simulations, the equivalent 2D blockage ratio<sup>3</sup>

---

<sup>3</sup> Widely used in wind tunnel tests, the blockage ratio is calculated as  $\delta = A_{ref}/(H_{wt}W_{wt})$ . In two-dimensional cases, obviously there is no width of the domain, and the reference frontal area ( $A_{ref}$ ) must be simplified to a reference height ( $H_{ref}$ ). Therefore, the two-dimensional blockage ratio would be written as  $\delta = H_{ref}/H_{wt}$ .

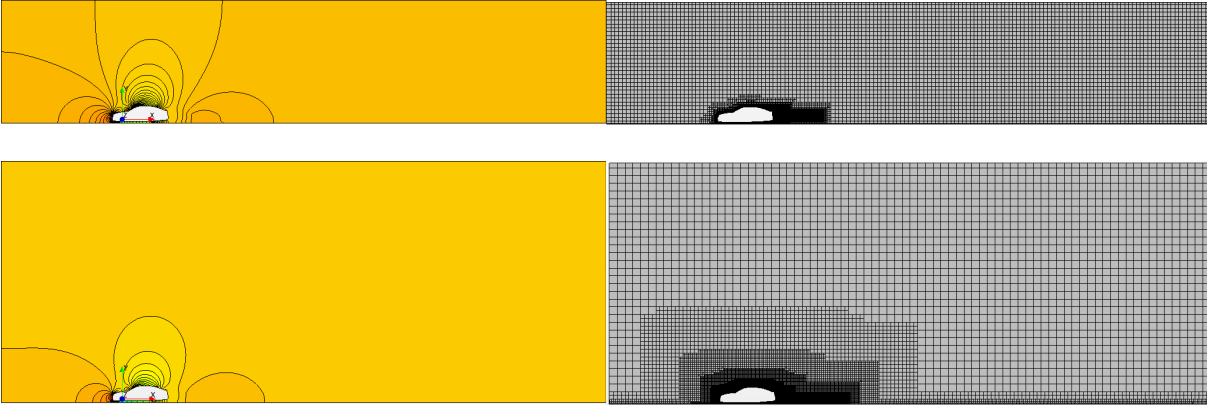


Figure 4.1: Comparison of pressure contours between the height of computational domain equal to  $2.2 L_{ref}$  (above) and  $4.4 L_{ref}$  (below).

would be approximately 20%. In other words, it would represent a massive restriction of the flow, *e. g.*, flow through a pipe with abrupt reduction of 10% in diameter.

A preliminary study concerning the influence of 2D blockage is performed, with the full-scale DrivAer Fastback profile (Figure 3.5) with freestream at  $U_{\infty} = 40 \text{ m/s}$ . Two heights are tested: (i)  $2.2 L_{ref}$ , equivalent to usual proportion in wind tunnel tests; and (ii)  $4.4 L_{ref}$ , which reduces the 2D blockage ratio to around 10%. The Figure 4.1 presents a comparison between pressure contours on both computational domains.

Indeed, the previous insight of influence of proximity of top boundary is confirmed, especially behind the car profile. Therefore, in order to minimize the equivalent 2D blockage ratio, the height of  $4.4 L_{ref}$  seems a suitable choice and henceforth adopted for two-dimensional cases.

#### 4.1.2 Meshing Process

Since the dimension of numerical domain has been selected properly, four levels of mesh base size over the car are generated, as seen at Figure 4.2.

Despite the different mesh base sizes, all meshes include equal refinement along the wake region to handle the flow separation. Likewise, all meshes contain the same prism layer: total thickness of layers (prism layer) of  $5 \text{ mm}$ , split into 3 layers under layer stretching of 1.2. These settings are assumed to generate an adequate prism layer for the wall function approach. In general automotive applications, standard wall functions are valid when  $y^+$  is



between 30 and 500 (Olander *et al.*, 2011). Consequently, all meshes have allowed to compute  $y^+$  in the range of 30 and 90, *i. e.*, feasible values for wall function treatment.

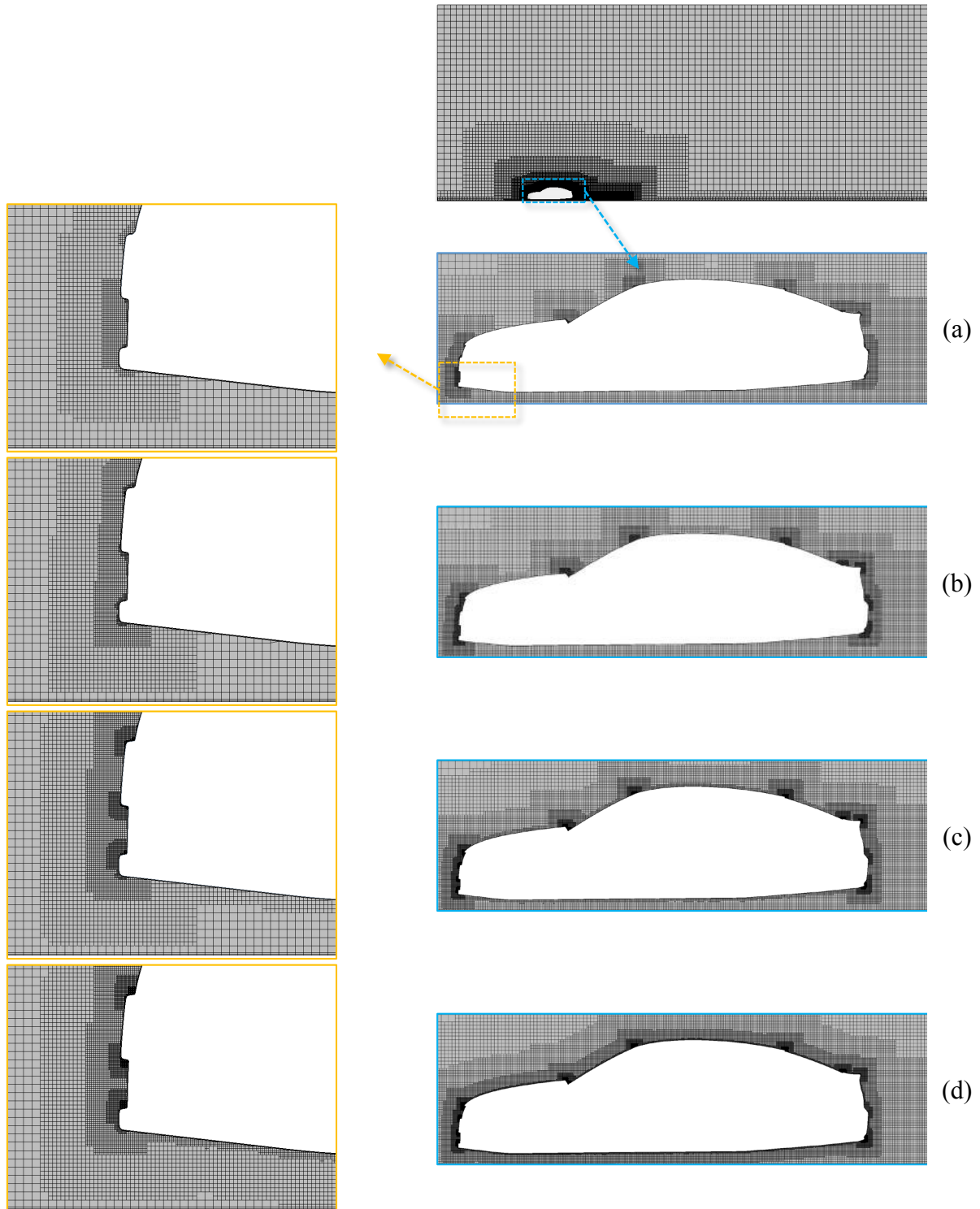


Figure 4.2: Illustration of four level of mesh base size setting surrounding the vehicle profile: (a) 40 mm, (b) 20 mm, (c) 10 mm, and (d) 05 mm.

### 4.1.3 Analysis of Two-Dimensional CFD Setup

Regarding the four mesh base sizes, two turbulence models, and three gradient schemes, a total of twenty-four parameters combinations have been simulated. The results for the drag coefficient obtained with Realizable  $k-\varepsilon$  two-layer and SST  $k-\omega$  turbulence models are presented in Figure 4.3 and Figure 4.4, respectively.

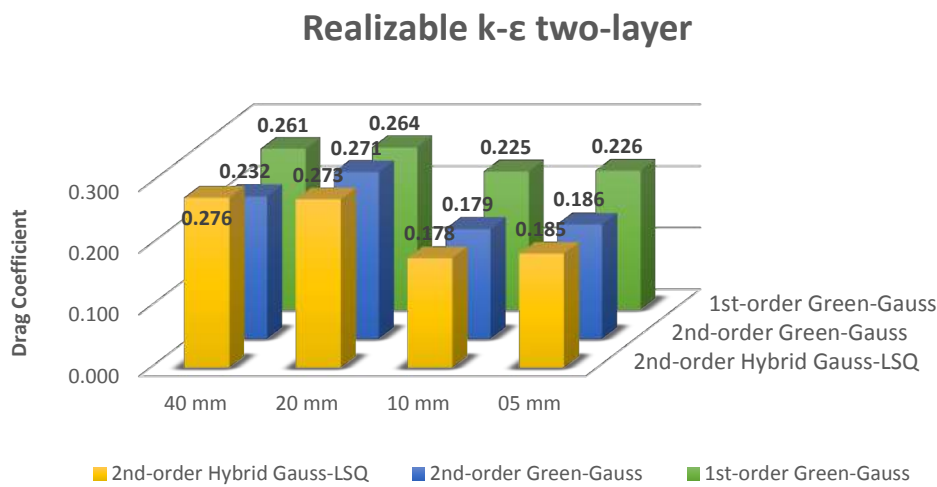


Figure 4.3: Realizable  $k-\varepsilon$  two-layer turbulence model: comparison of drag coefficient among all mesh base size and gradient schemes.

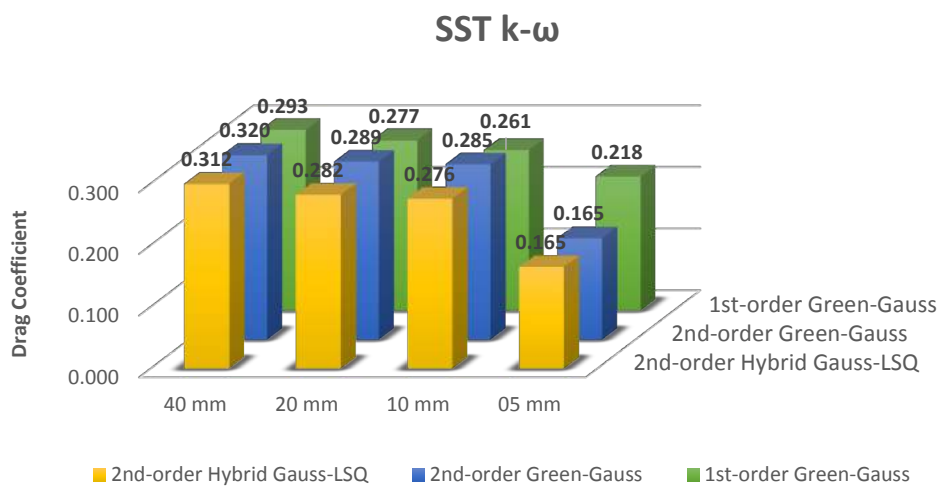


Figure 4.4: SST  $k-\omega$  turbulence model: comparison of drag coefficient among all mesh base size and gradient schemes.

As expected, the results for the different gradient schemes tend to the same value as the mesh base size is reduced. However, it is noticed that the SST  $k-\omega$  provide a higher variance and the 1<sup>st</sup>-order Green-Gauss also did not follow the results using 2<sup>nd</sup>-order gradient schemes, known as more accurate.

The optimum numerical setup should be close to the finest mesh base size, while both 2<sup>nd</sup>-order Green-Gauss and Hybrid Gauss-LSQ gradient schemes predict drag almost at same level, as shown in Figure 4.3 and Figure 4.4.

Subsequently, one additional simulation has been performed with such combination, with the Reynolds Stress (RSM) turbulence model. Figure 4.5 displays the prediction of drag coefficient with 2<sup>nd</sup>-order Green-Gauss gradient with different mesh base sizes and turbulence models.

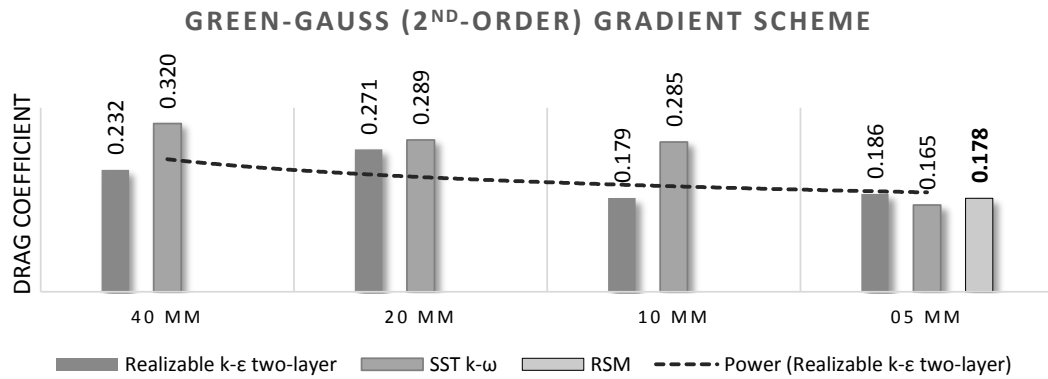


Figure 4.5: Drag coefficient prediction over different mesh base sizes and turbulence models, in 2<sup>nd</sup>-order Green-Gauss gradient scheme.

Notice that the RSM model predicts the drag coefficient between the values from the Realizable  $k-\epsilon$  two-layer and SST  $k-\omega$  turbulence models. Even though RSM turbulence model generally suffer from numerical stability issues, it provides more accurate prediction than two-equation models. Hence, such convergence among the prediction by these turbulence models indicates that the numerical setup is optimised enough to deal with reasonable prediction.

Another important point is the stability behaviour of drag prediction using Realizable  $k-\epsilon$  two-layer. While SST  $k-\omega$  matches the other models only with the finest mesh, the  $k-\epsilon$  based-model achieved similar results with a slightly coarser mesh. This feature allows a saving of computational time and/or resources when adopting that  $k-\epsilon$  based turbulence

model. To illustrate this point, the results via both 2<sup>nd</sup>-order Green-Gauss (Figure 4.6) and 2<sup>nd</sup>-order Hybrid Gauss-LSQ (Figure 4.7) indicate that Realizable  $k$ - $\varepsilon$  two-layer tends to stabilize the drag coefficient prediction in a coarser mesh than the SST  $k$ - $\omega$  model. In either 2<sup>nd</sup>-order gradient scheme, the former turbulence model requires a mesh base size of 10 mm, while the latter needs the minimum mesh base size of 5 mm.

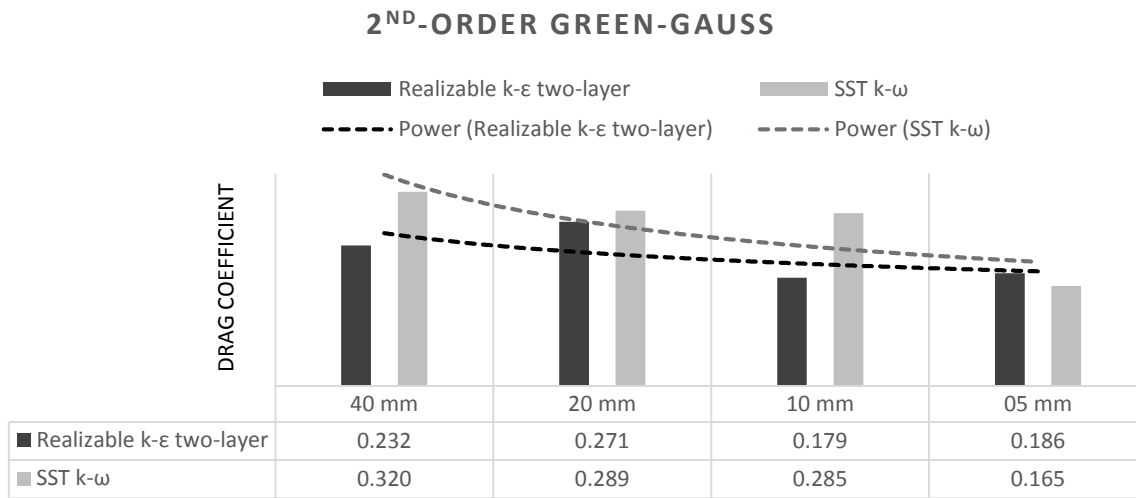


Figure 4.6: 2<sup>nd</sup>-order Green-Gauss gradient scheme: comparison of drag coefficient prediction.

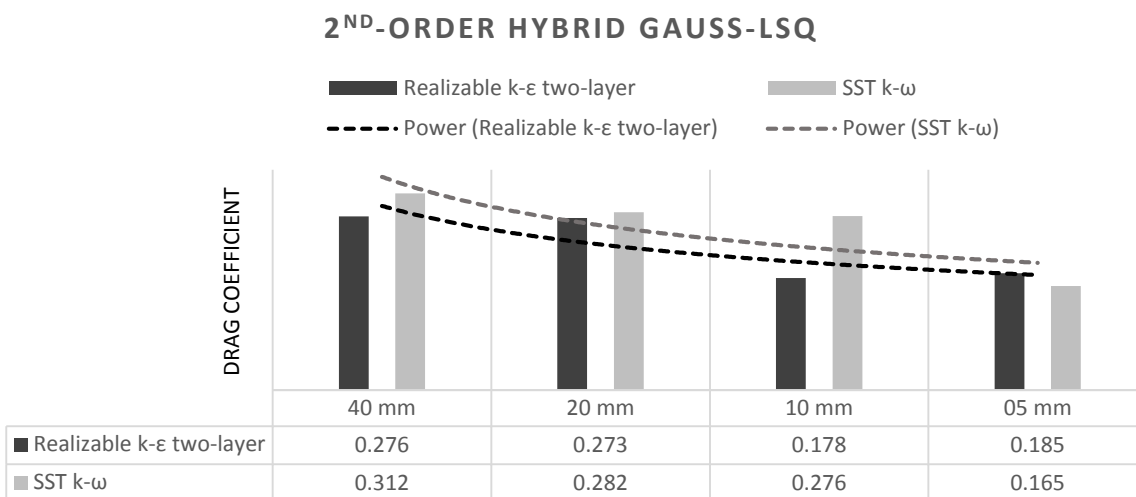


Figure 4.7: 2<sup>nd</sup>-order Hybrid Gauss-LSQ gradient scheme: comparison of drag coefficient prediction.

#### 4.1.4 Summary of Two-Dimension Analysis

An investigation of setup for CFD simulations of automotive applications is performed, concerning the following parameters: (i) turbulence models, (ii) mesh base sizes, and (iii) gradient methods. A total of 24 parameters combinations have been compared in two-dimensional domain.

Results show that the drag prediction is very sensitive to mesh base size. As the surface base size decreases, the drag prediction tend to decrease the variance prediction. The conclusion is that mesh base size has the major importance among the factors investigated.

In the turbulence model perspective, SST  $k-\omega$  turbulence model overpredicts the drag in comparison to Realizable  $k-\varepsilon$  under larger mesh base size. On the other hand, under smaller mesh base size, the SST  $k-\omega$  turbulence model underpredicts the results with Realizable  $k-\varepsilon$  results. Such behaviour is very clear when using  $2^{nd}$ -order gradient methods. It leads to the conclusion that the first turbulence model is very sensitive to mesh base size, while the second shows smaller variations over different mesh base sizes.

Regarding the gradient calculation method, they provide similar results under larger mesh base size. However, the  $1^{st}$ -order Green-Gauss has discrepant results from  $2^{nd}$ -order method as the mesh base size decreases.

In the end, the main contribution of this study is the preliminary best practice to be set in two-dimensional CFD setup, as suggested in Table 4.4.

Table 4.4: Proposal of best practice in CFD setup for two-dimensional automotive cases.

Factor	Description	Reason
Mesh base size	05 mm	Spatial accuracy
Turbulence model	Realizable $k-\varepsilon$ two-layer	Higher solution robustness
Gradient method	$2^{nd}$ -order (either Green-Gauss or Hybrid Gauss-LSQ)	Better numerical accuracy

## 4.2 THREE-DIMENSIONAL QUANTITATIVE ANALYSIS

This section describes the quantitative influence of ten numerical parameters on the drag coefficient of a realistic car model, aimed at offering a best practice in CFD for drag prediction of real road cars, at low computational cost.

The numerical simulations are carried out using the STARCCM+ code, under RANS approach with segregated algorithm. The air density ( $\rho$ ) is assumed constant and equal to  $1.18415 \text{ kg/m}^3$ , and the dynamic viscosity ( $\mu$ ) is  $1.85508 \times 10^{-5} \text{ Ns/m}^2$ .

Although the use of Realizable  $k$ - $\varepsilon$  two-layer turbulence model is endorsed by the previous study, other turbulence models also have been tested in this study to ensure the earlier results. In summary, the physical setup is presented in Table 4.5.

Table 4.5: Physical setup.

Feature	Properties
Domain	Three-dimensional
Time regime	Steady-, unsteady-state ( $\Delta t = 1 \times 10^{-4} \text{ s}$ )
Fluid properties	Air ( $\rho = 1.18415 \text{ kg/m}^3$ ; $\mu = 1.85508 \times 10^{-5} \text{ Ns/m}^2$ )
Flow Solver	Segregated
Equation of State	Constant density
Flow regime	Turbulent

The three different DrivAer body model (Heft *et al.*, 2012) have been chosen as the experimental reference for validation, *e.g.* Fastback, Notchback, and Estateback. According to the authors, the increase in Reynolds number from  $4.87 \times 10^6$  is not expected to change the drag coefficient significantly in the experiment over such a car model. For this reason, the cases in this study simulate the freestream at  $U_\infty = 16 \text{ m/s}$  for validation, and at  $U_\infty = 40 \text{ m/s}$  as an alternative speed to better represent a real road car in highway condition. This means that the Reynolds numbers are either  $4.7 \times 10^6$  and  $1.1 \times 10^7$ , corresponding to inlet velocities of  $16 \text{ m/s}$  and  $40 \text{ m/s}$ , respectively.

In order to minimize the computational cost, most of this study employed the computational domain over the symmetrical half of DrivAer Fastback with Smooth underbody (FS) model of 1:1 scale, split into trimmed cells. Nonetheless, even a full-car model in unsteady-

state have been performed, which amplifies the range of analysis about CFD setup via RANS methodology.

The computational domain over the half-car is a slab of width and height equal to 10 *m* each, and length has 60 *m*. The flow inlet positioned 10 *m* upstream from the front axle of the car model. Consequently, the width of the full-car domain is 20 *m*. The boundary conditions are presented in Table 4.6.

Table 4.6: Boundary conditions.

Boundary	Condition	Parameters
DrivAer car (half-, full-model)	wall	no-slip.
Inlet	velocity-inlet	$U_{\infty} = 16 \text{ or } 40 \text{ m/s}$ ; $I = 0.1\%$ ; $l_t = 0.1 \text{ m}$
Outlet	pressure-outlet	
Sym	symmetry	
Sides	symmetry	
Ground	wall	no-slip, no-slip with ground movement at $U_{GS} = 16 \text{ or } 40 \text{ m/s}$
Wheels	wall	no-slip, no-slip with local rotation rate at $\omega_w = 51 \text{ or } 127 \text{ rad/s}$

To build a database for the purpose of numerical validation and analysis of the effects of numerics, 48 simulations over the DrivAer car assemblies have been performed. These simulations involved the combination of ten factors, as shown in Table 4.7.

The simulations consist in three different DrivAer body models with one specific option for the underbody (the smooth underbody: FS, NS, and ES) in order to decrease at least one degree of freedom among the several parameters associated to numerical simulation of such a car model. Since the assembly FSwoMwW represents the most of simulations performed, thus henceforth the reference of this assembly is implicit along the analysis. Hence, only the other assemblies are explicit cited with the respective data.

Even so, it is essential to state that other factors may affect the analysis of a specific factor, since all factors are associated to the non-linear turbulence phenomenon. In addition, all combinations of factor and levels presented in Table 4.7 would involve 36864 simulation. Even if each case, in either steady- or unsteady-state simulation, would take one-

day time to be done, more than *101 years* of unstopping computing solution would be needed! Obviously, the full-factorial optimization process is unfeasible.

Table 4.7: Description of numerical factors and levels.

Factor	Number of Levels	Description
Car assembly	4	without (woW), with (wW) wheels; without (woM), with (wM) mirrors
Ground condition	2	without ground movement (wo/ GS), with ground simulation & wheel surfaces under local rotation rate (with GS & W)
Car type	3	Fastback, Notchback, Estateback
Domain	2	half-, full-car model
Time regime	2	steady-, unsteady-state
Flow condition	2	16 m/s, 40 m/s
Turbulence model	4	SST $k-\omega$ , Realizable $k-\varepsilon$ two-layer, Spalart-Allmaras, RSM (Quad. Pressure-strain)
Gradient method	4	1 <sup>st</sup> -, 2 <sup>nd</sup> -order Green-Gauss, 1 <sup>st</sup> -, 2 <sup>nd</sup> -order Hybrid Gauss-LSQ
Mesh base size	3	5 mm, 10 mm, 20 mm
Prism layer thickness	4	5 mm, 10 mm, 15 mm, 20 mm

#### 4.2.1 Analyses of Three-Dimensional CFD Setup

The effects of the previously mentioned parameters in the numerical drag prediction are all compared to the corresponding experimental data of Heft *et al.* (2012), as shown in Table 4.8.

Table 4.8: Experimental drag coefficient of DrivAer model assemblies (Heft *et al.* 2012).

DrivAer assembly	with ground simulation (with GS & W)				with no ground simulation (wo/ GS)			
	woMwoW	wMwoW	woMwW	wMwW	woMwoW	wMwoW	woMwW	wMwW
FS	0.125	0.141	0.227	0.243	0.124	0.140	0.242	0.254
NS	0.133	0.150	0.232	0.246	0.131	0.148	0.243	0.258
ES	0.195	0.209	0.280	0.292	0.195	0.208	0.283	0.296



#### 4.2.1.1 Influence of Time Approach and Domain

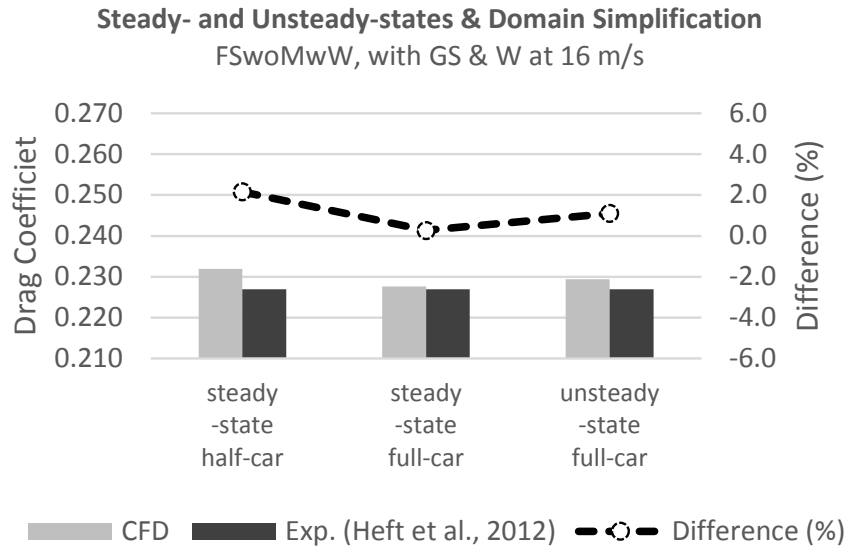


Figure 4.8: Effects of Time regime on drag coefficient prediction.

A costly simulation of the full-car has been carried out in unsteady-state, resulting a difference between the numerical and the experimental data of 2 drag counts (1.1%). Even though unsteady-state simulations can involve similar magnitude amount of RAM memory and hard disk (*e.g.* no saving time-step solution) in comparison to steady-state condition, the massive computing time is a key factor to avoid such simulation. Hence, the possibility of employing steady-state simulation would be aligned with the purpose of drag prediction at lower computational cost.

Indeed, the steady-state approach over both the full-car (0.3%) and the half-car (2.2%) also provide reasonable accuracy over FS. An important aspect of these results is that they are based in a realistic car shape, with ground simulation of movement and wheel surfaces under local rotation rate (*i.e.* artificial rotation of stationary wheel via tangential velocity of the wheel surfaces).

Henceforth, the steady-state approach over the half-car domain is a valid methodology in order to optimise the use of computational resources, unless the car geometry is not symmetric (full-car cases) and/or some unsteady aerodynamic phenomena are presented over the car (unsteady-state cases).

#### 4.2.1.2 Influence of the Mesh Base Size

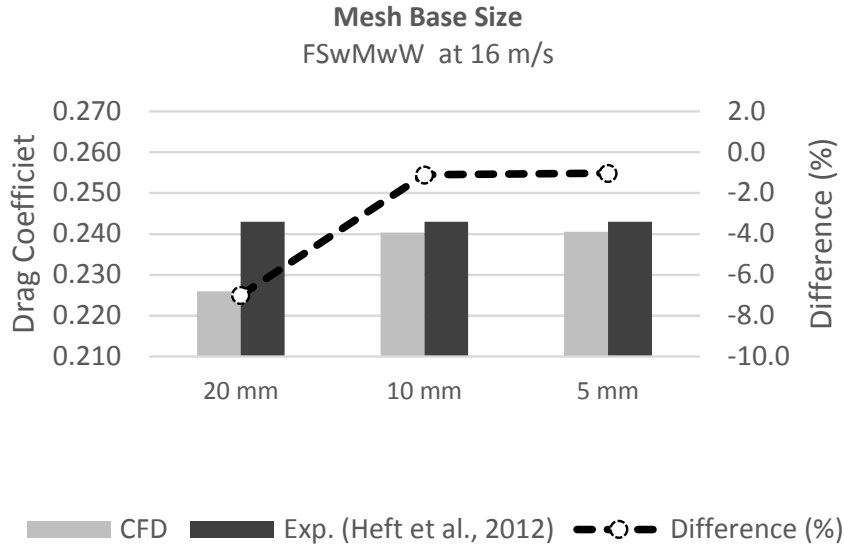


Figure 4.9: Effects of the mesh base size on drag coefficient prediction.

This parameter influences mainly the viscous drag prediction and the evaluation of properties gradients surrounding car surfaces, *i.e.* small surface cells can improve the evaluation of distribution and level of skin friction of surface. The mesh base size is characterized by the maximum size of cell edge over the car surface.

Drag prediction has been affected by the mesh base size until it decreases up to 10 mm (-1.1% from experimental data of FSwMwW). A further refinement to 5 mm of cell size gently change from the previous mesh base size (-1.0% over FSwMwW). On the other hand, the mesh size increases significantly as the mesh base size is reduced. The mesh base size of 20 mm, 10 mm, and 05 mm generated mesh with 3.38, 3.39, and 7.20 million cells, respectively.

Thus, the refinement from 10 mm to 05 mm requires more than twice the computational resources, whereas there is no substantial gain in accuracy, *i.e.*, improvement of 0.1% in accuracy towards experimental data only.

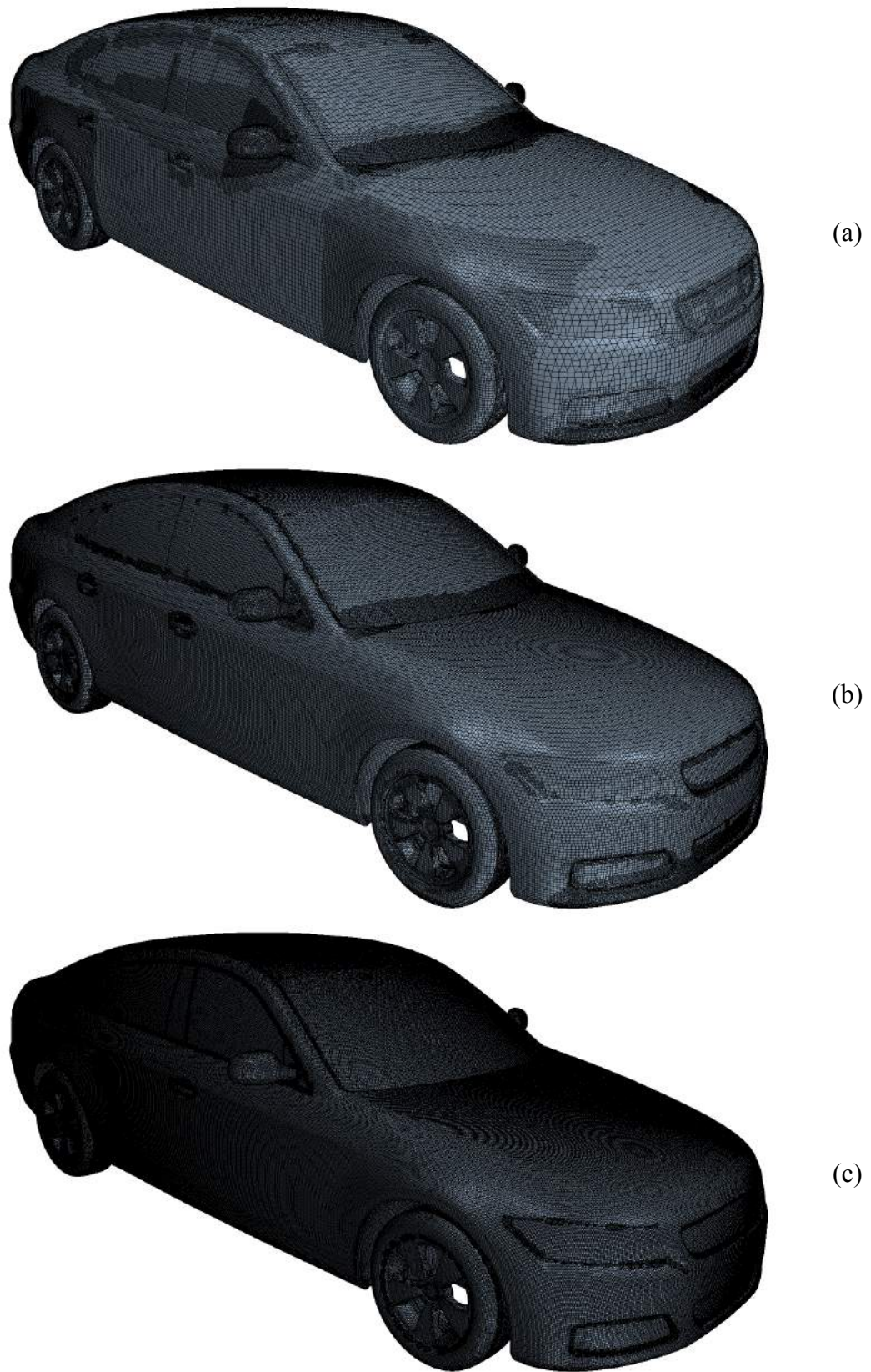


Figure 4.10: Mesh base size over the car surface: (a) 20 *mm*, (b) 10 *mm*, and (c) 05 *mm*.

#### 4.2.1.3 Influence of the Gradient Scheme

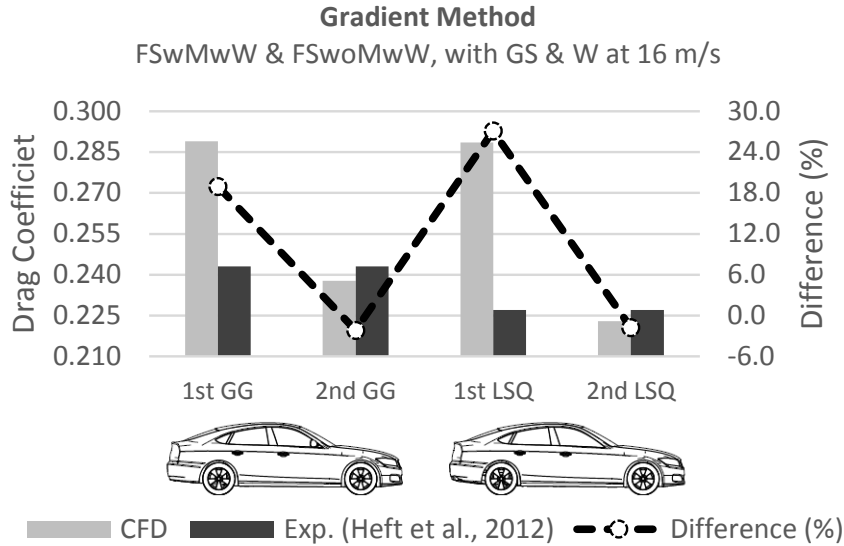


Figure 4.11: Effects of the gradient method on drag coefficient prediction.

There are different possible schemes for the gradient numerical approximation. The accuracy of the computation depends on the scheme chosen for the gradient calculation, which is necessary to calculate the fluxes over the faces of neighbouring control volumes.

The first-order scheme is based on linear relation of a cell to the adjacent cells, and thus represent poorly distribution of properties. By contrast, second-order schemes increase the degree of approximation function, which leads to better evaluation of flow gradients and lower numerical diffusion than first-order ones.

The results confirm that both Green-Gauss (FSwMwW) and Hybrid Gauss-LSQ (FSwoMwW) gradient schemes in 1<sup>st</sup>-order discretization lead to miscalculation of the drag when compared to experimental data (19% and 27% via Green-Gauss and Hybrid Gauss-LSQ, respectively).

Second-order schemes have provided realistic values of drag force. Hence, the squared approximation of Green-Gauss underestimates by 2.1% the experimental reference of the FSwMwW, while the same order of Hybrid Gauss-LSQ predicts the drag of the FSwoMwW assembly 1.8% lower.

#### 4.2.1.4 Influence of the Prism Layer Thickness

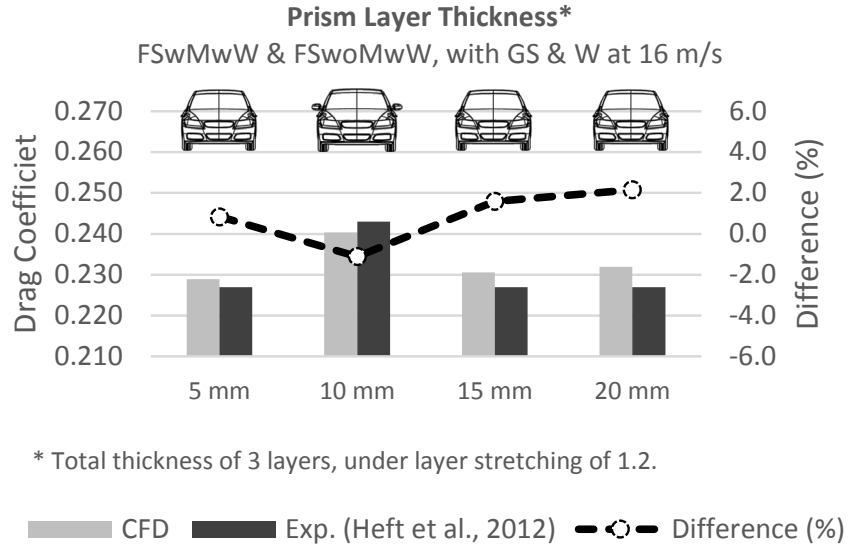


Figure 4.12: Effects of the total prism layer thickness on drag coefficient prediction.

The size of prism layers is directly associated to the wall function treatment, where it is proportional to non-dimensional height of boundary layer ( $y^+$ ). The variation of the prism layer thickness over the car surface has a slight impact upon drag prediction, since the *All  $y^+$  Wall Treatment* is used on the wall boundaries. However, it is recommended to set the prism layer thickness to achieve  $y^+$  values into the log region of law of the wall. In other words,  $y^+$  should be between 30 and 300, approximately.

This study assumed the total thickness of prism layer as an input parameter, where it is split into three prism layers with grown rate of 1.2 from the surface, *e.g.*, the first layer on the wall shares 27.5% of total prism layer thickness, and second and third layers have 33% and 39.5%, respectively.

As a car speed of 16 m/s is assumed, the thicker prism layer of 20 mm allow a drag prediction with a 2.2% from experimental results, while 15 mm (1.6%) and 10 mm (-1.1%, with FS wM wW) reduce the difference. The best matching is obtained by a prism layer thickness of 5 mm (0.8%). Nevertheless, the theoretical optimum thickness of prism layers ( $30 < y^+ < 300$ ) is recommended whenever the *All  $y^+$  Wall Treatment* is not available. Thus, the ideal prism layer thickness for a full-scale car at 16 m/s would be 12 mm in average, and 5 mm for 40 m/s of freestream, according to the evaluation of  $y^+$  during this research.



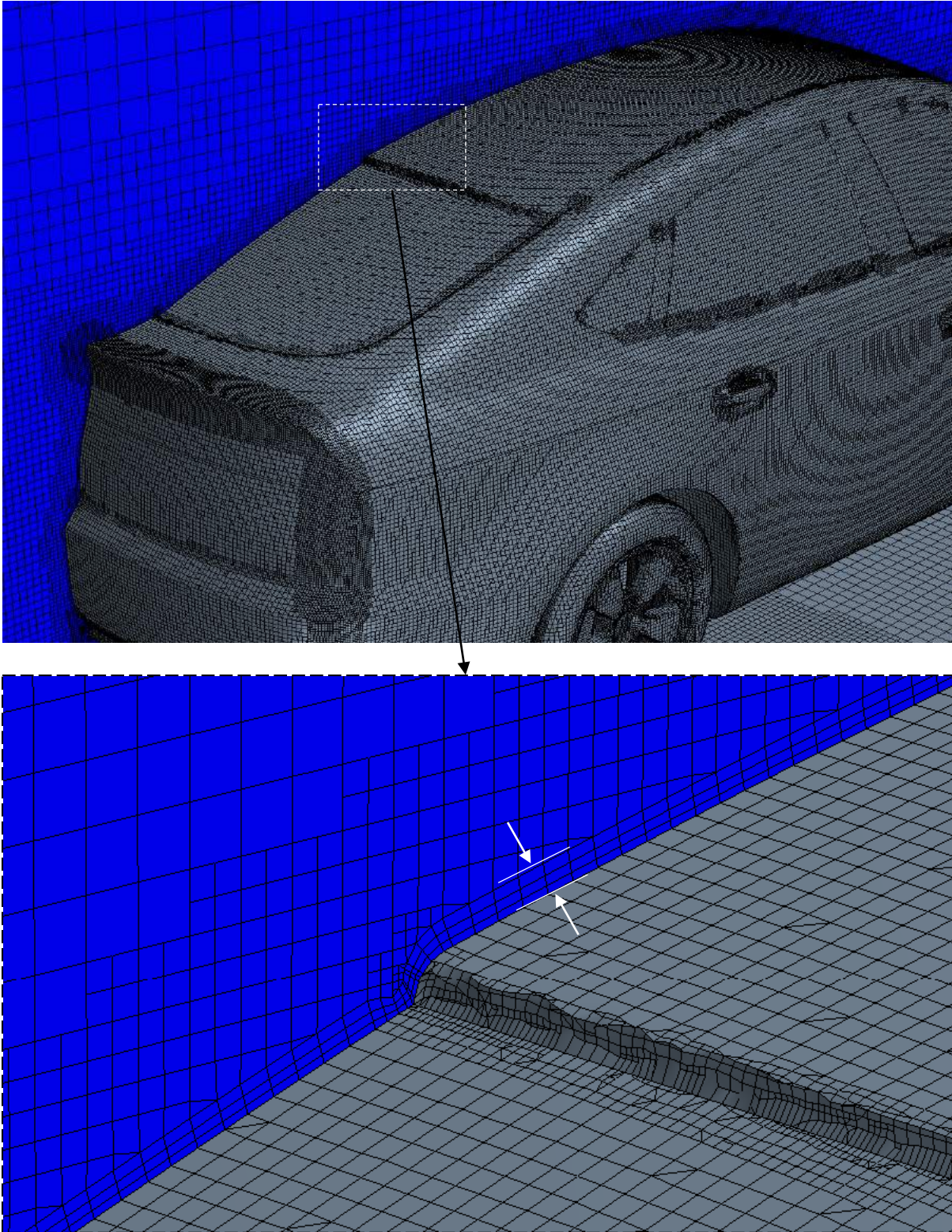


Figure 4.13: Sample of prism layers contouring the rear-end edge.

#### 4.2.1.5 Influence of the Ground & Wheel Simulation in different car assemblies

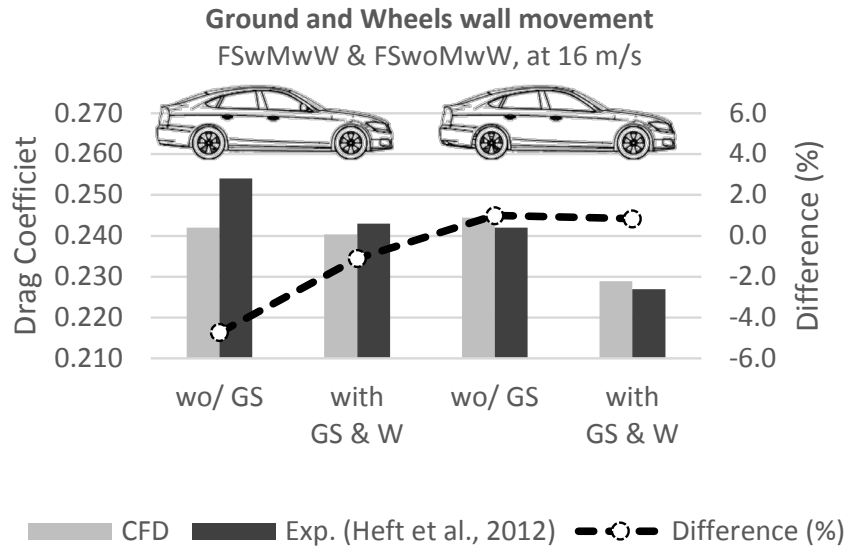


Figure 4.14: Effects of the ground condition in different car assemblies on drag coefficient prediction.

Similar to the previous subtopic, this one investigates the influence of ground & wheel conditions in drag prediction. However, such features are compared between two assemblies of DrivAer fastback model: FSwMwW and FSwoMwW.

Nevertheless, the car model holding mirrors is one of the most challenging DrivAer assemblies for numerical simulation. Usually external mirrors are critical in terms of unsteady-state forces. Separation at the mirror housing may be periodic and thus produce an oscillating mirror load (Hucho, 1998).

Indeed, the convergence with such feature is hard to achieve, but it is possible with appropriate mesh refinement in the wake region downstream the mirrors. On one side, a coarse mesh will provide less accurate results especially over the mirror. This problem can be solved with local mesh refinement. However, a highly refined mesh may lead to a side effect for the turbulence models. Few turbulence models may capture instabilities in the flow due to their mathematical approach, and they may be unable to handle a solution in steady-state. This last situation would require unsteady-state analysis due to the aerodynamic phenomena, even though the computational cost might be much higher.

Even so, the simulation of car with mirrors (FSwMwW) in steady-state has yielded relatively good results without ground simulation (-4.7%) and in well accordance with

ground & wheel simulation approach (-1.1%). The model without mirrors (FSwoMwW) achieved drag difference against the experimental data of 0.8% and 1.0%, corresponding to with (*with GS & W*) and without (*wo/ GS*) ground simulation approaches.

Therefore, the simulation with ground & wheels movement has provided better agreement with experimental reference than stationary ground condition. Such evidence also confirms that the artificial approach of wheel movement yields significant results in lower computing requirement.



#### 4.2.1.6 Influence of the Ground & Wheel Simulation at different flow speeds

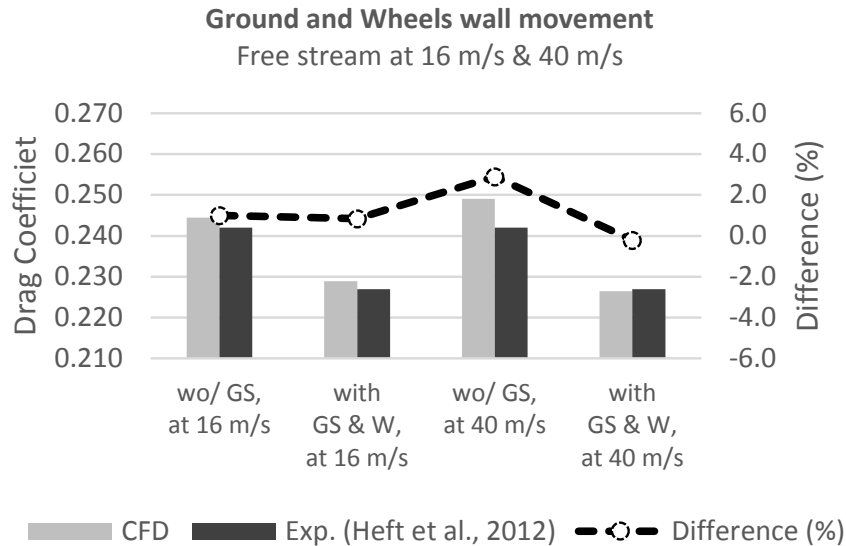


Figure 4.15: Effects of the ground condition at different flow regimes on the drag coefficient prediction.

Most of experimental literature about automotive aerodynamics have investigated vehicle in wind tunnel with stationary ground and wheels (whenever available). This means that this kind of experiments do not evidence the influences of neither relative ground movement nor the wheel rotation on the flow surrounding the car. Recently, automotive wind tunnels have employed powered moving belt system to simulate the ground moving under a fixed vehicle, and detached and independent wheels to allow its rotation.

Since stationary and ground & wheels movement cases are available in the experimental research of Heft *et al.* (2012), such data is used as reference to compare the influence of both conditions in numerical simulations. Two freestream conditions (16 m/s and 40 m/s) are tested in stationary and ground movement approaches, as previously described in Table 4.6 and shown in Figure 4.15.

Simulation of the model with and without ground simulation have closely matched the experimental results, apart from the larger difference (2.9%) in the case of model at 40 m/s on stationary ground & wheels. This demonstrates significant accordance between numerical simulation and experimental reference, either without ground movement and, especially, with ground simulation.

Above all, one of the most important facts is that the alternative approach for the wheel effect is successful. Instead of multiple remeshing steps to reproduce the effective rotation of such detailed wheels, the equivalent tangential velocity of each surface cell is imposed as boundary condition over a fixed wheel. The velocity is a function of angular velocity in each car axle. Although the rims do not rotate, the artificial velocity allows simulating such unsteady phenomena as steady-state simulation. As the results endorse this approach, the use of such methodology is highly recommended for the simulation of automotive aerodynamics.

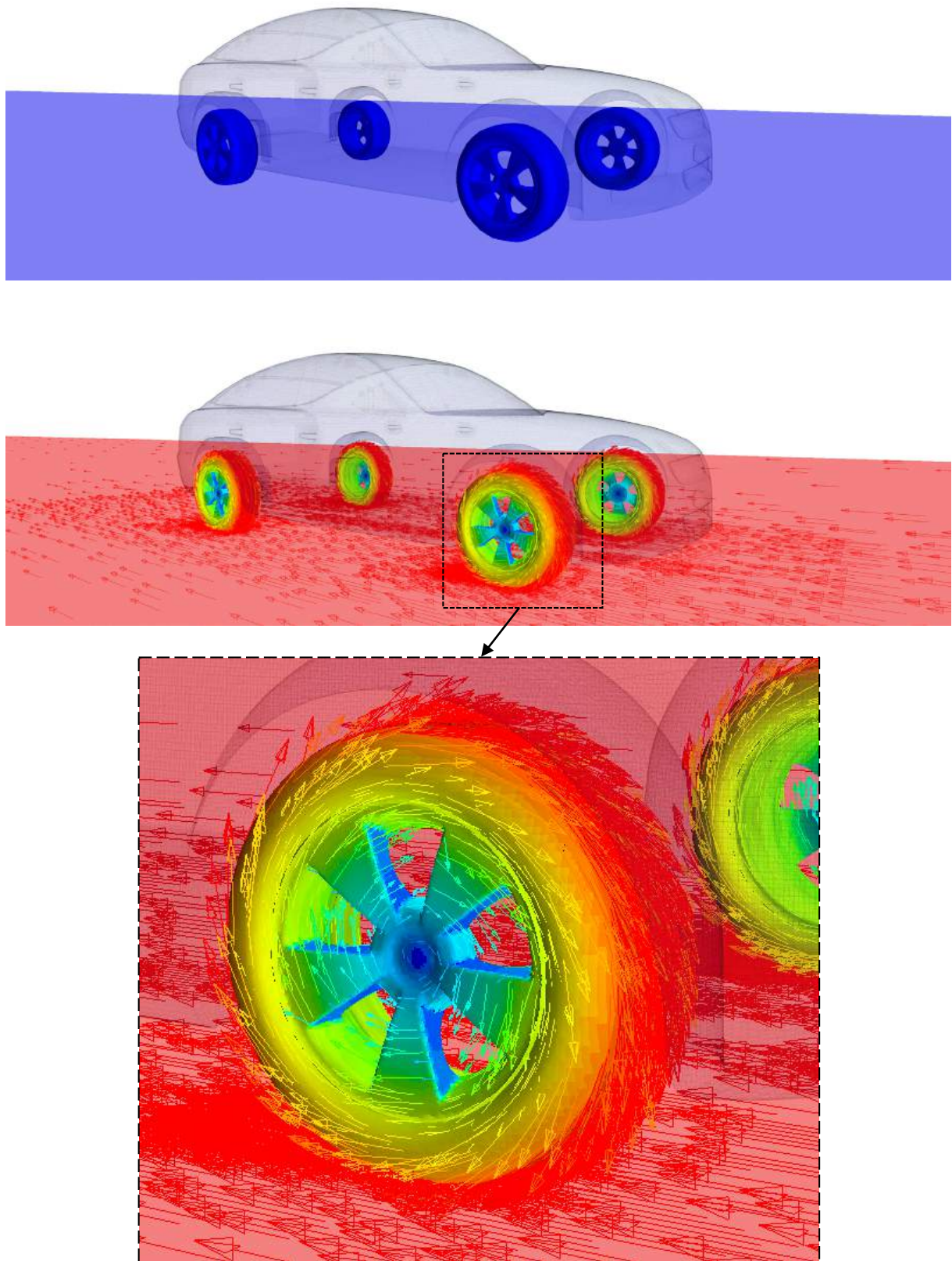


Figure 4.16: Vector velocity field on the ground and wheel surfaces: stationary ground & wheels (above), ground & wheels movement (centre), and front-right wheel in detail (below).

#### 4.2.1.7 Influence of the Turbulence Model

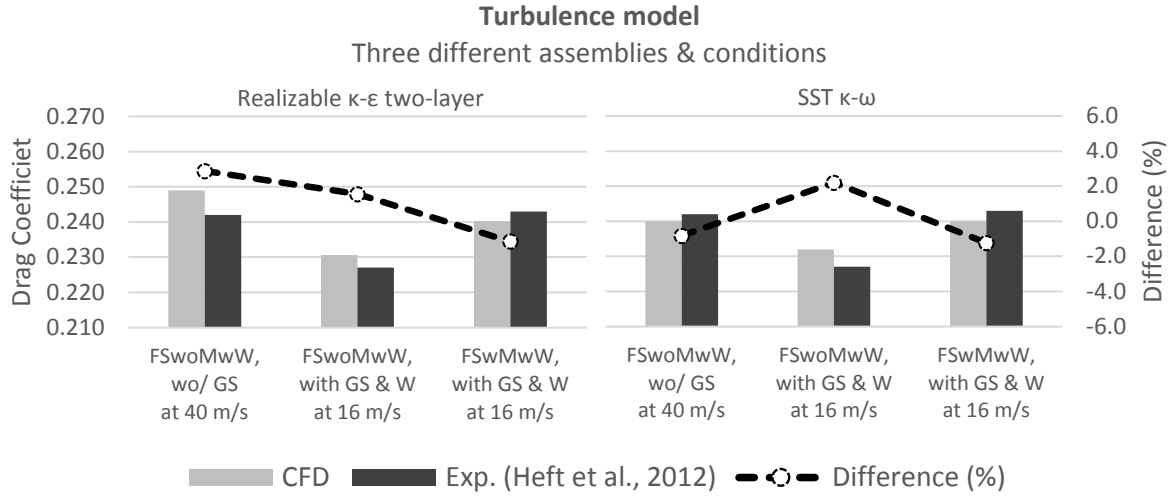


Figure 4.17: Comparison of Realizable  $k$ - $\epsilon$  two-layer and SST  $k$ - $\omega$  turbulence models.

Analogous to the subtopic 4.1, however over a three-dimensional car model, this section compares the drag results from Realizable  $k$ - $\epsilon$  two-layer and SST  $k$ - $\omega$  turbulence models. The simulations are based on the combination from assemblies (with or without mirror) and condition variations (with or without ground simulation, at freestream of either 16  $m/s$  or 40  $m/s$ ). The three combination chosen are: (i) FSwMwW, wo/ GS at 40  $m/s$ , (ii) FSwMwW, with GS & W at 40  $m/s$ , and (iii) FSwMwW, with GS & W at 40  $m/s$ . The prediction of drag coefficient with both turbulence models is presented in Figure 4.17.

Both the Realizable  $k$ - $\epsilon$  two-layer and the SST  $k$ - $\omega$  turbulence models estimate the trend drag over different car assemblies & conditions. The quantitative results also indicate that both have substantial accuracy, where all six simulation are in the range of -1.2% to 2.9% of difference in comparison to experimental database of Heft *et al.* (2012). However, the results from the  $k$ - $\omega$  model-based are considerable unstable solutions when the residuals and drag coefficient estimation are concerned. The results in Figure 4.17 are averaged due to these numerical issues. For instance, the fluctuation on the drag coefficient solution via SST  $k$ - $\omega$  over the combination *i* is nearly from 0.23 to 0.25, and even worse is the variation of 40 drag counts presented in the case *iii*. Conversely, the  $k$ - $\epsilon$  model-based estimated the drag coefficient in a suitable range for all three cases, and demonstrated stable results.

Therefore, the conclusions from the previous analysis of turbulence model (4.1.4 Summary of Two-Dimension Analysis) are confirmed in this subtopic. The results indicate that the Realizable  $k$ - $\epsilon$  two-layer is one step ahead from the SST  $k$ - $\omega$  turbulence model, whenever the robustness of the CFD methodology for low computational cost is concerned.

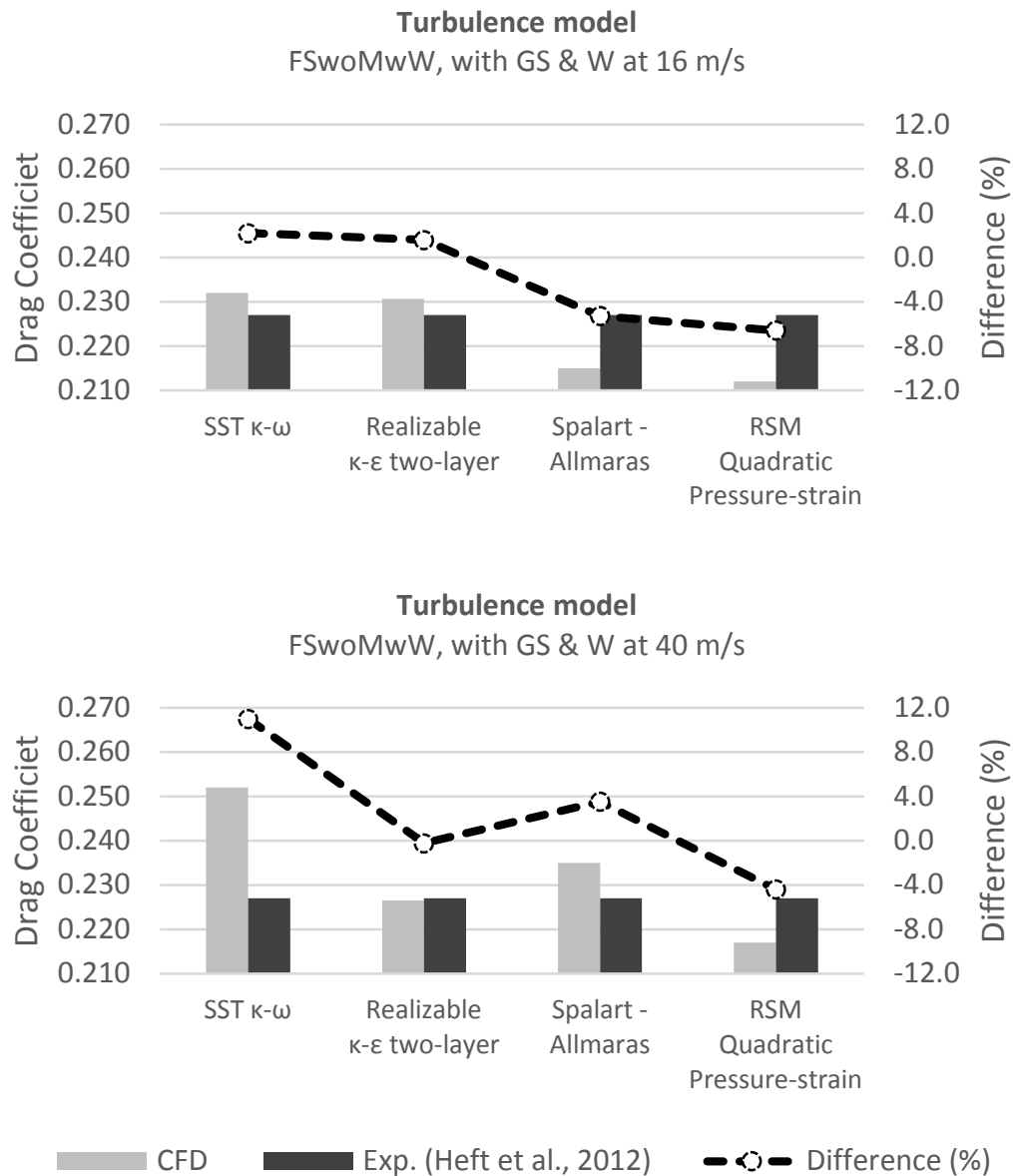


Figure 4.18: Effects of turbulence models on drag coefficient prediction at different freestreams.

Additionally, the Spalart-Allmaras and RSM (Quad. Pressure-strain) are compared to the other two turbulence models. A car assembly with ground simulation (FSwoMwW, *with GS & W*) has been simulated in steady-state at two flow speeds: (i) at

16 m/s, and (ii) at 40 m/s. The mesh in the case of freestream at 16 m/s has around 3 million cells, while a mesh of 3.5 million cells simulates the car at 40 m/s. The results of the four turbulence models are displayed in Figure 4.18.

The results for the freestream at 16 m/s indicate that the  $k$ - $\epsilon$  model is the most accurate among the four turbulence models, with difference of 4 drag counts (1.6%). At first sight, the Reynolds Stress Model (RSM) underpredicted the experimental data by nearly -7%. However, this is well known for being a very accurate turbulence model, whereas the convergence can be hardly achieved because of numerical instability. Indeed, the residual demonstrates that this model could not deal with the simulation over the mesh resolution and flow properties adopted. In the end, RSM has a reasonable accuracy for industrial purpose even with such a small mesh, but it is not recommended for steady-state simulations because of its lack of robustness. By contrast, the SST  $k$ - $\omega$  model overpredicts sharply the drag coefficient by approximately 19%. An even worst result is achieved by means of the Spallart-Allmaras model, where a difference of 23% between the CFD simulation and the experiment is found.

Regarding a higher car speed (*i.e.* higher Reynolds number), the results from simulation with freestream at 40 m/s become closer to the experimental reference, in a range of 8%. The Realizable  $k$ - $\epsilon$  two-layer provided the most accurate drag coefficient, with difference of around 0.5 drag count (-0.2%). This result is so accurate that even the experiment data may contain a larger fluctuation than such a difference. The Spalart-Allmaras estimated the non-dimensional force by 3.5%, standing the second position in accuracy. The Reynolds Stress Model still underpredicted the drag coefficient, but now by -4.4%. Even improving the accuracy in comparison to freestream at 16 m/s, the SST  $k$ - $\omega$  miscalculated the drag coefficient in approximately 27 drag counts (12%).

Based on the results, the  $k$ - $\epsilon$  model-based has proven a better option among the four RANS turbulent models tested, in steady-state. Hence, it is highly recommended for simulation of automotive aerodynamics whenever the goal is the best cost-efficient of computational resources.

#### 4.2.1.8 Influence of the Car Type

The DrivAer variations are tested in the same assemblies and conditions, in order to evaluate how the CFD technique deals with the drag prediction of each car type.

The Fastback, Notchback, and Estateback DrivAer variations, with Smooth underbody (FS, NS, and ES), are tested at 16  $m/s$  in three combinations of assembly & ground condition each: (i) wMwW, with GS & W; (ii) woMwW, with GS & W; and (iii) woMwW, wo/ GS.

The fastback type allows the better drag estimation over the simulations. A reason for this is the roof curvature of this class of car, which is the most aerodynamic shape among the DrivAer variations. The flow do not detaches over the car roof, and consequently flow solution is a little less complex than other cases. Moreover, the well-defined edges on the rear car model minimize the effects of unsteadiness in the flow separation.

The notchback type is similar to the fastback, except by the sharp inclination of the rear window and the well-defined trunk whose lid forms a distinct deck. This geometry leads to a small recirculation between the upper trunk surface and the rear window. Subsequently, the complexity of the external flow increases, and the numerical solution is a little more challenging than the fastback type. The drag prediction of this car type is a little more imprecise than the fastback.

The estateback is the more challenging car type for computational prediction of drag force. The bluff body shape of this class of car promote a full separation of external flow backwards the rear car surface. It results in a more intense turbulent wake, and thus higher loss of flow energy and increase of drag magnitude. The drag estimation of estateback car type shows the higher discrepancy, in comparison to fastback and notchback types.

As the combination of assembly & ground condition are concerned, the drag prediction is challenging whenever the mirrors are placed in the car model, *i. e.*, configuration *i*. The fastback type with mirrors differs -1.1% from experiments, while the notchback diverges in -3.8% and the estateback in -12.8%. Both configurations (*ii* and *iii*) without mirrors reaches significant accuracy in the drag prediction, with the exception of the estateback type.

Figure 4.19 present the drag prediction of all three DrivAer car types, each in three configurations of assembly & ground condition.

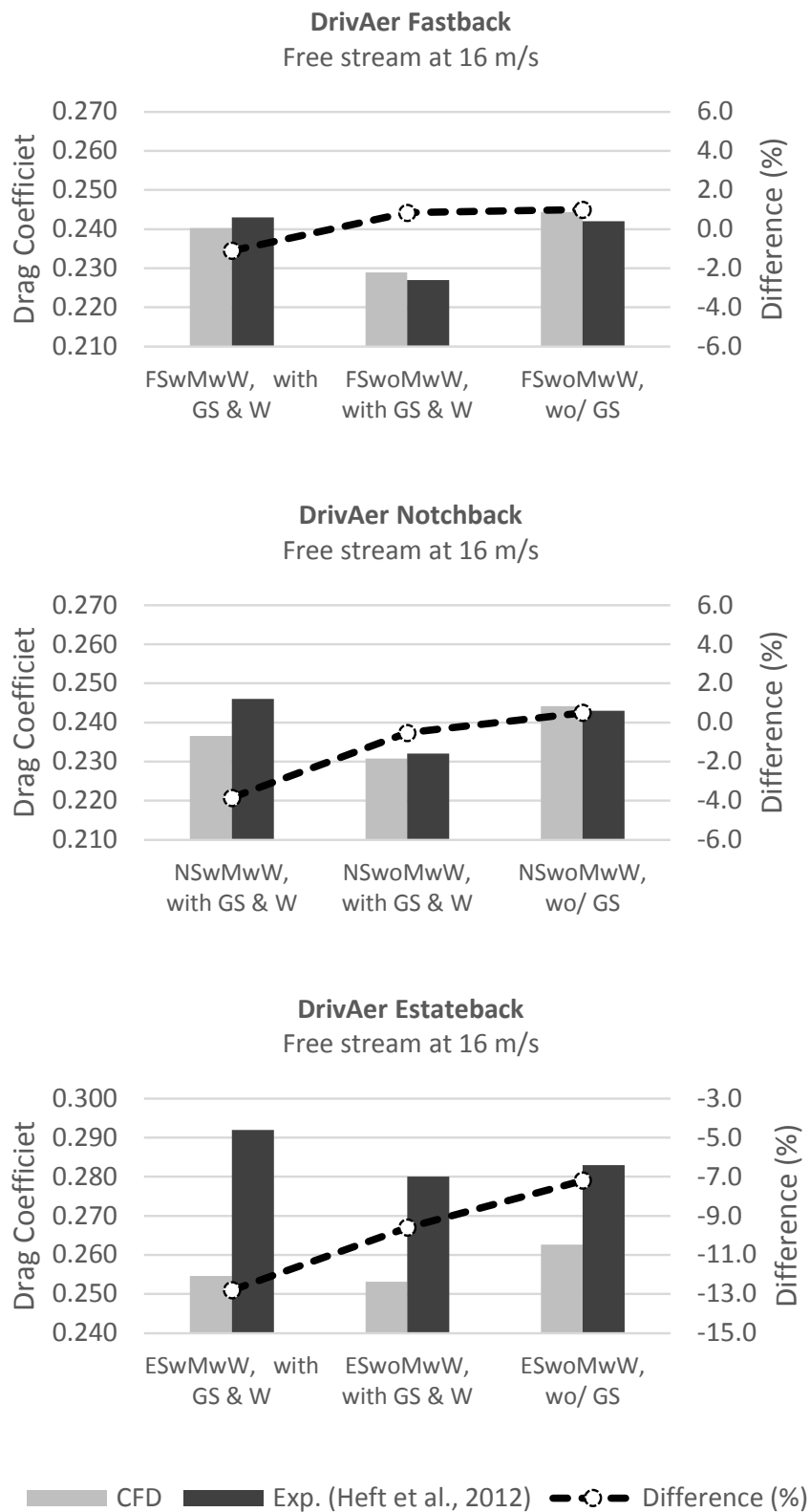


Figure 4.19: Effects of car model type on drag coefficient prediction.



#### 4.2.2 Summary of Three-Dimensional Analysis

The influence of numerical parameters on the drag prediction is analysed in this subtopic, based on experimental data of a realistic car model. The objective is to propose a best practice in CFD for drag prediction of real road cars, at low computational cost.

Besides the validation with full-car domain in unsteady-state simulation, the simplification of the domain by half and the steady-state regime were found to provide an acceptable approach for automotive simulation.

Another significant fact is that the alternative approach for the wheel effect is successful. The equivalent tangential velocity imposed as boundary condition over a fixed wheel, avoiding multiple remeshing steps to reproduce the effective rotation of such a detailed wheels. Even though the rims do not rotate, the artificial velocity allows simulating such unsteady phenomena in a steady-state simulation.

In the end, the main contributions of this study are: (a) to present the influences of meshing parameters on drag prediction, as well as (b) to outline a best practice in CFD simulation of a three-dimensional realistic car model for industrial purpose, as presented in Table 4.9 (bias towards low computational cost) and Table 4.10 (bias towards accuracy).

Table 4.9: Recommended CFD methodology: best cost-effective setup for drag prediction, biased towards the low computational cost.

Factor	Properties
Car simplification	with no mirrors and with wheels (woM wW)
Domain	half-car model
Ground condition	ground simulation & wheel surfaces under local rotation rate (with GS & W)
Time regime	steady-state
Turbulence model	Realizable $k$ - $\epsilon$ two-layer
Gradient method	2 <sup>nd</sup> -order, either Green-Gauss <i>or</i> Hybrid Gauss-LSQ
Mesh base size	10 mm
Total thickness of prism layers	12 mm (for standard wall treatment, at $U_\infty = 16$ m/s) 05 mm (for standard wall treatment, at $U_\infty = 40$ m/s)
Prism layer	3 layers with stretching rate of 1.2
Number of cells	$\sim 4 \times 10^6$

Table 4.10: Alternative CFD methodology: best cost-effective setup for drag prediction, biased towards the numerical accuracy.

Factor	Properties
Car simplification	with mirrors and with wheels (wM wW)
Domain	full-car model
Ground condition	ground simulation & wheel surfaces under local rotation rate (with GS & W)
Time regime	unsteady-state ( $\Delta t = 1 \times 10^{-4} \text{ s}$ )
Turbulence model	Realizable $k$ - $\varepsilon$ two-layer
Gradient method	2 <sup>nd</sup> -order Hybrid Gauss-LSQ
Mesh base size	05 mm
Total thickness of prism layers	05 mm (for <i>All <math>y^+</math> Wall Treatment</i> , at $U_\infty = 16 \text{ m/s}$ ) 05 mm (for <i>All <math>y^+</math> Wall Treatment</i> , at $U_\infty = 40 \text{ m/s}$ )
Prism layer	3 layers with stretching rate of 1.2
Number of cells	$\sim 9 \times 10^6$

## **CHAPTER V**

### **ANALYSIS OF THE FLOW OVER THE DRIVAER CAR MODELS**

This chapter discusses the flow phenomena by means of RANS simulations over the three DrivAer variations: Fastback, Notchback, and Estateback. Additionally, a DES simulation provides a more detailed flow over the DrivAer Fastback car model, in which the flow visualization via the Q-criterion and the Lambda-2 criterion are compared.

The main goal of this chapter is to present and to discuss about the flow visualization from RANS and DES simulations via different properties and criteria.

#### **5.1 ANALYSIS OF THE FLOW VIA RANS STEADY-STATE SIMULATIONS**

As the flow phenomena are concerned, three combinations of assembly & ground condition are chosen for comparison: (i) wMwW, with GS & W; (ii) woMwW, with GS & W; and (iii) woMwW, wo/ GS. These three combinations are tested over each DrivAer variation: Fastback (FS), Notchback (NS), and Estateback (ES).

##### **5.1.1 Brief analysis of the flow via turbulent kinetic energy**

The turbulent kinetic energy (TKE) distribution is concentrated around three major regions: the rear turbulent wake, the mirror, and the wheelhouse. Figure 5.1 displays the turbulent kinetic energy magnitude over three simulation condition: yz planes, within the range

of  $8 \text{ J/kg}$  (blue/cold colour) to  $15 \text{ J/kg}$  (red/red colour) for freestream at  $16 \text{ m/s}$ , and from 45 to  $70 \text{ J/kg}$  for cases at  $40 \text{ m/s}$ .

A higher amount of TKE is noticed close to the symmetry plane approximately  $1.1 \text{ m}$  downstream the car rear. Another region, of lower magnitude, is associated to the two vortex structures from the rear bumper corners. As the flow sweeps the car side surface and reaches the rear bumper, it detaches intensively. While the lower part of such flow sweeps the lower corner surface of the bumper, the stream  $100 \text{ mm}$  above it keeps straight a little longer. It leads to coherent vortices, one from each bumper corner. Both vortex generates a high TKE region.

Last, but not least, the surrounding wheelhouses are other regions of turbulence generation. A portion of the upstream flow, which flows over the front bumper and tends to follow the vehicle, reaches a local detachment of the flow at the wheelhouse border and its cavity. Likewise, another portion achieves that limit following the underbody. Additional pictures of TKE distribution are available in Appendix (from Figure 12.4 to Figure 12.6).

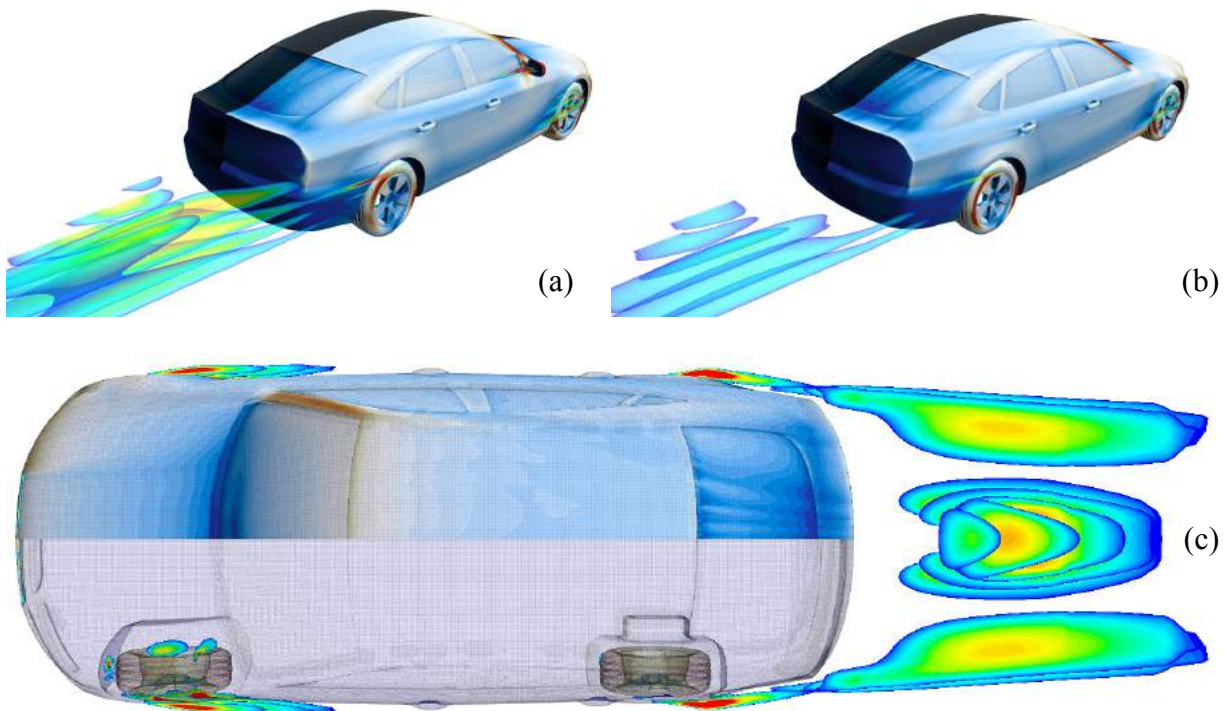


Figure 5.1: Turbulent kinetic energy magnitude over: (a) FSwMwW, with GS & W at  $16 \text{ m/s}$  and (b) FSwoMwW, with GS & W at  $16 \text{ m/s}$ ; and (c) FSwoMwW, with GS & W at  $40 \text{ m/s}$ .

### 5.1.2 Comparison of the external flow via iso-vorticity surface

The comparisons are based on seven regions over the car models, and are summarized in Table 5.1 (wMwW, with GS & W), Table 5.2 (woMwW, with GS & W), and Table 5.3 (woMwW, wo/ GS).

The iso-vorticity surface of  $100 \text{ rad/s}^2$  is adopted for comparison purpose among the nine cases compared (Figure 5.2). The car surfaces display the skin friction coefficient ( $C_f$ ) from 0 (blue / cold colour) to 0.01 (red / hot colour). Please note that larger pictures corresponding to each case are available in Appendix (from Figure 12.1 to Figure 12.3).

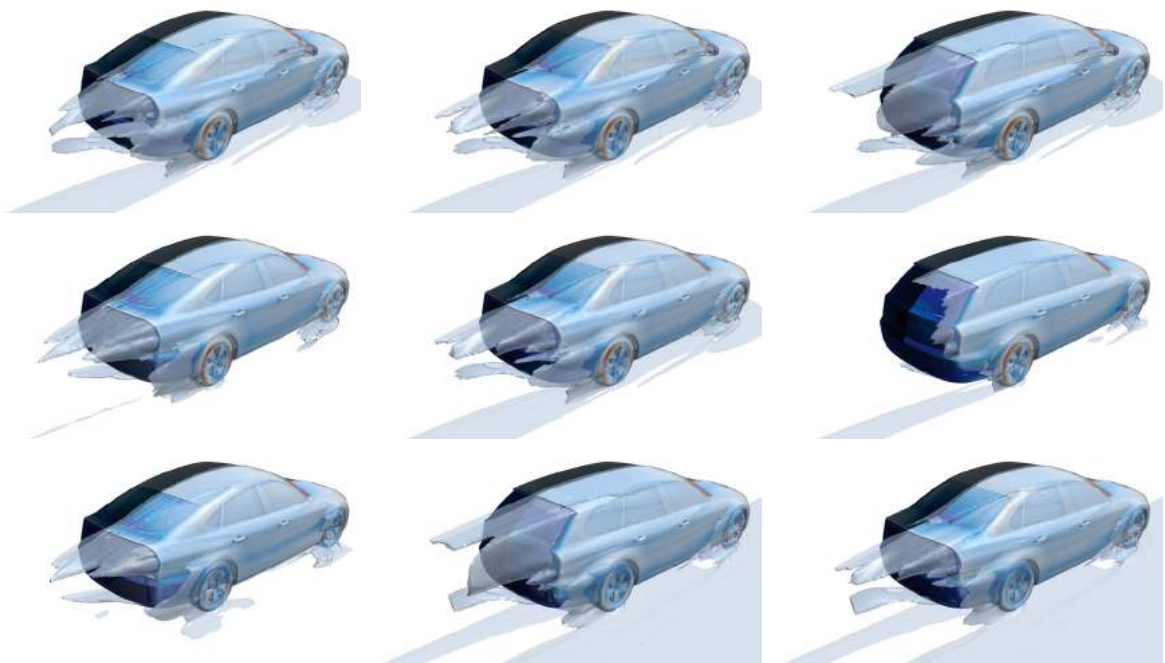



Figure 5.2: Comparison of RANS steady-state simulations via iso-vorticity surface of  $100 \text{ rad/s}^2$  over the three DrivAer variations. Each car type are presented in: wMwW, with GS & W (upper row); woMwW, with GS & W (middle row); and woMwW, wo/GS (lower row).

Table 5.1: Comparison of the external flow: wMwW DrivAer models, with GS & W.

Region	Fastback	Notchback	Estateback
<b>A-pillar vortex</b> 	The vortex is generated at A-pillar, contours upwards the front door window and reaches the roof at B-pillar.	The vortex is generated at A-pillar, contours upwards the front door window and reaches the roof a little after the B-pillar.	The vortex is generated at A-pillar, contours upwards the front door window and reaches the roof at the end of rear door window.


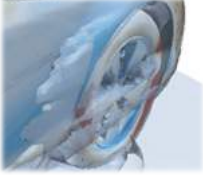




Region	Fastback	Notchback	Estateback
	It detaches almost at the rear upper edge, $\sim 150\text{ mm}$ from the symmetry plane.	It detaches completely over the rear window end, $\sim 200\text{ mm}$ from the symmetry plane.	It detaches at the rear roof end, $\sim 350\text{ mm}$ from the symmetry plane.
<b>Mirrors</b> 	Backwards intense mirror turbulent wake, forming counter-rotating vortices downstream of each mirror.	Similar to FS.	A little less intense than FS.
<b>Frontal wheelhouse</b> 	<p>Separation flow from the fender at the front wheelhouse edges.</p> <p>Reattachment at <math>\sim 200\text{ mm}</math> after the rear edge of frontal wheelhouse.</p>	Similar to FS.	Similar to FS.
<b>Rear wheelhouse &amp; rear bumper cornering</b> 	<p>Separation flow from the rear bumper surface at <math>\sim 100\text{ mm}</math> after the rear wheelhouse edge.</p> <p>Strong tendency to corner vortex trailing, backwards the vehicle.</p>	<p>Separation flow similar to FS, at <math>\sim 125\text{ mm}</math> after the rear wheelhouse edge.</p> <p>Moderate trend to corner vortex trailing, backwards the vehicle.</p>	<p>Less intense flow separation among the assemblies, in the range of <math>150</math> to <math>300\text{ mm}</math> after the rear wheelhouse edge.</p> <p>Smooth trend to corner vortex trailing, backwards the vehicle.</p>
<b>Diffuser</b> 	Upwards trend, with slight change backwards.	Similar to FS.	Similar to FS.
<b>Main turbulent wake</b> 	<p>The separation follows the upper curvature (downwards) and rear side panels (inwards).</p> <p>Smallest turbulent wake among the car types.</p>	<p>The separation follows the roof (downwards) curvature and rear side panels (inwards).</p> <p>The downwards trend is reduced by the slight trunk deflection.</p> <p>Small turbulent wake.</p>	The full separation occurs backwards, at the edges of trunk and roof end. Intense turbulent wake.
<b>Wheels</b> 	<p>Horse-shoe vortex generation: intense at front wheel, and insignificant at rear wheel.</p> <p>Strong turbulent wake for <math>\sim 300\text{ mm}</math> long.</p> <p>High friction on the tires surface.</p>	Similar to FS.	Similar to FS.

Table 5.2: Comparison of the external flow: woMwW DrivAer models, with GS &amp; W.














Region	Fastback	Notchback	Estateback
<b>A-pillar vortex</b> 	<p>The vortex is generated at A-pillar, contours upwards the front door window and reaches the roof a little bit before the B-pillar.</p> <p>It detaches only at the rear upper edge, <math>\sim 150\text{ mm}</math> from the symmetry plane.</p>	<p>Similar to NSwMwW, with GS &amp; W.</p>	<p>The vortex is generated at A-pillar, contours upwards the front door window and reaches the roof at the middle of rear door window.</p> <p>The A-pillar vortex is dissipated before the rear roof end.</p>
<b>Mirrors</b> 	*with no mirrors geometry	*with no mirrors geometry	*with no mirrors geometry
<b>Frontal wheelhouse</b> 	<p>A little less intense than FSwMwW, with GS &amp; W.</p>	<p>Similar to NSwMwW, with GS &amp; W.</p>	<p>Full separation flow from the fender at the front wheelhouse.</p> <p>Reattachment at <math>\sim 250\text{ mm}</math> after the rear edge of frontal wheelhouse.</p>
<b>Rear wheelhouse &amp; rear bumper cornering</b> 	<p>Full separation flow from the rear bumper surface at <math>\sim 50\text{ mm}</math> after the rear wheelhouse edge.</p>	<p>Similar to NSwMwW, with GS &amp; W.</p>	<p>Intense separation flow from the rear bumper surface at <math>\sim 50\text{ mm}</math> after the rear wheelhouse edge.</p>
<b>Diffuser</b> 	<p>Smooth upwards tendency.</p>	<p>Similar to NSwMwW, with GS &amp; W.</p>	<p>A little less intense than NS.</p>
<b>Main turbulent wake</b> 	<p>Similar to FSwMwW, with GS &amp; W.</p>	<p>Similar to NSwMwW, with GS &amp; W.</p>	<p>Similar to ESwMwW, with GS &amp; W.</p>
<b>Wheels</b> 	<p>Presumed horse-shoe vortex generation (numerical issues).</p> <p>Strong turbulent wake for <math>\sim 300\text{ mm}</math> long.</p> <p>High friction of the tires surface.</p>	<p>Similar to NSwMwW, with GS &amp; W.</p>	<p>Similar to ESwMwW, with GS &amp; W.</p> <p>Shorter turbulent wake.</p>



Table 5.3: Comparison of the external flow: woMwW DrivAer models, wo/ GS.

Region	Fastback	Notchback	Estateback
<b>A-pillar vortex</b> 	Similar to FSwoMwW, with GS &W.	Identical to NSwoMwW, with GS &W.	Similar to ESwMwW, with GS &W.
<b>Mirrors</b> 	*with no mirrors geometry	*with no mirrors geometry	*with no mirrors geometry
<b>Frontal wheelhouse</b> 	<p>Separation flow from the fender, only at the upper half of front wheelhouse edge.</p> <p>The complete reattachment occurs on the surface of front door, <math>\sim 300\text{ mm}</math> below of respective door handle.</p>	<p>A little less intense than NSwMwW, with GS &amp;W.</p> <p>Additional presence of vortex on the lower edge of front door.</p>	Similar to NS.
<b>Rear wheelhouse &amp; rear bumper cornering</b> 	Full separation flow from the rear bumper surface at $\sim 25\text{ mm}$ after the rear wheelhouse edge.	A little more intense than NSwoMwW, with GS &W.	Similar to ESwMwW, with GS &W.
<b>Diffuser</b> 	<p>Similar to FSwoMwW, with GS &amp;W.</p> <p>Influenced more strongly by the corner vortex trailing, backwards the vehicle.</p>	A little more intense than NSwoMwW, with GS &W.	Similar to NS.
<b>Main turbulent wake</b> 	Similar to FSwMwW, with GS &W.	Identical to NSwoMwW, with GS &W.	Identical to ESwMwW, with GS &W.
<b>Wheels</b> 	<p>Horse-shoe vortex generation: moderate at front wheel, and insignificant at rear wheel.</p> <p>Unshaped turbulent wake for <math>\sim 250\text{ mm}</math> long. Low friction on the tires surface.</p>	<p>Horse-shoe vortex generation: moderate at front wheel, and insignificant at rear wheel.</p> <p>Unshaped turbulent wake for <math>\sim 300\text{ mm}</math> long.</p>	Similar to NS.



## 5.2 ANALYSIS OF THE FLOW VIA DES UNSTEADY-STATE SIMULATION









Alternative to RANS methodology, Guilmineau *et al.* (2011) demonstrated the applicability of the DES (Detached Eddy Simulation) approach for automotive purpose. According to the authors, even though the bubble in the rear slant of experimental results of Ahmed body is not predicted, such approach provides an improvement compared with the RANS simulations. The side edge vortex is less intense than in the experiments. However, DES models predicts a confined separation where a massive separation behind the Ahmed body is expected.

Aligned with this approach, an additional unsteady-state simulation using Detached Eddy Simulation (DES, based on SST  $k-\omega$  model) has been run in order to provide a better understanding of flow features. The computational setup and boundary conditions are similar to the RANS simulations performed in Chapter IV (Table 4.5 and Table 4.6, respectively). The time step of  $1 \times 10^{-4}$  s was employed for good performance of the transient flow solution. The case adopted is the FSwoMwW, with GS & W at 40 m/s.

The identification of vortex structures are done via two approaches: Q-criterion and Lambda-2 criterion. Similar to the RANS comparison, Table 5.4 presents the comparison between both criteria, regarding the flow visualization at five regions over the car model.

Table 5.4: Comparison of external flow phenomena over DrivAer Fastback model: Q-criterion versus Lambda 2 criterion at  $10^4 \text{ rad/s}^2$  via DES unsteady-state simulation.

Q-criterion		Lambda-2 criterion	
Region	Description	Region	Description
A-pillar vortex	<p>The vortex is generated at A-pillar, contours upwards the front door window and reaches the roof at the B-pillar.</p> <p>The secondary A-pillar vortex contours the front door downwards, which is diffused on the rear door.</p> <p>Tender signs of large Tollmien–Schlichting-like structures on the roof surface, probably generated at the top windshield edge.</p>	A-pillar vortex	<p>Similar to Q-criterion, whereas the vortex reaches the roof a little after the B-pillar.</p> <p>No evidence of large Tollmien–Schlichting-like structures on the roof surface, as seen via the Q-criterion.</p>

Q-criterion		Lambda-2 criterion	
Region	Description	Region	Description
<p>Front wheelhouse</p> 	<p>Separation flow at the front wheelhouse edge, with intense instabilities generation.</p> <p>The most of the stronger structures are faded until the rear door.</p>	<p>Front wheelhouse</p> 	<p>Similar to the Q-criterion. However, the stronger structures are smaller and more spread.</p>
<p>Rear wheelhouse &amp; rear bumper cornering</p> 	<p>The generation of instabilities analogous to Kelvin-Helmholtz occurs at the upper part of rear wheelhouse edge. Further, the tire surface in motion blends them into hairpin structures.</p> <p>The artificial tangential velocity of the rear wheel intensifies the turbulence into the rear wheelhouse, generating small and strong structures, somewhat as the concentric Taylor-Couette flow.</p> <p>The turbulent flow over the rear bumper follows towards to corner vortex trailing.</p>	<p>Rear wheelhouse &amp; rear bumper cornering</p> 	<p>Similar to the Q-criterion. However, the stronger structures are smaller and more spread.</p> <p>The generation of instabilities analogous to Kelvin-Helmholtz is not clear as with the Q-criterion. The forward motion of instabilities are more evident than by the Q-criterion.</p>
<p>Main turbulent wake</p> 	<p>Massive turbulent wake backwards the rear car.</p> <p>The corner vortex trailing presents few large vortices surrounded by a cluster of smaller strong structures</p>	<p>Main turbulent wake</p> 	<p>Well-defined separation flow at the border of rear end and rear side panels.</p> <p>The corner vortex trailing is observed as a cluster of smaller strong structures only.</p>
<p>Wheels</p> 	<p>The geometry and surface velocity of front wheel promote larger structures such as Hairpin-like vortex, which contours the bottom edge of front door and are dissipated before the rear wheel region.</p>	<p>Wheels</p> 	<p>Similar to Q-criterion. Nevertheless, the stronger structures are smaller and more spread.</p>

### 5.3 SUMMARY OF CHAPTER V

This chapter discusses the flow phenomena by means of RANS simulations over the three DrivAer variations: Fastback, Notchback, and Estateback. Additionally, a DES simulation provides a more detailed flow over the DrivAer Fastback car model, where the flow visualization via the Q-criterion and the Lambda-2 criterion are compared.

The RANS approach provided a very feasible assessment among the different DrivAer car variations and assemblies & conditions. Even though these simulations have been run in steady-state, many averaged flow features can be observed via iso-vorticity surface. This allowed the observation of flow separation regions and the outline of specific vortex structures, such as A-pillar and horse-shoe vortices.

On the other hand, the DES approach undoubtedly provided a more realistic flow over the car. The unsteady-state solution indicated other flow features, such as the hairpin-like vortices downstream the front wheel, and the Kelvin-Helmholtz trend in the upper part of the rear wheelhouse edge. Regarding the flow visualization criteria compared over the DES solution, both Q-criterion and Lambda-2 criterion are similar in most of the flow features, as also pointed out by Bacchi (2009). The former highlighted larger vortices structures, while the latter indicated smaller, stronger, spread vortex structures. The Lambda-2 criterion also indicated less unrealistic structures in the flow visualization than via Q-criterion.

Finally, comparing the both RANS and DES approaches in the cost-effective perspective, the RANS solutions is more feasible and provides sufficient main trends about the external flow, such as separation regions and mean larger structures. Therefore, the RANS methodology is recommended because it offers the best cost-effectiveness in flow solution. The DES approach is recommended only for high detailed flow features, *i.e.*, the detailed optimization phase of the design development of vehicles.

Therefore, the main contributions of this chapter is to present a discussion about the flow visualization of external flow via RANS and DES approaches, as well as to compare different properties and criteria for both.



## **CHAPTER VI**

### **PROPOSAL OF AN AERODYNAMIC CONCEPT FOR DRAG REDUCTION**

A proposal of an aerodynamic concept for automotive drag reduction is presented in this chapter. The objective is to identify the potential of blowing and suction methods of momentum over the wake region of the car model.

The main contributions of this chapter are: (a) to highlight the optimum configuration found via two-dimensional analysis, and (b) to offer an aerodynamic concept to improve the drag coefficient of road cars.

#### **6.1 BACKGROUND**

In previous studies, Soares *et al.* (2014 a, b) presented the injection of momentum by jet as an effective method to achieve reattachment of boundary layer over aerofoils. One of the reason to explain such phenomenon is the influence of the additional turbulent kinetic energy over the aerofoil surface. As the air leaves the jet slot, it interacts with the flow over the aerofoil. This interaction generates vortices that increase the turbulent kinetic energy. As consequence, the flow keeps energized enough to delay its separation from the aerofoil upper surface. By contrast, cars usually have massive detachment backwards. Ahmed (1983) indicated in his well-known experiment over the Ahmed body that approximately 85% of the drag comes from the wake region behind the model. Therefore, this study presented in this chapter investigates the feasibility of such methods for automotive applications.

## 6.2 METHODOLOGY

Similarly to numerical investigations presented in the subtopic 4.1 (Two-Dimensional Qualitative Analysis), the symmetry plane profile of DrivAer Fastback model (Heft *et al.*, 2012) in 1:1 scale has adopted as baseline. These numerical simulations also are carried out using the STARCCM+ code, in steady-state. In compliance with the previously established best practice for two-dimensional cases (Table 4.4), the simulations were run with Realizable  $k-\varepsilon$  two-layer turbulence model, under 2<sup>nd</sup>-order Hybrid Gauss-LSQ gradient method.

The height of the rectangular domain is equal to  $4.4L_{ref}$  (see 4.1.1 Effect of Blockage Ratio for Two-Dimensional Cases), where the inlet is placed  $2L_{ref}$  upstream of the car profile. The ground is  $12L_{ref}$  long, and is  $0.065L_{ref}$  from the front axle position. The air density ( $\rho$ ) is assumed constant and equal to  $1.18415 \text{ kg/m}^3$  and its dynamic viscosity ( $\mu$ ) is  $1.85508 \times 10^{-5} \text{ Ns/m}^2$ . The freestream of  $U_\infty = 40 \text{ m/s}$  is chosen to simulate a highway driving condition.

The jet properties are the same as those of the freestream. The channel has a gap of 20 mm and the height of hole on the car surface is 400 mm, 640 mm or 900 mm from the ground level, illustrated in Figure 6.1. The blowing jet is positive in the x-direction, and suction is negative likewise. The Table 6.1 and Table 6.2 present the physical setup and boundary conditions, respectively.

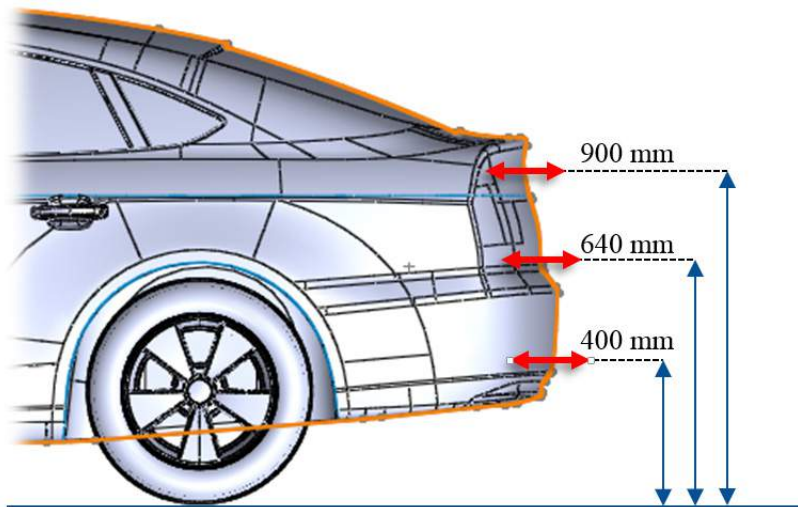


Figure 6.1: Exemplification of the three slot positions on the vehicle profile.

Table 6.1: Physical setup.

Feature	Properties
Domain	Two-dimensional
Time regime	Steady-state
Fluid properties	Air ( $\rho = 1.18415 \text{ kg/m}^3$ ; $\mu = 1.85508 \times 10^{-5} \text{ Ns/m}^2$ )
Flow Solver	Segregated
Equation of State	Constant density
Flow regime	Turbulent
Turbulence model	Realizable $k$ - $\varepsilon$ two-layer

Table 6.2: Boundary conditions.

Boundary	Condition
Car profile	wall: no slip
Inlet	velocity-inlet: $U_\infty = 40 \text{ m/s}$ ; $I = 0.1\%$ ; $\mu_t/\mu = 10$
Outlet	pressure-outlet
Top	symmetry
Ground	wall: no-slip, ground movement of $U_{GS} = 40 \text{ m/s}$
Slot - wall	wall: no slip
Slot - inner section	velocity-inlet: $U_j = 10 \text{ m/s}, 20 \text{ m/s}$ ; $I = 1\%$ ; $\mu_t/\mu = 10$ velocity-outlet: $U_j = 10 \text{ m/s}, 20 \text{ m/s}$ ; $I = 1\%$ ; $\mu_t/\mu = 10$

### 6.3 ANALYSIS OF RESULTS

Even before analysing the results, an important fact is that the momentum transfer (via blowing or suction methods) may lead the code to miscalculate (under or overpredicting) the drag. If only the profile drag ( $C_{D_{profile}}$ ) is concerned, it may occur because the code would compute the global drag ( $C_{D_{global}}$ ), where the jet momentum on the flow is taken into account. Thus, based on the Navier-Stokes equations, the real profile drag coefficient is obtained by removing the injection (or suction) jet momentum from the global drag coefficient achieved, as seen in Eq (6.4). The drag coefficient correction ( $C_{D_{jet}}$ ) is normalized as the drag coefficient profile.

$$C_{D_{profile}} = C_{D_{global}} - C_{D_{jet}} = \frac{F_D}{\frac{1}{2} \rho_{\infty} A_{ref_{car}} U_{\infty}^2} + \left( \frac{\vec{U}_{\infty} \bullet \vec{U}_{jet}}{U_{\infty} U_{jet}} \right) \left( \frac{\rho_{jet} A_{ref_{slot}} U_{jet}^2}{\frac{1}{2} \rho_{\infty} A_{ref_{car}} U_{\infty}^2} \right) \quad (6.4)$$

The scalar product operation takes into account the influence of the jet direction on profile drag coefficient. In these cases, blowing jets should result in profile drag coefficient values higher than global drag coefficient, while suction jets leads to the opposite effect. Since the correction between global drag and profile drag coefficient has been done, Figure 6.2 and Figure 6.3 show the global drag (achieved as an output from the solver) and the corrected profile drag (including the additional jet momentum).

From a quantitative point of view, the suction jet on rear of the DrivAer car profile does not seem to be a way to yield drag reduction. Suction on car rear with jet speeds of 10 m/s and 20 m/s does not affect the car profile drag. Thus, the changes in global drag (Figure 6.2 and Figure 6.3), in comparison to baseline (Figure 6.4), are only due to the portion of jet momentum. Moreover, it is noticed that the wake region is still similar to turbulent wake of the baseline configuration, as observed in all six suction jet cases (Figure 6.7 and Figure 6.8).

Regarding the injection method, the global drag coefficients from the three cases of jet at higher speed (20 m/s) would lead to conclude that such case is useful for the global drag reduction. However, when the drag prediction is corrected (taking into account the jet momentum), these cases actually display profile drag higher than the baseline model. In summary, injections at higher speeds (20 m/s) would be inappropriate for the purpose of profile drag reduction in the model adopted. All the six cases of blowing jet are presented in Figure 6.5 and Figure 6.6.

In spite of the blowing jet at higher speed, the same jet at lower speed (10 m/s) provides a valuable conclusion. The results from injection of momentum at lower speed suggest a reasonable application as drag reduction system of profiles. In all positions of such condition, the results indicate reduction compared to baseline car profile. In addition, the profile drag decreases, as the jet position is higher.

Finally, the best situation achieved a real reduction in the drag coefficient by 5 counts for the profile drag, and 7 counts for the global drag (by assuming some inner generation of the jet, *e. g.*, exhaust gases from the engine).



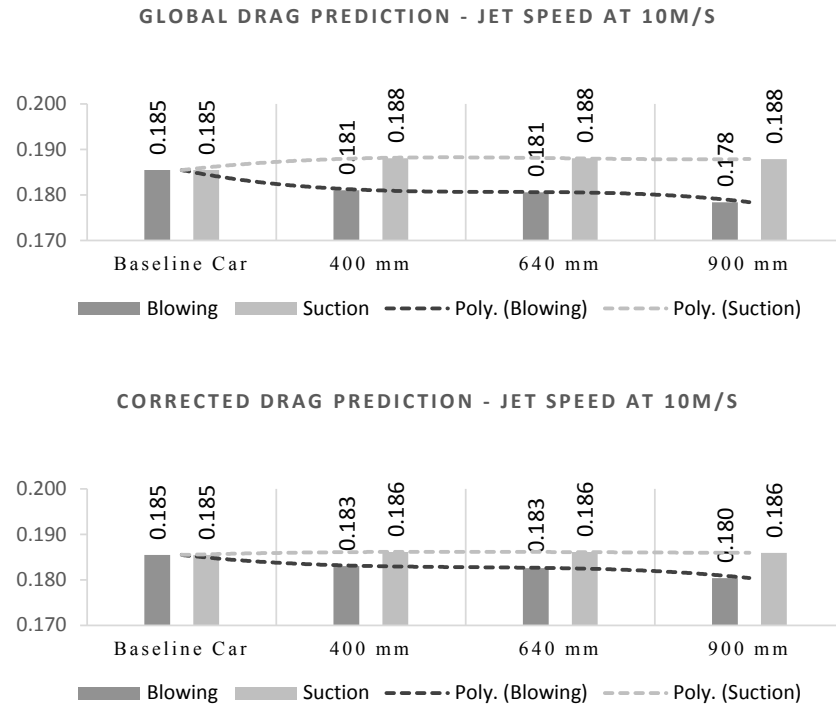


Figure 6.2: Jet speed at 10 m/s: Global (above) and corrected (below) drag coefficient.

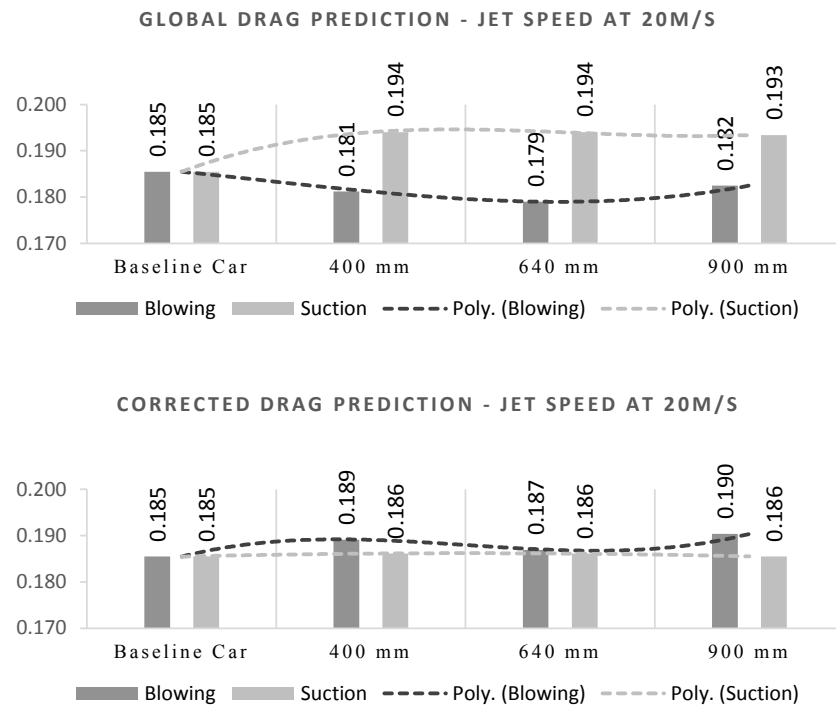


Figure 6.3: Jet speed at 20 m/s: Global (above) and corrected (below) drag coefficient.

The following figures show a comparison of wake region of DrivAer Fastback profile velocity contours, in the range of 0 (blue / cold color) to 5 m/s (red / hot color). Afterwards the baseline case in Figure 6.4, the Figure 6.5 to Figure 6.8 shown the cases with height of slot jet equal to 400 mm (below), 640 mm (middle), and 900 mm (above), from the ground level.

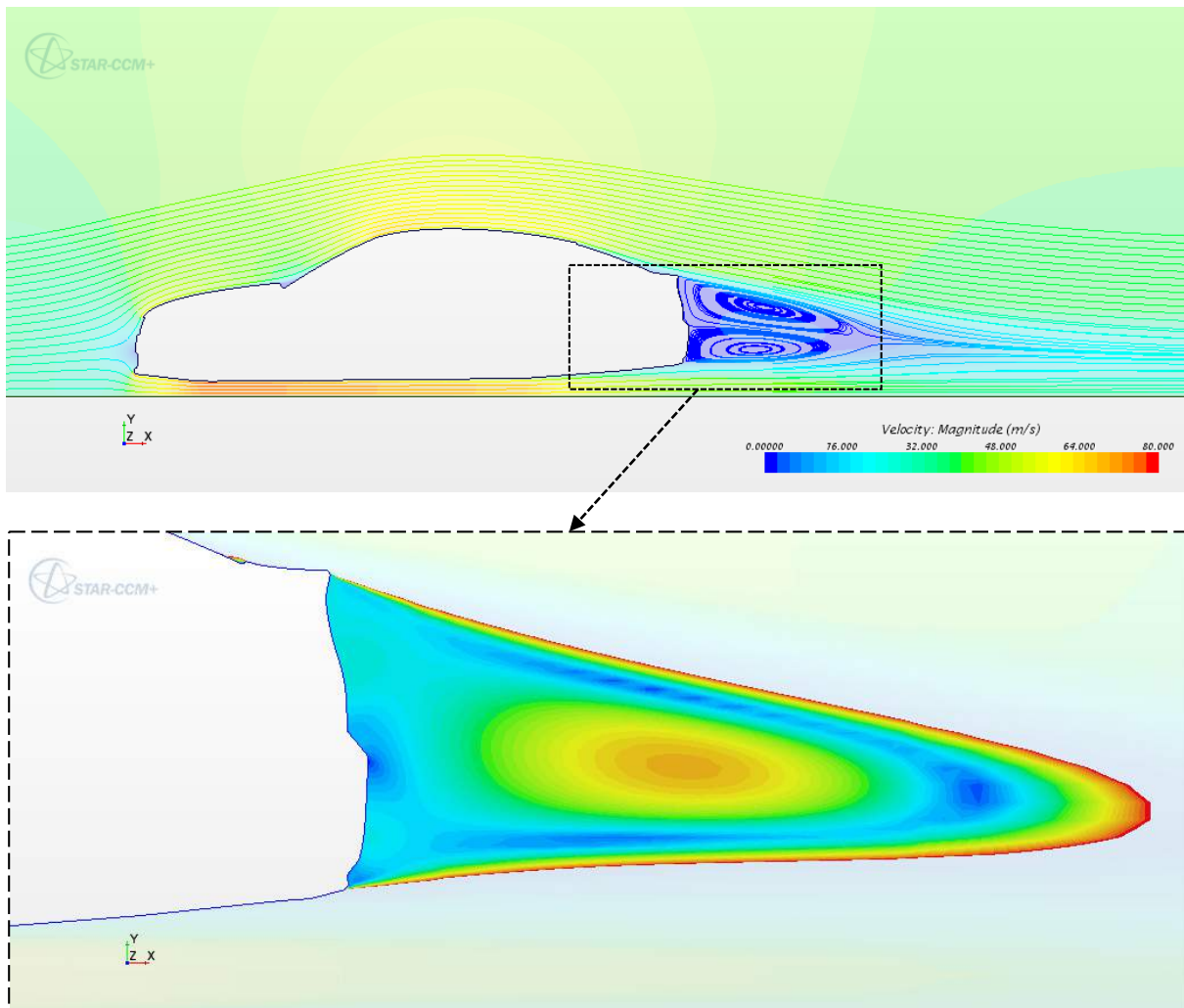


Figure 6.4: Streamlines over the DrivAer Fastback baseline profile at 40 m/s (above), and wake region behind its rear (below).

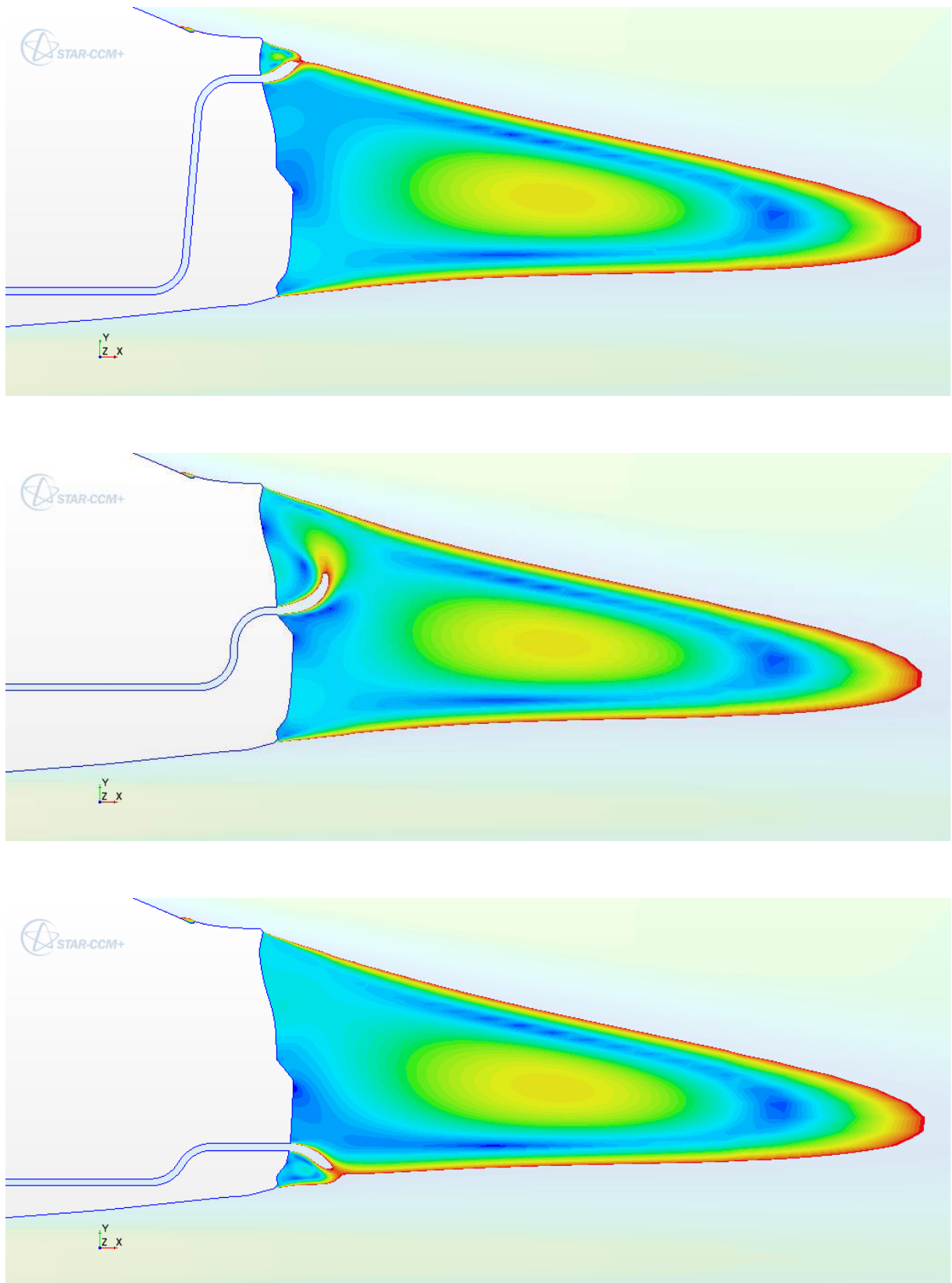


Figure 6.5: Velocity magnitude: blowing jet at 10  $m/s$ .

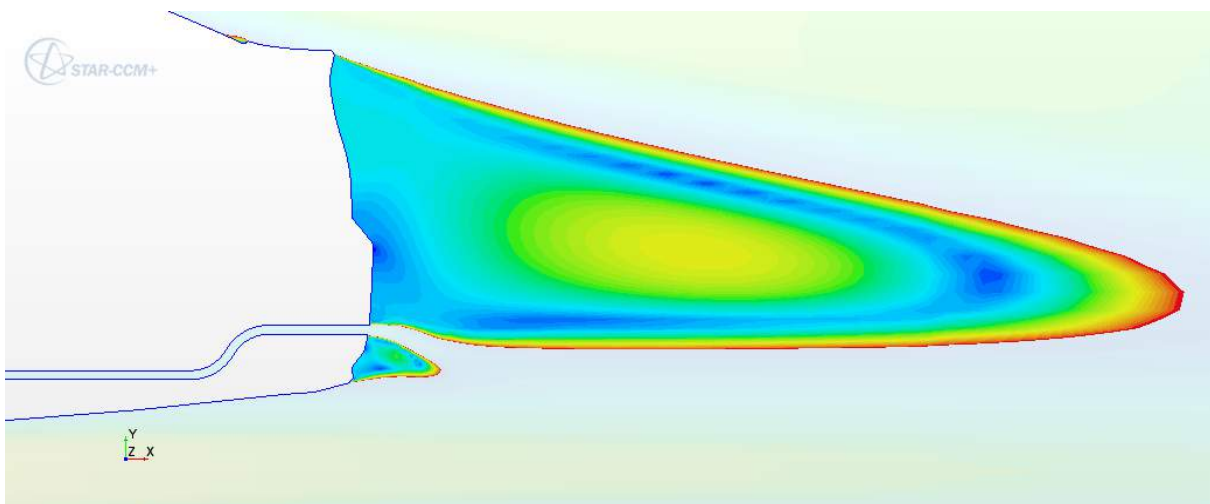
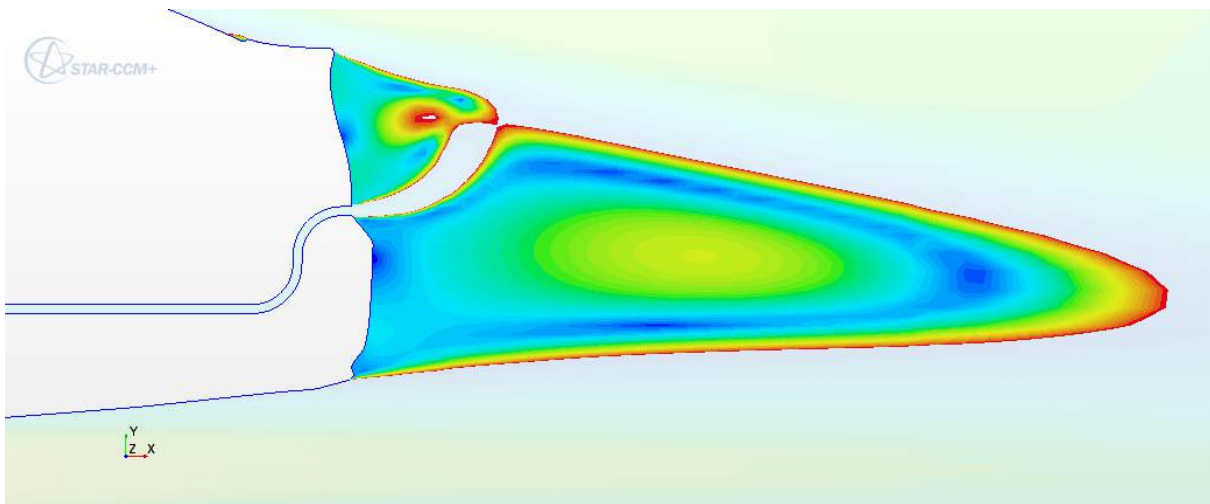
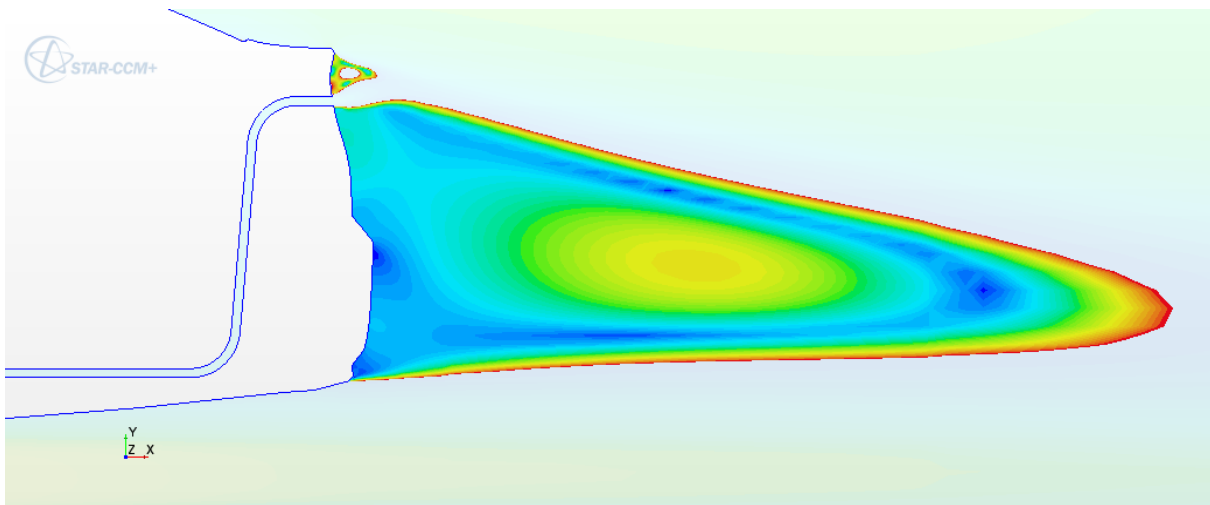


Figure 6.6: Velocity magnitude: blowing jet at 20 m/s.

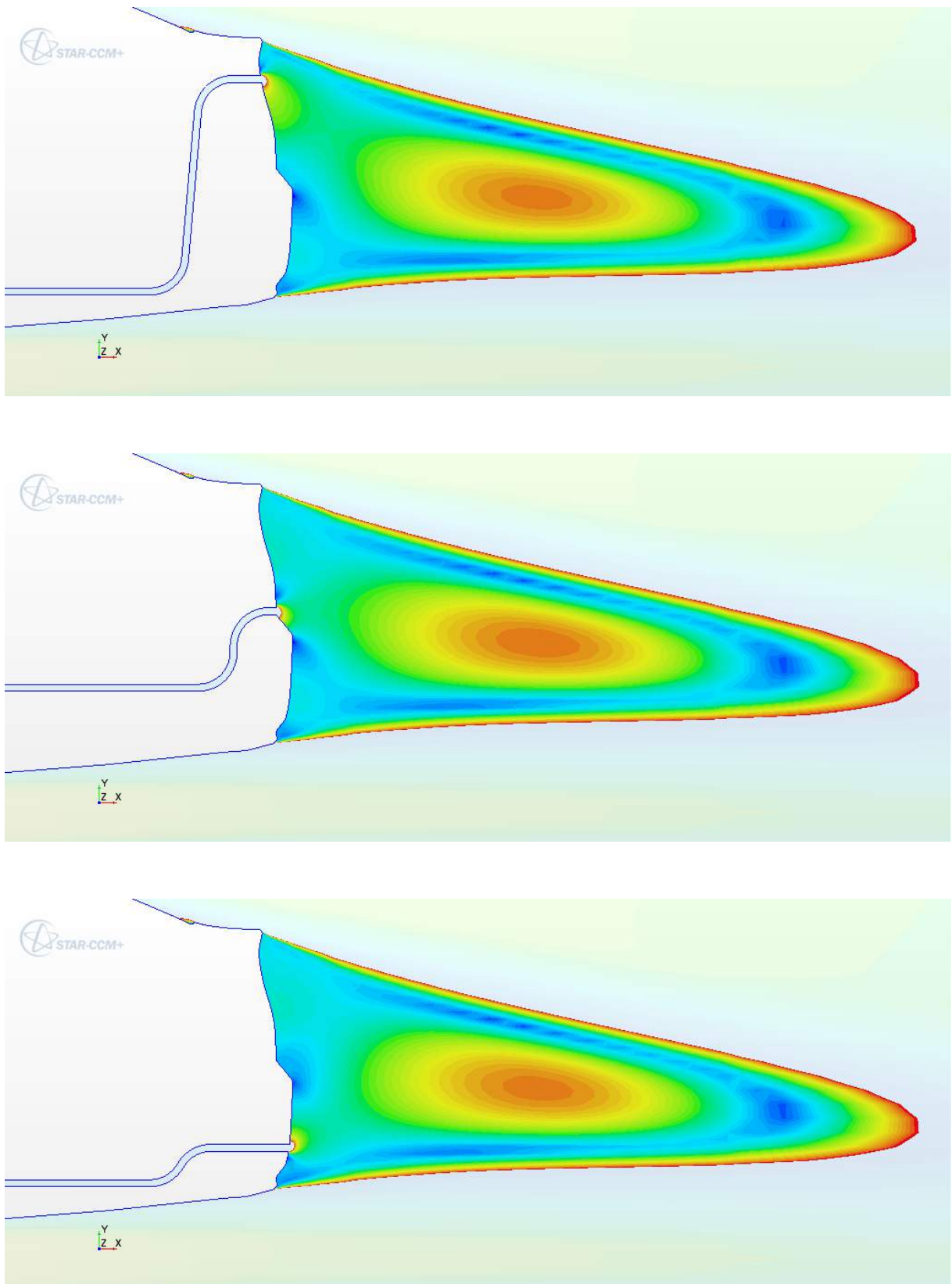


Figure 6.7: Velocity magnitude: suction jet at 10 m/s.

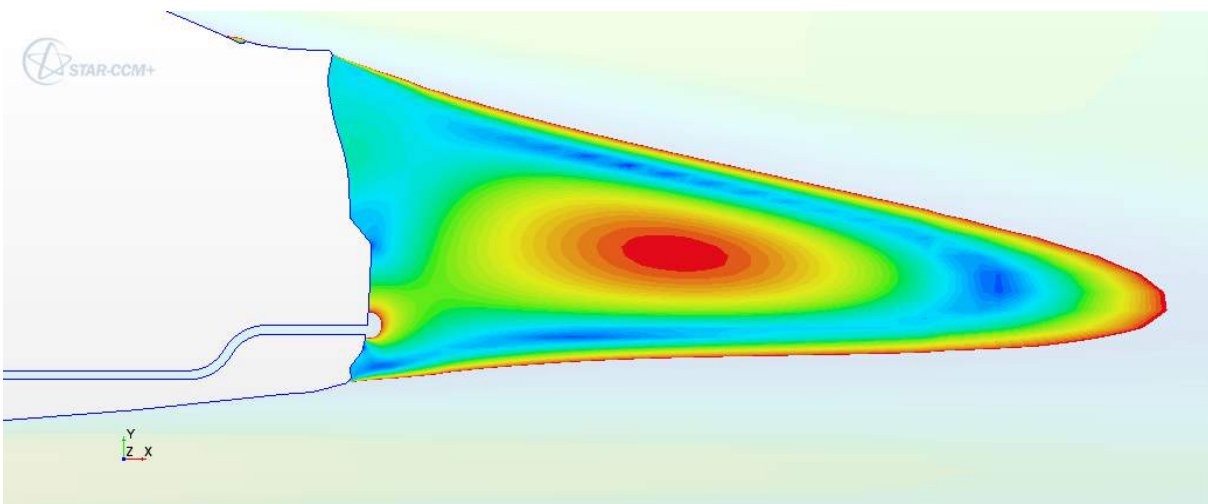
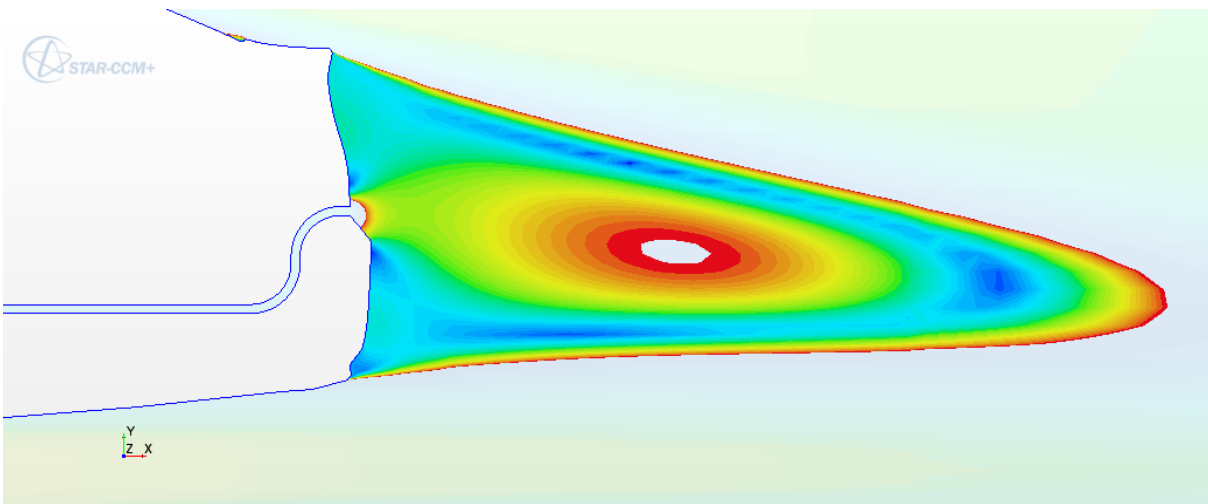
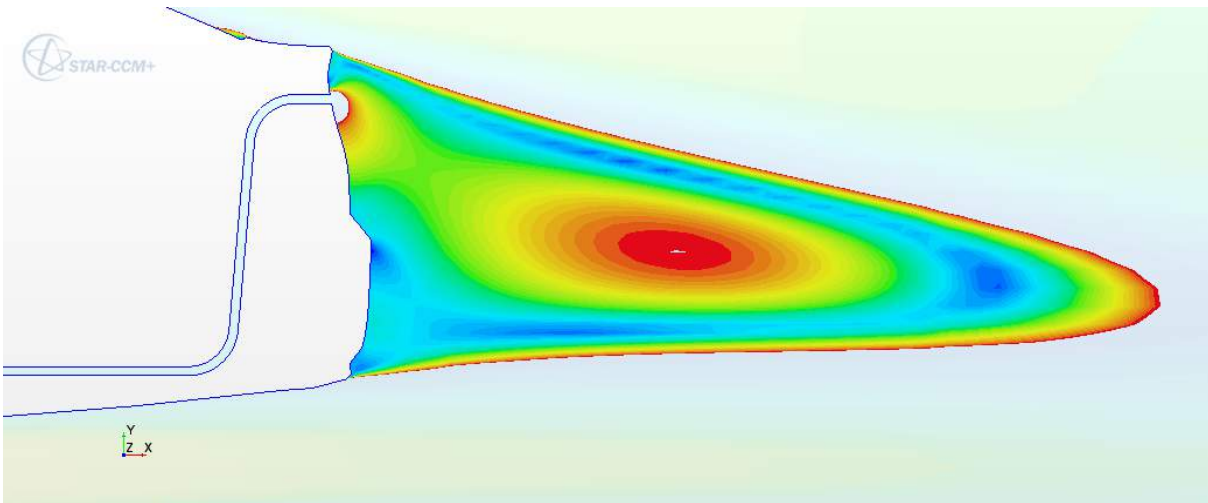


Figure 6.8: Velocity magnitude: suction jet at 20  $m/s$ .

## 6.4 PROPOSAL OF A ROAD CAR AERODYNAMIC CONCEPT

The previous section indicated that injecting momentum at the wake region can reduce the drag of a vehicle. Nonetheless, such injection and/or suction at rear car does not necessarily have to be by a forced or active system. This research proposes that the rear jet would occur as passive system by collecting air from:

(a) car areas of higher pressure than rear car surface; or

(b) regions of higher momentum in the x-axis direction, in order to overcome the adverse pressure throughout the collection channel.

In a view of applicability, the air intake and its position would be an agreement between performance and design targets, *e.g.* package, thermal, NVH, etc. To illustrate this point, the installation of jet slots on trunk lid is probably unlikely. Therefore, the optimum case of blowing jet at higher position from the ground would be a challenge in reason of the trunk lid.

In order to fit this concept properly in a generic car frame of fastback models, is recommended to place the slots between trunk lid and rear bumper. In addition, the Coanda effect can be used wisely to direct air jet upwards.

A representative sketch of this concept is shown in Figure 6.9, where generic air intakes gather a portion of main flow, *e.g.*, in the underbody or side car. Afterwards, it would be discharged on the rear car, between trunk lid and rear bumper.



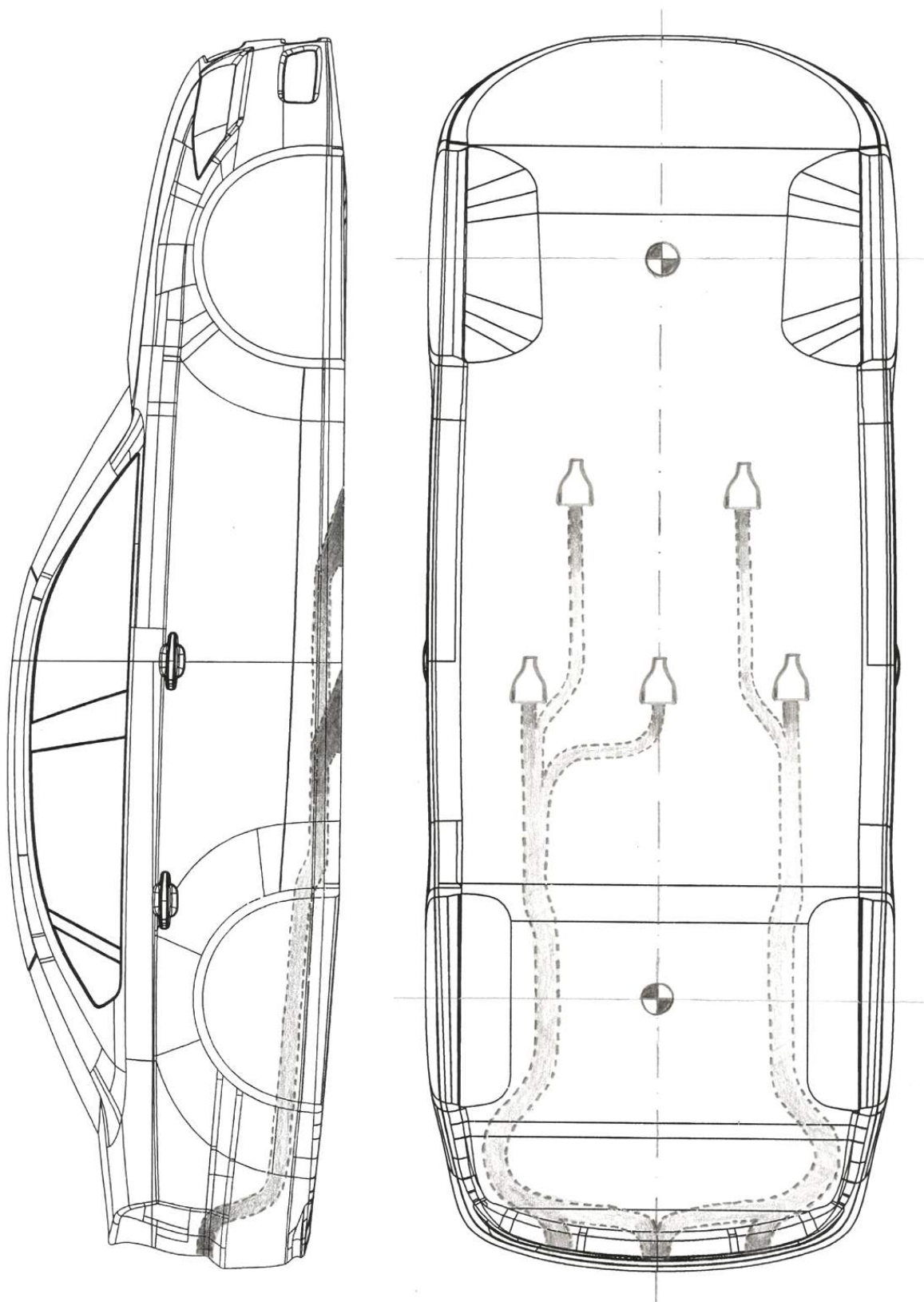


Figure 6.9: Representative sketch of the passive aerodynamic system concept over the DrivAer fastback model.



## 6.5 SUMMARY OF CHAPTER VI

A proposal of aerodynamic concept for automotive drag reduction has been presented in this study, supported by numerical investigation. The objective is to identify the potential of blowing and suction methods of momentum over the wake region of a fastback car model. In summary, three different heights of rear jet, two jet speeds, and two methods has been tested.

The suction jet method on rear of the DrivAer car profile does not seem to be a way to yield drag reduction, either at higher or lower jet speed. Thus, the changes in global drag are only due to the portion of the jet momentum.

The blowing jet at higher speed point to the smaller global drag than baseline profile. Although this positive first conclusion, the correction of drag due to jet momentum indicated that all three cases actually display profile drag higher than the baseline model. In other words, the blowing jet at higher speed is inapposite for the purpose of profile drag reduction, when compared to the baseline DrivAer Fastback profile.

On the other hand, the results from injection of momentum at lower speed suggest a reasonable application as drag reduction system. All positions of this case indicates reduction compared to baseline car profile. Also, profile drag decreases as the jet position is higher.

In the end, an aerodynamic concept is proposed. The blowing jet would occur as passive system by collecting air (a) from car areas of higher pressure than rear car surface, or (b) regions of higher momentum to overcome the adverse pressure throughout collection channel.

Therefore, the main contributions of this chapter are: (a) to highlight that the best drag reduction has been evidenced via lower speed blowing jet at highest rear car position, as well as (b) to offer an aerodynamic concept to improve drag reduction of road cars to automotive engineering.



## **CHAPTER VII**

### **THE BRAZILIAN AUTOMOTIVE SCENARIO OVER THE HATCH 2015 CAR MODELS**

This chapter deals with the profile comparison of ten Hatch 2015 cars models produced in Brazil, in regards to aerodynamic forces and geometry features: roof end angle, rear-end spoiler, and slant angle. The best-seller 2015 model of each one of the ten best-seller 2014 manufactures in Brazil are analysed.

The main contribution of this study is a qualitative comparison of the best-seller car profiles produced and commercialised in Brazil, in two-dimensional domain, in a view of geometry features and aerodynamic forces.

#### **7.1 BACKGROUND**

Since the Brazilian government established the Inovar-Auto program in 2012, the automotive industry has pursued tax savings by signing up for the program. This new policy (from 2013 to 2017) has three main objectives: fortification of the industry and domestic market; increase incentives of investment and innovation; and enhance energy efficiency of vehicles produced in Brazil. For instance, manufacturers can gain up to 2% extra in IPI tax credits (aside 30% from Inovar-Auto achievements) by producing even more fuel-efficient models from 2017.

The nomenclature Inovar-Auto means “Program of Incentive to Technological Innovation and Densification of the Productive Chain in the Automotive Industry”. Inovar-Auto defines itself as a Brazilian government's automotive program, which aims to create conditions for increasing competitiveness in the automotive sector. It encourages the production of more economical and safe vehicles, as well as investment in the supply chain, engineering, basic industrial technology, research and development, and training providers.

Created by Law nº 12715/2012, this programme is limited to vehicles manufactured between 2013 and 2017, which IPI (Tax on Industrialized Products) rates may return to pre-2013 percentage unless further modification to the decree are made. Therefore, such Tax Program are directed at new investments, raising the technological standards of vehicles and components, as well as the security and vehicle energy efficiency. To enable the program, companies must commit to specific targets.

From the view of manufactures, aside from facing severe reduction in sales from 2013 to present, the automotive industry has to focus on this second challenge: the Inovar-Auto programme. Even though it has been in force since 2013, not all automakers are in path to reach the program requirements. "Energy efficiency is the great nightmare of automotive industry during next 12 to 16 months along," says Valter Pieracciani (2015). He refers to the period that automakers have to implement adjustments before submitting results to the government, which must take place up to November 2016. Furthermore, estimation made by Automotive Business shows that manufactures can spend around R\$ 8000 (roughly US\$ 2600, by the current exchange rate) per car sold in taxes if requirements of fuel consumption and emissions are not achieved in 2017.

In this scenario, aerodynamic development also must embrace commercial vehicles in more intensive mode by automotive manufactures in Brazil. Since it is costly to build and maintain experimental tools for aerodynamics development, the industry is trying to reduce wind tunnel time by investing in CFD and advanced processing capability of the virtual development. For this reason, computational tools arise as the best cost-effective solution.

In compliance with this engineering tool, this study presents a comparison of the Hatch 2015 car profiles produced in Brazil, in the view of geometry features and aerodynamics.

## 7.2 HATCH 2015 CAR MODELS

The best-seller 2015 model of each one of the ten best-seller manufactures in Brazil through 2014 are analysed. According to Fenabrave, these ten Hatch 2015 models are: (1<sup>o</sup>) Fiat Novo Palio; (2<sup>o</sup>) Volkswagen Gol; (3<sup>o</sup>) Chevrolet Onix; (4<sup>o</sup>) Hyundai HB20; (5<sup>o</sup>) Ford New Fiesta; (6<sup>o</sup>) Renault Sandero; (7<sup>o</sup>) Toyota Etios; (8<sup>o</sup>) Citroen C3; (9<sup>o</sup>) Nissan March; and (10<sup>o</sup>) Peugeot 208. The Figure 7.1 illustrates the ten hatch 2015 models, in best-selling car ranking.

The vehicle profile of the hatch models are extracted via PlotDigitizer software, which allow extracting points from public figures of these vehicles. The overlapped car profiles are displayed in the Chapter III, in Figure 3.6, and are presented individually in Appendix (from Figure 12.20 to Figure 12.23). All profiles are full-scale, and the reference of each plot is the respective front axle.



Figure 7.1: The best-seller 2015 model of each one of the ten best-seller manufactures.

### 7.3 GEOMETRY FEATURES

This subtopic provides a brief analysis about geometry features, such as roof end angle, rear-end spoiler and rear slant angle of these ten Hatch 2015 car models.

#### 7.3.1 Roof End Angle

A relevant project parameter in hatch car design is the roof end angle. To illustrate this point, the well-known industrial case of drag reduction had been achieved by lowering the roof end of the Fiat Uno full-scale production car (Marioli, 1983). The ideal angle of 10 degrees was chosen as the optimum roof inclination, as shown in Figure 7.2.

As the best-sellers Hatch 2015 Brazilian car models are concerned, all models have such angle in the range of 6 to 15 degrees. It indicates that all manufactures have been applying such concept in an optimum manner over their projects.

The exception from the style of smooth curved roof is the large geometry of rear-end spoiler designed on Nissan March, as described in the next subtopic.

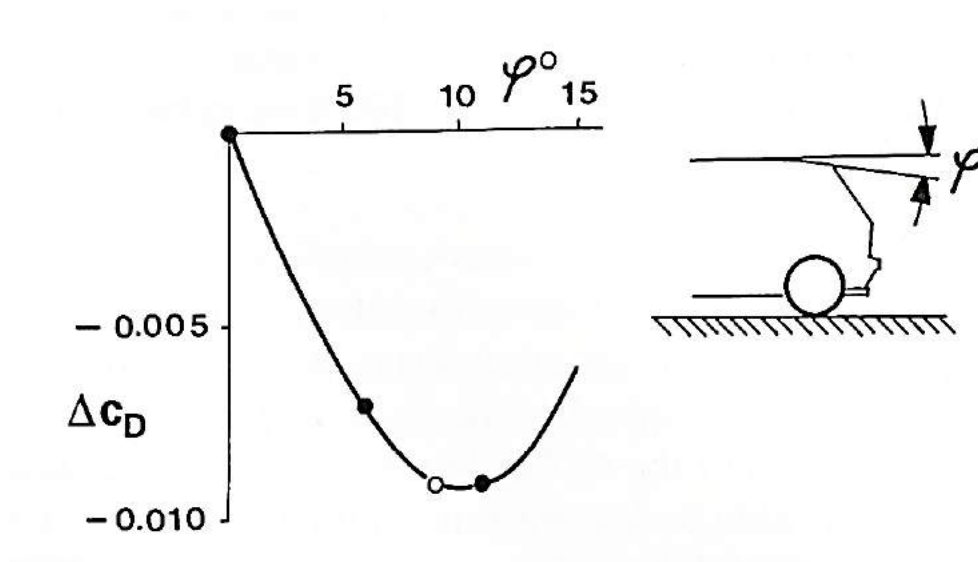


Figure 7.2: Influence of roof end angle in the drag of a full-scale car production.

### 7.3.2 Rear-end Roof Spoiler

Indeed, aerodynamics can influence substantially the design of vehicles, however other areas have also primary importance on design, as safety, performance, fuel economy, package, and aesthetics.

Whichever topics have been taken into account by the manufactures, all hatch car models present in this study hold a roof spoiler style in their design, following the design trend from recent years. Nevertheless, the spoilers of those can be divided into three categories: (i) small, sharing the roof curve; (ii) small, with slight change of trailing angle; and (iii) extended roof spoiler with a protuberance. The Figure 7.3 illustrates examples of these three spoiler designs.

Small roof spoilers, which preserve the roof curve, were designed for both Chevrolet Onix and Peugeot 208. This features promote the flow detachment above rear window, which takes place at the roof end edge and follows the roof curvature backwards.

Also small rear-end spoiler, but with slight change in trailing angle, was applied on Renault Sandero, Fiat Novo Palio, Hyundai HB20, and Citroen C3. These ones may deflate



Figure 7.3: Comparison of rear-end spoilers among Chevrolet Onix (small, sharing the roof curve), Citroen C3 (small, with slight change of trailing angle) and Nissan March (extended roof spoiler with a protuberance).

the flow by few degrees and recover a bit of local static pressure on the rear car, and consequently, reducing the lift effect on the rear axle.

A medium-size geometry was developed on Ford New Fiesta, Toyota Etios and Volkswagen Gol, where the highest trailing angle of roof spoiler is found on the solution of that German manufacturer.

As previous mentioned, the slight deviation of Nissan March roof spoiler provides a very smooth concaveness at the very beginning of the extended roof spoiler, just before the rear axle. In the view of lift effect, that position is a very clever option in order to increase local pressure and reduce lift effect on rear wheels, whereas it may increase the global drag over the vehicle as a side effect.

### **7.3.3 Rear Slant Angle**

In previous research, Janssen *et al.* (1975) describes the effect of slant angle on the drag coefficient. Although this feature is not explicit over the current trend of round-base car models, the definition of slant angle is the inclination between the roof plane and adjacent rear surface; *e. g.*, rear window. The age of square-based models has been reaching its end, however the influence of this geometry has remarkable importance in both technical and categorical issues.

From a technical perspective, Janssen *et al.* showed the influence of slant angle on drag coefficient. As slant angle increases from zero degree, drag coefficient decreases. Such characteristic reaches the optimum drag reduction at 10 degrees (roughly -15% from baseline). Subsequently, the non-dimensional force increases in a square proportion with slant angle until approximately 28 degrees (approximately +10% from baseline), where the flow still is attached on the rear surface. Slant angles from 28 to 32 degrees provide unstable flows over the rear car. Any inclination further this limit results in a fully flow separation. In contrast to the first insight of massive addition on drag coefficient via such flow separation, Janssen's research indicates that drag coefficient become surprisingly stable and in a lower level than the last limit of attached flow regime. The drag coefficient magnitude of fully separated flow is as the roof were flat (slant angle equal to zero degree).

These flow phenomena had been used as a parameter to separate car models into two categories: fastback models (attached flow, with slant angle lower than 30 degrees), and squareback/hatchback models (separated flow, slant angle higher than 30 degree). Each



category consist in particular flow pattern that may affect even small issues; *i. e.* performance or even the need of rear wiper is affect by flow characteristics related to rear slant angle.

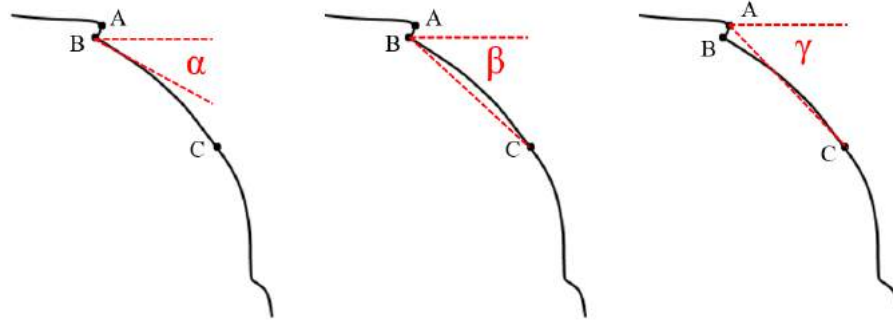


Figure 7.4: Definition of the three slant angles proposed:  $\alpha$ ,  $\beta$ , and  $\gamma$ .

This study proposes the measurement of modern slant angle in three modes, as illustrated in Figure 7.4. The three slant angles would be measured from x-axis up to three different segments: ( $\alpha$ ) tangent line at upper rear window border, ( $\beta$ ) line from upper to lower rear window border - BC, ( $\gamma$ ) line from rear-end spoiler to lower rear window border – AC.

These new parameters can assist the development and decision concerning design of modern models, since the design of contemporary car models are rounded-base rear window shapes with additional features, *e. g.*, rear-end spoiler. The proposed angles are measured on those ten cars profiles and presented in Table 7.1.

Table 7.1: Slant angles ( $\alpha$ ,  $\beta$ , and  $\gamma$ ) of Brazilian Hatch 2015 models.

Hatch model	Slant angle $\alpha$	Slant angle $\beta$	Slant angle $\gamma$
Novo Palio	45°	51°	54°
Volkswagen Gol	40°	42°	53°
Chevrolet Onix	34°	40°	46°
Hyundai HB20	32°	38°	45°
Ford New Fiesta	39°	44°	55°
Renault Sandero	40°	44°	50°
Toyota Etios	51°	52°	62°
Citroen C3	31°	42°	45°
Nissan March	45°	50°	66°
Peugeot 208	35°	41°	44°

## 7.4 ANALYSIS OF AERODYNAMIC FORCES

In this topic, the aerodynamic forces are analysed via Computational Fluid Dynamics over those ten bestselling Hatch 2015 models in Brazil.

This analysis consists in unsteady-state simulations adopting the Reynolds-Averaged Navier Stokes approach with temporal term (URANS). As previously indicated, Realizable  $k$ - $\varepsilon$  two-layer turbulence model is chosen. Aligned with the Chapter IV (4.1 Two-Dimensional Qualitative Analysis), the freestream of  $U_\infty = 40 \text{ m/s}$  is chosen to characterize a realistic motion of a vehicle in highway driving, where air density ( $\rho$ ) is equal to  $1.18415 \text{ kg/m}^3$  and its dynamic viscosity ( $\mu$ ) is  $1.85508 \times 10^{-5} \text{ Ns/m}^2$ .

The time step of  $1 \times 10^{-4} \text{ s}$  was employed for good performance of transient flow solution. Residual convergence criteria of  $1 \times 10^{-4}$  is set to mass conservation, momentum and properties of turbulence model. Briefly speaking, the physical setup is shown in Table 7.2, while the boundary conditions Table 7.3. The meshes are presented in Appendix.

Table 7.2: Physical setup.

Feature	Properties
Domain	Two-dimensional
Time regime	Unsteady-state ( $\Delta t = 1 \times 10^{-4} \text{ s}$ )
Fluid properties	Air ( $\rho = 1.18415 \text{ kg/m}^3$ ; $\mu = 1.85508 \times 10^{-5} \text{ Ns/m}^2$ )
Flow Solver	Segregated
Equation of State	Constant density
Flow regime	Turbulent
Turbulence model	Realizable $k$ - $\varepsilon$ two-layer

Table 7.3: Boundary conditions.

Boundary	Condition
Hatch car profile	wall: no slip
Inlet	velocity-inlet: $U_\infty = 40 \text{ m/s}$ ; $I = 0.1\%$ ; $l_t = 0.1 \text{ m}$
Outlet	pressure-outlet
Top	symmetry
Ground	wall: no-slip, ground movement of $U_{GS} = 40 \text{ m/s}$

If the realistic 3D geometries of the car models were available, a detailed study could be performed. Since this research had no access to these car geometries, this study is concerned with the qualitative analysis of aerodynamic forces in two-dimensional domain. Thus, mid-plane car profiles are taken into account.

This approach would be valid under hypotheses like irrelevant three-dimensional turbulence effects and constant car profile along itself, as shown in Figure 7.5. Unquestionably, neither hypotheses are true in real circumstances. Nevertheless, such approach allows the comparative studies in a reasonable equivalence over similar issues, *e. g.*, drag force.

The force unit of following results is  $N/m$ , where it is consequence of two-dimensional domain. In the analysis of three-dimensional domain, the mathematical approach of aerodynamic forces may be calculated in  $N$  units. As one dimension is removed in order to become a two-dimensional domain, the relation between result from two- and three-dimension is the length unit ( $m$ ). Hence, the force results of car profiles would be equivalent to the force over full-car models, divided by the car width. Conversely, the car profile drag multiplied by its width would be similar to a full-car drag.

In summary, the aim is not to understand independent quantitative result from a specific car model, but to identify a trend in aerodynamic forces over manufactures' model.

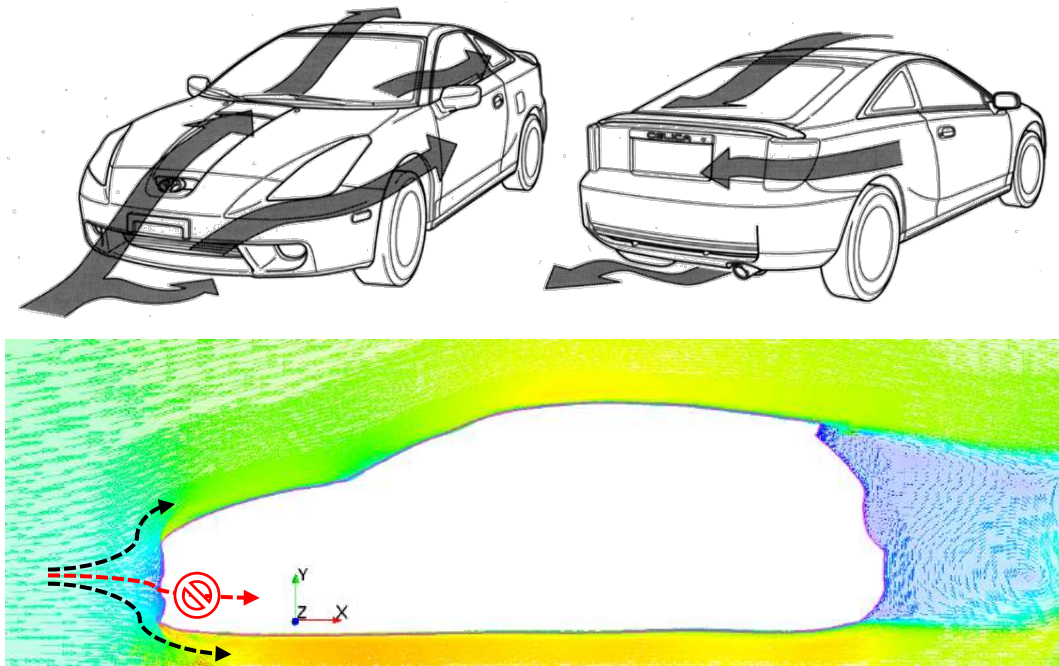


Figure 7.5: Flow direction: realistic 3D car body (above) and simplified 2D car profile (below).

### 7.4.1 Drag

Indeed, as previous stated by Hucho (1998), the pressure drag is the intense main share of the drag on Hatch cars. The viscous drag is inexpressive against the pressure drag due to emblematic shape of bluff bodies from those commercialized road vehicles in Brazil. Likewise, the lift-induced drag has a relative small effect on global drag force.

The time-averaged drag force of each Hatch model is shown in Figure 7.6. The result indicates that all models may be split into four group levels. Peugeot 208 provides the lowest drag among all Hatch models, followed by the second group of Ford New Fiesta and Volkswagen Gol. The third group has Chevrolet Onix, Hyundai HB 20 and Nissan March. The four group includes Citroen C3, Fiat Novo Palio, Toyota Etios and Renault Sandero, standing the car profile group with the highest drag.

The drag force is related to the shape and size of a vehicle. Taller cars usually have higher drag. In a view of drag coefficient, the effect of frontal area size (profile height, in two-dimensional approach) must be removed from drag results. Figure 7.7 displayed drag coefficient (and drag coefficient ratio) of all Hatch models, from the lowest to the highest value, where the height of car has no effect on such non-dimensional force.

In both comparison (drag and drag coefficient), almost all Hatch models stand the same raking of drag force, except by Citroen C3 and Renault Sandero. The reason is that both models have the highest profiles among those ten models. Hence, Citroen C3 become the

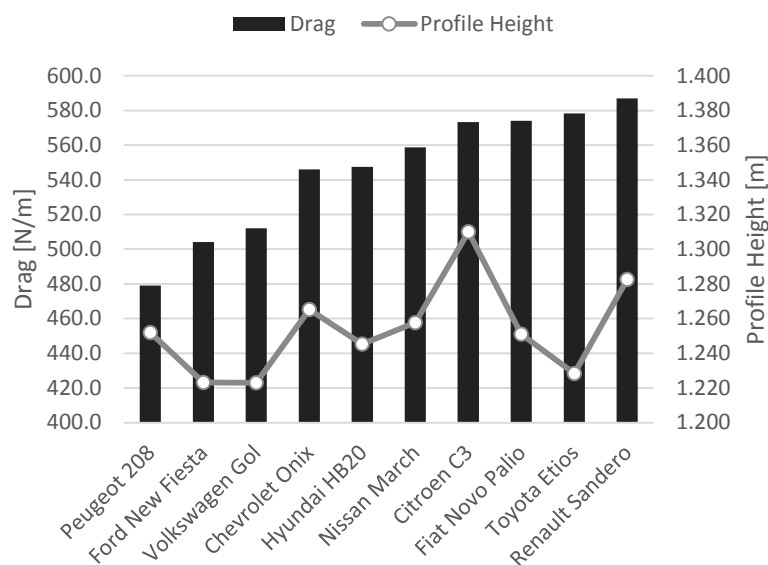


Figure 7.6: Comparison Drag force and profile height over the ten Hatch car models.

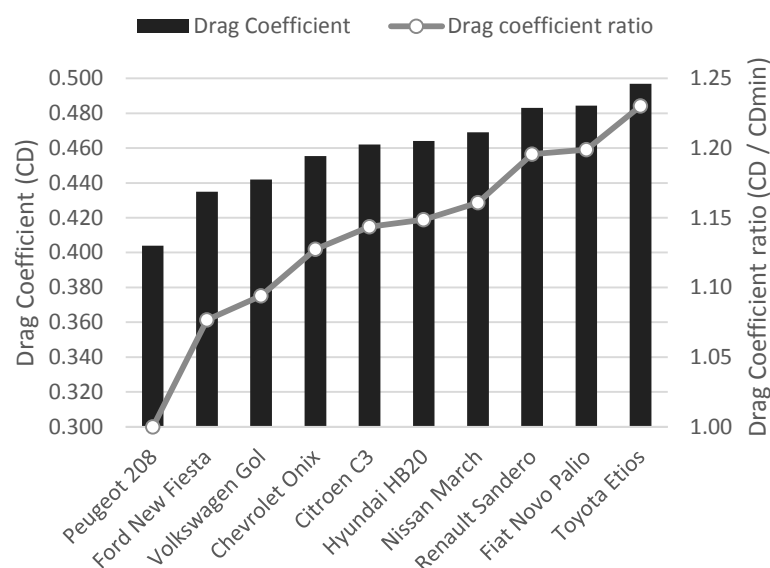


Figure 7.7: Drag coefficient and drag coefficient ratio over the ten Hatch car models.

sixth lower car profile in the non-dimensional drag ranking, and Renault Sandero left the last position on drag raking to stand in the eighth position on drag coefficient ranking.

#### 7.4.2 Lift

First, it is important to keep in mind that one target in car design is to reduce the lift force, mainly at rear axle of front-wheel drive vehicles (Hucho, 1998).

The definition of such force comes from aeronautics. Lift force is the perpendicular force component from flow direction, in order to maintain an aerodynamic body on flight. In automotive applications, it reduces the frictional forces between the tires and the road, thus changing dramatically the handling and stability characteristics of any typical road vehicle. The lift force is dependent on the overall shape of the vehicle. In crosswind angle at zero degree (with no crosswind), lift coefficient ( $C_L$ ) usually is from 0.3 up to 0.5 for modern passenger cars (Hucho, 1998). Nevertheless, the coefficient may increase dramatically and reaches value of 1 or more under crosswinds conditions. Especially on high performance motorsport, lift coefficient from 2 up to 3 is quite common via aerodynamic downforce devices.

In a three-dimensional real car, the flow sweeps the front car in all direction upwards, and a share of this flow sweeps the front bumper downwards. However, since the section between the ground and vehicle is quite small, this is a considerable flow restriction. The outer portion of frontal flow is forced enough to follow even further the front wheels.

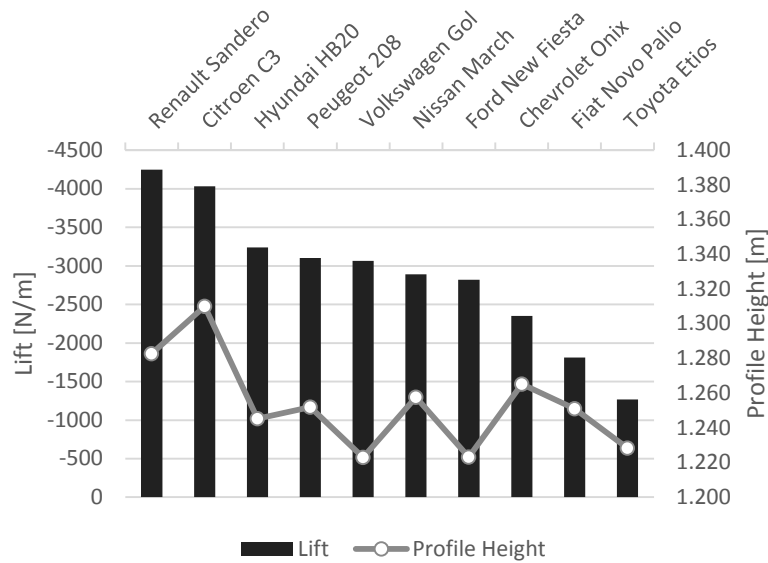


Figure 7.8: Lift force and profile height over Hatch car models.

Additionally, the accelerated flow over underbody region decreases the static pressure. As consequence, an adjacent flow next to lateral car surface goes towards that region, recovering a percentage of static pressure.

On the other side, the two-dimensional approach only allows the flow to sweep the front car either upwards or downwards. Particularly the downwards portion, it only deal with itself until the rear car. It means that the flow maintains such higher speed all through the underbody, with consequently pressure drop over the same region. Therefore, the ground effect in two-dimensional domain is intensified substantially, overpredicting the phenomenon from a real case. Therefore, the lift force prediction is overestimated in 2D analysis.

Regards to simulation results of lift force, unfortunately, the previous insight of overprediction has been confirmed due to two-dimensional approach. On grounds of such evidence, a comparison of lift force over the car models may lead to an erroneous analysis. Taking everything into consideration, the result of lift is presented in Figure 7.8.

Another point is that differences in car length also leads to differences in lift force, since the underbody area is proportional to lift force under such pressure drop. To illustrate this point, longer underbodies (Renault Sandero, Hyundai HB20, and Peugeot 208) have provided the most intense ground effect among the models, especially comparing to shorter underbodies (Toyota Etios, Fiat Novo Palio, and Nissan March).

### 7.4.3 Comparison of Drag and Fuel Consumption

As consequence of Inovar-Auto program, the National Institute of Metrology, Quality and Technology (INMETRO) has been testing car performance and fuel efficiency in Brazil (INMETRO, 2015).

Naturally, fuel consumption is a result of several factors, *e. g.*, rolling resistance of tires, powertrain efficiency, aerodynamic drag, *etc.* Figure 7.9 displays a comparison of such aerodynamic factor (drag coefficient) against the fuel consumptions (both ethanol and gasoline) of all those ten Hatch car models.

Even disregarding other fuel consumption factors and the inaccuracy from the two-dimensional approach, indeed it is evident via trendlines that there is a proportional relation between the drag and the energy consumption of road cars.

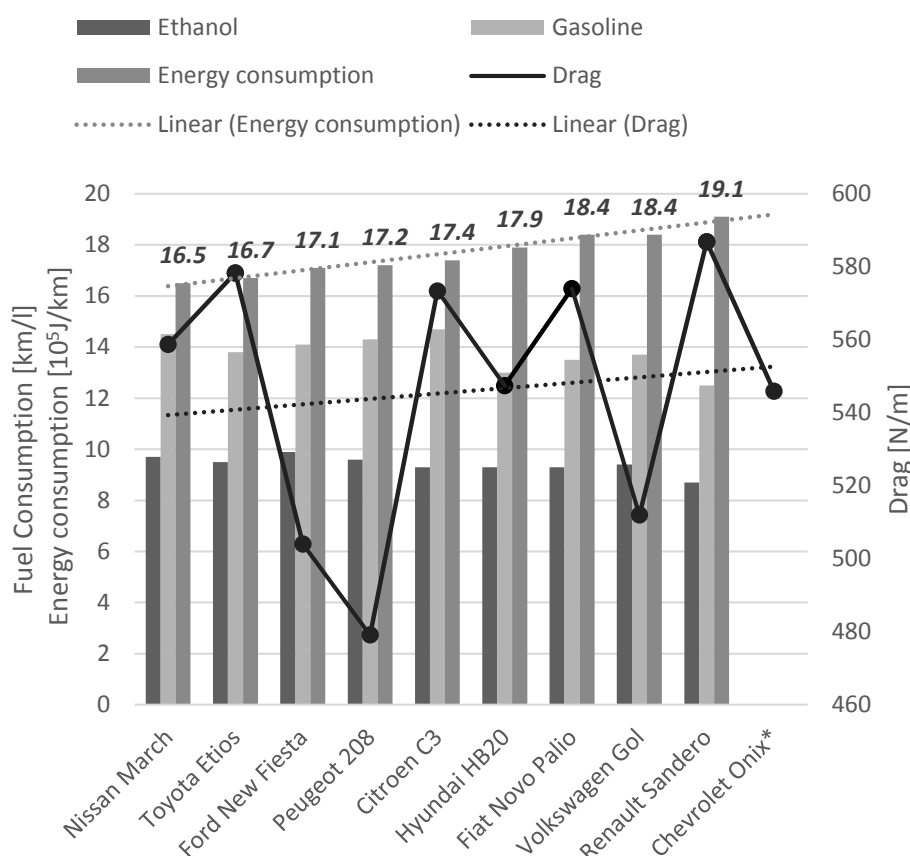


Figure 7.9: Comparison of fuel consumption (ethanol and gasoline) in highway cycle and drag force among the car models, from the lowest to the highest energy consumption.

\*INMETRO has no information about 2014 car models manufactured by Chevrolet brand.

## 7.5 SUMMARY OF CHAPTER VII

A view of aerodynamic related to ten Brazilian Hatch 2015 car models has been presented in this study. Those cars are the 2014 best-seller model from each of the ten best-seller manufactures in Brazil. In short, they are: (1°) Fiat Novo Palio; (2°) Volkswagen Gol; (3°) Chevrolet Onix; (4°) Hyundai HB20; (5°) Ford New Fiesta; (6°) Renault Sandero; (7°) Toyota Etios; (8°) Citroen C3; (9°) Nissan March; and (10°) Peugeot 208. The objective is to investigate geometry features and aerodynamic characteristics over Hatch car models.

First topic provides a brief analysis about geometry features, such as: roof end angle, rear-end spoiler, and rear slant angles. The roof end angle of all models are in the range of 6 to 15 degrees. This fact indicates that all manufactures have applied such concept in their projects, according to Marioli (1983). Whichever reason has been taken into account, all hatch car models presented in this study hold a rear-end roof spoiler in their design. They were split into three categories: (i) small, preserving the roof curve, (ii) small, with slight change of trailing angle, and (iii) extended rear-end roof spoiler with a gently protuberance. The last style seems a very clever option in order to increase local pressure and reduce lift generated on rear-wheels axle, whereas it may increase global drag over the vehicle as side effect. This study also proposes the measurement of modern slant angle in three modes, in reason of the contemporary design of rounded-base rear window shapes and the additional features, *e. g.*, rear-end spoiler. In addition, the correspondent angles over the studied models are described.

As aerodynamic forces are concerned, the pressure drag is the main share of drag on Hatch cars. The viscous drag is inexpressive against the pressure drag due to emblematic shape of bluff bodies from those commercialized road vehicles in Brazil. Analogously, the lift-induced drag has a small effect on global drag force. The results of drag lead to divide all car models into four categories of drag level, and the difference from the lowest to the highest in drag coefficient is around 25%. Even disregarding the other fuel consumption factors and the inaccuracy of two-dimensional approach, it is confirmed via trendlines that there is a proportional relation between the drag and the energy consumption of vehicles.

In summary, the main contribution of this study is to compare the best-seller car profiles produced and commercialised in Brazil, in a view of aerodynamic drag and geometry features.



## **CHAPTER VIII**

### **EFFECT OF TAILPIPE POSITION ON THE DRAG COEFFICIENT**

Based on the previous chapter of CFD methodology for realistic automotive external flow, this chapter investigates the relation between the drag force and the tailpipe position. In other words, the effect of exhaust tailpipe position on the drag coefficient over the 3D realistic DrivAer car model is presented.

The objective is to estimate the magnitude of drag variation and identify an optimum position on the rear of DrivAer Fastback car model, with the goal of drag reduction.

#### **8.1 VEHICLE GEOMETRY**

The baseline is the DrivAer Fastback assembly without mirrors, with smooth underbody and wheels (FSwoMwW). The mirrors are removed in order to increase the robustness of analysis via CFD. According to Hucho (1998), separation at the mirror housing may be periodic and thus produce an oscillating mirror load. Hence, external mirror are critical in terms of unsteady-state forces, and the convergence of numerical solution with such feature is hard to be achieved, although it is possible with appropriate mesh refinement in the wake region of mirrors. In addition, the hypothesis of negligible influence of mirrors on the flow behind the rear car allows simulating more stable external flows.

In the other hand, the proximity of rear axle leads to a significant influence of wheels movement on the adjacent flow backwards. The methodology adopted is to set an

artificial velocity of wheel surface as boundary condition over a fixed wheel. As previously described, this methodology prevents the need of multiple remeshing steps to reproduce the effective rotation of the detailed wheels, and have been proven an excellent approximation to simulate such unsteady phenomenon in a steady-state regime.

## 8.2 TAILPIPE GEOMETRY

The tailpipe geometry of the exhaust system is approximated to a straight short pipe, which has rectangular-based shape with full-rounded corners. The profile is similar to the tailpipe design over current trend of automotive models.

While the Figure 8.1 illustrates the tailpipe section, the Figure 8.2 shows how the positions are set. Ten conceptual positions of symmetric tailpipes on the rear car have been tested, as indicated in Table 8.1 and shown in Figure 8.3. The origin of coordinates from original DrivAer CAD are kept.

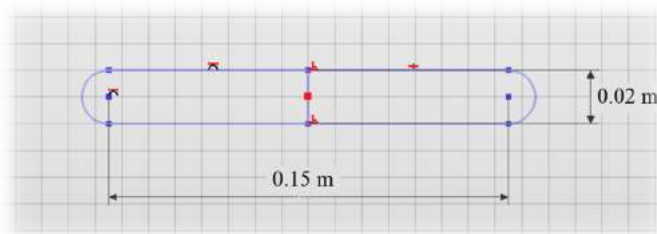


Figure 8.1: Sketch of tailpipe, in horizontal position in the Y-Z plane.

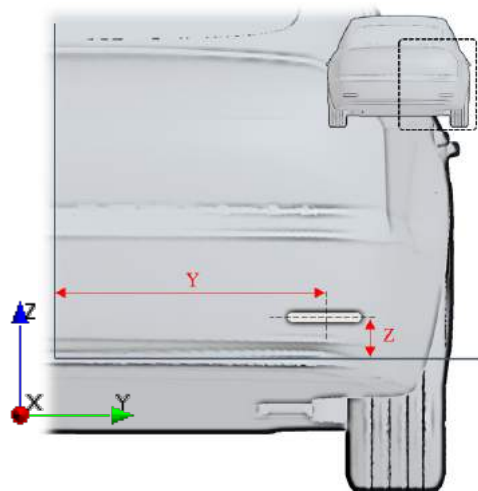


Figure 8.2: Definition of the tailpipe position on the rear car.

Table 8.1: Position and orientation of tailpipe on the rear car.

Position	Orientation	Z [mm]	Y [mm]
1	Horizontal	-60	600
2	Horizontal	0	600
3	Horizontal	100	600
4	Horizontal	250	600
5	Horizontal	-50	200
6	Horizontal	0	200
7	Horizontal	100	200
8	Horizontal	250	200
9	Horizontal	550	200
10	Vertical	100	700

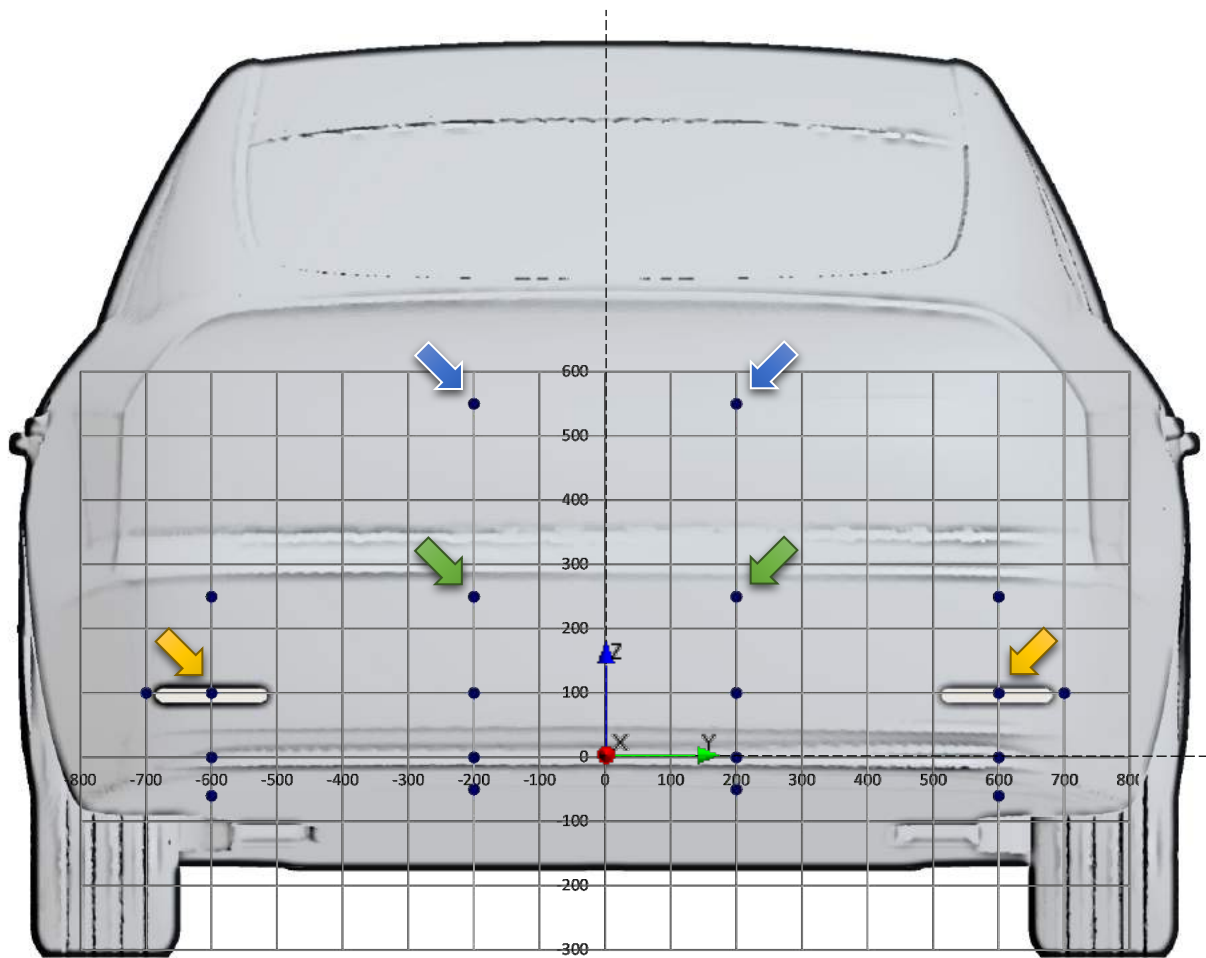


Figure 8.3: The ten positions of symmetric tailpipes on the rear car.

### 8.3 EXHAUST FLOW MODELLING

As the exhaust flow exiting the tailpipe is concerned, the flow rate value of a real road vehicle is unknown. Thus this subtopic estimates such magnitude, under the hypothesis of mass conservation of air and fuel over the powertrain. The path to the exhaust flow modelling is split into the sequential calculation of mass rate of fuel, fuel/air mass ratio, and exhaust mass flow. Afterwards, a realistic exhaust flow rate is calculated.

#### 8.3.1 Mass Rate of Fuel

The objective is to estimate the mass rate of fuel consumed during engine operation. As first step, an alternative approach to estimate the volumetric amount of fuel consumed per second ( $\Delta_f$  [l/s]) is calculated as function of car velocity ( $U_v$  [m/s]) and fuel consumption ( $\chi$  [km/l]), as expressed in Eq. (8.5).

$$\Delta_f = \frac{U_v}{1000\chi} \quad (8.5)$$

Then, based on  $\Delta_f$  and density of fuel ( $\rho_f$  [kg/m<sup>3</sup>]), Eq. (8.6) displays mass of fuel consumed per second ( $\dot{m}_f$  [g/s]).

$$\dot{m}_f = \rho_f \Delta_f = \frac{\rho_f U_v}{1000\chi} \quad (8.6)$$

#### 8.3.2 Fuel/Air Mass Ratio

On the other side, according to Heywood (1998), the combustion stoichiometry in the engine leads to evaluate the theoretical fuel/air mass ratio ( $\phi_{eq}$ ), as following in Eq. (8.7).

$$\phi_{eq} = \left( \frac{m_f}{m_{air}} \right)_{eq} \quad (8.7)$$

However, the real fuel/air mass ratio ( $\phi_R$ ) in the engine regime occurs due to difference of real and theoretical intake of air. The parameter  $r$  is adopted as air mixture ratio

of engine operation, where it is the ratio between real and theoretical mass of air that come into the engine.

The  $r$  ratio below 1 represents the engine regime of full combustion of oxygen, which provides the maximum power from the engine, *e. g.* maximum performance case, as in motorsport cars. On the other side,  $r$  higher than 1 is related to engine regime that ensure the full combustion of fuel, and avoids the misuse of fuel, *e. g.* maximum fuel economy condition, as road vehicles.

The Eq. (8.8) express the real fuel/air mass ratio, while Eq. (8.9) shows how the real and the theoretical mass of air ( $\dot{m}_{air}$ ) is related.

$$\phi_R = \left( \frac{m_f}{m_{air}} \right)_R \quad (8.8)$$

$$(m_{air})_R = r(m_{air})_{eq} \quad (8.9)$$

Afterwards, the relation between real and theoretical fuel/air mass ratio is derived from Eqs. (8.8) and (8.9), as presented in Eq. (8.10).

$$\left( \frac{m_{air}}{m_f} \right)_R = r \left( \frac{m_{air}}{m_f} \right)_{eq} \therefore \frac{1}{\phi_R} = r \frac{1}{\phi_{eq}}$$

$$\phi_R = \frac{\phi_{eq}}{r} \quad (8.10)$$

### 8.3.3 Exhaust Mass Flow

The total mass flow that exits the tailpipe ( $\dot{m}_T$  [g/s]) is almost the same as total inlet mass of fuel and air, as equivalently stated in Eqs. (8.11) and (8.12):

$$\dot{m}_T = \dot{m}_f + (\dot{m}_{air})_R \quad (8.11)$$

$$\dot{m}_T = \left( 1 + \frac{1}{\phi_R} \right) \dot{m}_f \quad (8.12)$$

Lastly, the mass flow across the exhaust system is based on Eqs. (8.6), (8.10), and (8.12), as presented in both Eq. (8.13) and Eq. (8.14).

$$\dot{m}_T = \left(1 + \frac{1}{\phi_R}\right) \frac{\rho_f U_V}{1000 \chi} \quad (8.13)$$

$$\dot{m}_T = \left(1 + r \frac{1}{\phi_{eq}}\right) \frac{\rho_f U_V}{1000 \chi} \quad (8.14)$$

### 8.3.4 Estimation of a Realistic Exhaust Flow

According to Heywood (1998), the stoichiometry model of internal combustion is given by Eq. (8.15).

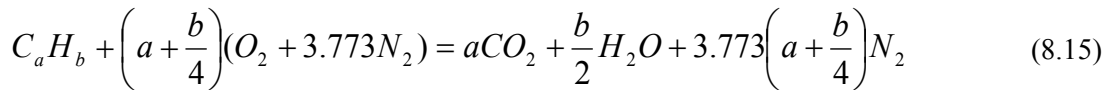


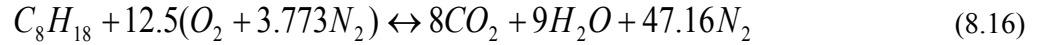
Table 8.2 shows the hypothesis of parameters adopted to estimate the exhaust mass flow rate. Since the fuel adopted is C<sub>8</sub>H<sub>18</sub>, the Eq. (8.16) presents the stoichiometry model of internal combustion with such fuel. Based on Eq. (8.7), the theoretical fuel/air mass ratio of this case is expressed in Eq. (8.17).

Table 8.2: Parameters for estimation of exhaust mass flow.

Parameter		Description
Fuel		Isooctane (C <sub>8</sub> H <sub>18</sub> )
Fuel density <sup>4</sup>	$\rho_f$	740 kg/m <sup>3</sup>
Fuel consumption <sup>5</sup>	$\chi$	12.3 km/l
Car speed	$U_\infty$	40 m/s
Air mixture ratio	$r$	1.05 (hypothesis of engine operation in road car)

<sup>4</sup>According to Sincopetro, the fuel density is in the range of 720 to 760 kg/m<sup>3</sup>.

<sup>5</sup>Average fuel consumption of BMW 335i xDrive model, at cruise speed of 140 km/h (approximately 40 m/s).



$$\phi_{eq} = \left( \frac{m_f}{m_{air}} \right)_{eq} = \frac{m_{C_8H_{18}}}{m_{12.5(O_2 + 3.773N_2)}} \cong \frac{1}{15.1} \quad (8.17)$$

Thus, the mass flow rate of exhaust system is estimated from Eq. (8.14), data in Table 8.2, and theoretical fuel/air mass ratio calculated in Eq. (8.17), as shown in Eq. (8.18) below.

$$\dot{m}_T = (1 + r\phi_{eq}) \frac{\rho_f U_v}{1000 \chi} \cong 40.4 [g/s] \quad (8.18)$$

Nonetheless, please note that this study assumed dual and symmetric tailpipes. Hence, the total exhaust flow must split by them. As the exhaust flow is split to both tailpipes, the boundary that represents the flow of each tailpipe is an inlet mass flow rate equal to 20.2 g/s, as shown in Eq. (8.19).

$$\dot{m}_{exhaust} = \frac{\dot{m}_T}{2} \cong 20.2 [g/s] \quad (8.19)$$

## 8.4 COMPUTATIONAL APPROACH

As previously indicated in the Chapter IV, the simulation of half-car domain is a suitable approach for drag prediction. The best practices for CFD setup established in the same chapter are assumed in this study. The physical setup and the best practices are presented in Table 8.3 and Table 8.4, respectively.

Table 8.3: Physical setup.

Feature	Properties
Domain	Three-dimensional
Time regime	Steady-state
Fluid properties	Air ( $\rho = 1.18415 \text{ kg/m}^3$ , $\mu = 1.85508 \times 10^{-5} \text{ Ns/m}^2$ )
Flow Solver	Segregated
Equation of State	Constant density
Flow regime	Turbulent

Table 8.4: Best practices for CFD setup: exhaust flow analysis.

Factor	Best cost-effective methodology
Car simplification	with no mirrors and with wheels (woM wW)
Domain	half-car model
Ground condition	ground simulation & wheel surfaces under local rotation rate (with GS & W).
Time regime	steady-state
Gradient method	2 <sup>nd</sup> -order Green-Gauss
Mesh base size	10 mm
Prism layer thickness	05 mm (for All $y^+$ Wall Treatment)
Turbulence model	Realizable $k$ - $\epsilon$ two-layer

The boundary conditions of this study is also similar to the validation topic, except for: (i) the cruise speed, and (ii) the addition of symmetrical tailpipes on the rear car. The cruise speed of 40 m/s is chosen to better fit a real car operation on highway.



Consequently, the wheel has angular velocity of  $127 \text{ rad/s}$ . Table 8.5 describes all boundary conditions and parameters associated to the numerical domain.

Table 8.5: Boundary conditions.

Boundary	Condition	Parameters
DrivAer car	wall	no-slip
Inlet	velocity-inlet	$U_\infty = 40 \text{ m/s}$ ; $I = 0.1\%$ ; $l_t = 0.10 \text{ m}$
Exhaust jet	mass flow inlet	$\dot{m}_{exhaust} = 20.2 \text{ g/s}$ ; $I = 1.0\%$ , $l_t = 0.01 \text{ m}$
Exhaust pipe	wall	no-slip
Outlet	pressure outlet	
Sym	symmetry	
Sides	symmetry	
Ground	wall	no-slip with ground movement at $U_{GS} = 40 \text{ m/s}$
Wheels	wall	no-slip with local rotation rate at $\omega_w = 127 \text{ rad/s}$

## 8.5 RESULTS OF DRAG COEFFICIENT

The Position 1 is the reference case, since such position is typically adopted in aesthetic design of recent car models.

The Table 8.6 presents the drag coefficient prediction from ten tailpipe positions on the rear car. The comparison of drag coefficient among these several positions are shown in percentage format.

Table 8.6: Comparison of drag coefficient from several tailpipe positions.

Position	Orientation	Z [mm]	Y [mm]	$C_D$	$\Delta C_D / C_{D_{baseline}}$ [%]
1	Horizontal	-60	600	0.22630	baseline
2	Horizontal	0	600	0.22572	-0.3
3	Horizontal	100	600	0.22556	-0.3
4	Horizontal	250	600	0.22597	-0.1
5	Horizontal	-50	200	0.22470	-0.7

Position	Orientation	Z [mm]	Y [mm]	$C_D$	$\Delta C_D / C_{D_{baseline}}$ [%]
6	Horizontal	0	200	0.22595	-0.2
7	Horizontal	100	200	0.22620	0.0
8	Horizontal	250	200	0.22628	0.0
9	Horizontal	550	200	0.22629	0.0
10	Vertical	100	700	0.22589	-0.2

## 8.6 ANALYSIS OF RESULTS

The analysis of results is split in qualitative and quantitative point of view, as summarised below.

### 8.6.1 Qualitative Perspective

From the qualitative point of view, the change in the position of tailpipes provide slight difference in drag coefficient of the DrivAer Fastback car model.

The first thought was that the tailpipe would provide a planar jet, which could interfere with the wake region behind the car. Thus, some significant difference in drag would be found as consequence of such intrusion from this secondary flow. Unfortunately, the exhaust flow momentum is not enough, and the maximum variance is roughly 1%.

The bright side is that those results offer support to project decisions beyond performance issues. For instance, designers can use such evidence to propose new car concepts, where the tailpipes can be highlighted and placed in alternative positions.

### 8.6.2 Quantitative Perspective

Even though the range of drag coefficient is small, there is an optimum region to install the exits of exhaust system. Surprisingly, the baseline that has been adopted in many sport cars provide the worst results in regards to aerodynamic efficiency. Likewise, most of the positions close to the centre ( $y = 200\text{mm}$ ) are equally misplaced, *e. g.*, positions 7, 8, and 9.



Figure 8.4: Illustrations of the optimum tailpipe position (position 5) on the DrivAer Fastback car model.

The outer region ( $y = 600 \text{ mm}$ ) seems to be the best region to place tailpipes, mainly on the surroundings of the rear bumper ( $z$  from 0 up to  $250 \text{ mm}$ ). Nonetheless, the optimum position is found just below the rear bumper, in the inner region (position 5:  $y = -50 \text{ mm}$ ;  $z = 200 \text{ mm}$ ), as illustrated in Figure 8.4.

One reason for such phenomena is that the exhaust flow leaves both tailpipes in favour of external flow, instead what occurs with another position above, *e. g.*, cross flow from position 7. The exhaust flow from position 5 migrates to upper region of rear car, apparently increasing the local pressure. The Figure 8.7 highlights the phenomena on the cases of positions 5 and 7, respectively.

### 8.6.3 Drag Coefficient Map of Tailpipe Position

The drag prediction is interpolated over the rear region of the vehicle, in order to expand the understanding about the trend of drag coefficient as function of the tailpipe position. Figure 8.5 and Figure 8.6 presents the drag coefficient map generated from the database built, into the range of  $y$  and  $z$  tailpipe positions tested, *i. e.*,  $200 < y < 700$  and  $-60 < z < 550$ .

Indeed, the trend to place the tailpipes at the outer region for lower drag is evident. However, the inner-lower position still provides the most favourable drag magnitude for vehicle performance.

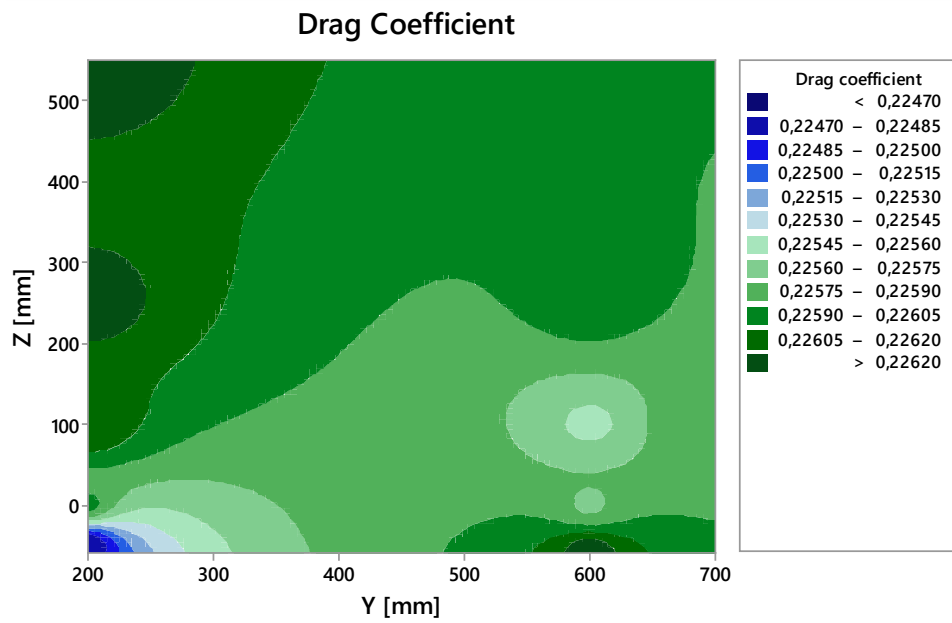


Figure 8.5: Plot of drag coefficient map via interpolation process.

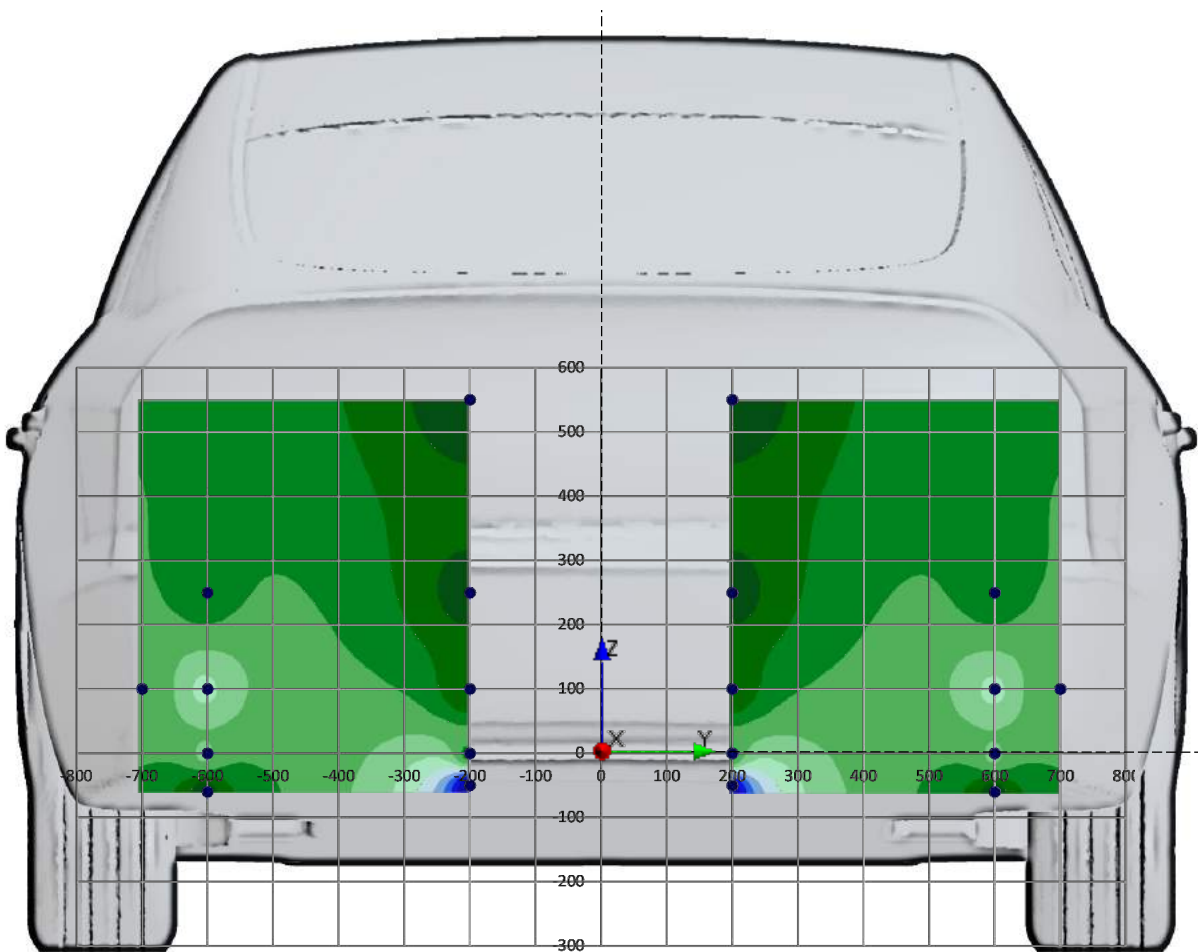


Figure 8.6: Drag coefficient map from all ten tailpipe positions on the rear car.

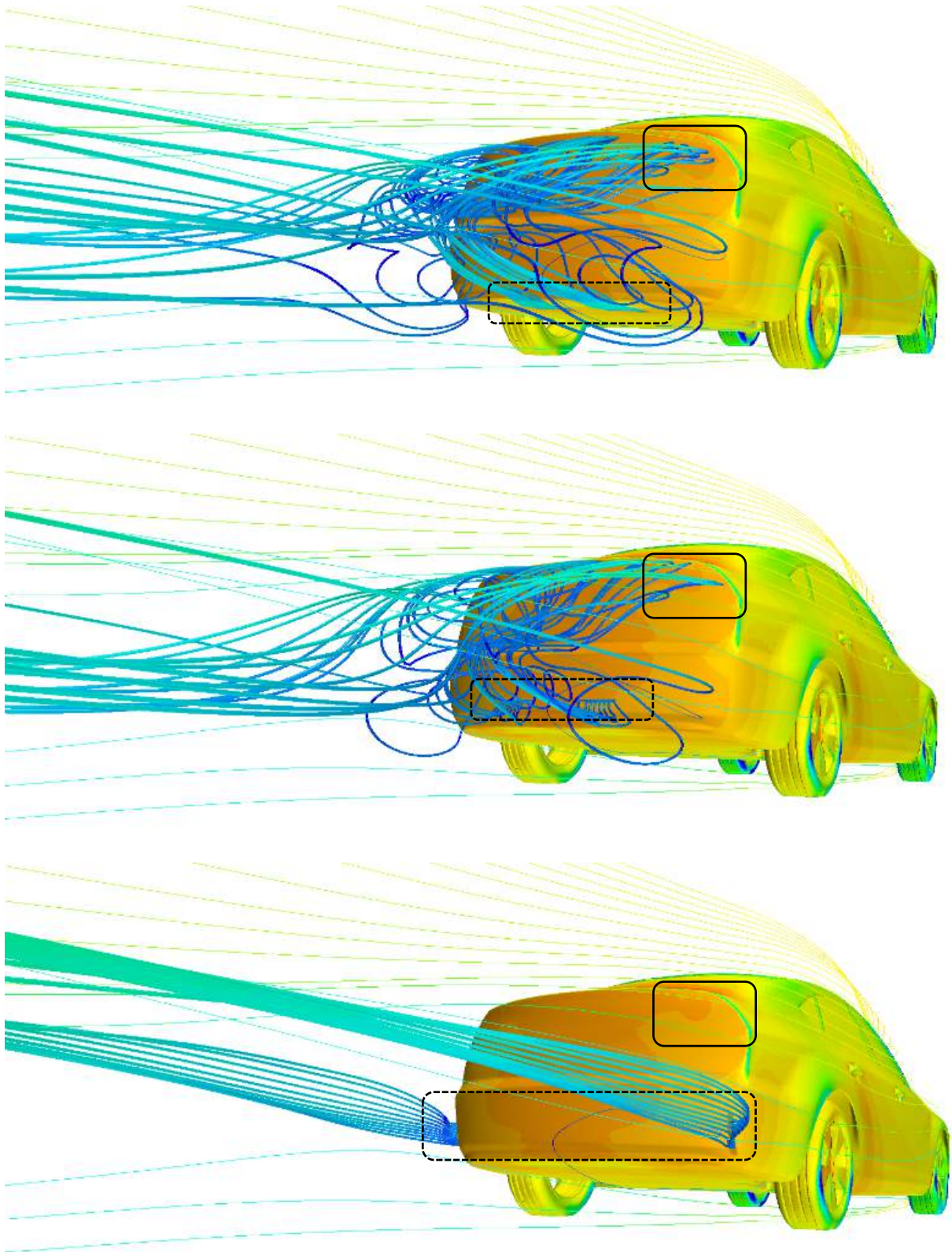


Figure 8.7: Comparison of streamlines from the tailpipes in position 5 (above), position 7 (centre), and position 10 (below). The car surface display the pressure on the vehicle.

## 8.7 SUMMARY OF CHAPTER VIII

The effect of exhaust tailpipe position on the drag coefficient over a 3D realistic road car model has been presented in this study. The objective is to estimate the magnitude of drag variation and identify an optimum position on the rear of DrivAer Fastback car model.

From the quantitative point of view, the effect of tailpipe position on the rear car is very smooth. The maximum variation corresponds to less than 1% of the drag coefficient. In other words, the exhaust flow has slight influence on the drag over a vehicle.

In the other side, the results can support design decisions concerning aesthetics. New design concepts of tailpipe shape and position might be developed without compromise aerodynamic performance of the vehicle, if the spatial range investigated were concerned.

Even if the drag change has minor magnitude, there is an optimum position. Adopting the baseline as typical position of tailpipes on sport cars, the position 5 of this study indicates the reduction 0.7%. In motorsport perspective, this value is considerable significant indeed.

In conclusion, the main contributions of this study are: (i) to present the effect of tailpipe position on the drag of realistic road vehicle model, as well as (ii) to provide a database and drag coefficient map that may support technical decision concerning performance and/or design targets on road car projects.

## **CHAPTER IX**

### **RESEARCH SUMMARY**

This master thesis has pursued the goal of investigation of automotive aerodynamics by means of CFD methodology, especially at low computation requirement. Indeed, all simulations presented throughout the research have been run via the STARCCM+ software (Version 9.04) on Intel Core i5-2500 CPU at 3.3 GHz (2 cores/4 threads), with 16 GB RAM memory. The only exception was the costly simulation of the full-car model in unsteady-state regime, due to limitation of hard disk.

This fact demonstrates by itself how the CFD methodology presented can handle automotive external flow with any typical workstation or even simple computers of our time. In other words, it implies that the best practice provided may lead to a significant cost-effective use of such engineering tool for solutions in aerodynamics of vehicles, especially for industrial design purpose.

Last, but not least, the researcher hopes that the topics concerning the aerodynamic concept, the comparison of Brazilian 2015 Hatch car profiles, and the investigation of effect of tailpipe position of road cars may also be useful for both academic and industrial research.





## CHAPTER X

### RECOMMENDATIONS FOR FUTURE RESEARCH

Regarding realistic car geometries, this research has adopted one of the most recent benchmark in automotive aerodynamics: the DrivAer body. For future work, the use of a real commercial car model is recommended, since this would lead to a step ahead in CFD methodology for automotive aerodynamics. New challenges from a more detailed geometry could not only improve the versatility in the use of such computational design tool, but also allow performing a further detail optimization process with more confidence about interference drag in real cases.

In compliance to the CFD methodology for drag prediction presented in this work, further studies on aeroacoustics simulation could provide other best practices for such research field. Indeed, passenger comfort by improving acoustic performance is also a relevant target in a car design process, especially on sportcars models.

Another point for future research is the simulation approach on the wheels. In this study, the rotational effects from the wheel surfaces have been imposed by tangential velocity on stationary wheels. In another words, the surface of the detailed wheels received a velocity vector corresponding to the angular rotation and distance from the respective axle. However, this approach could deal with velocity vectors normal to cell surfaces, which might cause numerical issues in the computational solution, *e.g.*, mass balance. Therefore, the study of this approach and/or other methods are also recommended as future research.

The tailpipe position was investigated regarding the influence on the drag coefficient over a vehicle. Nevertheless, other topics are related to this feature, such as: (i)

engine performance (pressure magnitude at the end of the exhaust system), and (ii) stains on the rear bumper (particle deposition from the exhaust flow and/or tailpipe temperature). Future research in this topic is highly recommended, since few academic studies concerns the exhaust flow in the view of fluid dynamics are available.

## **BIBLIOGRAPHY**

- AHMAD, N. E. et al. **Mesh Optimization for Ground Vehicle Aerodynamics**. CFD Letters, Vol. 2, 2010.
- AHMED, S. R. Wake Structure of Typical Automobile Shapes. **Trans. ASME. Journal of Fluids Engineering**, 103, p. 162-169, 1981.
- AHMED, S. R. Influence of Base Slant on the Wake Structure and Drag of Road Vehicles. **Trans. ASME. Journal of Fluids Engineering**, 105, p. 429-434, 1983.
- AKA, H. **Study on Aerodynamic Characteristics of a Passenger Car in a Wind Tunnel**. 2003. MSc Thesis, Gazi University, Ankara.
- BACCHI, Raphael David Aquilino. **O Que Se Deseja De Uma Definição De Vórtices?**. 2009. 324 p. MSc Thesis, Universidade Federal Fluminense. Niterói.
- CAKIR, Mustafa. **CFD Study on Aerodynamic Effects of a Rear Wing/Spoiler on a Passenger Vehicle**. 2012. 62 p. MSc Thesis, Santa Clara University, Santa Clara.
- CAÑADA, Eduardo. **Aerodynamic analysis and optimization of the rear wing of a WRC car**. 2011. 81 p. MSc Dissertation, Oxford Brookes University, Oxford.
- DOVAL, Peter Nicholas. **Aerodynamic Analysis and Drag Coefficient Evaluation of Time-Trial Bicycle Riders**. 2012. 95 p. Theses and Dissertations. Paper 28. University of Wisconsin-Milwaukee.

GM Media. **GM Breaks Ground on New Reduced-Scale Wind Tunnel**. Interview. N.p., 13 Mar. 2014. Web. 30 Jan. 2015. <<http://media.gm.com/media/us/en/gm/news.detail.html/content/Pages/news/us/en/2014/mar/0313-wind-tunnel.html>>.

HÅKANSSON, Christoffer; LENNGREN, Malin J. **CFD Analysis of Aerodynamic Trailer Devices for Drag Reduction of Heavy Duty Trucks**. 2010. 50 p. Master thesis, Chalmers University of Technology, Göteborg.

HEFT, Angelina; INDINGER, Thomas; ADAMS, Nikolaus. **Introduction of a New Realistic Generic Car Model**. 2012 SAE World Congress, 2012a. doi: 10.4271/2012-01-0168.

HEFT, Angelina; INDINGER, Thomas; ADAMS, Nikolaus. Experimental and Numerical Investigation of the DrivAer Model. **ASME 2012 Fluids Engineering Summer Meeting**. Rio Grande, Puerto Rico, 2012b. doi:10.1115/FEDSM2012-72272.

HUCHO, W-H. **Aerodynamics of Road Vehicles**. Fourth Edition. Society of Automotive Engineers Inc, 1998.

INMETRO. **Programa Brasileiro de Etiquetagem - PBE**. Web. 16 Apr. 2015. <[http://www.inmetro.gov.br/consumidor/pbe/veiculos\\_leves\\_2015.pdf](http://www.inmetro.gov.br/consumidor/pbe/veiculos_leves_2015.pdf)>.

JANSSEN, L. J. *et al.* **Aerodynamische Entwicklung von VW Golf und Scirocco**. ATZ, Vol. 77, 1975.

LE GOOD, Geoffrey M.; GARRY, Kevin P. **On the Use of Reference Models in Automotive Aerodynamics**. 2004 SAE World Congress, Detroit, USA, 2004.

MARIOLI, M. Fuction Versus Appearance, The Interaction Between Customer, Stylist and Engineer in Vehicle Design. **Int. Journal of Vehicle Design**, Vol. 5, 1983.

PIERACCIANI, V., **Eficiência Energética Será Pesadelo Da Indústria**. Interview. Automotive Business. N.p., 24 Apr. 2015. Web. 30 Apr. 2015. <<http://www.automotivebusiness.com.br/>>.

SOARES, Renan Francisco. **Estudo Fluidodinâmico Computacional (CFD) Aplicado à Aerodinâmica do Esporte Automobilístico**. 2013. 146 p. Bachelor Thesis, Universidade Tecnológica Federal do Paraná. Cornélio Procópio.

SOARES, Renan Francisco; DE SOUZA, Francisco José; CORREA, Alexandre Felipe Medina. **Análise Preliminar do Efeito da Turbulência sobre um Mecanismo de Recolamento da Camada Limite**. IX Escola de Primavera de Transição e Turbulência, 2014a, doi: 10.13140/2.1.4189.2166.

SOARES, Renan Francisco; DE SOUZA, Francisco José; CORREA, Alexandre Felipe Medina. Preliminary Analysis of Boundary Layer Reattachment by Momentum Injection Method over NACA0012. **XXXV Ibero-Latin American Congress on Computational Methods in Engineering**, 2014b, doi:10.13140/2.1.2053.2005.

TAŞTAN, Umur. **Investigation of Turbulence Models used in Automotive Industry**. 2011. 134 p. MSc Thesis. Middle East Technical University.

## APPENDIX

This appendix is split into three groups:

- (i) Flow visualization (Chapter V)
  - a. RANS flow visualization of the three DrivAer variations
    - i. Iso-vorticity surfaces
    - ii. TKE magnitudes
    - iii. Q-criterion
  - b. DES flow visualization of the DrivAer Fastback
    - i. Vorticity magnitude
    - ii. Q- and Lambda-2 criteria
    - iii. Vortex structures into the wheelhouses
- (ii) Hatch 2015 cars (Chapter VII)
  - a. Car profiles
  - b. Car meshing
- (iii) Tailpipe position (Chapter VIII)
  - a. Car geometries
  - b. Vector velocity fields
  - c. Streamlines from exhaust system

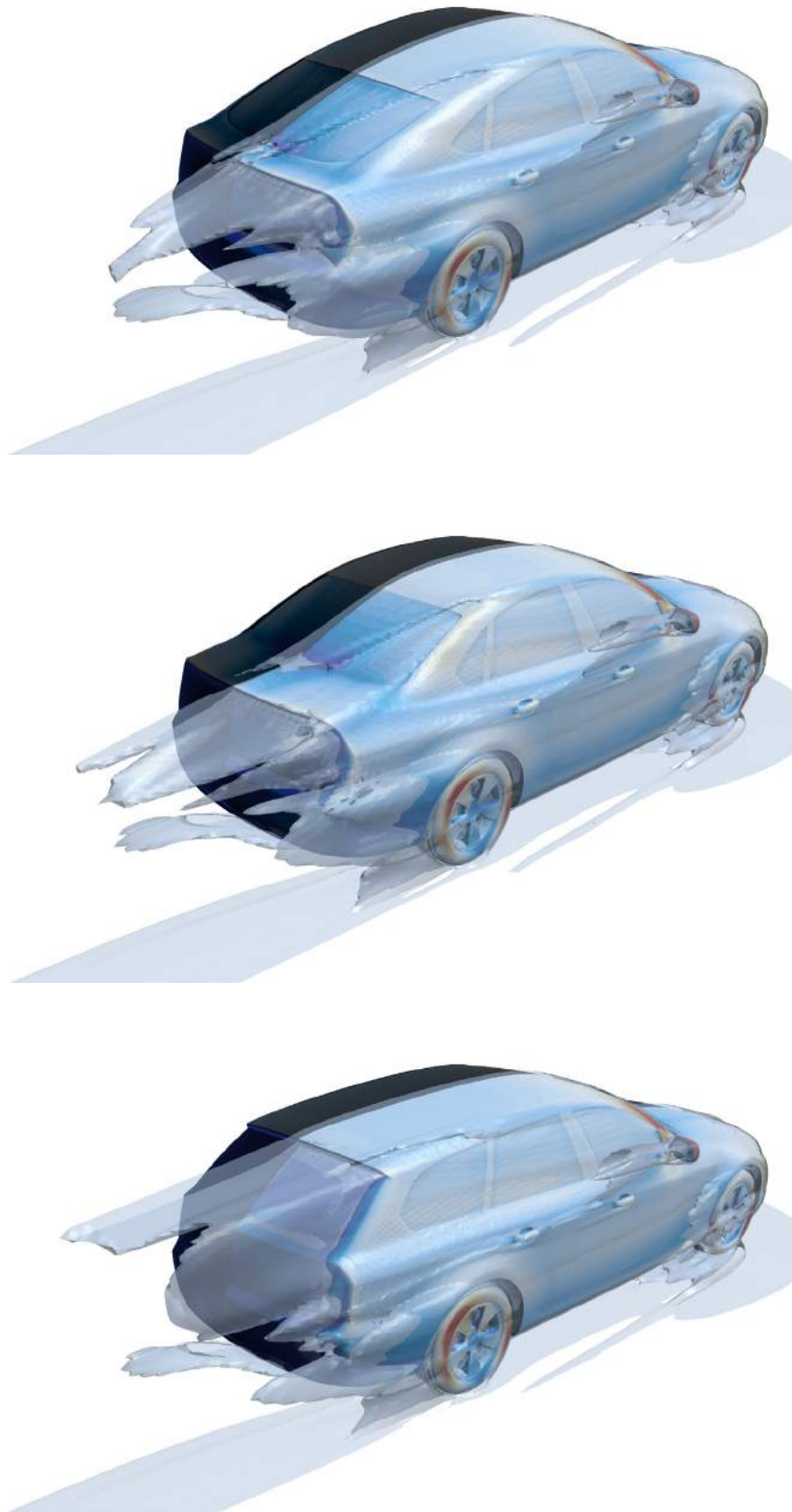


Figure 12.1: Iso-vorticity surface of 100 rad/s<sup>2</sup>: wMwW, with GS & W.

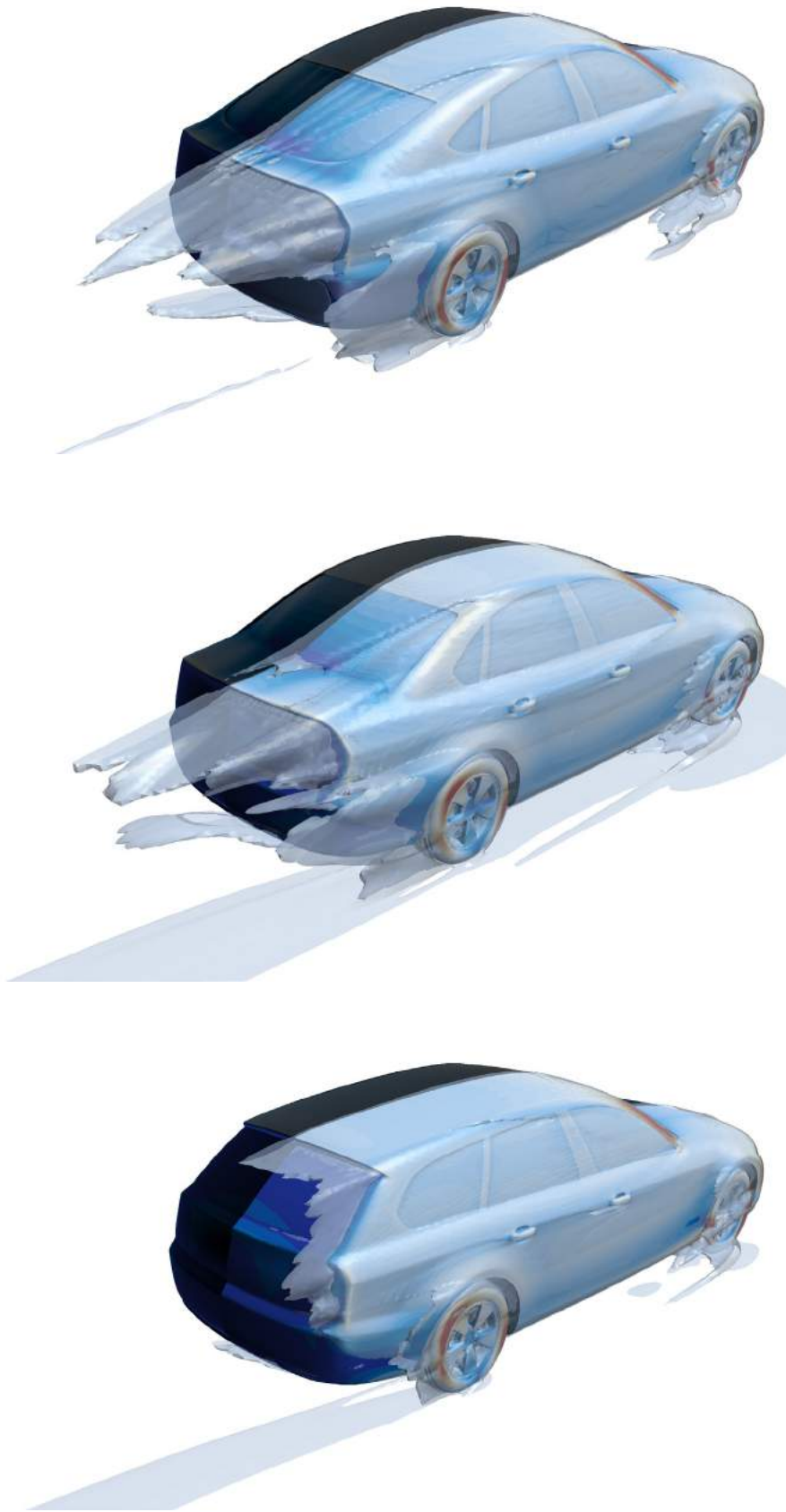


Figure 12.2: Iso-vorticity surface of  $100 \text{ rad/s}^2$ : woMwW, with GS & W.



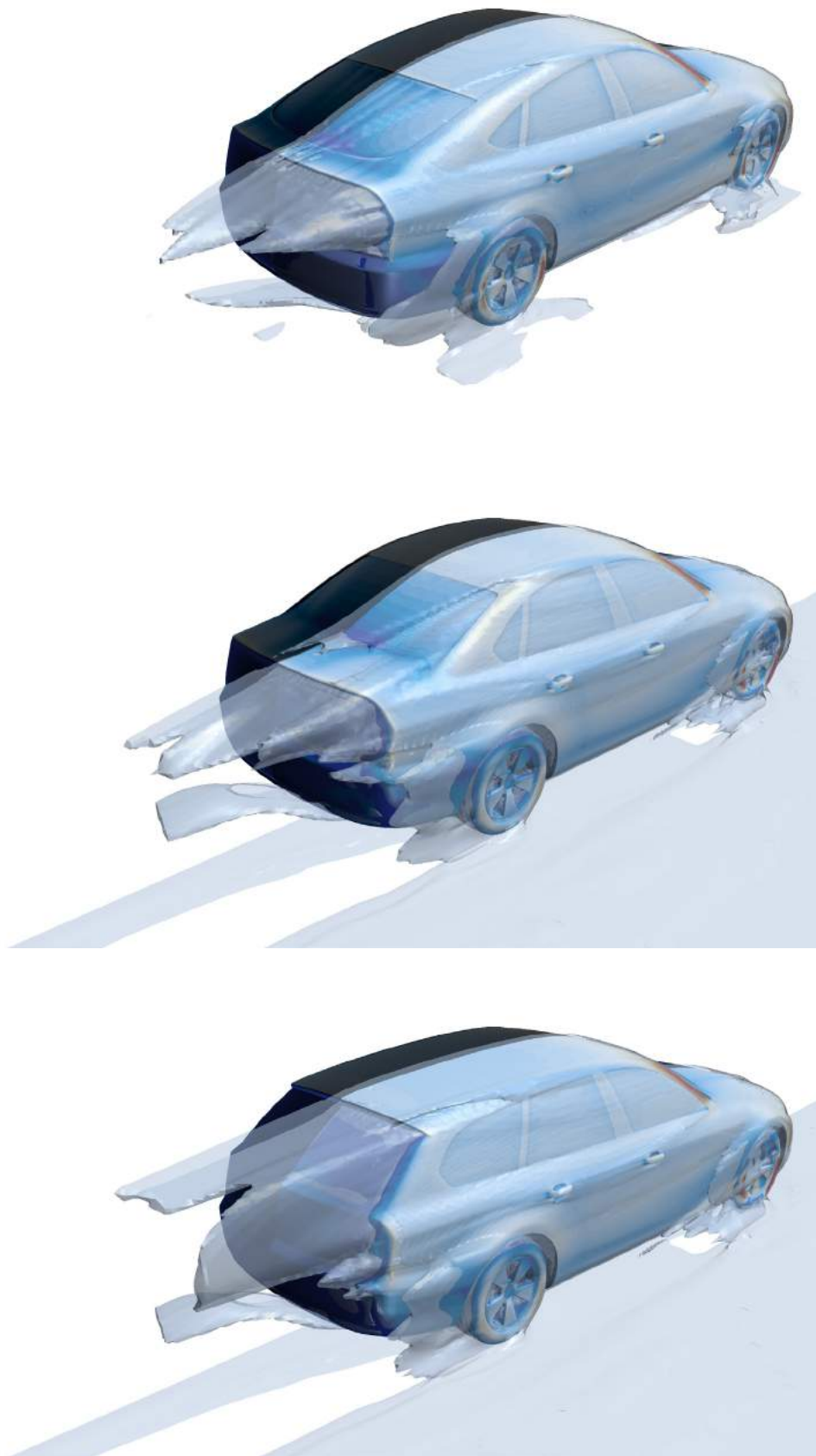


Figure 12.3: Iso-vorticity surface of 100 rad/s²: woMwW, wo/ GS.

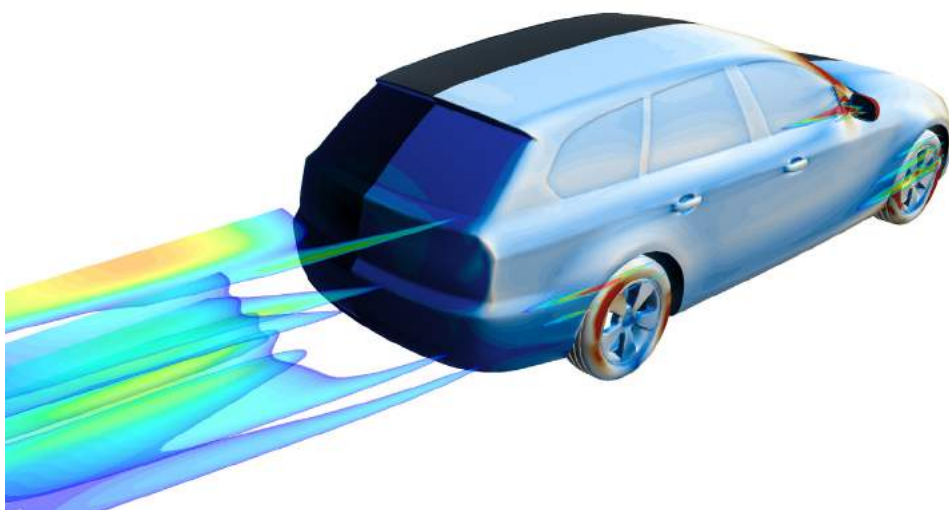
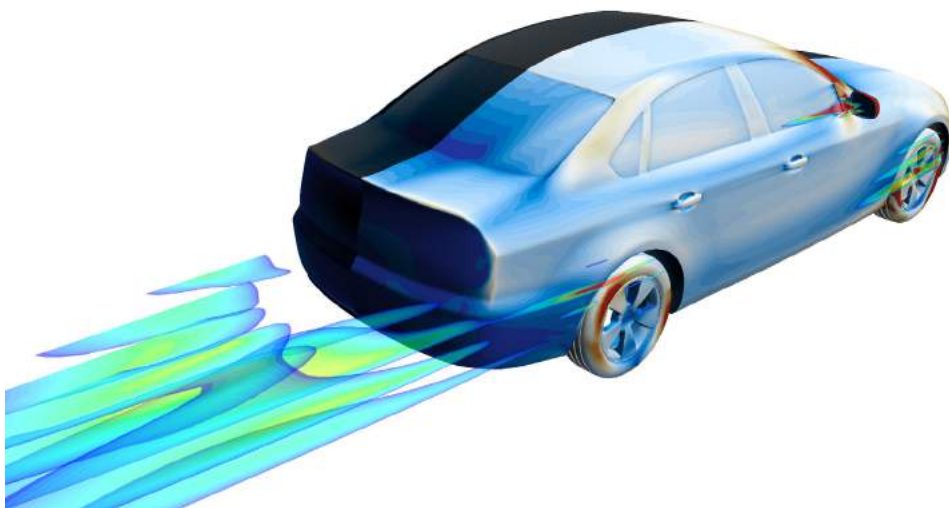
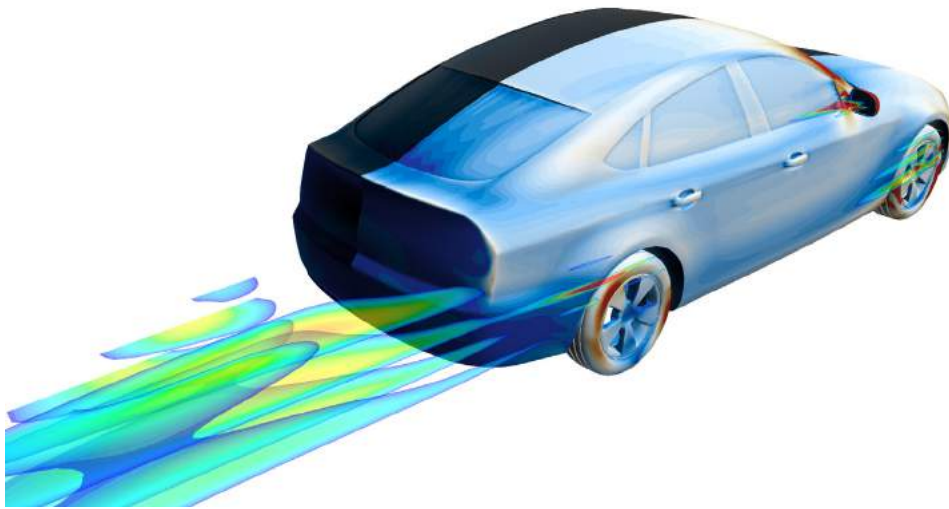


Figure 12.4: TKE magnitude from 8 to 15 J/kg: wMwW, with GS & W.

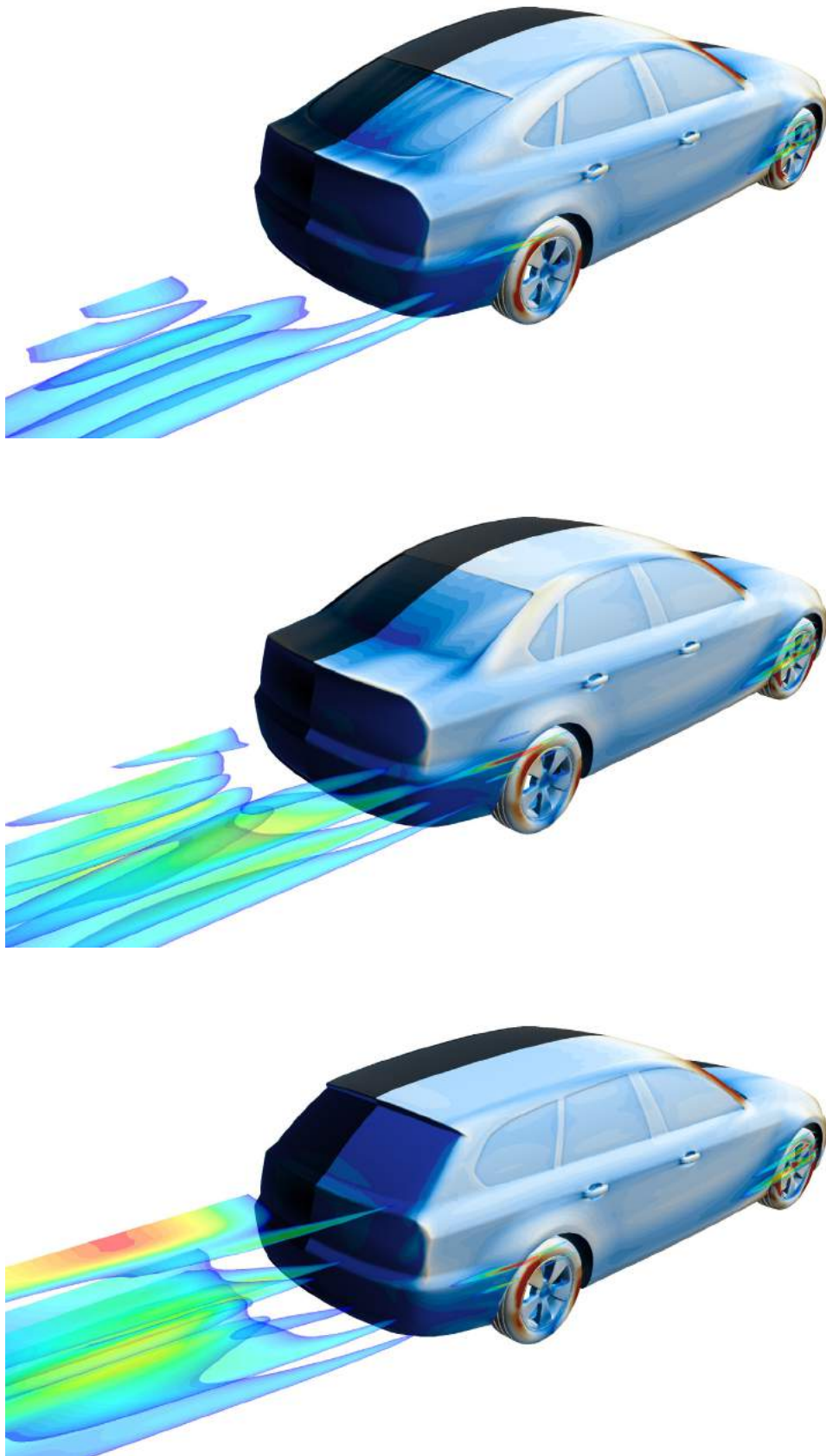


Figure 12.5: TKE magnitude from 8 to 15 J/kg: woMwW, with GS & W.

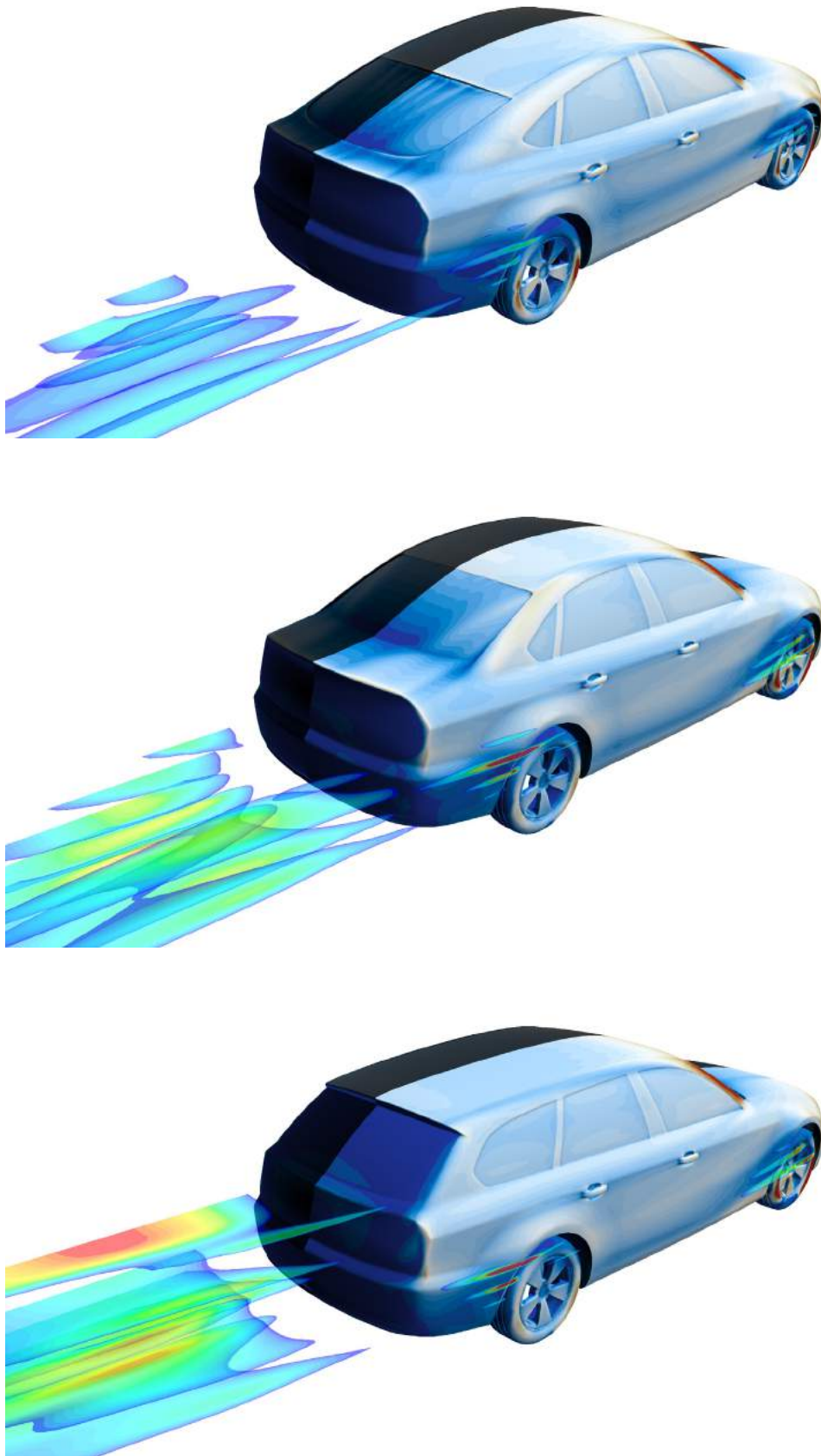


Figure 12.6: TKE magnitude from 8 to 15 J/kg: woMwW, wo/ GS.



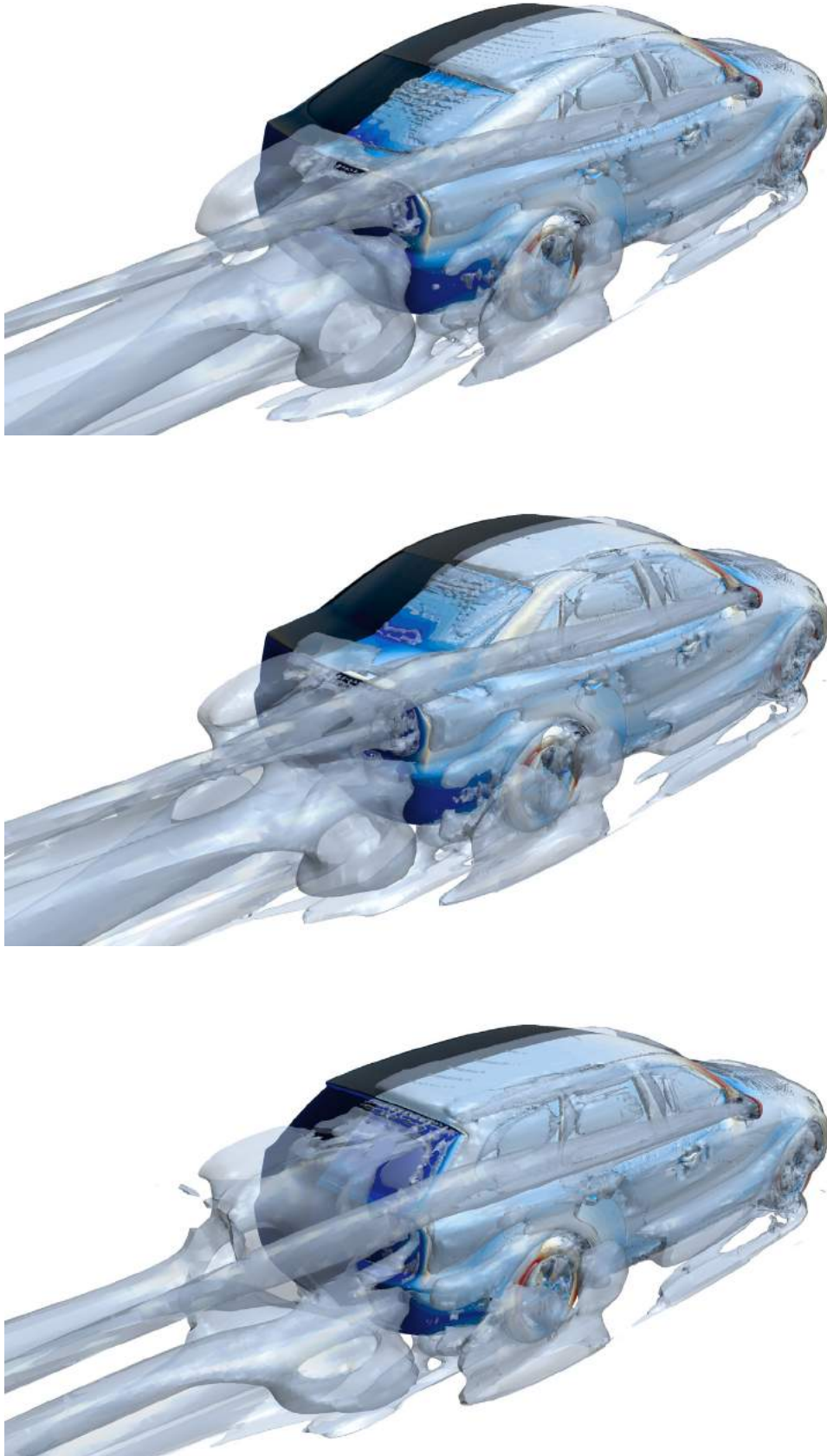


Figure 12.7: Q-criterion at  $10 \text{ rad/s}^2$ : wMwW, with GS & W.

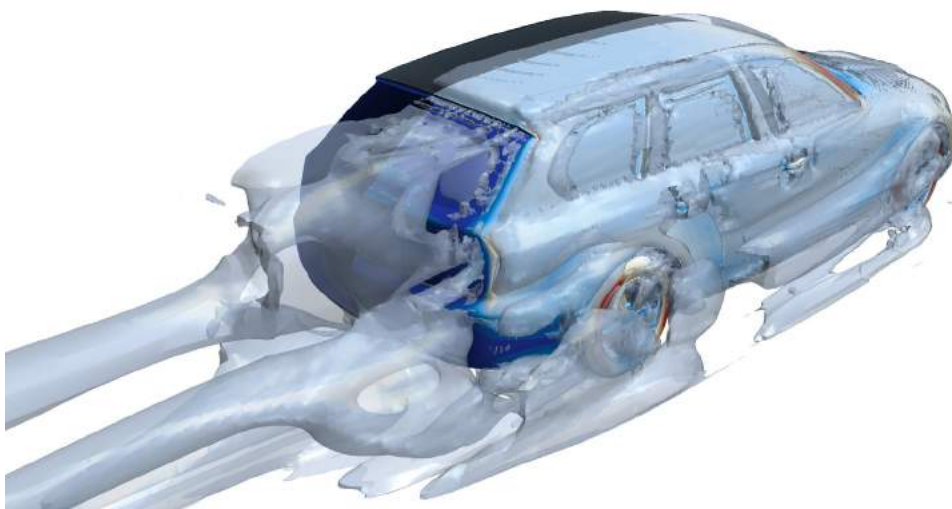
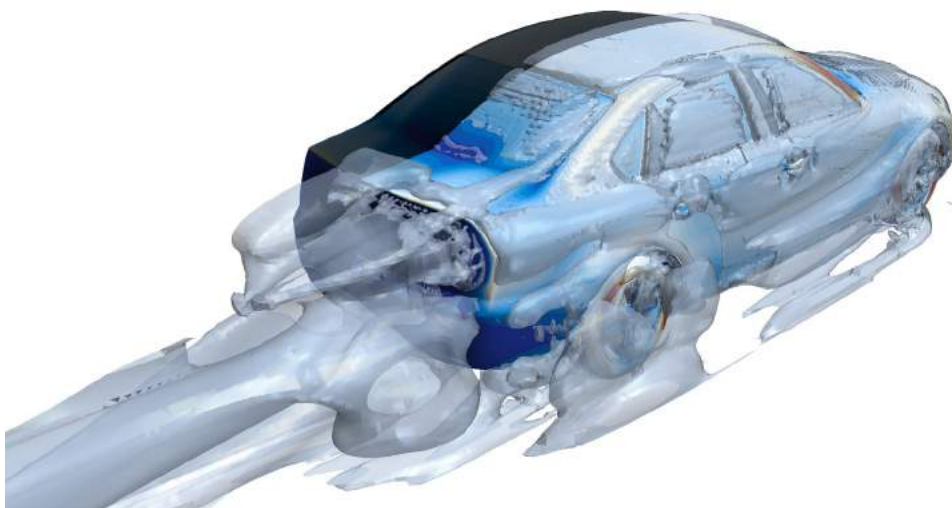
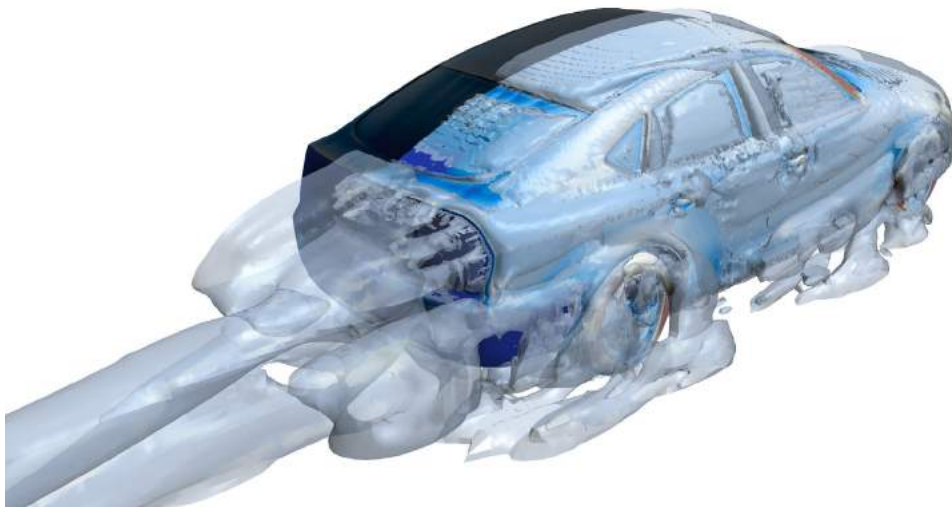


Figure 12.8: Q-criterion at 10 rad/s<sup>2</sup>: woMwW, with GS & W.

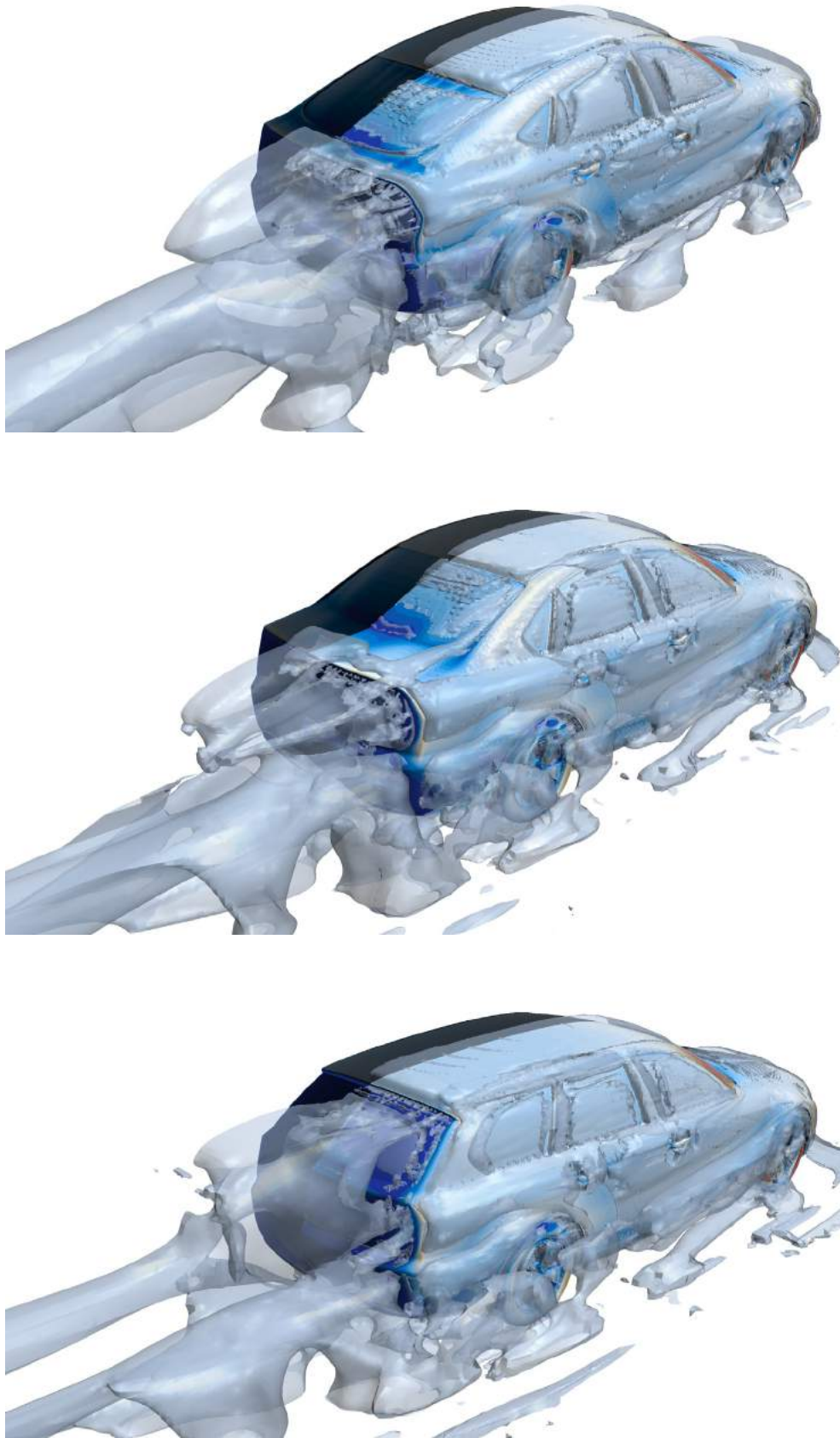


Figure 12.9: Q-criterion at 10 rad/s<sup>2</sup>: woMwW, wo/ GS.





Figure 12.10: Q-criterion at  $200 \text{ rad/s}^2$ : wMwW, with GS & W.



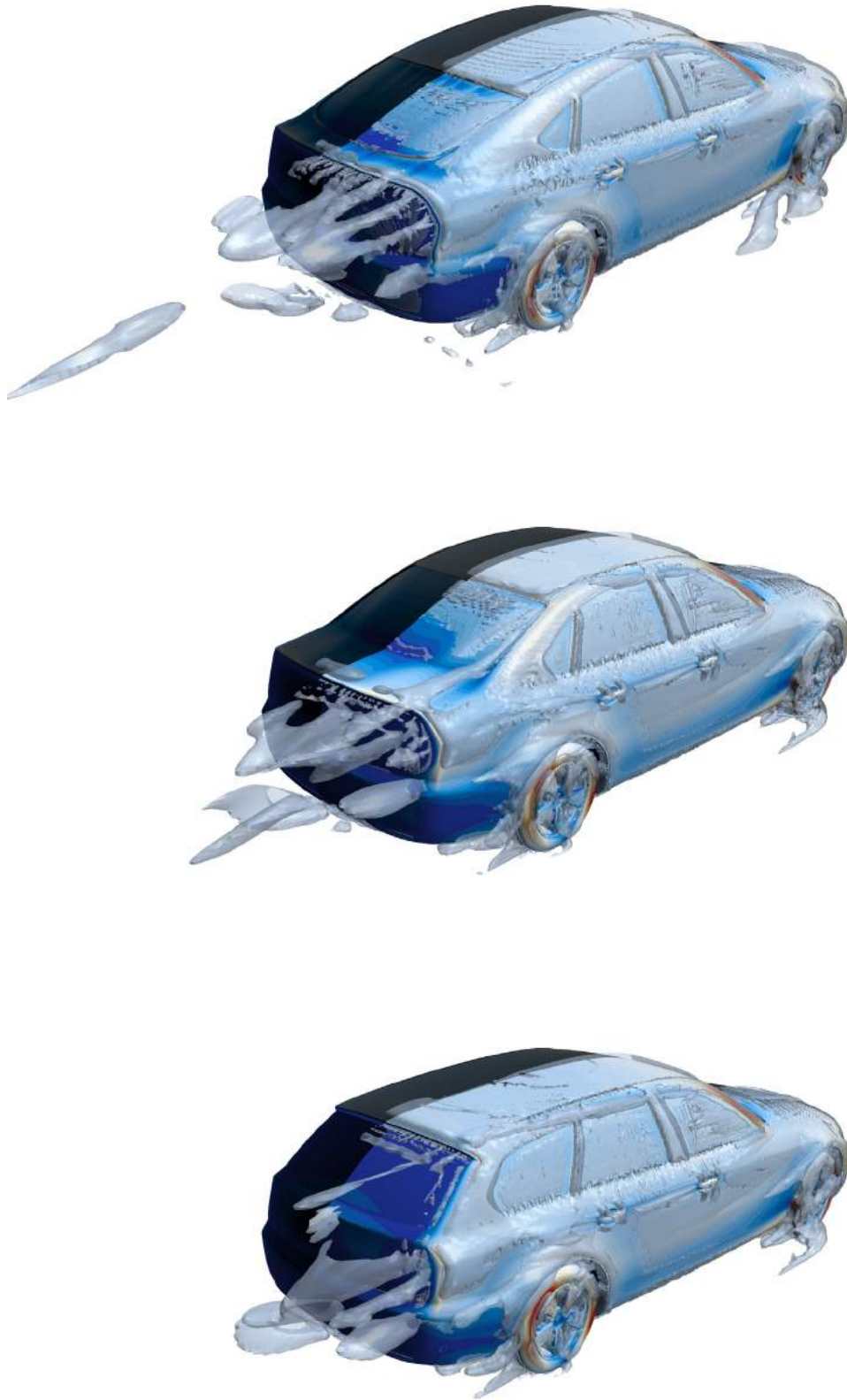


Figure 12.11: Q-criterion at 200 rad/s²: woMwW, with GS & W.

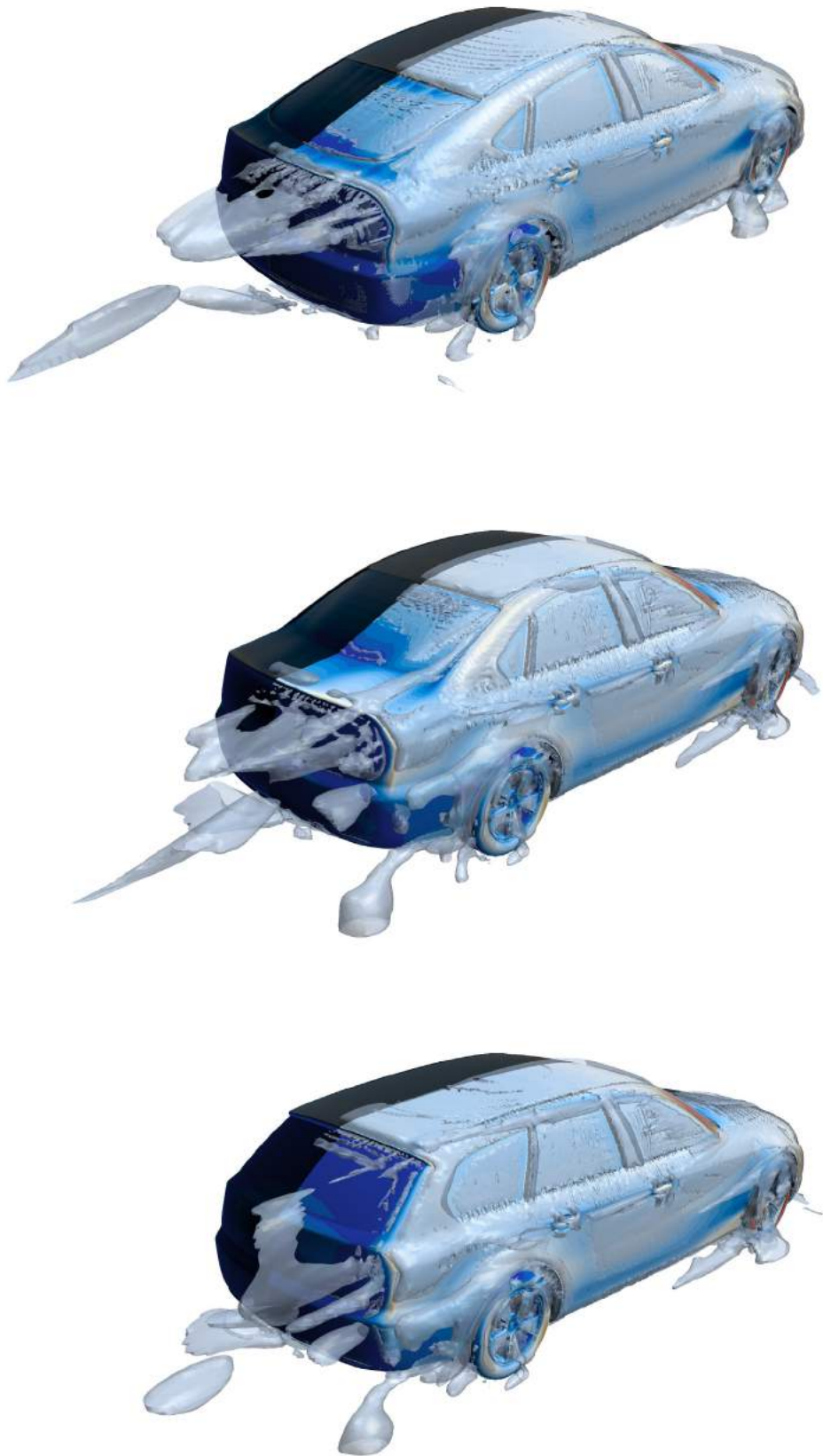


Figure 12.12: Q-criterion at 200 rad/s<sup>2</sup>: woMwW, wo/ GS.

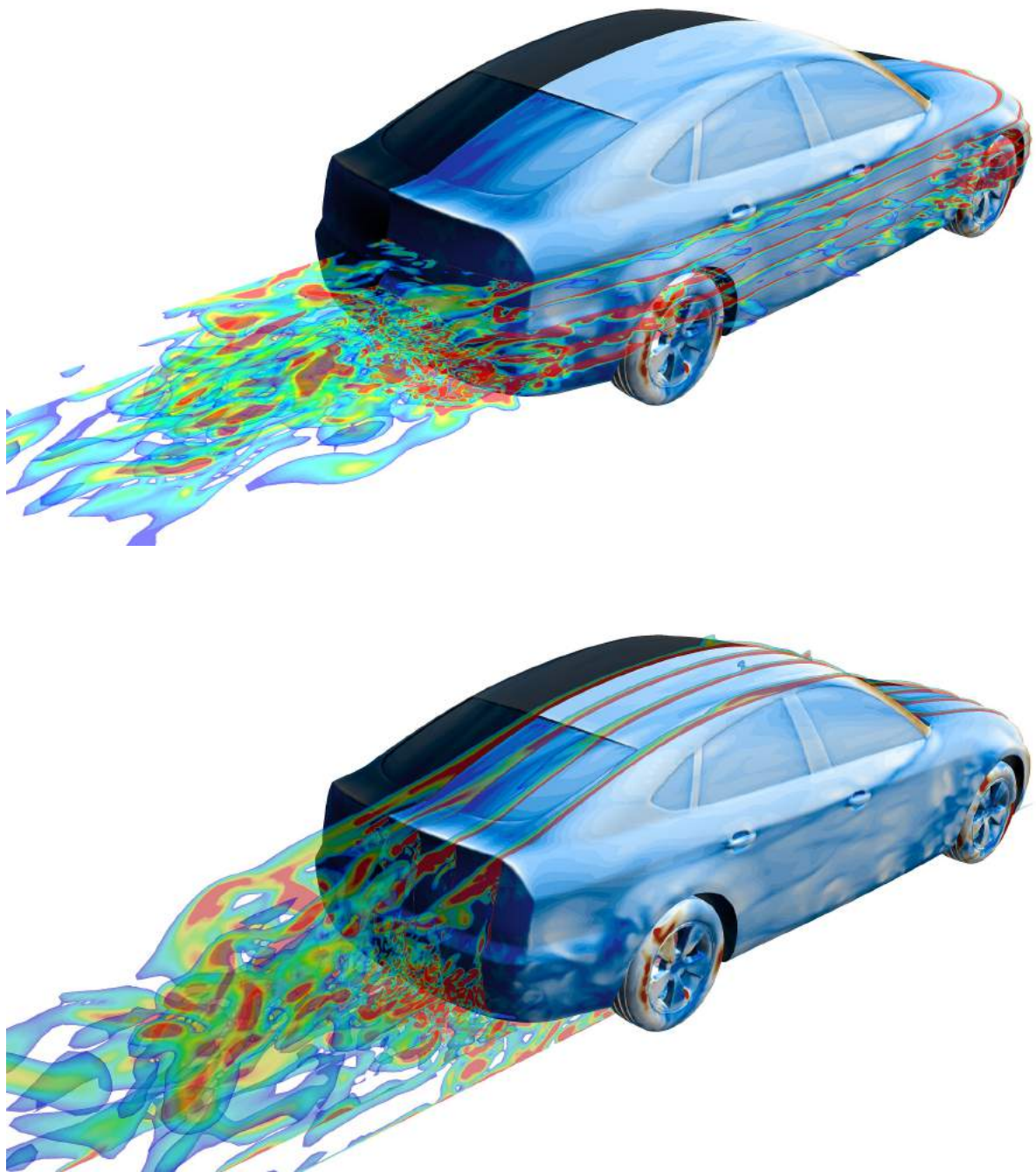


Figure 12.13: DES simulation: vorticity magnitude in xy planes (above) and zx planes (above).



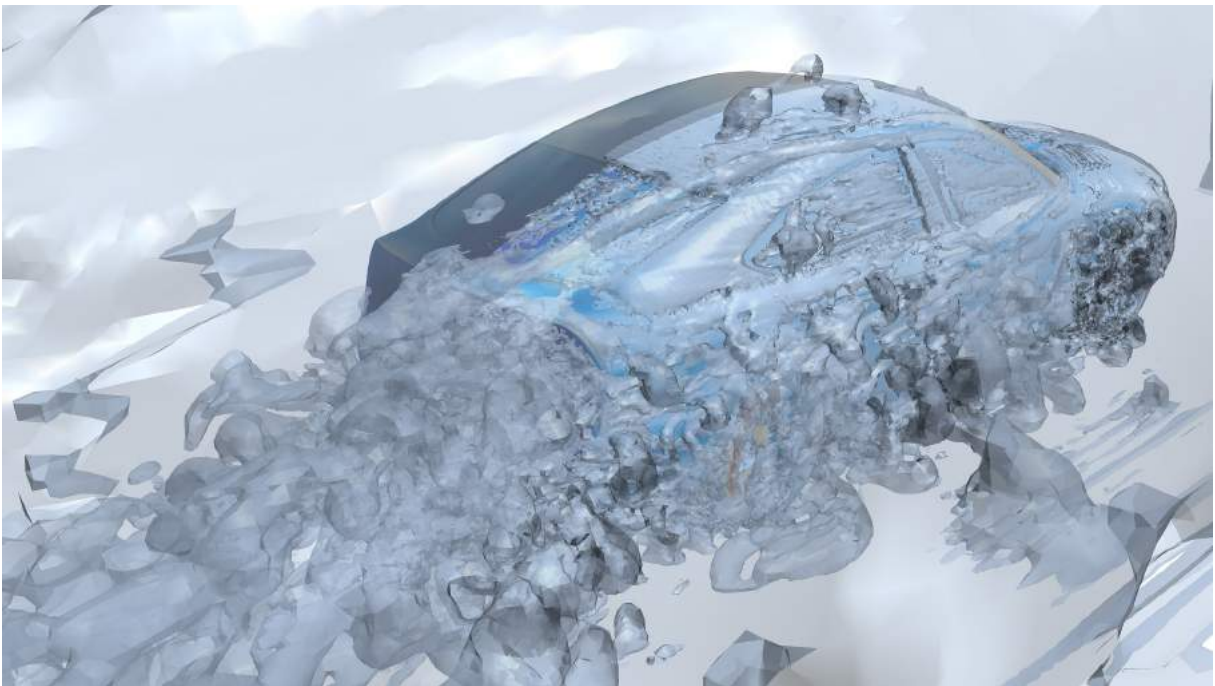
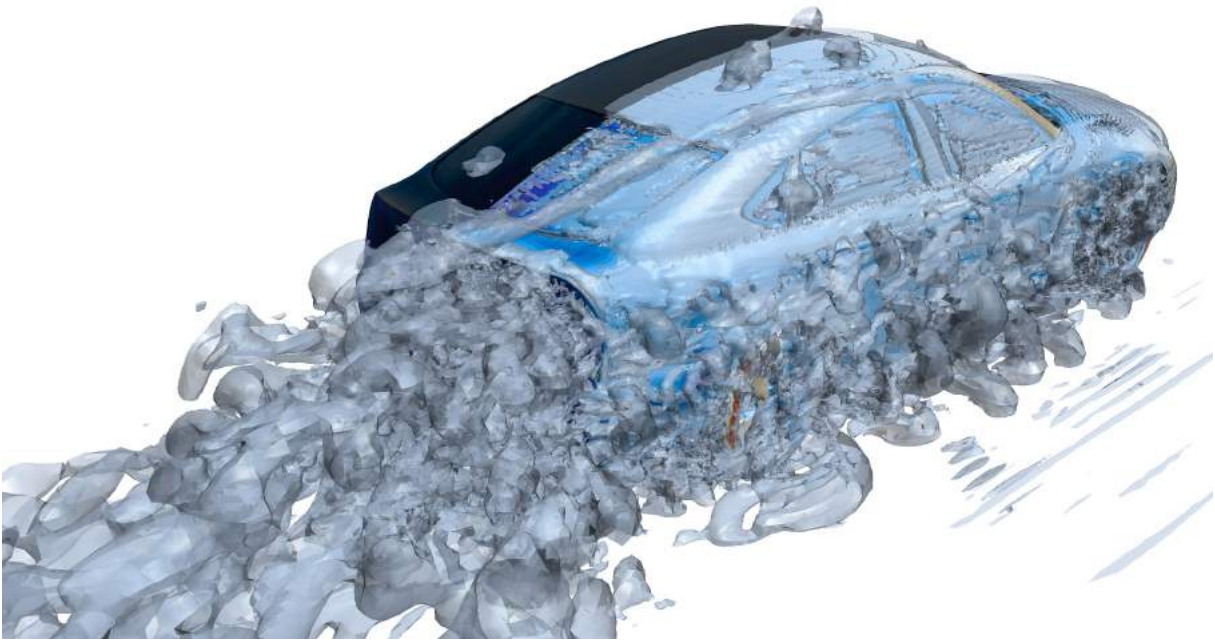


Figure 12.14: DES simulation: Q- (above) and Lambda-2 criteria (below) at  $1 \text{ rad/s}^2$ .



Figure 12.15: DES simulation: Q- (above) and Lambda-2 criteria (below) at  $10 \text{ rad/s}^2$ .



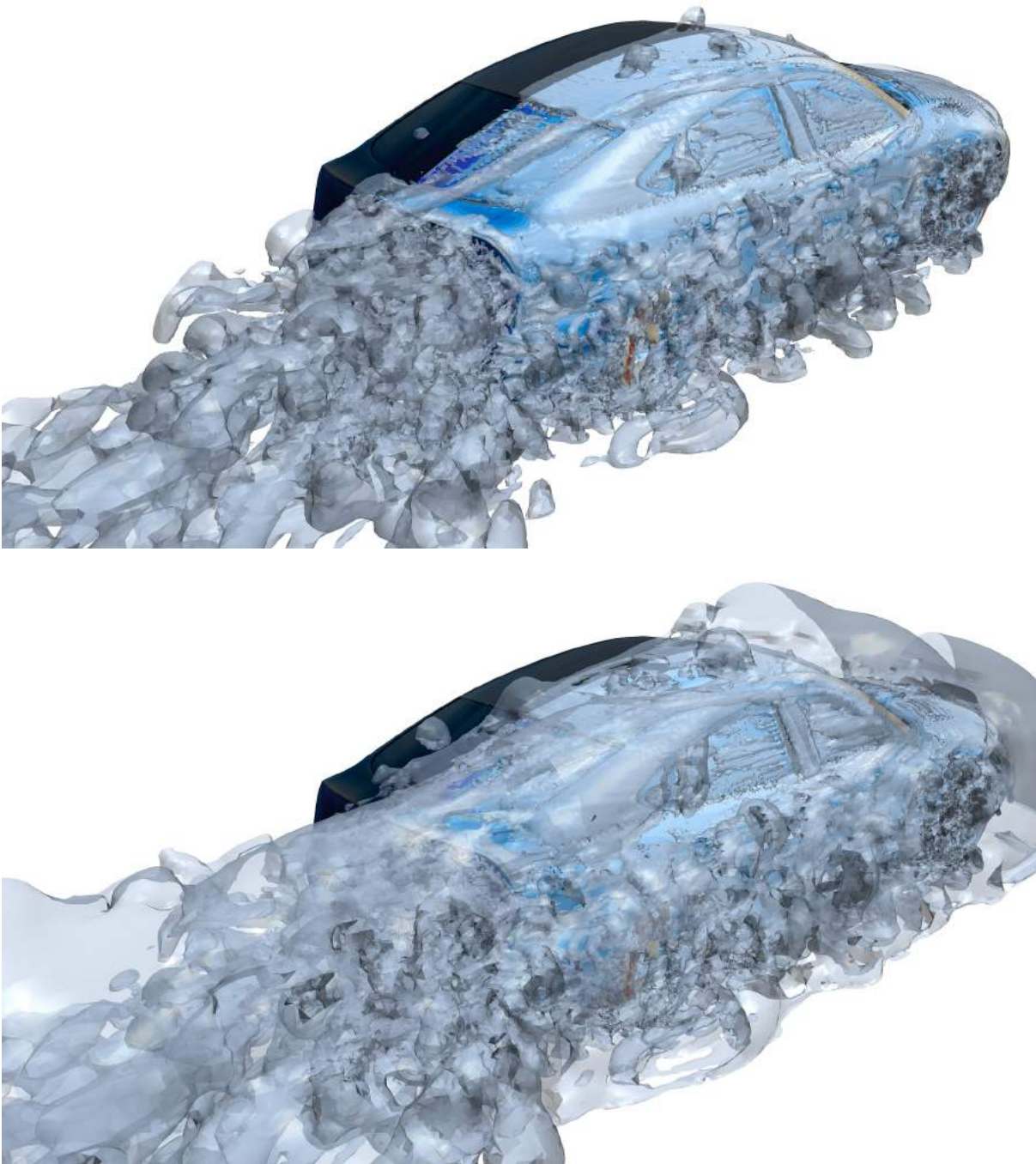


Figure 12.16: DES simulation: Q- (above) and Lambda-2 criteria (below) at  $100 \text{ rad/s}^2$ .

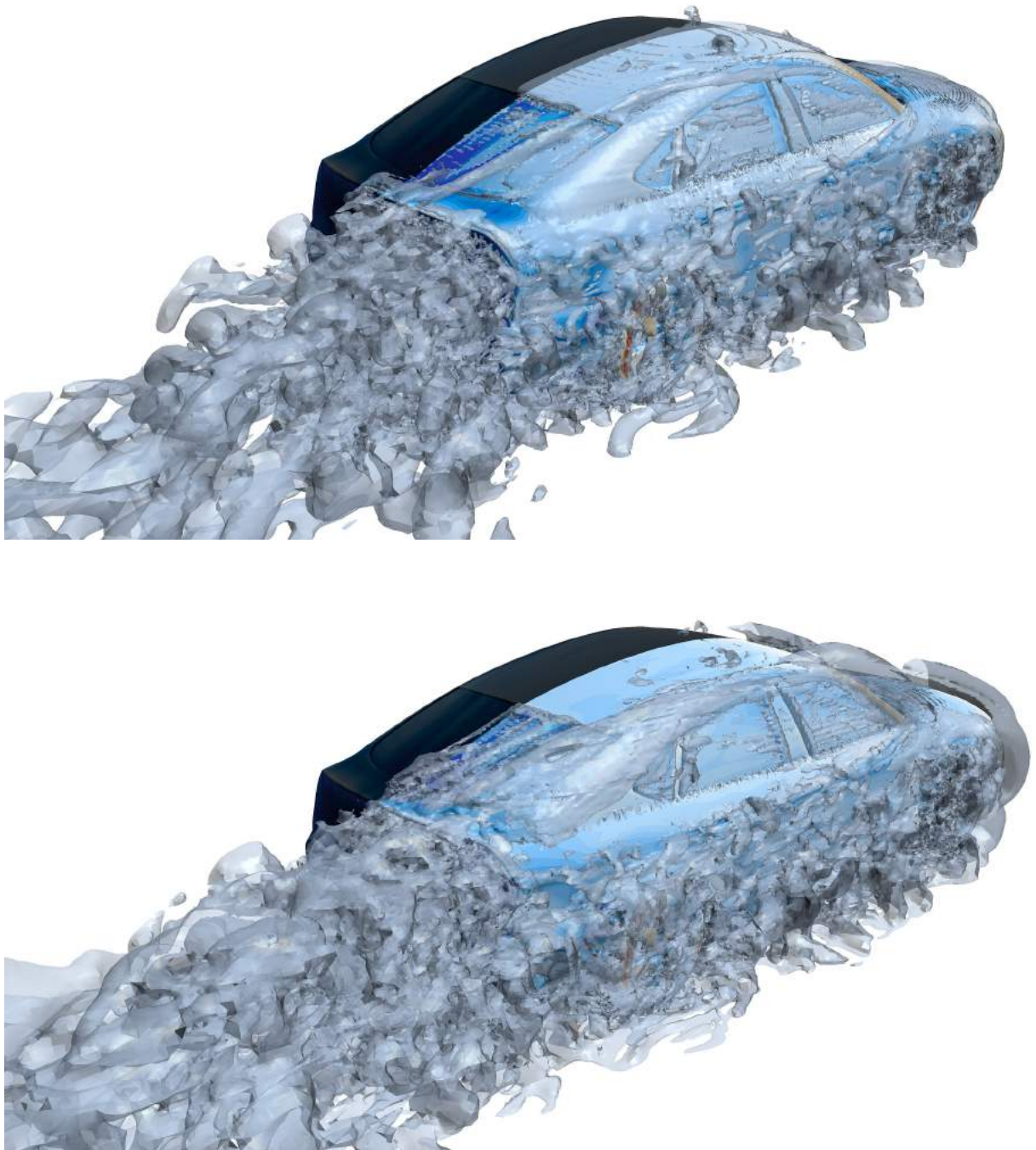


Figure 12.17: DES simulation: Q- (above) and Lambda-2 criteria (below) at  $1000 \text{ rad/s}^2$ .

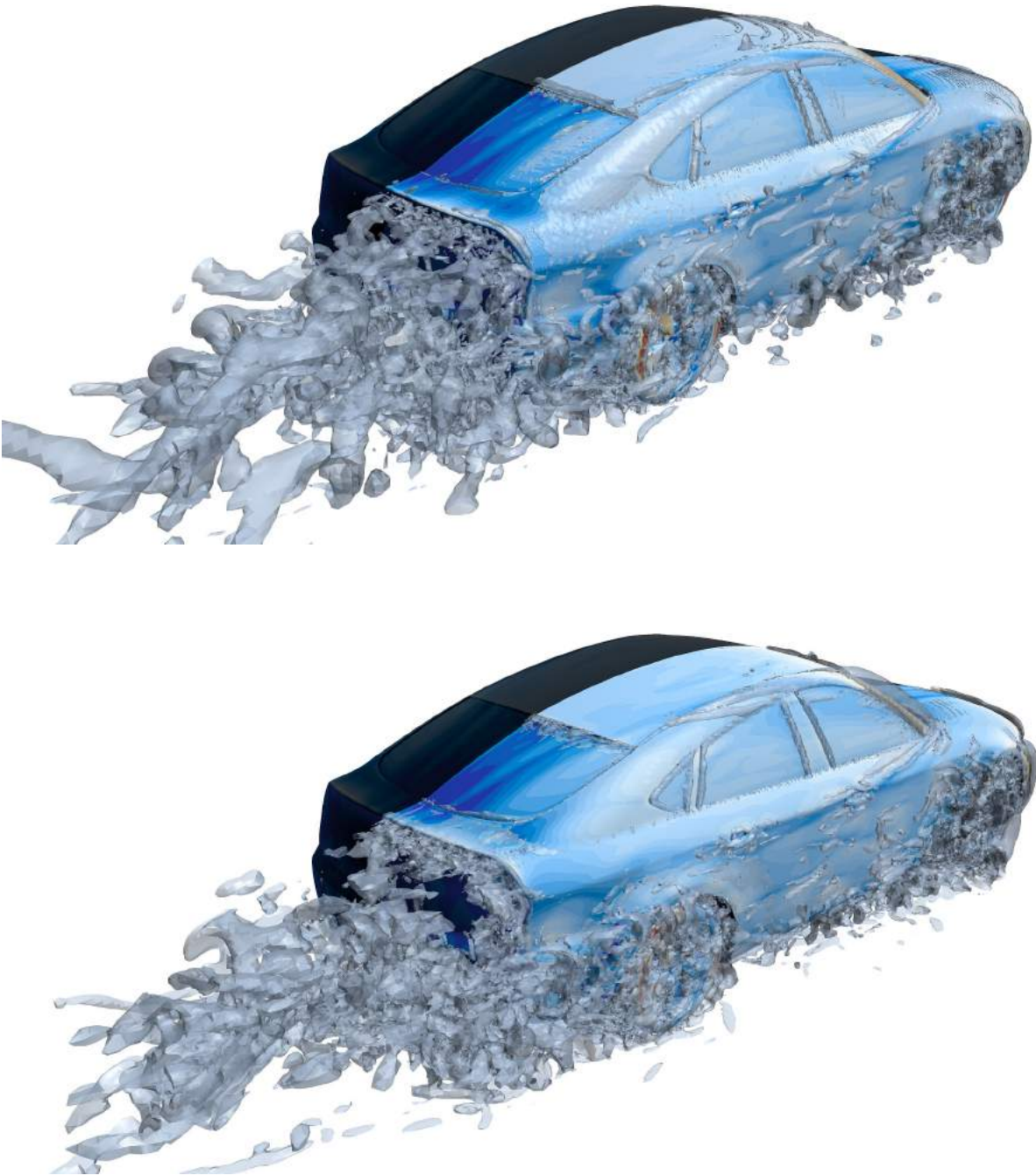


Figure 12.18: DES simulation: Q- (above) and Lambda-2 criteria (below) at  $10000 \text{ rad/s}^2$ .



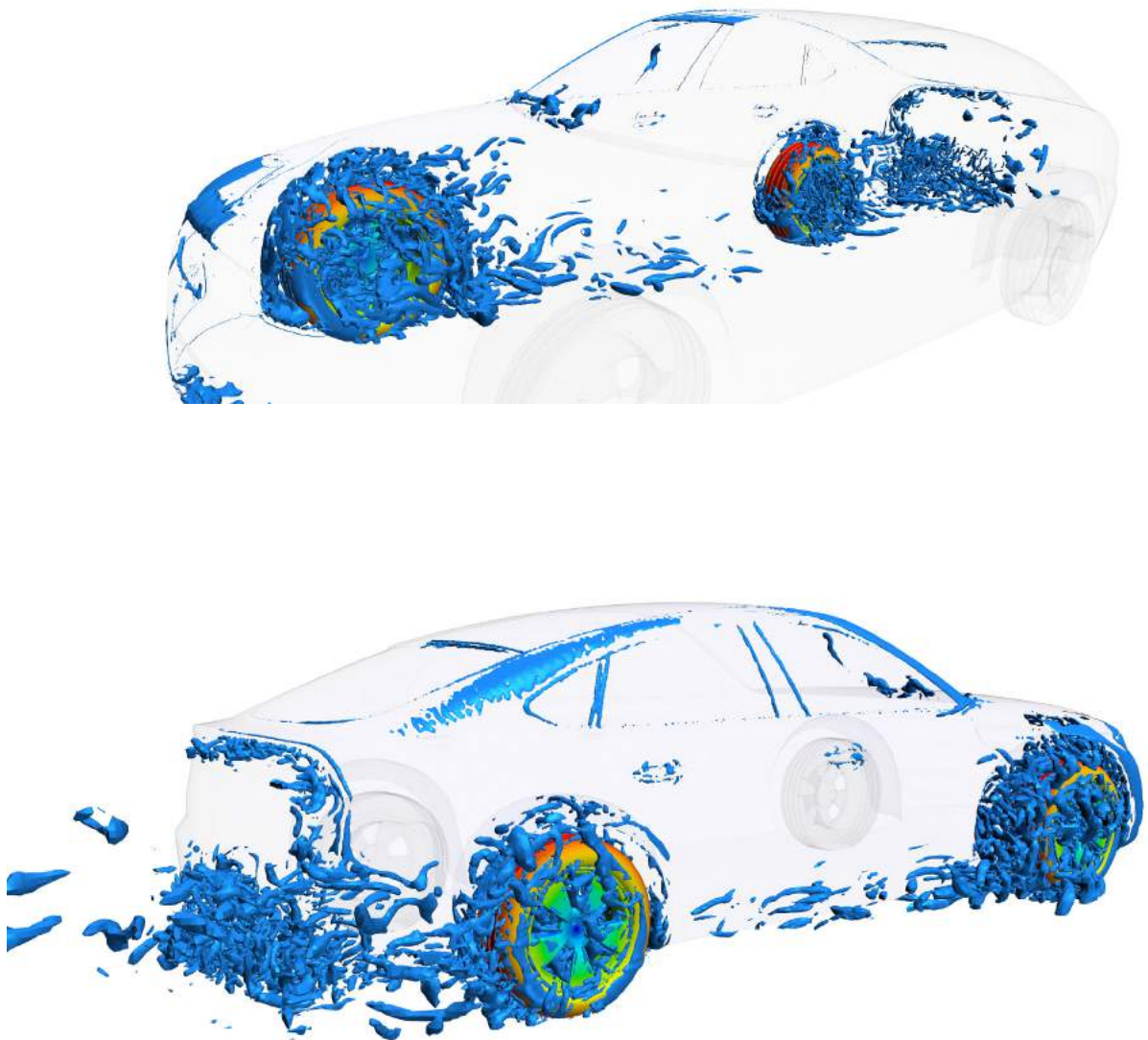


Figure 12.19: DES simulation: Q-criterion at  $10000 \text{ rad/s}^2$ , highlighting the vortex structures into the wheelhouses.

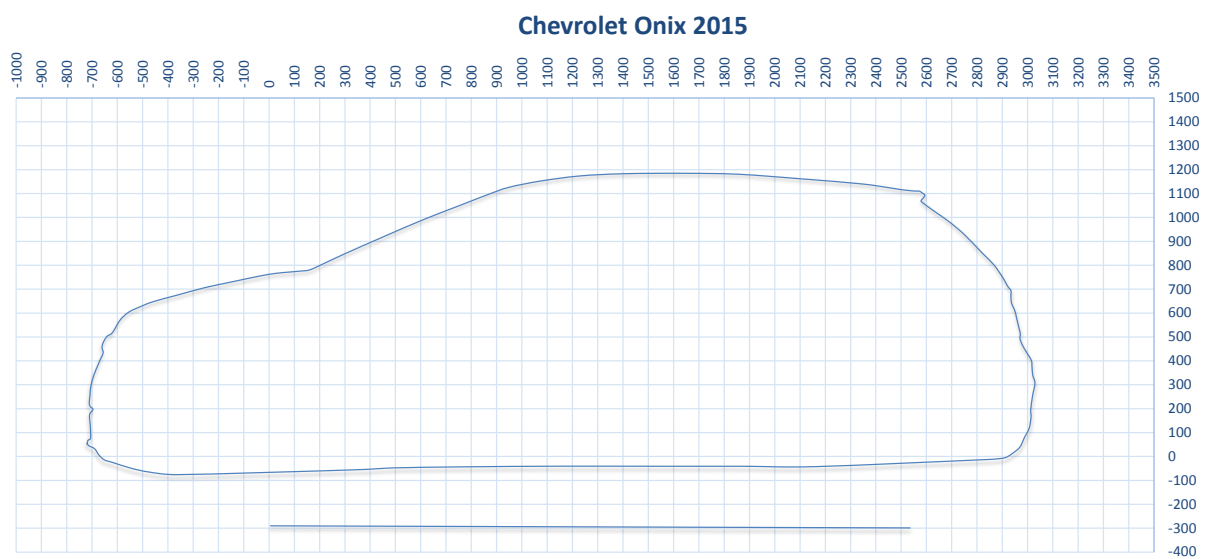
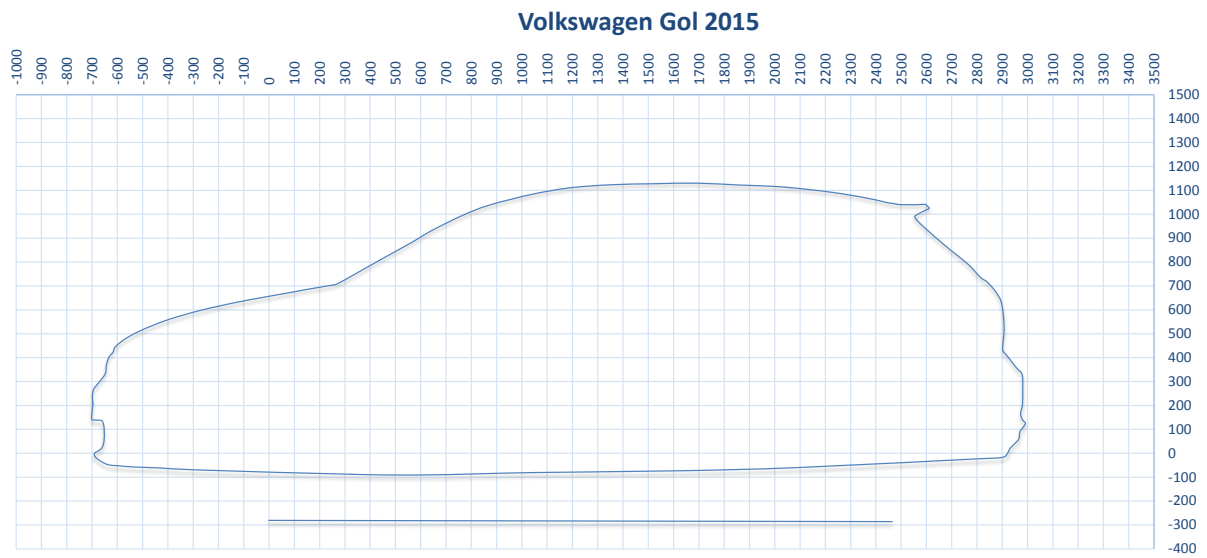
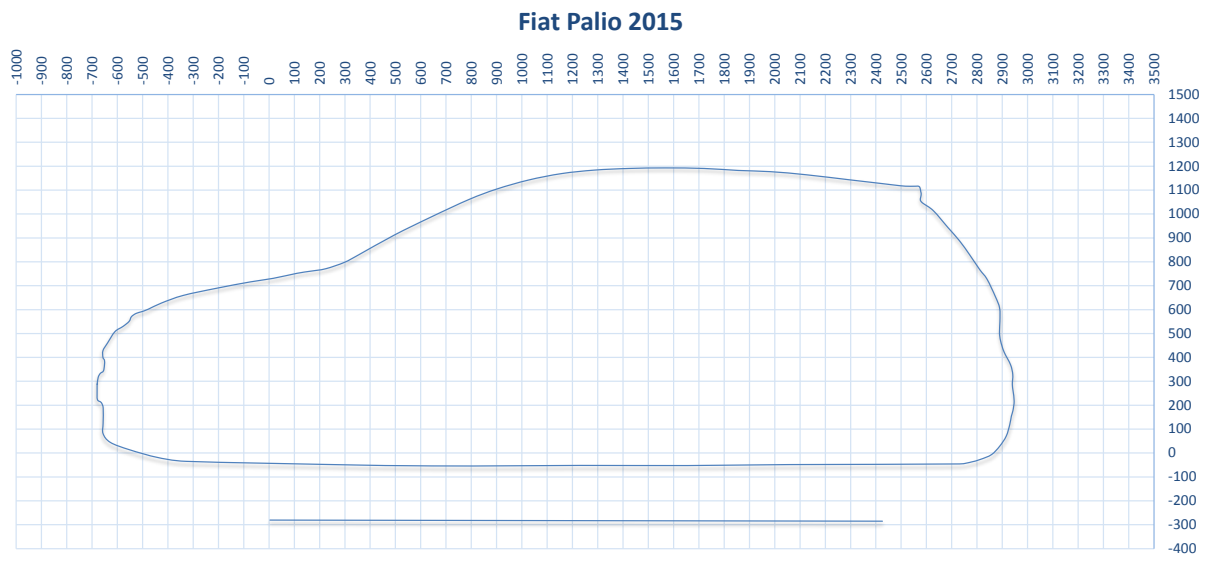


Figure 12.20: Hatch 2015 car profiles: Fiat Palio, Volkswagen Gol, and Chevrolet Onix.

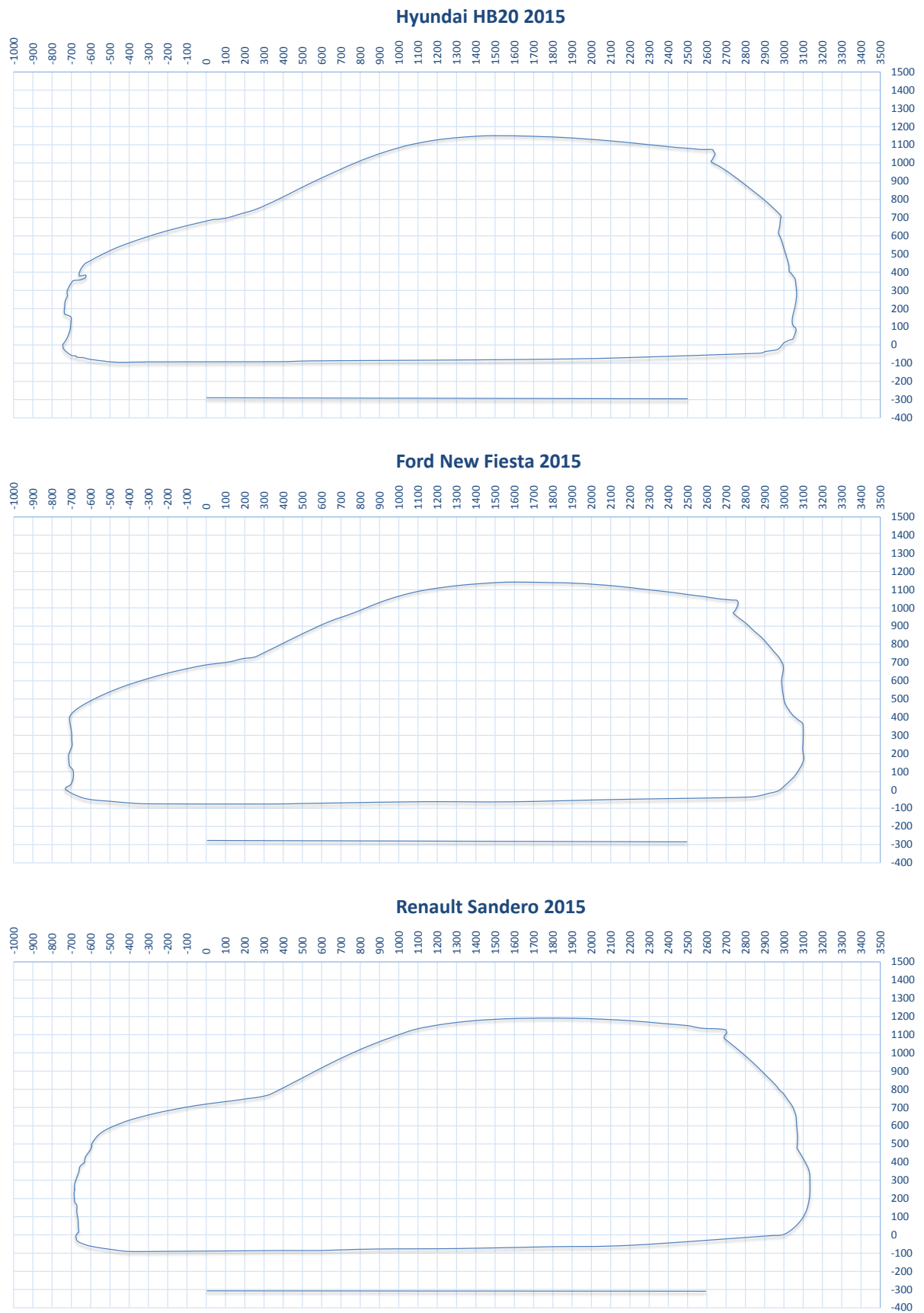


Figure 12.21: Hatch 2015 car profiles: Hyundai HB20, Ford New Fiesta, and Renault Sandero.

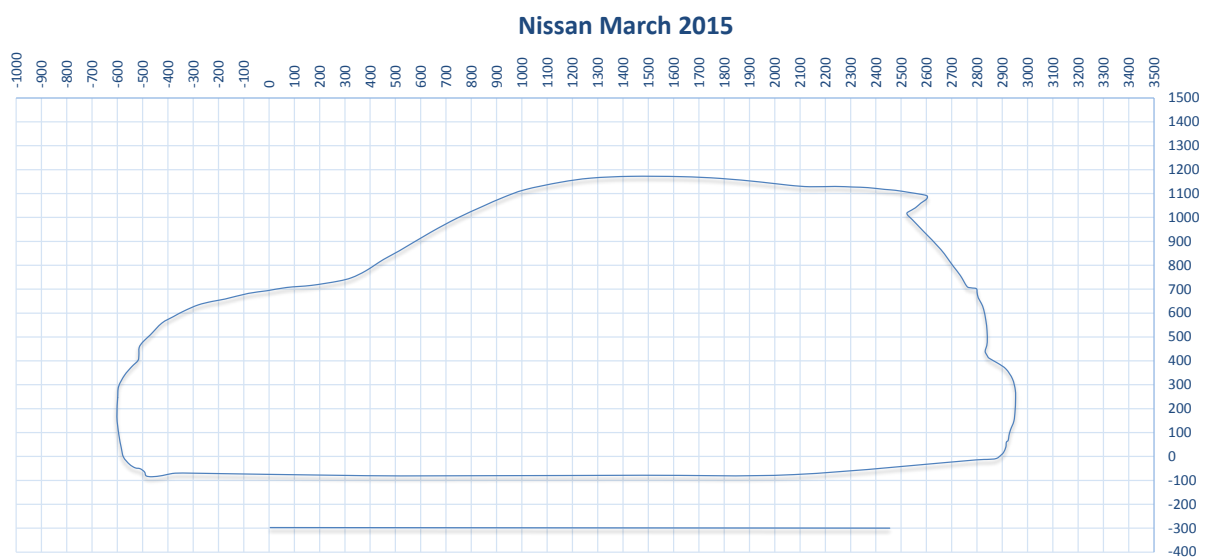
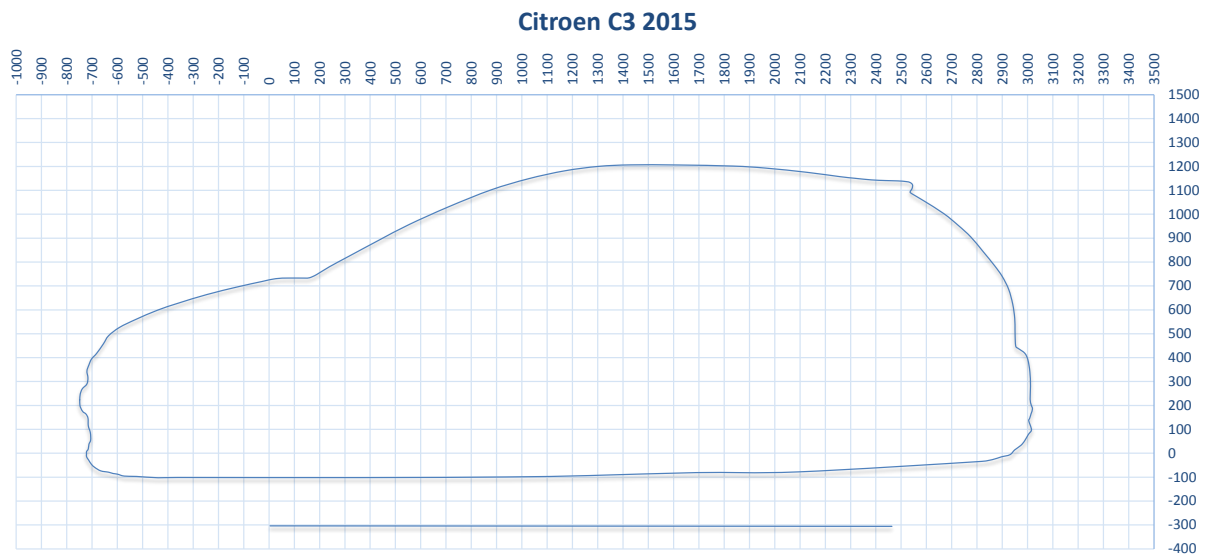
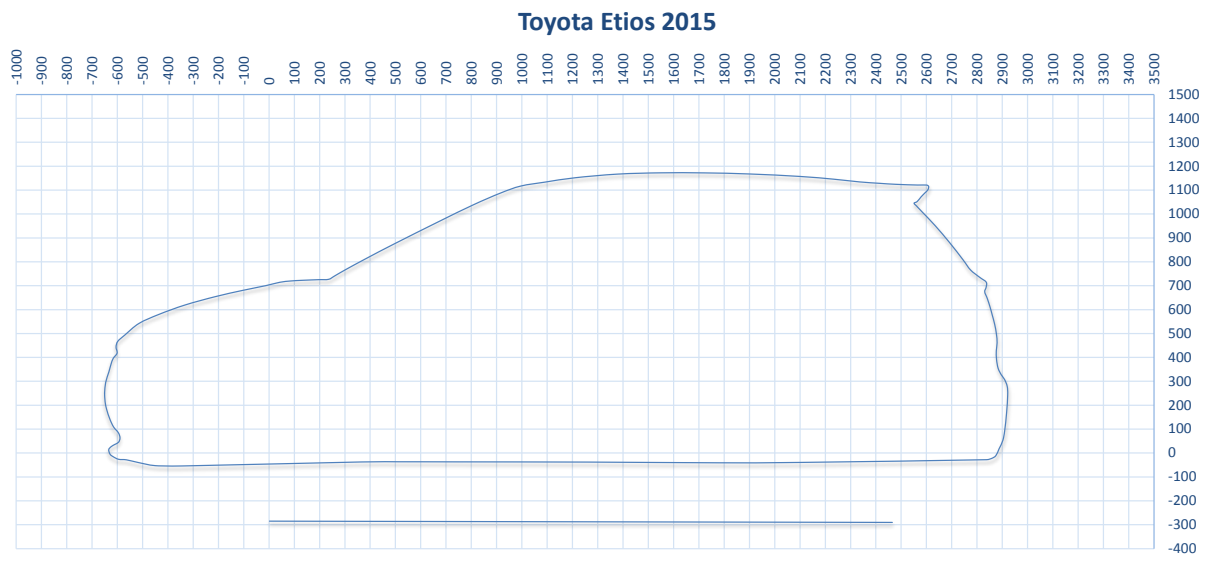


Figure 12.22: Hatch 2015 car profiles: Toyota Etios, Ford New Fiesta, and Renault Sandero.

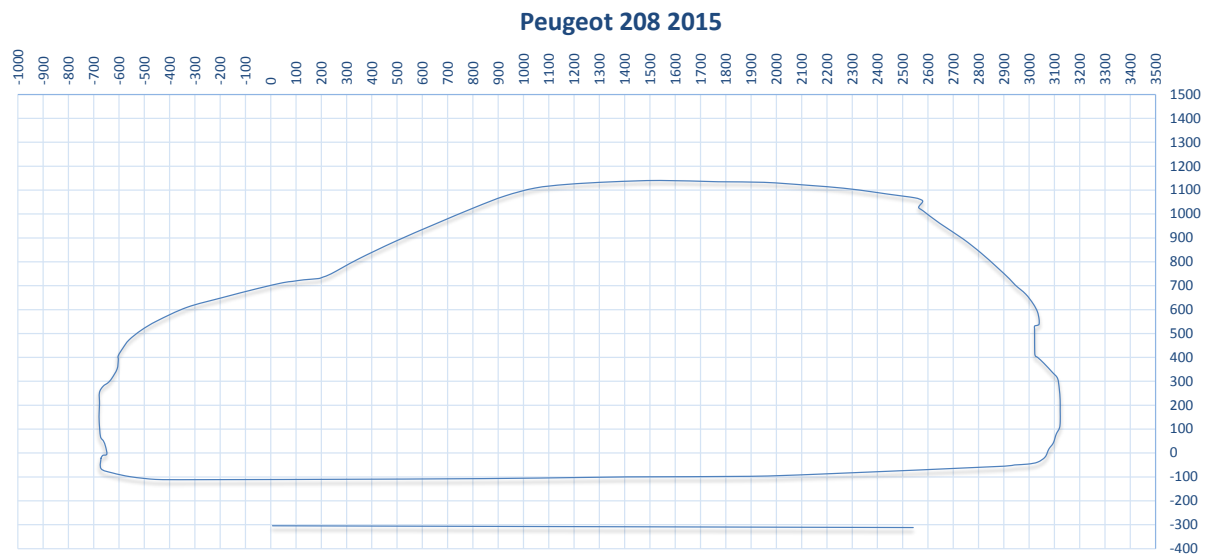


Figure 12.23: Hatch 2015 car profiles: Peugeot 208.

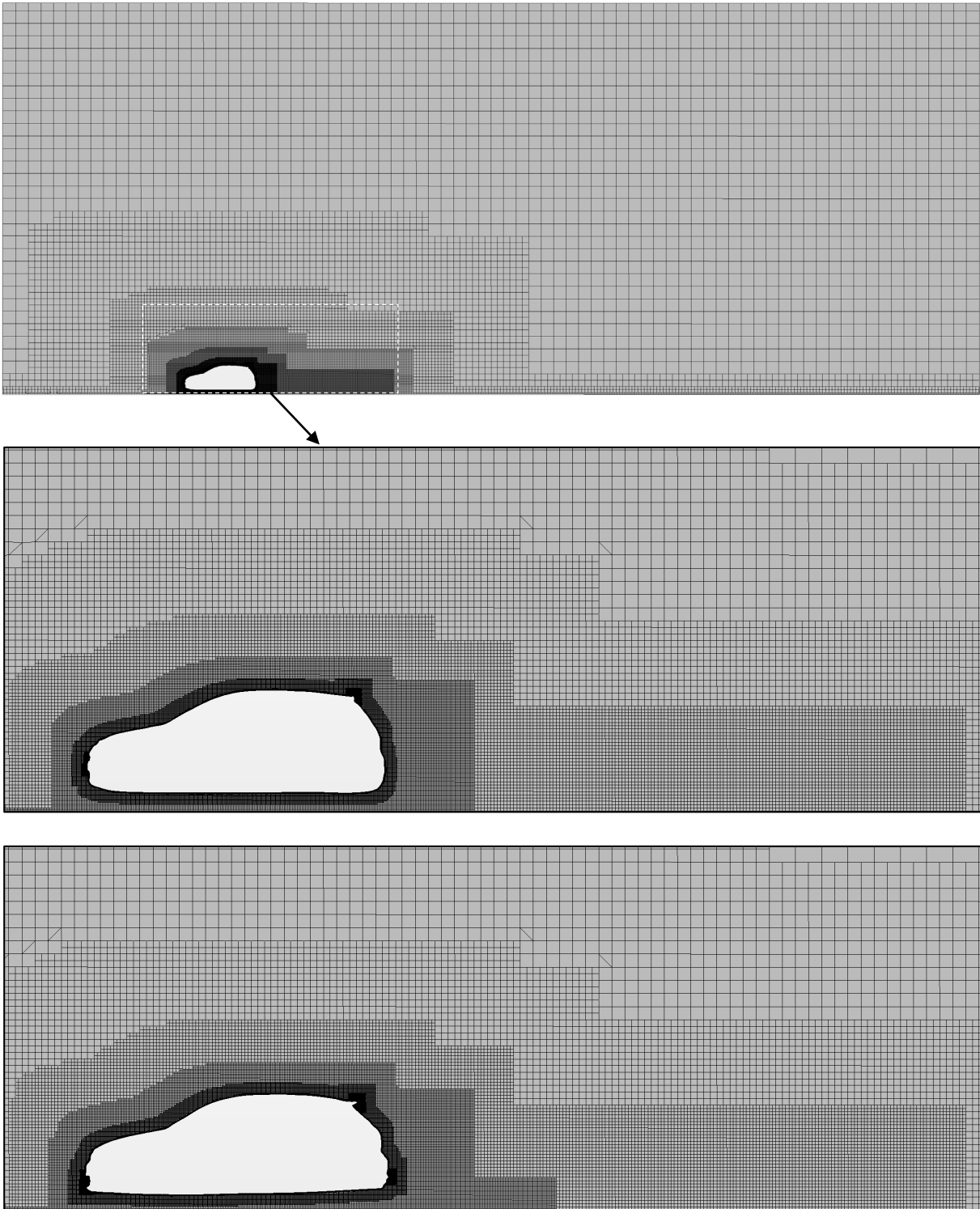


Figure 12.24: Hatch 2015 car meshing: Fiat Palio, and Volkswagen Gol.

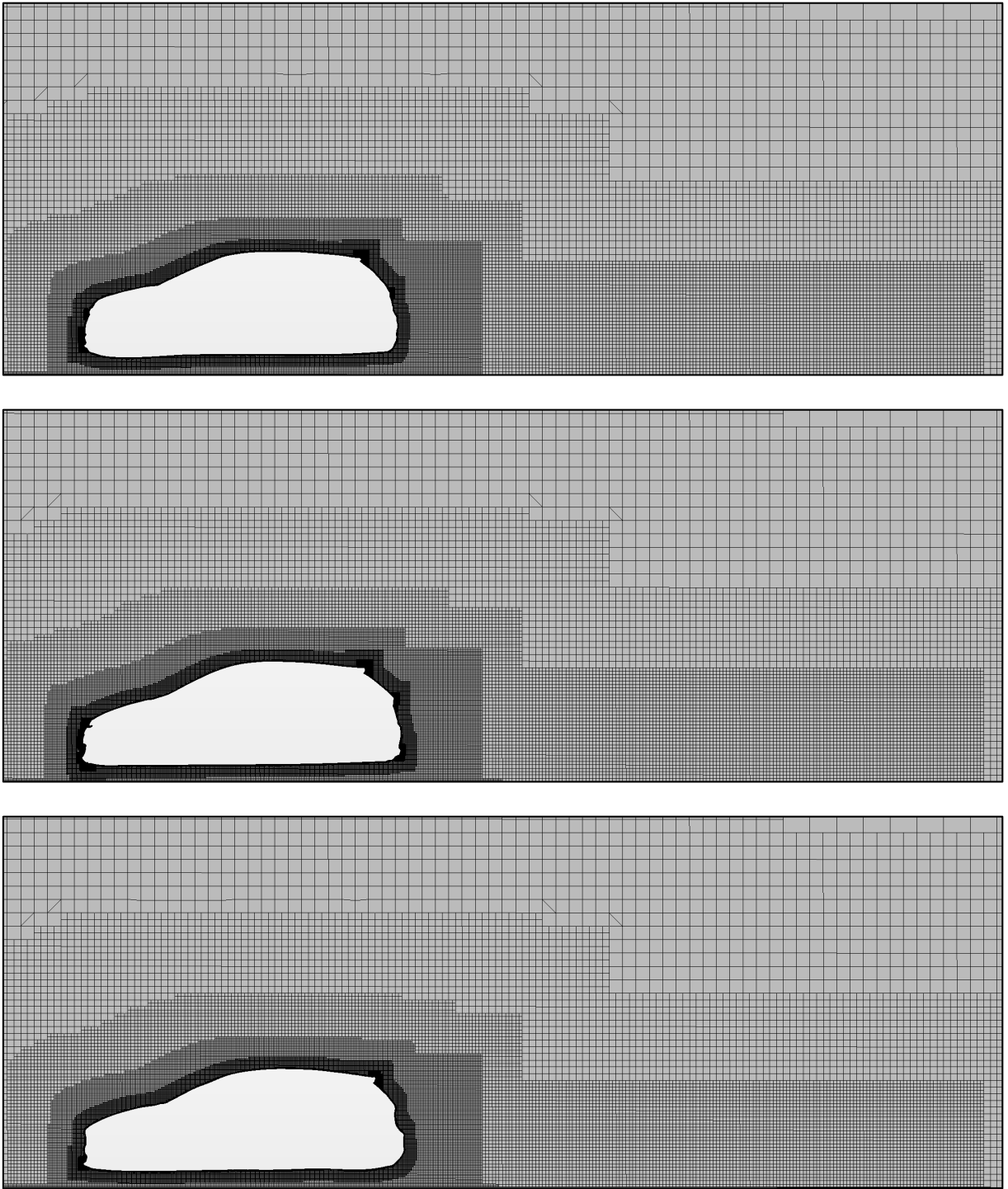


Figure 12.25: Hatch 2015 car meshing: Chevrolet Onix, Hyundai HB20, and Ford New Fiesta.

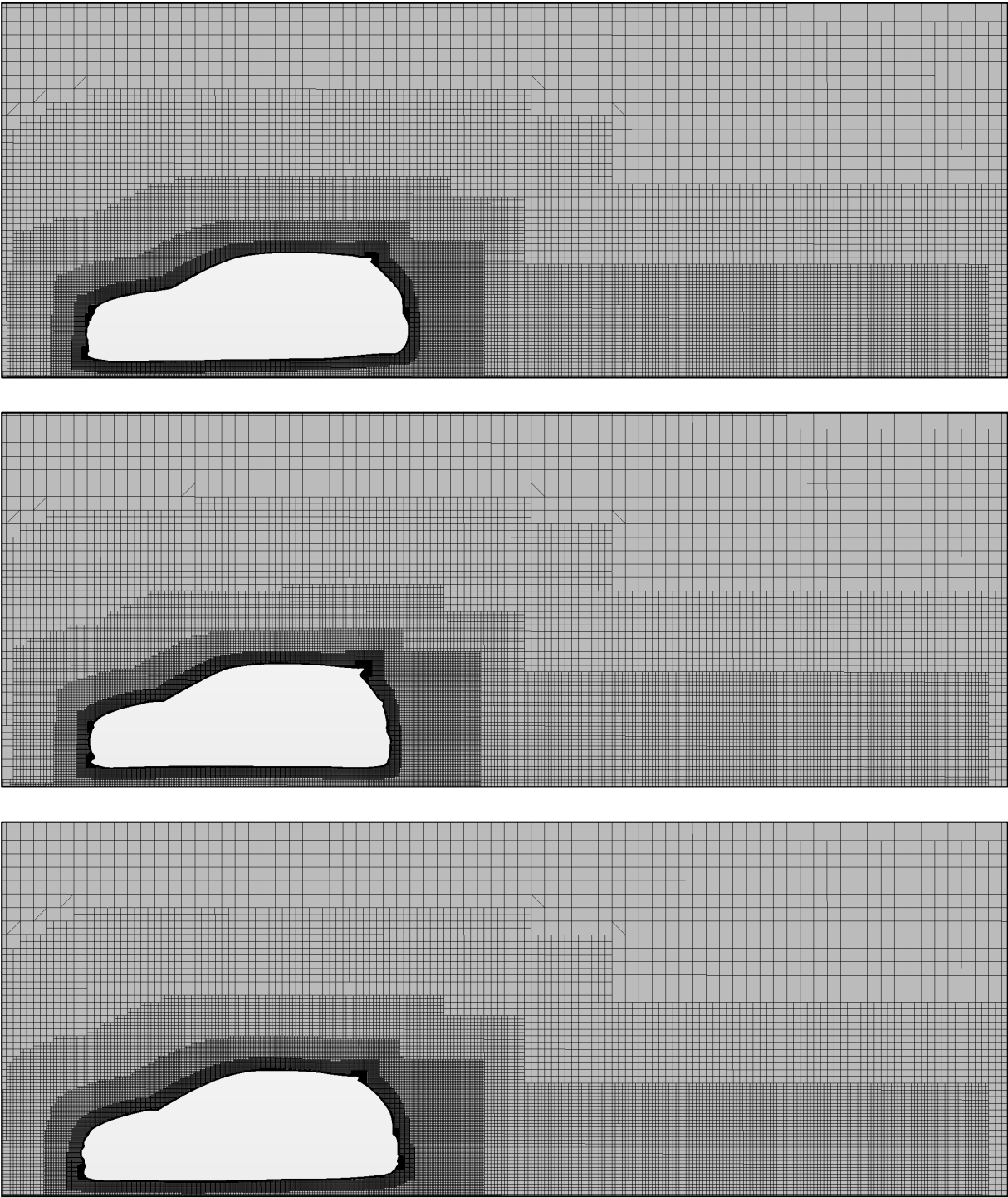


Figure 12.26: Hatch 2015 car meshing: Renault Sandero, Toyota Etios, and Citroen C3.



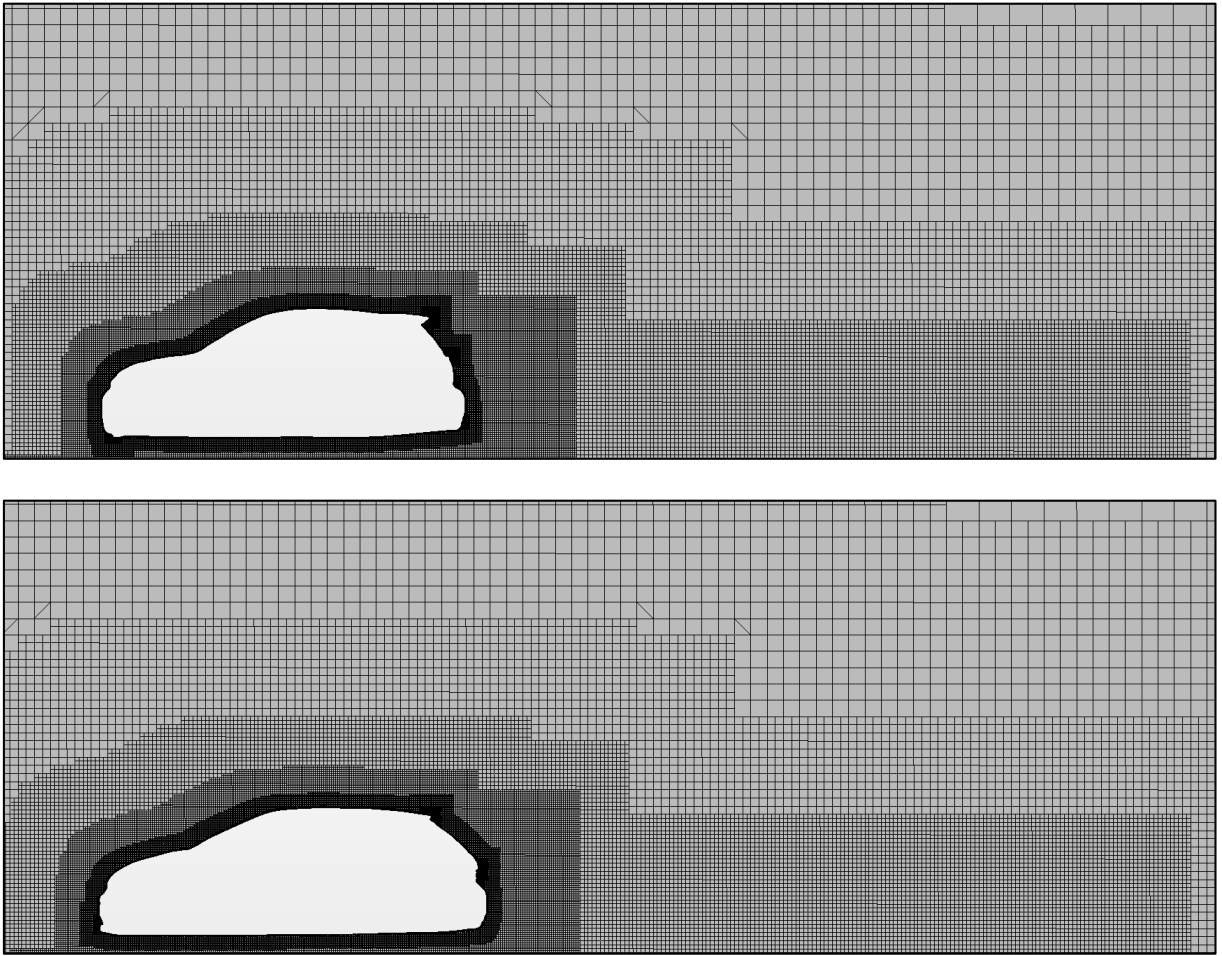


Figure 12.27: Hatch 2015 car meshing: Nissan March, and Peugeot 208.



(a) -050 x 200 - H



(b) -060 x 600 - H



(c) 000 x 200 - H



(d) 000 x 600 - H



(e) 100 x 200 - H



(f) 100 x 600 - H



(g) 250 x 200 - H



(h) 250 x 600 - H



(i) 550 x 200 - H



(j) 100 x 700 - V

Figure 12.28: Rear car view: the ten positions of symmetric tailpipes tested.



(a) -050 x 200 - H



(b) -060 x 600 - H



(c) 000 x 200 - H



(d) 000 x 600 - H



(e) 100 x 200 - H



(f) 100 x 600 - H



(g) 250 x 200 - H



(h) 250 x 600 - H



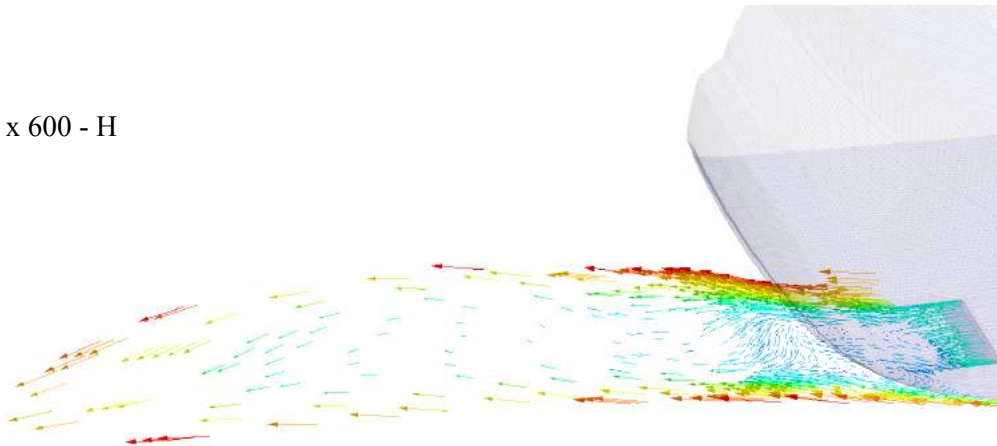
(i) 550 x 200 - H



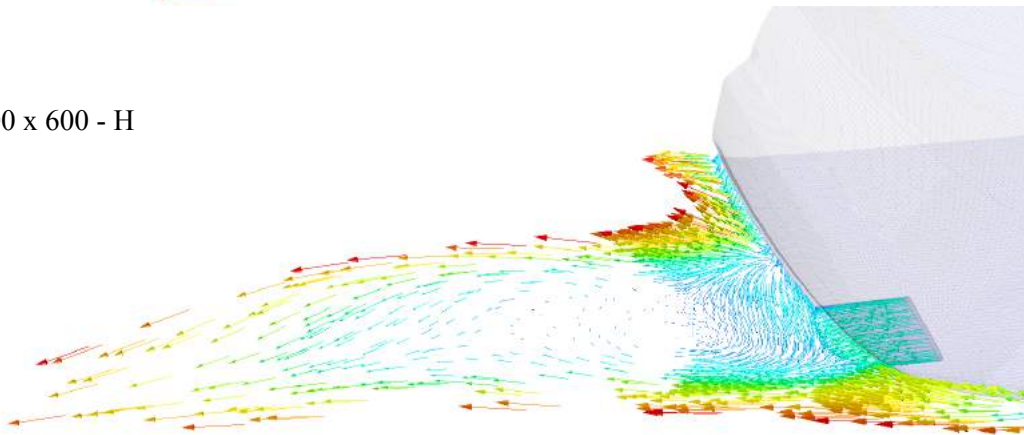
(j) 100 x 700 - V

Figure 12.29: Perspective view: the ten positions of symmetric tailpipes tested.

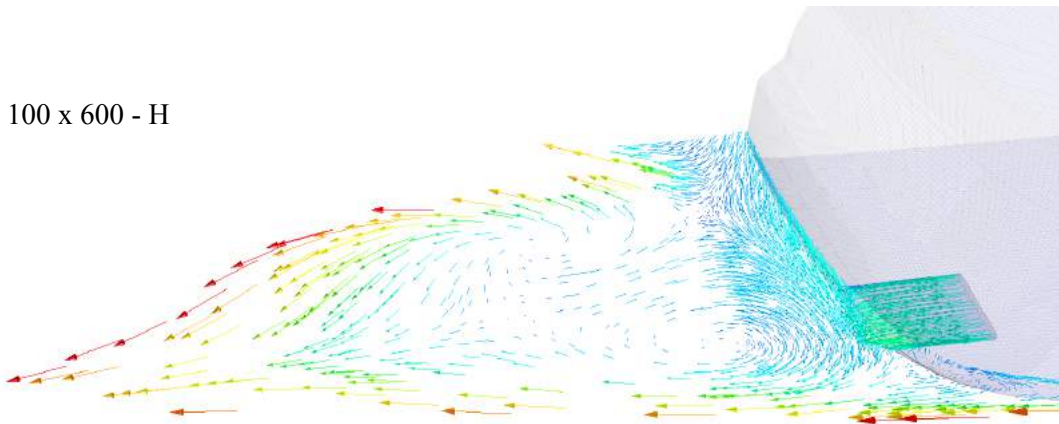
(i) -060 x 600 - H



(ii) 000 x 600 - H



(iii) 100 x 600 - H



(iv) 250 x 600 - H

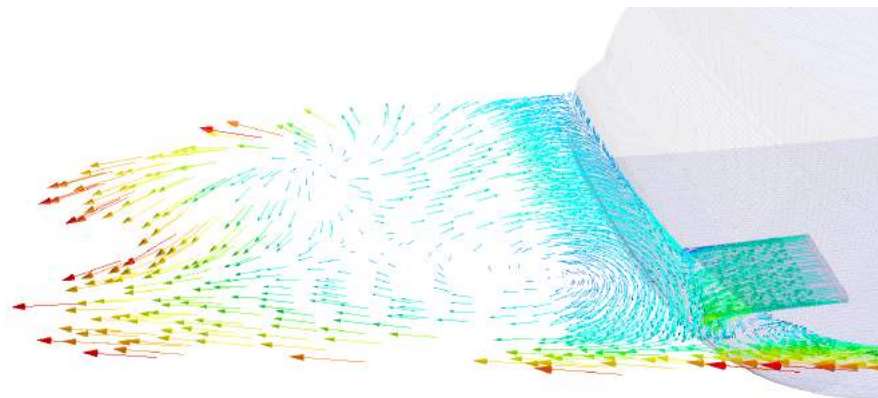
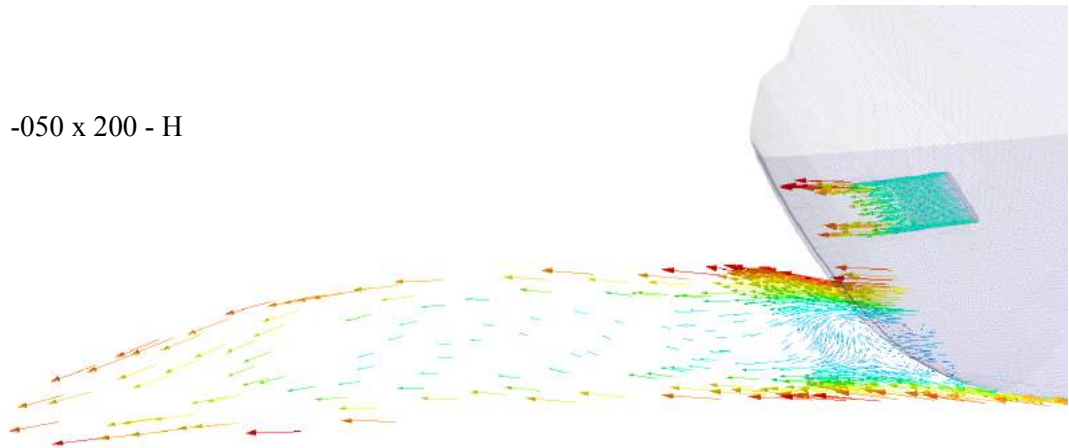
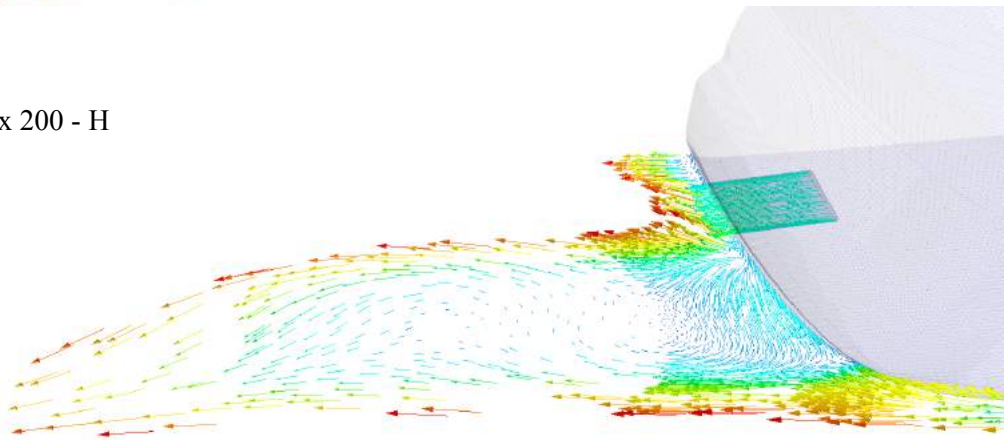


Figure 12.30: Vector velocity field crossing the tailpipes in the  $zx$  plane (part A).

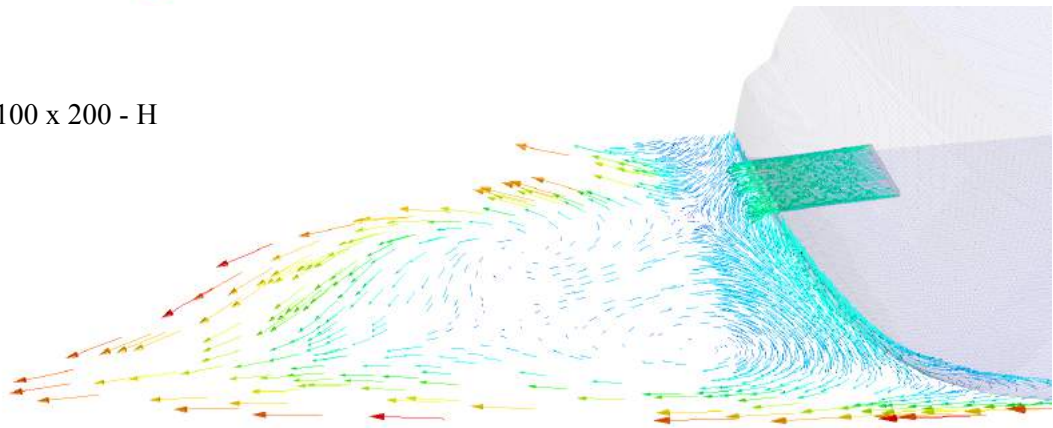
(v) -050 x 200 - H



(vi) 000 x 200 - H



(vii) 100 x 200 - H



(viii) 250 x 200 - H

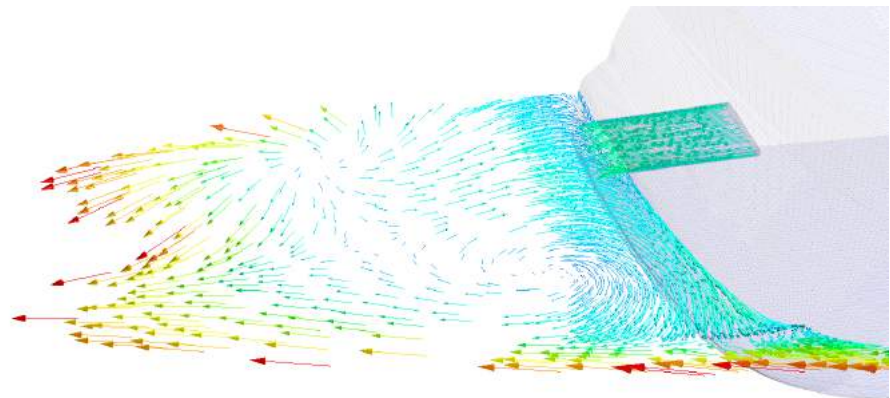
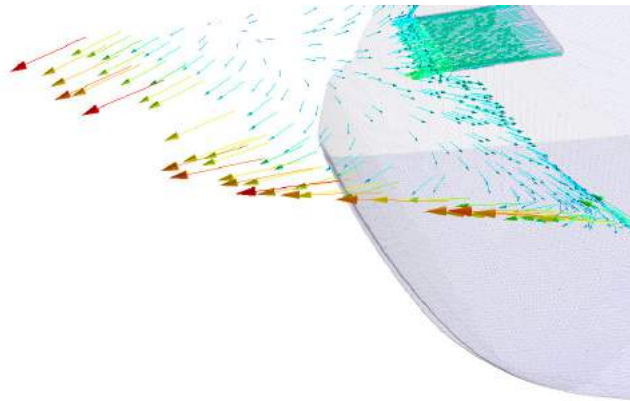


Figure 12.31: Vector velocity field crossing the tailpipes in the zx plane (part B).



(ix) 550 x 200 - H



(x) 100 x 700 - V

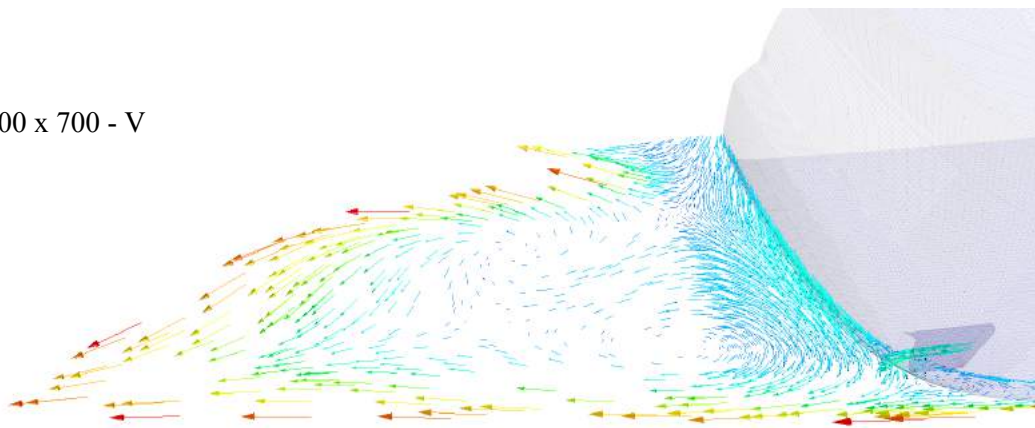


Figure 12.32: Vector velocity field crossing the tailpipes in the  $zx$  plane (part C).

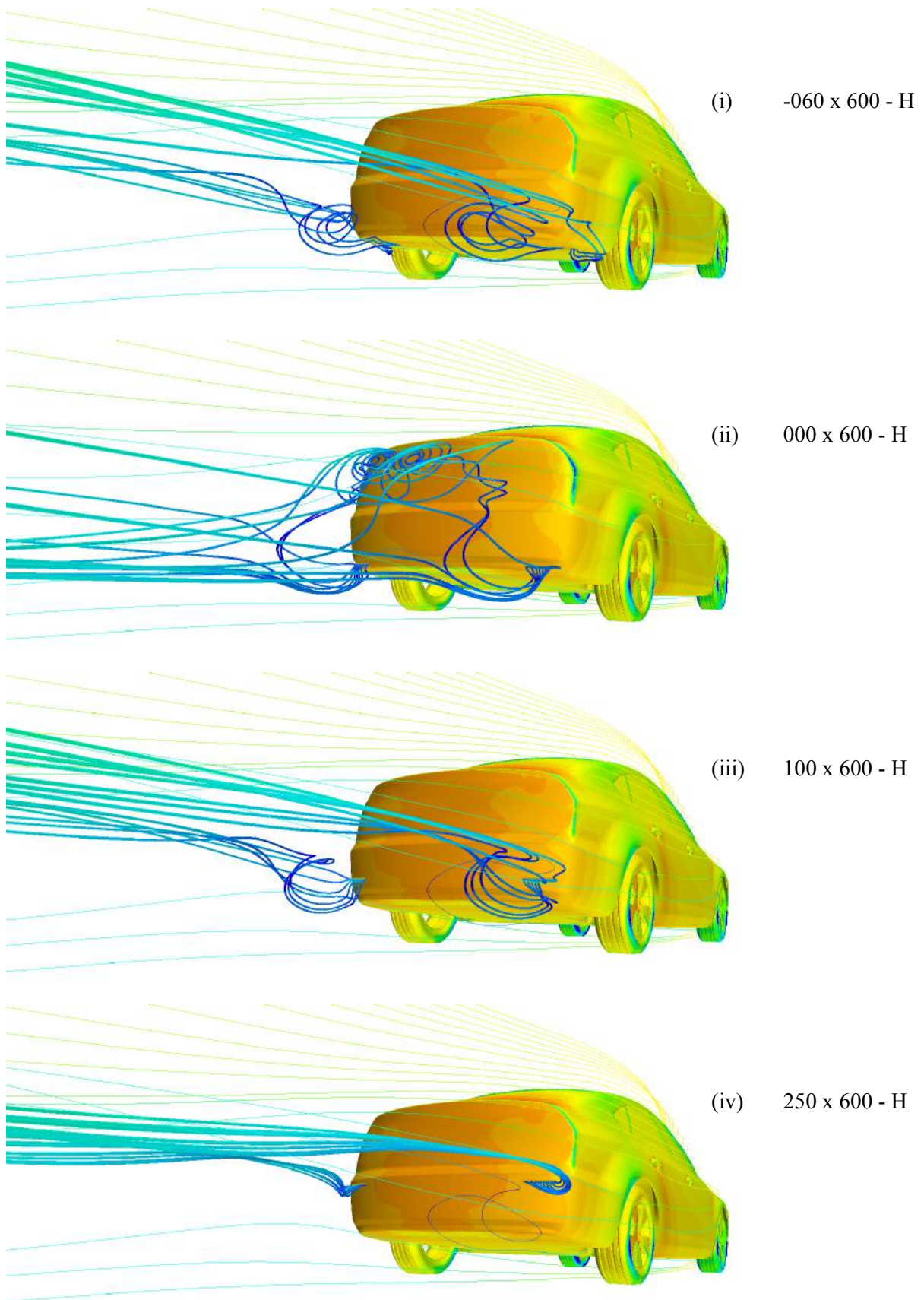


Figure 12.33: Streamlines from exhaust system (part A).

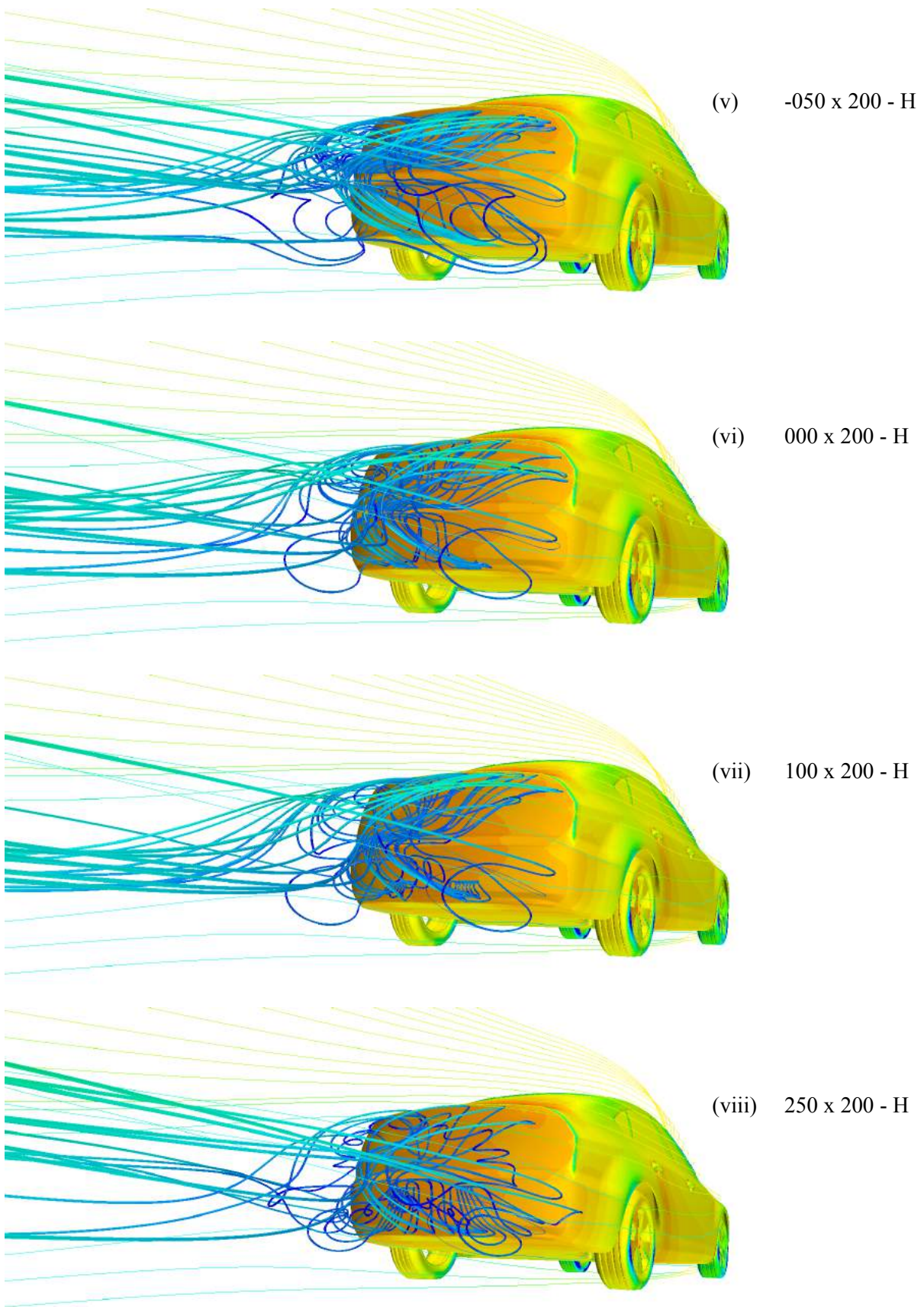


Figure 12.34: Streamlines from exhaust system (part B).



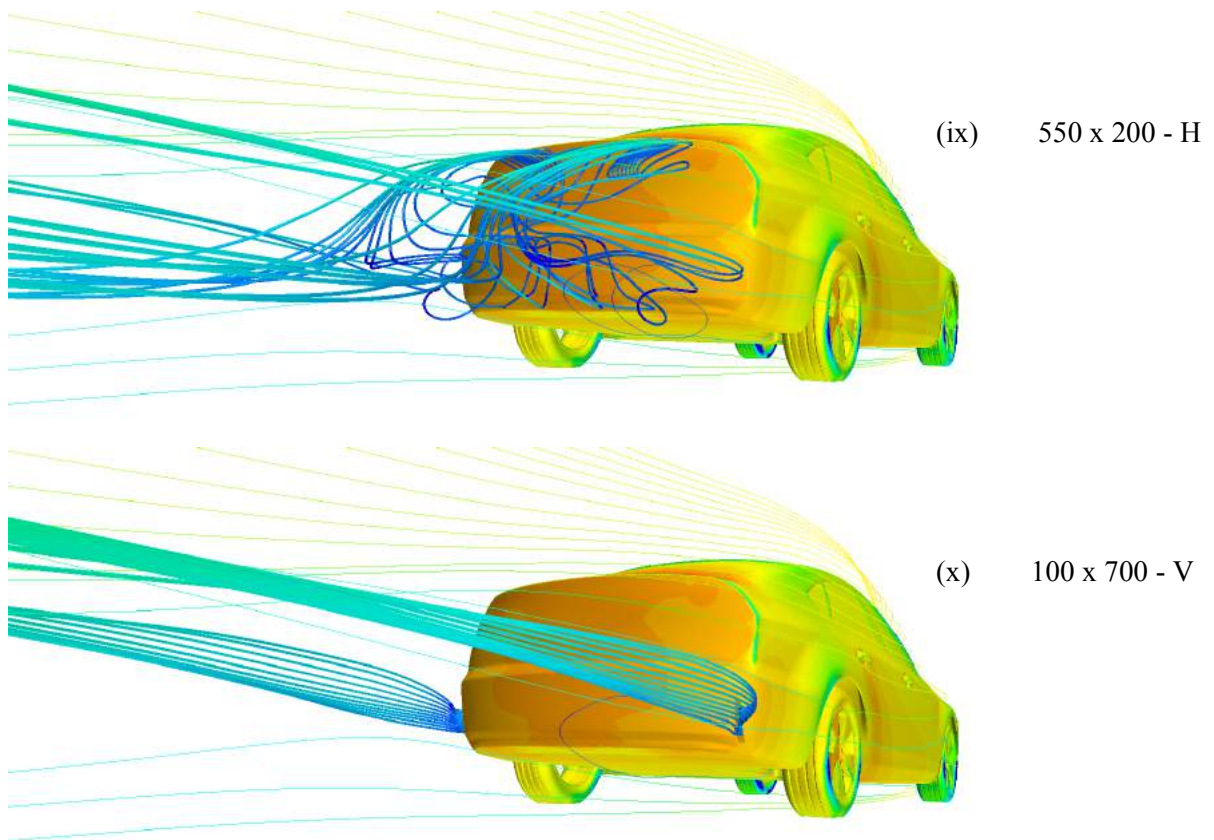


Figure 12.35: Streamlines from exhaust system (part C).